UNIVERSITÉ DU QUÉBEC À TROIS-RIVIÈRES

VALORISATION DES RÉSIDUS DE BOIS DE CONSTRUCTION, DE RÉNOVATION ET DE DÉMOLITION (CRD) EN BIOCHARBON DE VALEUR

VALORIZATION OF CONSTRUCTION, RENOVATION, AND DEMOLITION (CRD) WOOD RESIDUES TO VALUABLE BIOCHAR

THÈSE PRÉSENTÉE COMME EXIGENCE PARTIELLE DU DOCTORAT EN SCIENCES ET GÉNIE DES MATÉRIAUX LIGNOCELLULOSIQUES - 3148

PAR

ARAVIND GANESAN

Août 2025

`

UNIVERSITÉ DU QUÉBEC À TROIS-RIVIÈRES

DOCTORAT EN SCIENCES ET GÉNIE DES MATÉRIAUX LIGNOCELLULOSIQUES - 3148 (Ph.D)

Direction de recherche :

Simon Barnabé, Ph.D.	Université du Québec à Trois-Rivières
Prénom et nom	directeur de recherche
Patrice Mangin, Ph.D.	Université du Québec à Trois-Rivières
Prénom et nom	codirecteur de recherche

Jury d'évaluation :

Bruna Rego De Vasconcelos, Ph.D.	Université de Sherbrooke
Prénom et nom	évaluatrice externe
Paul Stuart, Ph.D., Ing.	Polytechnique Montréal
Prénom et nom	évaluateur externe
Samaneh Shahgaldi, Ph.D.	Université du Québec à Trois-Rivières
Prénom et nom	évaluatrice interne
Simon Barnabé, Ph.D.	Université du Québec à Trois-Rivières
Prénom et nom	directeur de recherche
Patrice Mangin, Ph.D.	Université du Québec à Trois-Rivières
Prénom et nom	codirecteur de recherche

Thèse soutenue le 25 08 2025

DEDICATION

I dedicate this Ph.D to my wonderful family, professors, mentors, friends, and colleagues without whom this would not have been possible!

ACKNOWLEDGEMENTS

Firstly, I would like to extend my heartfelt gratitude to the almighty, for keeping me safe and healthy during the course of this Ph.D program. I would like to thank from the bottom of my heart, my dear wife Kripa Sridhar, my parents Ganesan Venkatraman and Padma Ganesan, my sister Arthi Aadhithya, my brother-in-law Aadhithya, my nephew Advaith, my niece Aadhya, and my kind in-laws Mr. Sridhar and Mrs. Neela Sridhar, and last but not least, my sister-in-law Krithika Sridhar, for their unwavering support throughout this journey.

As part of the leadership group, I would like to thank Professor Patrice Mangin for recruiting me as a doctoral candidate and giving me the first opportunity to study in Canada, that too immediately after a tumultuous global pandemic. Dr. Olivier Rezazgui, man oh man, the person who stood beside me like an irreplaceable pillar of support right from the first day of my arrival here in Trois-Rivières – no amount of words in the English Language Dictionary can help me explain how encouraging, kind, straightforward, and collaborative this gentleman was and continues to be, towards me. The man has been one side of the coin in my career, guided me to become a better researcher each day, and strives to give the best of his answers to all my mind-numbingly silly questions, be it subjective or non-subjective, anytime any day! I sincerely hope he would agree to continue being a mentor throughout my career, and not just within the boundaries of Trois-Rivières, haha! Speaking of another side of the coin, its Dr. Simon Langlois! If mentorship had a physical representation, it would be this kind gentleman. The way he delivers facts, information, knowledge, etc., it was done to perfection and this made me redefine my doctoral degree objective amidst a field that is gaining global attention today. The professional clients he has introduced me to, the projects we worked together on, and countless days of brainstorming via his "food four thoughts" phrases foster great memories during the past two years. Here, I would like to thank myself actually, to have sent that one email to Dr. Simon immediately after the PAPTAC conference where both of us had presented our research – cannot believe it's already two years since then! Next, I would like to express my gratitude to Mr. Jean-Philippe Jacques, the Director of Innofibre, who was very kind to give me an opportunity to work with this great CCTT and its team (the Thermobiom as well as on-campus at CIPP). He was instrumental in sealing funding requests and cementing my doctoral candidate role through a collaborative venture between I^2E^3/UQTR and Innofibre. Even today, there are great projects I am working on because of this kind gentleman. Professor Simon Barnabé has been a great mentor in the last couple of years and encouraged my travel abroad to international conferences to present our team's research. It is from this kind gentleman, I learnt how to network with like-minded peers and researchers – a skill I will take with me wherever I go. Another gem of a person, Dr. Younès Bareha, the kind gentleman who I met for seeking advise on some research questions at our academic department in UQTR, turned out to be a not only a research guide, but taught me how to carry out and present any of my findings, small or large, in a digestible manner. It was a great opportunity given by him to work on an article topic away from my comfort zone. He made me understand the concepts flawlessly and with such ease and grace. Thank you Dr. Younès and sorry for my really lengthy writing habits that tested your patience while correcting the work, haha!

Cyrine Boussabbeh, my project manager, great friend, and one of the kindest humans I have come across! It is through her, that I received an opportunity from a very supportive local company here in Trois-Rivières. Who knew that this project would turn out to be a seed for my entire doctoral study! Absolutely surreal! Also, she was my first French teacher unofficially (haha!) and helped me learn the language (which I am still bad at while speaking, LOL), understand, and converse at least to a certain extent without people getting mad. Ms. Josée Doucet, our great technical expert at Innofibre, has been a constant support and a great mentor. Apart from her great help in all our projects', she has been yet another unofficial French language coach for me. I would like to thank all my great colleagues at the Thermobiom: Mr. Emmanuel, Mr. Vincent, Mr. Bruno, Mr. Alain, Mr. William, and Ms. Maude who have been very kind to me throughout my stay there. If I have mistakenly forgotten names here, please remember you all have played a huge part in my study program. Thank you!

Saved on of the best for last! A special friend who treated my wife and me like family, through these 3-4 years of our stay in this lovely city – Dr. Sadeshkumar Natarajan. An epitome of knowledge and wisdom combined, is what I see him as! His wonderful wife Mrs. Kavitha and their children have been showering us with tremendous support and strength. Here I stand, with no words to describe these great people, and in utter awe of their humility.

Once again, thank you all from the bottom of my heart – hope I made you all proud to the best extent I can. Cheers.

RÉSUMÉ

L'urgence mondiale de solutions énergétiques durables, motivée par la croissance démographique et la reprise industrielle postpandémique, met en évidence la nécessité de s'affranchir des combustibles fossiles. Malgré des engagements internationaux tels que l'Accord de Paris, les progrès restent limités en raison de la dépendance persistante à l'égard des combustibles fossiles et des contraintes économiques. Parmi les différentes sources d'énergie renouvelables, la biomasse se distingue par sa neutralité carbone, sa grande disponibilité et sa polyvalence dans la conversion en chaleur, en électricité et en combustibles. Dans ce contexte, les déchets de bois de construction, de rénovation et de démolition (CRD) représentent une ressource de biomasse sous-utilisée avec un fort potentiel de valorisation par pyrolyse. Cette thèse explore la conversion thermochimique du bois de CRD en biochar par pyrolyse lente dans des conditions variées en laboratoire et à l'échelle pilote. Le bois de CRD, généralement contaminé et très hétérogène, présente des difficultés pour le recyclage conventionnel et est souvent relégué dans les décharges, ce qui soulève des problèmes environnementaux. La pyrolyse apparaît comme une alternative prometteuse pour la gestion de ces déchets, capable de produire un biochar stable, dense en énergie et multifonctionnel. L'étude a utilisé des fours tubulaires horizontaux et des fours à cornue rotative pour optimiser les paramètres opératoires tels que la température de pyrolyse (300-850 °C), le temps de résidence (30-240 minutes), la vitesse de chauffage (10-55 °C/min) et la masse de matière première (100 g – 3 kg). Les biochars obtenus ont été caractérisés à l'aide de différents outils : analyses proximales et élémentaires, diagrammes de Van-Krevelen, profils thermogravimétriques, spectroscopie Raman, microscope électronique à balayage - spectroscopie de rayons X à dispersion d'énergie (SEM-EDX), spectroscopie infrarouge à transformée de Fourier (FTIR), analyse Brunauer-Emmett-Teller (BET) mais également évaluation de l'auto-échauffement.

Les principales conclusions indiquent que des températures de pyrolyse plus élevées et des temps de séjour plus longs augmentent considérablement la teneur en carbone, la fraction de carbone fixe (FC), l'aromaticité et la stabilité thermique du biochar - des qualités essentielles pour les applications dans la séquestration du carbone et les industries métallurgiques. Inversement, la teneur en matières volatiles, les niveaux d'oxygène et d'hydrogène et la présence de groupes fonctionnels diminuent, ce qui démontre l'importance des réactions de dévolatilisation et de condensation. Les biochars produits à des températures élevées présentaient également une surface et une microporosité plus élevées, ce qui les qualifient pour des utilisations en adsorption, telles que l'élimination des colorants dans les solutions aqueuses. Parallèlement, des études cinétiques et thermodynamiques utilisant l'analyse thermogravimétrique (TGA) et plusieurs approches basées sur des modèles reconnus (Coats-Redfern (CR), Ozawa-Flynn-Wall (OFW), Kissinger-Akahira-Sunose (KAS) et Friedman (FM)) ont été menées pour comprendre le comportement en pyrolyse de cette biomasse post-consommation (CRD). L'analyse a révélé un mécanisme de dégradation en plusieurs étapes dominé par des modèles de diffusion et de réaction interfaciale, avec des énergies d'activation et des changements d'enthalpie comparables à ceux de la biomasse lignocellulosique conventionnelle. Les paramètres thermodynamiques ont confirmé que la réaction de pyrolyse est endothermique et non spontanée, nécessitant un apport d'énergie externe, mais qu'elle produit des résidus carbonés très stables.

Ces travaux soulignent la viabilité du bois de CRD en tant que matière première d'intérêt et présentent la pyrolyse comme une approche évolutive et durable pour sa conversion en biochar de haute qualité. Les résultats soutiennent la mise en œuvre future du biochar dans les secteurs de l'industrie, de l'environnement et de l'énergie; tout en encourageant la poursuite de l'exploration des systèmes de pyrolyse à grande échelle et l'activation des produits. Ils proposent également des solutions nouvelles à des problématiques environnementales et ouvrent la porte à la décarbonation du milieu industriel. . Cette recherche contribue enfin à une compréhension globale de la pyrolyse du bois de CRD et renforce son rôle dans l'avancement des pratiques de l'économie circulaire et des voies de développement à faible émission de carbone.

Mots clés : Biomasse, décarbonation, pyrolyse, biochar, activation, environnement, bois de CRD

ABSTRACT

The urgent global need for sustainable energy solutions, driven by rising population growth and post-pandemic industrial recovery, highlights the necessity of transitioning away from fossil fuels. Despite international commitments like the Paris Agreement, progress remains limited due to persistent fossil fuel dependency and economic constraints. Among various renewable energy alternatives, biomass stands out for its carbon neutrality, widespread availability, and versatility in conversion to heat, electricity, and fuels. In this context, construction, renovation, and demolition (CRD) wood waste represents an underutilized biomass resource with high potential for valorization through pyrolysis. This thesis explores the thermochemical conversion of CRD wood into biochar via slow pyrolysis under varied laboratory- and pilot-scale conditions. CRD wood, typically contaminated and highly heterogeneous, presents challenges for conventional recycling and is often relegated to landfills—raising environmental concerns. Pyrolysis emerges as a promising waste management alternative, capable of producing stable, energy-dense, and multifunctional biochar. The study employed horizontal tube and rotary retort furnaces to optimize process parameters such as pyrolysis temperature (300–850 °C), residence time (30–240 minutes), heating rate (10–55 °C/min), and feedstock mass (100 g – 3 kg). Resulting biochars were characterized using proximate and elemental analysis, Van-Krevelen plots, thermogravimetric profiling, Raman spectroscopy, scanning electron microscope – energy dispersive x-ray spectroscopy (SEM-EDX), Fourier transform infrared spectroscopy (FTIR), Brunauer-Emmett-Teller (BET) analysis, and self-heating assessments.

Key findings indicate that higher pyrolysis temperatures and longer residence times significantly enhance carbon content, fixed carbon (FC) fraction, aromaticity, and thermal stability of biochar - qualities critical for applications in carbon sequestration and metallurgical industries. Conversely, volatile content, oxygen and hydrogen levels, and functional group presence decreased, demonstrating strong devolatilization and condensation reactions. Biochars produced at elevated temperatures also exhibited higher surface area and microporosity, qualifying them for adsorptive uses, such as dye removal from aqueous solutions. In parallel, kinetic and thermodynamic studies using thermogravimetric analysis (TGA) and multiple model-based approaches (Coats-Redfern (CR), Ozawa-Flynn-Wall (OFW), Kissinger-Akahira-Sunose (KAS), and Friedman (FM)) were conducted to understand the pyrolysis behavior of CRD biomass. The analysis revealed a multi-stage degradation mechanism dominated by diffusion and interfacial reaction models, with activation energies and enthalpy changes comparable to those of conventional woody biomass. Thermodynamic parameters confirmed that pyrolysis is endothermic and non-spontaneous, requiring external energy input, but results in highly stable carbonaceous residues.

The work underscores the viability of CRD wood as a valuable biomass feedstock and presents pyrolysis as a scalable, sustainable approach for its conversion into high-quality biochar. The outcomes support future implementation of biochar in industrial, environmental, and energy sectors while encouraging further exploration into full-scale pyrolysis systems, product activation, and tailored end-use applications. This research contributes a comprehensive understanding of CRD wood pyrolysis and reinforces its role in advancing circular economy practices and low-carbon development pathways.

Key words: Biomass, decarbonization, pyrolysis, biochar, activation, environment, CRD wood

TABLE OF CONTENTS

LIST OF FIGURES

LIST OF TABLES

LIST OF ABBREVIATIONS

AAEM – Alkali and alkaline earth metals

ACC – Chromated copper arsenate

AEC – Anion exchange capacity

ANOVA – Analysis of variance

ANZBIG – Australia NewZealand biochar industry group

BET – Brunauer-Emmett-Teller

BQM – Biochar quality mandate

BRT – Biomass residence time

CCA – Copper, chromium, and arsenic

CCD – Central composite design

CEC – Cation exchange capacity

CDR – Carbon dioxide removal

CHP – Combined heat and power

CR – Coats-Redfern

CRD – Construction, renovation, and demolition

DB – Dry basis

DMW – Demineralized water

DOE – Design of experiments

DTG – Differential thermogram

EAF – Electric arc furnace

EBC – European biochar certificate

EBI – European biochar industry

EDX – Energy dispersive spectroscopy

FC – Fixed carbon

FM – Friedman

FTIR – Fourier transform infrared

GHGs – Greenhouse gases

HHV – Higher heating value

HTC – Hydrothermal carbonization

HTL – Hydrothermal liquefaction

HTT – Heat treatment temperature

IBI – International biochar initiative

ICI – Institutional commercial and industrial

KAS – Kissinger-Akahira-Sunose

MAH – Monoaromatic hydrocarbon

MP-AES – Microwave plasma atomic emission spectrometer

Mt – Million tons

NCG / NCGs – Non-condensible gas/gases

NMR – Nuclear magnetic resonance

OFW – Ozawa-Flynn-Wall

PAH – Polyaromatic hydrocarbon(s)

PE – Polyethylene

PHT – Post-heat treatment

PP – Polypropylene

PR:1 – Pyrolysis round 1

PR:2 – Pyrolysis round 2

R&R – Repeatability and reproducibility

RMSE – Root mean square error

RSM – Response surface methodology

SEM – Scanning electron microscope

SEM-EDX – Scanning electron microscope – energy dispersive X-ray

SGS – Singapore standard

SPT – Setpoint temperature

TGA – Thermogravimetric analysis

TSF – Thermostable fraction

VC – Volatile carbon

VM – Volatile matter

VOC – Volatile organic compound

wt% – Weight percent (used interchangeably with % wherever applicable)

CHAPTER 1 - INTRODUCTION

1. Background

The construction industry and its activities around the world are mass drivers of economic prosperity but at the same time generate vast amounts of wastes. These are termed as construction, renovation, and demolition (CRD) residues. Among these rejected material streams as in Figure 1, CRD wood constitutes a major portion and yet, remains underutilized owing to its end-of-life, non-recyclable stages that is evident from its damaged and under-appealing morphology (Laadila et al., 2022). The CRD wood sometimes, can also be rendered unusable due to microbial or fungal degradation. For instance, approximately 1.85 million tons (Mt) of CRD wastes are generated in Quebec annually of which 56% are wood residues, that are discarded in substantial quantities (*Recyc-Québec, 2018*). However, CRD wood recycling may be viable for particleboard production as stated by Azambuja et al., 2018 that can be used in furniture and cabinets.

Figure 1: CRD wastes including wood residues. Source: BRQ CRD waste processing site

Usually, despite regulatory norms and standards that aim at hazardous waste segregation, CRD wood bypasses proper classification. Its high sorting costs due to the necessity for superior instrumentation and lack of public awareness have created loopholes to get rid of this waste by irresponsible means (Zhang et al., 2024). Thus, as an easy way of disposal, CRD wood is landfilled or incinerated, causing adverse environmental ramifications in the form of global greenhouse gases (GHGs) emission (*e.g.*: CH_4), dioxin/dust/particulate release into the atmosphere, and leachates which contaminate land, water, and soil – threatening ecotoxicity-related consequences. It has also resulted in spatial and regulatory burdens for landfill operators where remediating overly-polluted landfill sites because of CRD wood disposal is also incurring huge economic constraints. To mitigate such negative effects on the society and environment and also due to a rise in stringent governmental legislations pertinent to landfilling practices globally, alternative CRD wood waste diversion or valorization technologies are the need of the hour for reversing missed recycling opportunities.

1.1 Role of pyrolysis in reclamation of CRD wood waste

Thermochemical biomass conversion techniques like pyrolysis have immensely advanced in terms of their technology readiness level (TRL) to process wastes of different kinds, shrink the volumes generated, divert them from landfills, and concomitantly generate multitude of products (Kazimierski et al., 2022). In other words, it offers quaternary benefits in terms of building up resource efficiency, energy recovery, circular economy, and revenue generation. Pyrolysis is a process which converts organic lignocellulosic feedstock like CRD wood waste in the absence of ambient oxygen (but present in the feedstock) and at moderate to high temperatures (400-800 °C), into three product streams: solid biochar, liquid biooil, and pyrolysis gas (Ganesan et al., 2025). The thermal

decomposition can be tuned depending on the product and application under focus, as: slow, fast, or flash pyrolysis (Jerzak et al., 2024). The first major difference between these is how biomass feedstock is heated, *i.e*, the heating rate. The second difference is the amount of time biomass, or the pyrolytic volatiles spend within the reactor, also known as the residence time, and thirdly, it is the feedstock processing temperature. Slow pyrolysis produces greater amounts of char, fast pyrolysis produces biooil, and flash pyrolysis increases pyrolysis gas yields (Roshan et al., 2023).

Biochar, a solid carbonaceous product typically derived in significant quantities from slow pyrolysis, has found several applications in the field of agriculture, soil fertility, automotive, construction, and water treatment (Gusiatin et al., 2024). When produced under extreme conditions of heat, biographene, biocarbon (activated carbon alternative), carbon nanotubes (CNTs) can be derived that could find high-value applications (Waluyo et al., 2024). Off-late, biochar is also being experimented in the metallurgical industry, specifically sintering of iron containing ores and steel-making, where it could either be used in parts with metallurgical coal for coke making or can be used directly with coke itself within smelters or blast furnaces for roasting and reduction (Al Hosni et al., 2024). Even though, it could be leveraged for substituting such fossil fuels, this replacement can be accomplished only in proportions since 100% substitution is not viable for final product characteristics, at least presently, due to constraints associated to superior quality of char and its high production costs (Wang et al., 2023). The condensed pyrolytic gases or the biooil is composed of hundreds of chemical compounds, moisture, acids, aromatics, and is packed with energy, also easing transport and storage steps (Hu et al., 2024). It could be further treated with engineered catalysts coupled with hydrogenation steps for modifying its physicochemical properties similar to fossil crude or even conventional diesel/gasoline-range hydrocarbons (El Bari et al., 2024). In other cases, it is subjected to simple refining and used as an energy source for heat and electricity production. Pyrolysis gas harboring CO, CO_2, H_2, CH_4, and C_1-C_3 hydrocarbon gases to name a few, could be recovered within the process to contribute for a part of the pyrolyzer's energy demand or can be combusted to generate heat and electricity (Panwar, 2024). In other cases, it may serve as a repository for syngas, a mixture of CO and H_2, which could be separated, purified, and further processed via other thermochemical conversion technologies like Fischer-Tropsch Synthesis (FTS), to produce liquid biofuels (Slatter et al., 2022).

Among these products, biochar could offer industrial and environmental benefits including but not limited to other vital applications like carbon sequestration, soil remediation, and pollutant gas (*e.g.:*H_2S) adsorption. Despite its flourishing potential, many research gaps exist in harnessing a complex feedstock like CRD wood as a feedstock for its production.

2. CRD wood composition

On this note, complexity in CRD wood wastes originates from their heterogeneity with natural wood, treated wood (*e.g.:* panels), adhesives, rubbers, paints, plastics, gypsum, metals, preservatives containing formaldehyde, varnishing compounds, and laminates (El-Haggar et al., 2019). Also, their composition and level of contamination could vary geographically. In countries where the construction sector has been extensively utilizing wood, remnants from electric poles, bridge parts, and buildings also show presence of heavy metals such as Cr, Cu, As, and Pb that are hazardous (Laadila et al., 2022, Safa et al., 2020). This variability in composition may affect biochar characteristics, quality, and might also lead to desorption concerns of these trapped heavy metals that makes it a questionable choice for soil, water, and agricultural applications. These inorganics also increase biochar ash content, reactivity (some may be catalytically active under a broad range of temperatures), heat conductivity, and surface charges. Internationally renowned biochar consortiums like the International Biochar Initiative (IBI), European Biochar Certificate (EBC), Biochar Quality Mandate (BQM), and the Australia New Zealand Biochar Industry Group (ANZBIG) have laid down permissible limits for such heavy metals, over which they could be deemed unfit for usage (Lin et al., 2025). For CRD wood, there may be another unavoidable problem that has to be encountered during pyrolysis steps due to volatile and other organics – formation of carcinogenic polyaromatic hydrocarbons (PAHs) which are produced due to rampant polymerization of volatile organic compounds (VOCs) generated during pyrolysis (Buss et al., 2022). Proper CRD wood waste sorting, size reduction by chipping or milling, cleaning/washing, drying, and other upstream pre-treatment steps for decontamination and volatiles content reduction have to be followed, if necessary, prior to pyrolysis. This could lessen problems during its thermal decomposition and also ensure a safer biochar product utilization. Since natural wood is also big part of the CRD wood mix, the inherent biopolymer composition in the form of hemicellulose, cellulose, and lignin also present differences in yield and the nature of pyrolysis products (Mukherjee et al., 2022). These components also cause differences in terms of surface charge and ion exchange capacity (Dey et al., 2023). Hemicellulose and

cellulose, due to their lower degradation temperatures, produce more small or low-molecular weight compounds collected within pyrolysis gas and biooil fractions resulting from dehydration and ring opening reactions (Zhang et al., 2023). Whereas, the more stable and scattered lignin may be partly responsible for increasing biochar generation (Zhang et al., 2023). Rearrangements of these polymers during pyrolysis could also influence biochar's porosity and surface area depending on the pyrolysis parameters employed.

3. Pyrolysis conditions and their influence on biochar properties

As discussed before, pyrolysis temperature, heating rate, and biomass residence time (BRT) are crucial parameters to determine the yield and tailor biochar properties suitable for the application under focus (Wang et al., 2019). Since each component amidst CRD wood wastes could decompose only at a specific temperature, a myriad of process conditions has to be tested through a comprehensive design of experiments (DOE) consisting of a broad range of temperatures, BRT, heating rates, masses of feedstock treated, and even particle sizes of biomass. Till now, such a study according to the best of our knowledge could not be found making it a potential research area.

3.1 Temperature

As different studies qualify the severity of pyrolysis temperatures in different ways, the estimated range for a low-pyrolysis temperature can be 300-400 °C, moderate temperature pyrolysis can be 400-600 °C, and high temperature pyrolysis temperature can be over 600 °C. Every range has both upsides and downsides. For instance, lower pyrolysis temperature processes conserve biochar yield, surface chemistry, acidic to neutral pH, and macroporosity that is beneficial for its agriculture applications focusing on water and nutrient retention (Dhar et al., 2022). Here, biochar retains maximum hydrophilicity and anion exchange capacity (AEC). The major downside, however, is ineffective carbonization and preservation of some amorphous carbon from the initial biomass which might cause stability concerns in the open environment. In some case, low temperatures can perform the role of a typical torrefaction process which reduces moisture content, improves FC, and overall grindability of biomass (Wang et al., 2019). Whereas, at higher pyrolysis temperatures, due to high degrees of carbonization, there is reduction in biochar yields, surface volatile functionalities, with a simultaneous increase in hydrophobicity, pH (basicity due to growing inorganics percentage in the form of ash), porosity (meso-microporous), surface area, aromatization, and thermal/oxidative stability (Adhikari et al., 2024). Here, biochar is good for applications concerning carbon sequestration, metallurgy, carbon black substitutes in automotive industry, and energy storage materials. It is the moderate temperature pyrolysis processes that maintain a balance of all these aforementioned biochar properties and deem it useful for application in soil nutrient amendments, pH remediation, hydrophilic pollutant (*e.g.:* dyes) removal from wastewater by adsorption, and sometimes as catalysts dye to its tendency for supporting diffusion phenomena through heterogeneous porosities. Such biochars also show the presence of active binding sites retaining some oxygen-based functional groups on the surface, beneficial for heavy metal adsorption. This property of biochar is called cation exchange capacity (CEC).

3.2 Heating rate, BRT, and particle size – The trio!

Pyrolysis heating rate and BRT function on related concepts. Both these variables determine how biomass is converted as a function of time. Low heating rates and long BRT allow for complete decomposition, effective charring of biomass, increasing biochar yields, and removal of volatiles, because heat transfer limitations are subdued (Kumar et al., 2025). In other words, once the boundary layer of a biomass particle is heated, this heat has enough time for permeation and to reach the particle's core, degrading its constituents to fruition and giving rise to well-developed biochar morphology, porosity, and yield. Complete carbonization here also eliminates as much volatiles in biochar as possible leading to high fixed carbon (FC), low volatile carbon (VC), high carbon content, aromatics condensation (low H/C, O/C), and promoting other stability indices (*e.g.:* R50 recalcitrance index, Raman I_D/I_G) (Kalina et al., 2022, Ganesan et al., 2025). All of this could aid in biochar's environmental permeance applications and therefore, its intrinsic organic carbon content remains sequestered in the land or soil for hundreds to thousands of years without easily getting degraded to CO_2 and CH_4 that would be the case if untapped organics-rich biomass like CRD wood is left to decompose in landfills or rot in nature (Grojzdek et al., 2024). Albeit in the course of complete transformation during pyrolysis, more volatiles residence time in the reactor could lead to two outcomes: a) increase in second char yield from promoted primary char-volatiles reaction (Wang et al., 2023); and b) Repolymerization or recondensation of light oxygenated volatiles that could form higher aromatics (Wang et al., 2023). Thus, the process design can be optimized here by using a vacuum suction unit which rapidly evacuates pyrolytic volatiles generated either to the condensers, a combustion chamber, or recycled within the system (Ganesan et al., 2025). A second approach could be to maneuver the flow of inert

carrier gas without causing a cooling effect in the reaction zone (may form hot spots due to temperature differences).

On the other hand, high heating rates and short BRT lead to insufficient breakdown of the biomass's structure and pose thermal gradient effects resulting in ineffective charring (Kumar et al., 2025). As a result, rapid depolymerization and volatile release occur, favoring more gas release with some biooil yields too, rather than maximizing yields of biochar with developed pore structures (Babu et al., 2024). More meso or macropores could be formed due to the bulk of volatiles getting released within a short period of time, contributing to incomplete carbonization. As a result, biochar has low thermal/oxidative stability and implicitly shows overarching VC, H/C, O/C (Van-Krevelen indices), and low FC – an extrapolation from Babu et al., 2024.

The third player here to have a synchronous effect, especially on reaction mechanisms, is biomass particle size (Mariyam et al., 2023). The smaller it is, the better conversion it undergoes since heat transfer is fast due to available surface area and also due to short distances from the gas-solid interphase to the particle's core (Zaman et al., 2018). Smaller particle sizes also reduce activation energy and volatiles mass transfer barriers, leading to better carbonization (Suriapparao & Vinu, 2018). That too, with a low moisture content, the time taken to heat biomass to set point temperatures is fast since a high moisture content would by itself, absorb more heat first and then only relay this heat to the particle's boundary layer (Tomczyk et al., 2020). This also favoured high carbon content, microporosity development, and high surface area under moderate to high pyrolysis temperatures, low heating rates, and long BRT (Barszcz et al., 2024). Due to eventual smaller biochar particle sizes obtained, these may experience high affinity towards ambient air or oxygen due to the available surface area but could be balanced with their superior stability properties.

4. Biochar self-heating and causative factors

A critical challenge that cannot be overlooked when it comes to biochar production, cooling, handling, and storage, is its potential to undergo self-heating (also called self-ignition, auto-ignition, or auto-combustion) (Phounglamcheik et al., 2022). A typical self-heating problem can be depicted as in Figure 2.

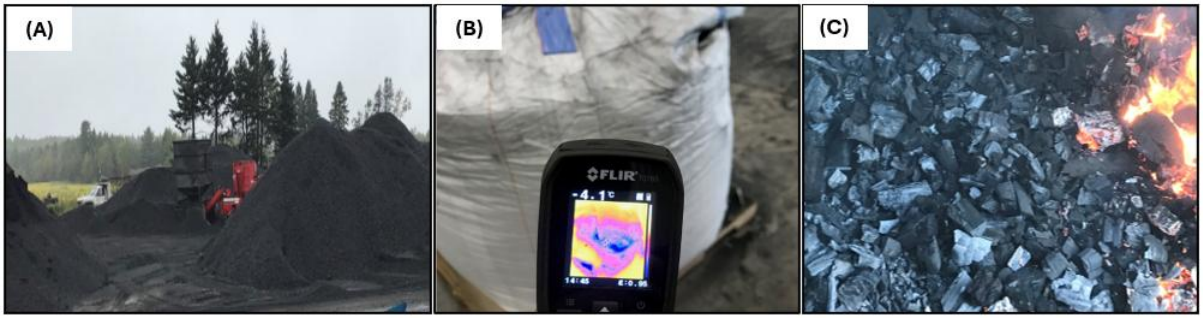

Figure 2: Biochar self-heating problem: (A) biochar stockpiles at production/usage sites; (B) hand-held thermal imaging camera to detect radiations or temperature hotspots in the stockpile; and (C) smoldering and eventual ignition of biochar. Source: Industrial client sites

As understood from Panahi et al., 2020, the volatiles content comprising of tarry hydrocarbons/oxygenated compounds, along with biochar surface area, may make it susceptible to reactions with ambient air atmospheres contributing to exothermic oxidation, temperature hot spots formation, and eventually ignition. These volatiles could be rich in carboxyl, hydroxyl, carbonyl, or phenolic functionalities that house adsorption sites with high binding energies for air, oxygen, and moisture as well (Restuccia, 2017). In particular, low temperature biochars house such reactive species rendering it prone to self-heating. Whereas high temperature biochars, although with reactive stability, can still interact with its high surface area and pore volume (Pariyar et al., 2020). Besides underlying biomass properties and pyrolysis conditions, physicochemical, and morphological properties of biochar, the volume it occupies in a storage pile of known geometry, its particle size, and its internal moisture content could also exacerbate ignition tendencies (Miura, 2016, Restuccia et al., 2019). Till now, this area is vastly underexplored not only for CRD wood biochar but for all biochars in general.

4.1 Mechanism of self-heating and the underlying reasons

To understand the steps involved in biochar self-heating, coal can be taken as another reference porous carbonaceous material (Xi et al., 2022). There are different grades of coal varying in terms of volatiles, oxygen, ash, carbon, and other impurities. Low rank coals like lignite and bituminous, are less oxidatively stable and can spontaneously react with oxygen in ambient air that is adsorbed on their surfaces resulting in localized heat generation. To be precise, the surface functional groups, light hydrocarbons, and volatiles in these coals are the unstable reactive species that attract oxygen and form oxy-carbon complexes. Following initial surface oxidation, if the heat produced is not dissipated sooner and if the overall rate of heat (due to chemical or microbial oxidation of biochar) accumulation exceeds its rate of dissipation as time progresses, it leads to a drastic rise in surface temperatures (Restuccia et al., 2019; Bluvshtein et al., 2020). Especially, in the case of fine biochar particles where there are more surface sites available for exothermicity to develop, self-heating is unavoidable if biochar is present within poorly ventilated surroundings (Castells et al., 2020). It is worse when the foundational pyrolysis conditions were along the lines of low temperatures, high heating rates, or short BRTs for a large mass of feedstock, usually conferring low oxidative and thermal stability due to sparse carbonization. Thirdly, most or all oxy-carbon surface functionalities, VC, and other less-stable organic biochar components, may start embracing accelerated decomposition reactions amidst the rapid heat generation. As the concluding stage, thermal runaway might cap all other mechanisms. At this stage, the surface temperature of biochar could cross its critical point and initiate burn-off (Phounglamcheik et al., 2022). If the ambient conditions continue to fuel this burn-off, the heat transfer is quite rampant to travel from the outer surface of biochar to its inner core and consume the material, generating ash. Now, the entire carbon matrix of biochar could be subjected to combustion, collapsing its entire framework.

4.2 Strategies for reducing biochar oxidative reactivity and self-heating

To control biochar ignition, mitigation strategies like biochar secondary activation treatments under inert or non-inert conditions could be followed that have shown capabilities to reduce volatiles content, VC, oxygen, and increase FC, aromatization, thermal stability (Panahi et al., 2020, Pariyar et al., 2020). The role of ash components (*e.g.*: oxides of iron) in treated biochars is debatable since it could either offer inertness or could catalyze oxidation/combustion reactions due to its ability to efficiently uptake oxygen (Peterson & Brown, 2020). Secondary treatments include activations by thermal, steam/CO_2, chemicals, minerals, and mechanical methods. A combination of these methods may also be viable especially considering the variability in the initial complex feedstock like CRD wood resulting in a diverse range of volatiles content of the final biochar. Nevertheless, irrespective of the type of activation technique followed, the quantity or flow rate of activator, activation time, activation temperature, and final storage conditions are important aspects to consider during biochar engineering (Diaz et al., 2024).

Thermal activation usually takes place between 400-800 °C in the presence of inert (nitrogen) or oxidizing (air) atmospheres that could passivate the biochar surface by clearing unstable oxygen functionalities and gaining control over these formerly perturbing reactive sites (Zhu et al., 2018, Xiao, 2022). Here, settled tars and other volatiles on biochar are driven off through a process called controlled degassing (Xiao, 2022). Thus, reactive precursors are eliminated with a corresponding rise in material stability but at the expense of some yield loss. Physical activation during pyrolysis or as part of secondary treatment steps includes presence of reactive atmospheres such as CO_2 (Sun et al., 2020) and steam (Anderson & Bergman, 2021) at high temperatures (600-1000 °C), that could assist in volatilizing tarry pyrolytic residues condensed on the surface of biochar reducing its oxidative reactivity, improving microporosity, and also lowering the chances for it to catch on fire during post-production cooling or storage. Such annealing steps can also improve the crystallinity of biochar's structural lattice. Steam, because of a smaller molecular size than CO_2, can diffuse faster within biochar pores and complete the reactions sooner. It may also perform pore reaming, a process where tarry residues condensed even within biochar pores (aside from the surface) can be released. Although, in some studies, it has been stated that pyrolysis under a CO_2 atmosphere is efficient than under inert N_2 conditions in producing biochar with greater porosity and recalcitrance, bypassing the need for post-pyrolysis activation (Premchand et al., 2023). Since both the physical activation agents here are oxidizing in nature, surface properties of biochar could also be enhanced with tailored active sites for gas and pollutant adsorption. Chemical activation is very frequently followed using acid (*e.g.:* H_2SO_4, HNO_3, H_3PO_4), alkali (*e.g.:* NaOH, KOH), or metal salts (*e.g.:* $ZnCl_2$, $MgCl_2$) of varying strengths, heating temperatures, and incubation times, to increase porosity, surface area, and removal of tarry matter on biochars (Pathy et al., 2023). But these methods usually cause downstream water pollution from the use of such chemicals. Surface modification of biochar using minerals like clay might also form an oxygen diffusion barrier tapering the risk of self-heating. Incorporating minerals containing metals like Si and Al within the biochar carbon lattice

(resembling a metal organic framework (MOF)) contributes to its overall reactive and structural stability (Ghaedi et al., 2024). However, it may not be suitable for applications like metallurgy since the final ash content in mineral-enriched biochars may reach high levels affecting the quality of reduced metals following the high temperature reduction reactions. Albeit, biochar-clay composites have been used to entrap heavy metals in soil-based applications as discussed in Wang et al., 2022. A final choice for secondary treatment is also rapid quenching of biochars using water directly after pyrolysis. Here, the sudden temperature gradient could lead to cracks and breakdown any surface-borne condensed residues mimicking a solvent-leaching process. Alkali and alkaline earth metals (AAEM) like Na, K, Mg, and Ca in biochar's ash could form hydroxides upon contact with water and penetrate via biochar pores (mild chemical activation-like), clearing out these paths that were once clogged with tarry compounds.

4.3 Future directions on biochar self-heating

Since biochar self-heating brings about safety concerns during supply chain operations and utilization, interpreting the reaction mechanisms is key. Unfortunately, only a niche perception exists since the causative factors are not understood well in depth. Future research could leverage various modelling methods such as Semenov, Frank-Kamenetskii, and Thomas models which postulate self-heating w.r.t heat transfer theory and geometry of biochar storage piles (Schwarzer et al., 2021). As particle size of biochar plays an important role in determining its ignition tendency, various sizes right from lumps to less than 100 µm must be tested to evaluate the role of surface area in combination with biochar's physicochemical properties, in attracting ambient reactive species. Feedstock pre-treatment and pyrolysis conditions should also be checked vigorously since they dictate biochar's oxidative and thermal stability. Integrating some strategies based on coal handling, and collaborations between coal and biochar sectors can accelerate the overall progress.

5. Globally unaddressed topics in CRD wood valorization to pyrolytic biochar

A list of unresolved questions has been identified circumventing CRD wood residues and their conversion to pyrolytic biochars. They can be categorized as follows:

A) Assessment of CRD wood waste composition and contamination

- Sorting, size separation, and contaminant removal
- Washing, leaching of inbound metal content in acidified and non-acidified medium
- A comprehensive characterization of CRD wood classes, especially treated, painted, and laminated wood
- Biochemical composition of hemicellulose, cellulose, and lignin
- A thorough metal analysis, especially heavy metals like Cr, Cu, Pb, and their concentration in biochar post-pyrolysis at different temperatures

B) Optimization of pyrolysis process conditions

- Influence of different pyrolysis parameters such as temperature, BRT, heating rate, and mass of feedstock on biochar via a robust DOE
- That too, specifically for heating rates, CRD wood pyrolysis kinetic modelling and thermodynamic parameter calculations are essential
- Evaluating biochars for persistent organic pollutants presence (*e.g.:* PAHs, PCBs) that are toxic
- Influence of reactor, its thermal inertia patterns, and pyrolysis process design on material energy balance, pyrolyzer efficiency, and biochar yields

C) Biochar properties and relevant applications

- In-depth characterization of CRD wood biochar - proximate, elemental, weight loss patterns under thermal settings, surface chemical composition, amorphous or crystalline nature of biochar, stability indices
- Self-heating or self-ignition performance of different grades of biochar and the underlying causes/mechanisms
- Use of bio-based binders for densifying biochars, with further characterization of pellets produced
- Diversifying the use of CRD wood biochar in carbon markets, sequestration projects, metallurgical processes, and wastewater pollutant adsorption

D) Co-product valorization and engineering

- Pyrolysis gas recycling
- Biooil characterization, upgrading using engineered catalyst (could be CRD wood biochar itself due to it good surface chemistry at moderate pyrolysis temperatures)

E) Post-pyrolysis activation of biochar

- Aside from physical and chemical activation of biochar that are quite common, other methods are underexplored - thermal activation of biochar without the use of chemicals or reactive atmospheres

F) Co-pyrolysis of CRD wood waste – an integrated waste management approach

- Using other organic or fossil wastes such as agricultural residues, pulp and paper mill waste, organic fraction of municipal waste, low-value plastics like polyethylene (PE) and polypropylene (PP), coal-mine waste (gangue), steel plant waste (slag)

G) Lifecycle assessment (LCA) and technoeconomic analysis

- A comparative LCA of pyrolysis versus other CRD wood waste management options such as incineration, landfilling, or recycling
- Technoeconomic evaluation of these processes right from biomass sourcing, upstream conditioning, pyrolytic conversion, product separation, and market value of biochar and co-products

H) Regulatory frameworks and environmental considerations

- Vast heterogeneity of CRD wood leading to inconsistencies in management and classification, with unclear safety standards
- Environmental impacts of CRD wood storage, especially in open areas subjected to rain or snow, which could cause hazardous leachates to seep and contaminate soil and ground water
- Release of volatiles into the air risking human health

I) Policies and incentives

- Economic incentives for CRD wood waste handlers to undertake the associated complex tasks
- Logistical advancements to transport wood waste from the source site to segregation or processing sites
- Firm local, regional, or national policies for CRD wood waste diversion from landfills and incineration plants

6. Summary

Pyrolysis offers a sustainable solution for managing CRD wood debris and this thermochemical transformation not only treats the volumes of waste generated but also makes a carbonaceous high value material called biochar with environmental and industrial importance. Albeit, obstacles surrounding composition of CRD wood waste, pyrolysis conditions employed, secondary treatments, oxidative and thermal instability via self-heating must be addressed at a broader scale before scaling its production and utilization. These factors can significantly influence CRD wood biochar's carbon conversion, reactivity, and permeance which govern its applications in adsorption, energy, metallurgy, carbon sequestration, soil enhancement, and agriculture. Advancing process optimization with effective reactor design upholding carbon conversion, mass balance, and energy efficiency are extremely critical. Supporting incentives, sorting/classification standards, ecotoxicity assessments, and policy frameworks will be instrumental in promoting the conceptual adoption of CRD wood waste valorization to biochar, within a sustainable circular economy.

7. Research gaps, hypotheses, objectives, and methodology

The following chapters are based on articles either ready to be submitted, submitted and awaiting editor/reviewer decisions, or already published. The research questions to be addressed, hypothesis, objectives, and methodology will be discussed here. These address the research gaps A, B, C, and E listed in **section 5** above. The research progresses from analyzing CRD wood feedstock and establishing a reliable pyrolysis setup to optimizing process

parameters through DOE experiments. It scales the work to pilot trials with larger feedstock volumes while engineering biochar for improved stability and performance. The study concludes with kinetic and thermodynamic analyses to understand the energy dynamics of the system.

7.1 Chapter 2

The chapter entails an article published in the journal, "Science of the Total Environment", by Elsevier publishers (https://doi.org/10.1016/j.scitotenv.2025.178650). The work here encircles the topic, "Pyrolytic conversion of construction, renovation, and demolition (CRD) wood wastes in Québec to biochar: Production, characterization, and identifying relevant stability indices for carbon sequestration".

This chapter investigates the core research question: "How could CRD wood wastes be effectively converted to biochar, a bio-based carbonaceous product derived through the thermochemical pyrolysis process, and what characteristics of this biochar make it suitable for applications relying on its stability and environmental permeance?"

For answering this, the framed hypotheses are multifaceted. Firstly, it is proposed that mechanical separation of CRD wastes into wood and inorganic fractions will significantly reduce the interference of mineral and metal components during pyrolysis. Furthermore, optimizing the right particle size for CRD wood can enhance a complete pyrolysis via uniform and unhindered heat transfer. The second hypothesis suggests that upstream (prior to pyrolysis) washing of CRD wood will leach out appreciable concentrations of AAEM, thereby maximizing carbon and minimizing oxygen as well as ash in the final biochar product. Thirdly, the use of a scaled-up horizontal tube furnace with higher feedstock mass loads, is expected to facilitate a better conversion of biomass due to low thermal inertia or heat loss. Lastly, it is hypothesized that pyrolysis temperature exerts the most dominant influence on biochar properties and is considered to be a vital parameter for engineering biochar to suit various industrial and environmental applications.

The objectives of this chapter are to highlight the effectiveness of CRD wood sorting, milling, and chemical pre-treatment in removing problematic metal ions; to evaluate two reactor configurations at laboratory-scale for CRD wood pyrolysis along with optimization of process design and operating conditions (temperature, BRT, and/or heating rate); and to conduct detailed characterizations of biochar for analyzing its physicochemical and morphological properties. Based on characterization results, a further goal is to establish potential stability indices for biochar that can be leveraged to determine if its suitable for carbon sequestration and carbon dioxide reduction (CDR) applications.

The methodology will begin by selecting relevant biochar aromaticity, stability, and permeance assessment techniques and outlining their theoretical foundations with equations wherever applicable. Next, the CRD wood biomass from a local provider is transported to the factory where its manual separation from inorganic and less-desirable organic impurities will take course followed by size separation in a mechanical gravimetric sieve. Once the particle size distribution is verified, milling the CRD wood to about 3 mm to 2.5 cm will be carried out using screens of corresponding pore sizes if necessary. Then pyrolysis in the smallest and scaled-up horizontal tube furnace reactors under laboratory conditions will be performed at different temperatures and BRT. One of the major preliminary variations here will be the mass of feedstock loaded into each of these reactors initially (15 g versus 400 g). Other variations will be circumventing the prevention of condensed volatiles from settling over biochar surface and limiting thermal inertia in the reactor – more related to process design. Post-pyrolysis proximate and elemental properties, thermogravimetric analysis (TGA/TGA R50), BET surface area, micropore volume, scanning electron microscopy (SEM), and Raman spectral characterizations will be carried out to determine how feedstock composition and pyrolysis process conditions will influence the structural and physicochemical properties of biochars. Statistical methods encompassing p-value significance tests will accompany any findings. From this mapping, the study will conclude by proposing the most reliable indicators for assessing biochar stability and permeance followed by extrapolating these indices to practical applications.

7.2 Chapter 3

The chapter consists of an article published in the journal "Energies", by MDPI Publishers. The article can be found via: https://doi.org/10.3390/en18153902. The topic addressed here is, "Turning Construction, Renovation, and Demolition (CRD) Wood Waste into Biochar: A Scalable and Sustainable Solution for Energy and Environmental Applications ".

This chapter builds on the previous findings from chapter 2, by exploring how a robust DOE framework can be used to study the influence of CRD wood pyrolysis conditions on the characteristics of biochar. The chapter also examines the potential for scaling up pyrolysis from laboratory to semi-pilot-scale conditions. The principal research questions addressed here is: "To what extent do pyrolysis process parameters such as temperature, BRT, and mass of feedstock affect biochar quality and usage for viable applications, and how these insights can be translated to higher operation scales?"

The hypotheses suggest that chemical complexity of CRD wood makes it difficult to be recycled via conventional methods, but slow pyrolysis can offer a technically sound pathway for conversion into biochar harbouring desirable properties. Among other pyrolysis parameters, temperature has the most pronounced effect, surpassing both BRT and feedstock mass. Moreover, process scalability holds promise for at least a demonstrative deployment in the impending time period. It is also hypothesized that non-activated biochar derived from CRD wood waste can effectively adsorb industrial dyes such as methyl orange without the need for final regeneration.

The objectives of this chapter include sorting and pre-processing CRD wood without solvent-based AAEM removal (making the process realizable for small-scale producers also), conducting pyrolysis trials through a robust DOE by varying temperature, BRT, and mass of feedstock, and replicating the most prominent, chosen conditions at a larger scale to assess reactor performance in delivering biochar with similar properties. The study also aims to statistically investigate the results obtained from the DOE, choose the best-case biochar for dye adsorption experiments with contaminated water, and also explore the kinetics/thermodynamics of the adsorption process.

To achieve these objectives, CRD wood will first be sorted, screened for contaminants, and reduced in particle size as carried out in chapter 2 with the same instrumentation. Next, 16 different pyrolysis conditions extracted from Stat-Ease's Design expert software using its response surface methodology (RSM) technique, will be carried out first in the larger horizontal tube furnace reactor. Statistical evaluations using model significance (p-value), model fit (R^2), and independent variable coefficients will be performed to narrow down on the most influential pyrolysis parameter(s) followed by affirmations with surface/contour plots, perturbation curves, and the predicted versus actual value graphs for certain chosen response variables as examples. Five random conditions will be selected from the initial DOE list for scale up experiments in a semi-pilot rotary retort-furnace unit. These conditions will make sure that a full range of the most influential process variable is covered. After gauging how similar the biochars produced in both these reactors are in terms of physicochemical properties from proximate and elemental tests, higher characterizations like TGA, TGA R50, BET surface area, micropore volume, SEM, and Raman spectroscopy will be executed to determine the morphological and structural transformation in biochars produced by the horizontal tube furnace only. With the most ideal biochar, finally, adsorption studies will be conducted using batch experiments, and the data will be fitted with kinetic, equilibrium, and thermodynamic models for describing the nature and underlying mechanisms of the adsorption process.

7.3 Chapter 4

The chapter focuses on an article already submitted to the journal "Journal of Analytical and Applied Pyrolysis", by Elsevier publishers. Currently, this work has passed the journal editor's preliminary screening and is now under peer-review. The article is on the topic, "Pilot-scale slow pyrolysis, post-production thermal activation, and self-heating performance of biochar fuels derived from construction, renovation, and demolition (CRD) wood waste".

A focus here is on a third reactor configuration, capable of processing at least 15-20 kg biomass feedstock at once. Additionally, a vastly pressing topic on various causative factors for post-production biochar auto-ignition and its safety implications during handling and storage is also negotiated. So, the key research question is: "How do processing scale, pyrolysis temperature, and secondary activation treatments impact the quality, stability, selective reactivity, and auto-ignition characteristics of CRD wood derived biochar?"

To counter this question, the hypotheses suggest that pyrolysis temperature plays a largely critical role in CRD wood conversion, regardless of the processing scale. It is also hypothesized that thermal treatment can be employed after pyrolysis to enhance biochar morphology, minimize unstable volatiles, and also improve thermal/oxidative stability without the use of chemical, CO_2, or steam activation as commonly done in most studies nowadays. Lastly, the flammability of biochar is believed to also depend on its particle size, inherent

moisture, and, the volume it occupies in a storage pile of a specific geometry (small or large), aside from its physicochemical properties.

On the objective's forefront, it is aimed to pyrolyze larger masses of CRD wood in a pilot rotary retort-furnace reactor and to examine properties of resulting biochar, accompanied by a comparison with fossil coal or coke used as reductants in metallurgical processes. Secondly, it explores the potential of post-pyrolysis thermal activation of biochar to reduce VC, H/C, O/C, and increase FC, carbon content, and thermal stability. Another key objective is to theoretically and experimentally investigate self-heating and ignition risks associated with biochar logistics.

The methodology will begin by providing a theoretical overview of biochar oxidation and self-heating risks. This will be followed by a brief description of CRD wood isolation procedure and characterization methods like previous instances. Then, instrumentational set up and attributes of the convectively heated pilot vertical tubular retort-kiln pyrolyzer, rotary retort-furnace activation reactor, and the self-heating testing unit will be discussed. After pyrolysis, physicochemical, structural, and morphological characterizations of biochars as is, and post heat-treated (PHT) trial biochar will be performed to analyze the effect of pyrolysis temperature and secondary activation on its thermal and oxidative stability indices. Then, comparative self-heating experiments will be conducted between untreated and thermally activated biochar, and the findings will be discussed in relation to similar studies, drawing meaningful conclusions for safe industrial applications. Finally, an increase in PHT duration will be adopted for subsequent tests if and only if the trial PHT run was effective in reducing VC and increasing FC of that biochar. Heat-treated biochars at higher durations will also be independently characterized.

7.4 Chapter 5

The chapter consists of an article draft submitted to the journal "Energies", by MDPI publishers. The topic addressed here is, "Kinetic analysis of construction, renovation, and demolition (CRD) wood pyrolysis using model-fitting and model-free methods by thermogravimetric analysis (TGA) ". Presently, the article has been published online. The DOI for the article is: https://doi.org/10.3390/en18102496

This chapter delves into the pyrolysis kinetics and thermodynamics of heterogeneous CRD wood waste. The primary research question is: "How do the kinetic and thermodynamic behaviours of CRD wood affect its pyrolysis mechanisms and energy requirements, and what models best describe this conversion process?"

This study is premised on three major hypotheses. First, CRD wood, due to its heterogeneous composition and varying inorganic content, behaves differently during pyrolysis compared to conventional woody biomass. Secondly, pyrolysis of CRD wood involves multiple degradation phases governed by both surface-bound and diffusion-limited reactions. Finally, the thermodynamic behaviour of CRD wood pyrolysis is expected to reflect high external energy requirements, particularly due to the complexity of the biomass structure.

The objectives include presenting theoretical foundations of both model-fitting and model-free kinetic methods; examining the physicochemical, biochemical, and surface properties of CRD wood; and fitting the thermal degradation data obtained from CRD wood TGA experiments at different heating rates to the aforementioned models to calculate kinetic parameters for understanding the pyrolytic decomposition mechanisms involved.

To address these goals, the CRD wood will be initially subjected to proximate and elemental analysis. Its surface chemistry will be studied through the Fourier transform infrared (FTIR) spectroscopy whereas its biochemical composition entailing holocellulose, extractives, and lignin content will be studied by controlled acid hydrolysis. Metal content in CRD wood will be analyzed through microwave plasma atomic emission spectrometer (MP-AES). Next, TGA experiments will be conducted under an inert atmosphere (nitrogen) at four different heating rates of 10, 20, 30, and 40 °C/min till 900 °C. The weight loss data from TGA is fitted with model-fitting (Coats-Redfern) and model-free (Ozawa-Flynn-Wall (OFW), Kissinger-Akahira-Sunose (KAS), and Friedman (FM)) methods. Kinetic parameters like activation energy, pre-exponential factor, and the overall model fit are then used to arrive at meaningful conclusions about each method. The final analysis attempts to match specific kinetic models with different biomass conversion stages for better mechanism prediction.

P.S: Another published review article on a prior PhD topic related to the Integrated Hydropyrolysis and Hydroconversion (IH2) technology, part of the Bioenergie La Tuque (B.E.L.T), can be found via: https://doi.org/10.1016/j.biombioe.2024.107516. This was presented at the 31st European Biomass and Conference Exhibition, EUBCE (2023) in Bologna, Italy, and garnered a student award.

8. References

Adhikari, S., Moon, E., & Timms, W. (2024). Identifying biochar production variables to maximise exchangeable cations and increase nutrient availability in soils. *Journal of Cleaner Production*, *446*, 141454.

Al Hosni, S., Domini, M., Vahidzadeh, R., & Bertanza, G. (2024). Potential and environmental benefits of biochar utilization for coal/coke substitution in the steel industry. *Energies*, *17*(11), 2759.

Anderson, N., Gu, H., & Bergman, R. (2021). Comparison of novel biochars and steam activated carbon from mixed conifer mill residues. *Energies*, *14*(24), 8472.

Babu, K. K. B. S., Nataraj, M., Tayappa, M., Vyas, Y., Mishra, R. K., & Acharya, B. (2024). Production of biochar from waste biomass using slow pyrolysis: Studies of the effect of pyrolysis temperature and holding time on biochar yield and properties. *Materials Science for Energy Technologies*, *7*, 318-334.

Barszcz, W., Łożyńska, M., & Molenda, J. (2024). Impact of pyrolysis process conditions on the structure of biochar obtained from apple waste. *Scientific Reports*, *14*(1), 10501.

Bluvshtein, N., Villacorta, E., Li, C., Hagen, B. C., Frette, V., & Rudich, Y. (2020). Early detection of smoldering in silos: Organic material emissions as precursors. *Fire safety journal*, *114*, 103009.

Buss, W., Hilber, I., Graham, M. C., & Mašek, O. (2022). Composition of PAHs in biochar and implications for biochar production. *ACS Sustainable Chemistry & Engineering*, *10*(20), 6755-6765.

Castells, B., Amez, I., Medic, L., & García Torrent, J. (2020). Particle size influence on the transport classification labels and other flammability characteristics of powders. *Applied Sciences*, *10*(23), 8601.

da Rosa Azambuja, R., de Castro, V. G., Trianoski, R., & Iwakiri, S. (2018). Utilization of construction and demolition waste for particleboard production. *Journal of Building Engineering*, *20*, 488-492.

Dey, S., Purakayastha, T. J., Sarkar, B., Rinklebe, J., Kumar, S., Chakraborty, R., ... & Shivay, Y. S. (2023). Enhancing cation and anion exchange capacity of rice straw biochar by chemical modification for increased plant nutrient retention. *Science of the Total Environment*, *886*, 163681.

Dhar, S. A., Sakib, T. U., & Hilary, L. N. (2022). Effects of pyrolysis temperature on production and physicochemical characterization of biochar derived from coconut fiber biomass through slow pyrolysis process. *Biomass Conversion and Biorefinery*, *12*(7), 2631-2647.

Díaz, B., Sommer-Márquez, A., Ordoñez, P. E., Bastardo-González, E., Ricaurte, M., & Navas-Cárdenas, C. (2024). Synthesis methods, properties, and modifications of biochar-based materials for wastewater treatment: A review. *Resources*, *13*(1), 8.

El Bari, H., Fanezoune, C. K., Dorneanu, B., Arellano-Garcia, H., Majozi, T., Elhenawy, Y., ... & Ashour, F. H. (2024). Catalytic fast pyrolysis of lignocellulosic biomass: Recent advances and comprehensive overview. *Journal of Analytical and Applied Pyrolysis*, *178*, 106390.

El-Haggar, S., Samaha, A., El-Haggar, S., & Samaha, A. (2019). Sustainable Utilization of Construction and Demolition Waste. *Roadmap for Global Sustainability—Rise of the Green Communities*, 169-188.

Ganesan, A., Rezazgui, O., Burgos, J. B., Mangin, P. J., & Barnabé, S. (2025). Valorization of lignocellulosic biomass forest residues in quebec via the integrated hydropyrolysis and hydroconversion (IH2) technology: A review. *Biomass and Bioenergy*, *193*, 107516.

Ganesan, A., Rezazgui, O., Langlois, S., Boussabbeh, C., & Barnabé, S. (2025). Pyrolytic conversion of construction, renovation, and demolition (CRD) wood wastes in Québec to biochar: Production, characterization, and identifying relevant stability indices for carbon sequestration. *Science of The Total Environment*, *965*, 178650.

Ghaedi, S., Rajabi, H., Mosleh, M. H., & Sedighi, M. (2024). MOF biochar composites for environmental protection and pollution control. *Bioresource Technology*, 131982.

Grojzdek, M., Novosel, B., Klinar, D., Golob, J., & Žgajnar Gotvajn, A. (2024). Pyrolysis of different wood species: influence of process conditions on biochar properties and gas-phase composition. *Biomass Conversion and Biorefinery*, *14*(5), 6027-6037.

Gusiatin, M. Z. (2024). Advantages of Co-Pyrolysis of Sewage Sludge with Agricultural and Forestry Waste. *Energies*, *17*(22), 5736.

Hu, B., Liu, J., Xie, W. L., Li, Y., & Lu, Q. (2024). Biofuels production using pyrolysis techniques. In *Advances in Biofuels Production, Optimization and Applications* (pp. 103-125). Elsevier.

Jerzak, W., Acha, E., & Li, B. (2024). Comprehensive review of biomass pyrolysis: conventional and advanced technologies, reactor designs, product compositions and yields, and techno-economic analysis. *Energies*, *17*(20), 5082.

Joseph, S., Cowie, A. L., Van Zwieten, L., Bolan, N., Budai, A., Buss, W., ... & Lehmann, J. (2021). How biochar works, and when it doesn't: A review of mechanisms controlling soil and plant responses to biochar. *Gcb Bioenergy*, *13*(11), 1731-1764.

Kalina, M., Sovova, S., Svec, J., Trudicova, M., Hajzler, J., Kubikova, L., & Enev, V. (2022). The effect of pyrolysis temperature and the source biomass on the properties of biochar produced for the agronomical applications as the soil conditioner. *Materials*, *15*(24), 8855.

Kazimierski, P., Januszewicz, K., Godlewski, W., Fijuk, A., Suchocki, T., Chaja, P., ... & Kardaś, D. (2022). The course and the effects of agricultural biomass pyrolysis in the production of high-calorific biochar. *Materials*, *15*(3), 1038.

Kumar, V. S., Lee, Z. H., Tan, K. T., & Sim, J. H. (2025). Pyrolysis of sawdust in a horizontal tube furnace: Effects of temperature and heating rate on product composition. In *E3S Web of Conferences* (Vol. 603, p. 03001). EDP Sciences.

Laadila, M. A., LeBihan, Y., Caron, R. F., & Vaneeckhaute, C. (2022). Physical and chemical characterization of construction, renovation and demolition waste in the Quebec province. *Cleaner Waste Systems*, *1*, 100002.

Lin, G., Wang, Y., Wu, X., Meng, J., Ok, Y. S., & Wang, C. H. (2025). Enhancing agricultural productivity with biochar: Evaluating feedstock and quality standards. *Bioresource Technology Reports*, 102059.

Mariyam, S., Al-Ansari, T., & McKay, G. (2023). Particle size impact on pyrolysis of multi-biomass: a solid-state reaction modeling study. *Energy Sources, Part A: Recovery, Utilization, and Environmental Effects*, *45*(2), 3681-3691.

Miura, K. (2016). Adsorption of water vapor from ambient atmosphere onto coal fines leading to spontaneous heating of coal stockpile. *Energy & Fuels*, *30*(1), 219-229.

Mukherjee, A., Patra, B. R., Podder, J., & Dalai, A. K. (2022). Synthesis of biochar from lignocellulosic biomass for diverse industrial applications and energy harvesting: effects of pyrolysis conditions on the physicochemical properties of biochar. *Frontiers in Materials*, *9*, 870184.

Panahi, H. K. S., Dehhaghi, M., Ok, Y. S., Nizami, A. S., Khoshnevisan, B., Mussatto, S. I., ... & Lam, S. S. (2020). A comprehensive review of engineered biochar: production, characteristics, and environmental applications. *Journal of cleaner production*, *270*, 122462.

Panwar, N. L. (2024). Pyrolysis technologies for biochar production in waste management: a review. *Clean Energy*, *8*(4), 61-78.

Pariyar, P., Kumari, K., Jain, M. K., & Jadhao, P. S. (2020). Evaluation of change in biochar properties derived from different feedstock and pyrolysis temperature for environmental and agricultural application. *Science of the Total Environment*, *713*, 136433.

Pathy, A., Pokharel, P., Chen, X., Balasubramanian, P., & Chang, S. X. (2023). Activation methods increase biochar's potential for heavy-metal adsorption and environmental remediation: A global meta-analysis. *Science of The Total Environment*, *865*, 161252.

Peterson, C. A., & Brown, R. C. (2020). Oxidation kinetics of biochar from woody and herbaceous biomass. *Chemical Engineering Journal*, *401*, 126043.

Phounglamcheik, A.; Johnson, N.; Kienzl, N.; Strasser, C.; Umeki, K. Self-Heating of Biochar during Postproduction Storage by O2 Chemisorption at Low Temperatures. Energies 2022, 15, 380. https://doi.org/10.3390/en15010380

Premchand, P., Demichelis, F., Chiaramonti, D., Bensaid, S., & Fino, D. (2023). Biochar production from slow pyrolysis of biomass under CO2 atmosphere: a review on the effect of CO2 medium on biochar production, characterisation, and environmental applications. *Journal of Environmental Chemical Engineering*, *11*(3), 110009.

Recyc-Québec, 2018. Construction, Renovation, and Demolition Residues (CRD). https://www.recyc-quebec.gouv.qc.ca/sites/default/files/documents/Fiche-info-crd.pdf. Accessed on 1 November 2024.

Restuccia, F. (2017). *Self-heating ignition of natural reactive porous media* (Doctoral dissertation, Imperial College London).

Restuccia, F., Mašek, O., Hadden, R. M., & Rein, G. (2019). Quantifying self-heating ignition of biochar as a function of feedstock and the pyrolysis reactor temperature. *Fuel*, *236*, 201-213.

Roshan, A., Ghosh, D., & Maiti, S. K. (2023). How temperature affects biochar properties for application in coal mine spoils? A meta-analysis. *Carbon Research*, *2*(1), 3.

Safa, M., O'Carroll, D., Mansouri, N., Robinson, B., & Curline, G. (2020). Investigating arsenic impact of ACC treated timbers in compost production (A case study in Christchurch, New Zealand). *Environmental Pollution*, *262*, 114218.

Schwarzer, L., Jensen, P. A., Wedel, S., Glarborg, P., Karlström, O., Holm, J. K., & Dam-Johansen, K. (2021). Self-heating and thermal runaway of biomass–Lab-scale experiments and modeling for conditions resembling power plant mills. *Fuel*, *294*, 120281.

Slatter, N. L., Vichanpol, B., Natakaranakul, J., Wattanavichien, K., Suchamalawong, P., Hashimoto, K., ... & Charusiri, W. (2022). Syngas production for Fischer–tropsch synthesis from Rubber wood pellets and eucalyptus wood chips in a Pilot horizontal gasifier with CaO as a tar removal catalyst. *ACS omega*, *7*(49), 44951-44961.

Sun, C., Chen, T., Huang, Q., Zhan, M., Li, X., & Yan, J. (2020). Activation of persulfate by CO2-activated biochar for improved phenolic pollutant degradation: performance and mechanism. *Chemical Engineering Journal*, *380*, 122519.

Suriapparao, D. V., & Vinu, R. (2018). Effects of biomass particle size on slow pyrolysis kinetics and fast pyrolysis product distribution. *Waste and biomass valorization*, *9*, 465-477.

Tomczyk, A., Sokołowska, Z., & Boguta, P. (2020). Biochar physicochemical properties: pyrolysis temperature and feedstock kind effects. *Reviews in Environmental Science and Bio/Technology*, *19*(1), 191-215.

Waluyo, J., Purba, I. T., Linanggeng, Z. A., Maulana, M. L., Kanchanatip, E., Yan, M., & Hantoko, D. (2024). Biomass Pyrolysis: A Comprehensive Review of Production Methods, Derived Products, and Sustainable Applications in Advanced Materials.

Wang, J., Meng, H., & Zhou, H. (2023). Effect of biochar substitution on iron ore sintering characteristics based on optimization of fuel distribution through the bed. *Fuel Processing Technology*, *247*, 107817.

Wang, Y. Y., You, L. C., Lyu, H. H., Liu, Y. X., He, L. L., Hu, Y. D., ... & Yang, S. M. (2022). Role of biochar–mineral composite amendment on the immobilization of heavy metals for Brassica chinensis from naturally contaminated soil. *Environmental Technology & Innovation*, *28*, 102622.

Wang, Y., Li, B., Gao, A., Ding, K., Xing, X., Wei, J., ... & Zhang, S. (2023). Volatile-char interactions during biomass pyrolysis: Effect of biomass acid-washing pretreatment. *Fuel*, *340*, 127496.

Wang, Y., Qiu, L., Zhu, M., Sun, G., Zhang, T., & Kang, K. (2019). Comparative evaluation of hydrothermal carbonization and low temperature pyrolysis of eucommia ulmoides oliver for the production of solid biofuel. *Scientific reports*, *9*(1), 5535.

Xi, Z., Xi, K., Lu, L., & Li, X. (2022). Investigation of the influence of moisture during coal self-heating. *Fuel*, *324*, 124581.

Xiao, F. (2022). A review of biochar functionalized by thermal air oxidation. *Environmental Functional Materials*, *1*(2), 187-195.

Zaman, K. K., Balasundram, V., Ibrahim, N., Samsudin, M. D. M., Kasmani, R., Hamid, M. K. A., & Hasbullah, H. (2018). Effect of particle size and temperature on pyrolysis of palm kernel shell. *Int. J. Eng. Technol*, *7*(4), 118-124.

Zhang, H., Liu, M., Yang, Y., Chen, W., Zhu, J., Zhang, S., ... & Chen, Y. (2023). Mechanism study on the interaction between holocellulose and lignin during secondary pyrolysis of biomass: In terms of molecular model compounds. *Fuel Processing Technology*, *244*, 107701.

Zhang, L., Wu, H., Wang, X., Wu, F., Ding, Z., Song, L., ... & Zhong, P. (2024). Investigation of rates of demolition waste generated in decoration and renovation projects: An empirical study. *Buildings*, *14*(4), 908.

Zhu, X., Li, C., Li, J., Xie, B., Lü, J., & Li, Y. (2018). Thermal treatment of biochar in the air/nitrogen atmosphere for developed mesoporosity and enhanced adsorption to tetracycline. *Bioresource technology*, *263*, 475-482.

CHAPTER 2 – SCIENTIFIC ARTICLE (1)

Pyrolytic conversion of construction, renovation, and demolition (CRD) wood wastes in Québec to biochar: production, characterization, and identifying relevant stability indices for carbon sequestration

Aravind Ganesan [1,2,*], Olivier Rezazgui [1], Simon Langlois[1], Cyrine Boussabbeh[1], Simon Barnabé[2]

[1]Innofibre – Centre d'Innovation des Produits Cellulosiques, 3351, boul. des Forges C.P.97. Trois-Rivières G9A 5E6, Québec, Canada

[2] Institut d'Innovations en Écomatériaux, Écoproduits et Écoénergies, Pavillon CIPP, Université du Québec à Trois-Rivières, boul. des Forges, Trois-Rivières G8Z 4M3, Québec, Canada

* Correspondence: Aravind.Ganesan@uqtr.ca

https://doi.org/10.1016/j.scitotenv.2025.178650

Abstract

Management of heterogeneous construction, renovation, and demolition (CRD) wood residues in Québec brings into light, a widespread topic under discussion related to their current disposal methods in landfills, that may lead to environmental concerns. With rising forfeitures from a legal standpoint, alternative treatment methods for CRD wood wastes are being explored. Thermochemical biomass conversion techniques can be employed to depolymerize low-quality end-of-life CRD wood and valorize it to bio-based products. Biochar, a carbonaceous material obtained through heat treatment of wood under the absence of oxygen via slow pyrolysis, can be tailored for specific end-use applications in hard-to-abate industrial sectors pertinent to energy, composite materials, and environmental amendments. However, there is a scarcity of comprehensively understanding CRD wood pyrolysis and projecting the biochar product's stability due to a lack of relevant studies and frequent inconsistencies amidst currently available methods. Nevertheless, in the present study, CRD wood is pyrolyzed in a horizontal tube furnace of two scales under laboratory conditions. Temperatures ranging from 300-800 °C, biomass residence time (BRT) of 30-120 min, heating rates of 20-55 °C/min, and mass of feedstock between 100-500 g were the operational conditions chosen for experimentation. Evaluation of biochar stability was carried out by the proximate and ultimate analysis, Van-Krevelen plots, TGA/DTG profile, R50 recalcitrance, SEM-EDX, and Raman I_D/I_G methods. Data analysis indicated that carbon content (89-90%), FC (70-74%), TSF (73-75%), R50 (0.64-0.65), and I_D/I_G (0.972) increased with an increase in BRT (120 min) and pyrolysis temperature (800 °C) rendering its utilization in metallurgical applications as a reductant. A surface area of 220-270 m^2/g was also detected for these biochars at 800 °C recommending its implementation for adsorption applications. Biochar's cation exchange capacity (CEC), pH, and hydrophobicity also increased at high temperatures nurturing the ability to be used for soil pH adjustment as part of remediation activities. SEM-EDX proved that ash content predominantly harboring alkali and alkaline earth metals (AAEM) like Ca and K also increased but to a certain point from where their devolatilization is implicit, thereby concentrating stable carbon. As for functionalities in biochar, they decreased from 500-800 °C verifying the rejection of oxychemicals groups. Noticeable striations associated to C-H/C-O/C=O vibration, stretching, and bending from FTIR spectral bands were linked to terminal dehydrogenation, condensation, and aromatization reactions highlighting the development of C-C and C=C linkages commonly assigned to aromatics. Evident from low Van-Krevelen H/C (0.51-0.09) and O/C (0.08-0.02) indices, it can be extrapolated that high-temperature biochars in PR:1 and PR:2 possess a high permeance that could bolster its utilization in carbon sequestration/draw-down and other CDR applications.

Key words: CRD, biochar, stability, pyrolysis, biomass, aromatic, thermochemical

1. Introduction

The Québec Ministry of Forests, Wildlife, and Parks has prioritized sustainable construction practices through policies like the Wood Charter which promotes the use of responsibly sourced timber in residential, industrial, and commercial sectors. Québec's forests, rich in hardwood and softwood species, support eco-friendly building initiatives while generating economic benefits such as job creation, R&D, investments, and trade, all contributing to climate change mitigation. CRD waste management remains a challenge, with Québec producing 1.85 Mt annually, including 56% wood alongside metals, plastics, and other materials (Recyc-Québec, 2018). These include significant contributions from municipal, industrial, and commercial sectors (Recyc-Québec, 2021). Though 53% of CRD wood waste is recovered for alternative uses, 63% among this is diverted for energy recovery and 37% is repurposed for products like furniture and panels (Recyc-Québec, 2018).

This work focuses exclusively on CRD wood sourced from Québec, emphasizing the environmental and economic benefits of recycling locally available wood waste. CRD wood recycling faces hurdles such as issues related to wear/damage and economic constraints with recovery costs ranging from $31.6/t to $181/t depending on quality (Schorr and Boivin, 2023). CRD wood recycling in the province is also hindered by contamination from chemicals (e.g., arsenic, chromium, copper, creosote, and lead) in treated and painted wood, variability in wood composition, and logistical barriers. Treated wood poses environmental risks, releasing these heavy metals, chemicals, and VOCs during disposal if not managed properly. Since Québec contributes to 13% of Canada's CRD wood waste with over 50% comprising of such treated wood, emphasizing the importance of localized valorization is necessary (Schorr and Boivin, 2023). Provincial legislations such as "Q2, r.19 – landfill and incineration" monitor the handling of hazardous CRD materials. Components like gypsum in drywalls release harmful gases (*e.g.,* H_2S) upon landfill disposal, exacerbating environmental penalties. Stricter legal mandates coupled with stakeholder collaboration and policy incentives necessitate alternative treatment methods for heavily contaminated CRD wood management.

Owing to certain difficulties in the recycling and landfilling spheres, CRD wood waste to energy conversion could be an approach that is well-sought-after. Firstly, being a renewable source, it can be replenished via the highly - appreciated sustainable forestry practices in Québec like preventing illegal logging, regeneration and harvesting, reforestation, and agroforestry. Secondly, since it is biomass, it is considered carbon-neutral because the CO_2 released from its energetic valorization is re-captured by trees during their lifecycle. Thirdly, since CRD wood wastes will be diversely available in future because of enhanced utilization in construction within the province, there could be a steady source of supply. Fourthly, utilizing CRD wood fosters local energy security and reduces the reliance on imports. Next, it promotes a genuinely healthy image of waste reduction via a circular economy principle that minimizes landfill treatment and ecological/societal concerns. Finally, the province's abundant natural resources, historical use of wood in construction, and industrial landscape—home to leading metal and alloy producers in the world—test the use of non-recyclable, contaminated CRD wood nowadays as an engineered metallurgical-grade energy source to replace fossil coal or coke. Regional demands promoting carbon sequestration and climate resilience further strengthen the potential for utilizing bioproducts derived from locally sourced CRD wood waste in other applications like soil remediation, horticulture, and agriculture.

Heat aids in faster depolymerization of wood wastes and produces a gamut of products in the solid, liquid, and gaseous forms that can find many attributes. Pyrolysis is an effective thermochemical treatment for the valorization of wood waste at increasing temperatures with limited intervention of air or oxygen to bioproducts of added value like biochar, pyrolysis gas, and biooil (Tian et al 2020). It can be streamlined into either slow, fast or flash pyrolysis corresponding to the employed pyrolysis temperature, heating rate, and BRT (Panwar, 2024). Slow pyrolysis is distinguished by a low pyrolysis temperature, long BRT, and slow heating rate that favours solid biochar yield. An intermediate or moderate pyrolysis temperature, short BRT, and high heating rate maximizes liquid biooil yield via fast pyrolysis. Whereas an exceedingly high pyrolysis temperature, noticeably short BRT, and very high heating rate indicate flash pyrolysis that enhances gas yield (Hasan et al 2022).

As delineated in **Supplementary figure 1**, CRD wood pyrolysis can be bifurcated into two types: primary and secondary pyrolysis (Muema et al 2024). During primary pyrolysis, the hemicellulose, cellulose, and lignin polymers in biomass breakdown in an order, to produce steam (surface and loosely bound water), light gases, primary condensable volatiles (biooil), and primary biochar composed of mono-aromatic rings that begin to confer its stability (Yang et al 2021). The onset of secondary heterogeneous pyrolysis reactions is kicked off at higher temperatures where in-bound/interstitial water molecules are volatilised to form secondary steam, followed by cracking of more unstable/low-molecular weight volatiles that induces the formation of condensed secondary

biooil along with secondary char entailing polyaromatic rings. *i.e*, 2 or more benzene rings attached (Dieguez-Alonso et al 2015). Cracking is also mainly insinuated by primary condensed volatiles settled on biomass and primary biochar, when exposed to prolonged heated atmospheres without being entrained from the reactor (Dieguez-Alonso et al 2015). Extrapolating a finding from Fawaz et al 2021, a major drawback associated to secondary pyrolysis through such cracking reactions is that it could yield low carbon conversion in biochar and biooil due to significant loss of carbon in secondary pyrolysis gases (including CO, CO_2, CH_4, and other C_1-C_3 gases).

Biochar is a carbon rich substance that characterized by its porous, honeycomb-like framework with appreciable physico-chemical properties for use in agriculture, construction, and metallurgical sectors (Bindar et al 2024). Biooil is the liquid, organic product fraction that is rich in a myriad of chemical compounds including but not limited to alcohols, acids, aldehydes, ketones, and aromatics (Steven et al 2024). The biooil can be further refined to optimize its physical and chemical properties for the production of chemicals and fuels (resembling gasoline, diesel, jet fuel, or marine fuel) or can be burnt directly in boilers or furnaces for energy generation. It can also be used to produce distillate fractions serving as precursors for sustainable chemicals (Oktavia et al 2024). Pyrolysis gas consists of components such as CO, CO_2, CH_4, CO_2, SO_X, and NO_X (Kasmiarno et al 2024). Pyrolysis gas can either be combusted to produce heat/electricity in a combined heat and power (CHP) plant, can be looped back to supply a part of the energy for pyrolysis, or can be a foundation for the production of synfuels. Relative to other thermochemical treatments like hydrothermal liquefaction (HTL), gasification or combustion, pyrolysis offers a multitude of product stream with appreciable yields, can be optimized, does not require air, water or oxygen, specialized gas cleaning/upgrading equipment, high temperature or catalyst (Dada et al 2021).

Ideally, CRD wood wastes like furniture wood, plywood, panels, and particle boards could be converted to biofuels or bioproducts through slow or fast pyrolysis (Kim et al 2014). Some articles highlight the production of biooil from CRD wood material through fast pyrolysis in batch and fluidized bed reactors where a moderate temperature of 400-550 °C can produce yields ranging from 30-60 wt% (Heo et al 2010, Jung et al 2012, Kim et al 2014). Higher temperatures with low BRT produced more gases particularly comprising of CO, CO_2, H_2, H_2S, SO_x, NO_X, and C_1-C_3 gases. Whereas lower temperatures and higher BRT produced more biochar with yields ranging from 30-35 wt%.

In recent time, biochar is being researched as a promising carbon dioxide removal (CDR) tool by virtue of its thermostability, high carbon pool locked in, and partly recalcitrant nature in natural surroundings. On grounds of its ideal micro to meso porosity, surface functional groups, surface area and pore volume, biochar is being investigated for multi-disciplinary end-uses like soil fertility improvement, substitute for peat in plant growth media, adsorbent material in feed for rumen animals, wastewater treatment, coloring agent for automotive parts, and construction materials. CRD wood wastes can be pyrolyzed under a myriad of process parameters including but not limited to treatment temperature, BRT, heating rate, and/or mass of feedstock processed. These conditions mainly, can be optimized to produce biochar of appreciable quality and yield, with respect to the intended application under focus. For example, in metallurgical processes involving high temperatures and pressures, pyrolytic biochar could partially substitute coal, coke or anthracite in the blast or electric arc furnace (EAF) as an effective chemical reductant without adverse degradation provided it has a high carbon content, low oxygen, low moisture and ash, high stability, heat conductivity, heating value, and minimal to moderate surface area (well-distributed pore network) (Ye et al 2019). These properties of biochar can also support the slag interaction and metal ore melting processes. Whereas, for areas concerning pollutant gas adsorption or treating wastewater, with high surface area and porosity probably being supportive, a very high carbon (>90%) is not a pre-requisite.

The focus on locally sourced CRD wood ensures relevance to Québec's specific environmental, economic, and industrial contexts, reinforcing the province's leadership in sustainable wood recycling and biochar production. This concentrated approach enhances the feasibility of integrating biochar into Québec's sustainability efforts while addressing the region's unique challenges and opportunities. To the best of our knowledge, there has not been a study on the pyrolytic valorization of CRD wood wastes in Québec to biochar with its characterization pertinent to stability and environmental permeance which is viewed as a major research gap.

Using this knowledge gap as a foundation, the following hypotheses are outlined sequentially: 1) mechanical methods of CRD waste separation to wood and inorganic fractions will eliminate the influence of minerals and metal components during pyrolysis. Additionally, size separation of the wood fraction tapers the optimal particle size for pyrolysis; 2) mild acid washing of milled CRD wood (as chips) will leach higher AAEM concentrations; 3) horizontal tube furnace facilitates efficient conversion of pre-treated CRD wood chips due to better heat

management and lower thermal inertia; 4) pyrolysis under a range of different temperatures, BRT, and/or heating rate can greatly influence the properties of biochar circumventing physical and chemical stability

Therefore, in the present article, we will be covering the following objectives: a) importance of CRD wood sorting and chemical pre-treatment to leach labile AAEM and other soluble metals; b) testing two types of horizontal tube reactors with augmented process design to produce biochar; c) characterization of CRD wood biochars and analyzing the role of pyrolysis parameters, biomass composition on its properties; and d) establishing some "potential" stability indices for biochar-based carbon sequestration and other applications

As deliverables, firstly, various biochar stability assessment methods and their respective categories, which will be leveraged to address the core aim of the study, will be shortlisted. A brief description of each method will then be provided along with an explanation of the mathematical equations/formulae to be utilized. Following this, CRD wood biomass size separation, contaminant removal, milling, and characterizations will take place. Pyrolysis of biomass using a laboratory small-scale horizontal tubular furnace reactor and a scaled-up tubular furnace reactor will proceed, followed by the characterization of the resulting biochars to analyze the effect of feedstock composition, pyrolysis conditions, and process optimization on their physiochemical and structural properties. Finally, the most reliable parameters for indexing biochar stability along with potential applications will be discussed.

2. Materials and methods

Prominent methods to quantify biochar stability into three classes is discussed here prior to deciding the characterizations to be performed.

2.1 Biochar stability - Theory

Despite its potential in climate change mitigation, assessing biochar's stability remains complex, necessitating improved evaluation techniques. Biochar's permeance is not as permanent as minerals and strongly depends on its carbon ring structures, which are formed through rapid chemical transformations during pyrolysis (Chiaramonti et al 2024; Adhikari et al 2024). Stability indices are categorized into three domains. Firstly, alpha indices like Van-Krevelen parameters (H/C and O/C) are widely used, cost-effective indicators of biochar's aromatic condensation and environmental resistance (Budai et al 2013). Proximate analysis, assessing fixed carbon (FC), volatile carbon (VC), and ash content, also aids in understanding stability (Spokas, 2010). Other methods of correlation to study biochar's permeance as a carbon sink are still being optimized mainly due to biochar's heterogeneous carbon pools that are not uniformly represented (Klasson et al 2017). These beta methods include incubation experiments, involving chemical aging with oxidizing agents (*e.g.:* H_2O_2, $KMnO_4$) evaluate biochar's oxidation behavior and mean residence time in soil but are labour-intensive and time-consuming (Cross and Sohi, 2013) procedures. Finally, gamma indices harboring instrumental techniques like ^{13}C-NMR, FTIR, Raman spectroscopy, and XRD analyze biochar's structural properties including aromaticity and crystalline composition to infer durability (Wood et al 2024).

Although these methods provide valuable insights, they require rigorous updates to account for environmental variables such as soil acidity, alkalinity, and composition, especially when biochar is used in agriculture or soil-based CDR applications.

2.1.1 Other metrics for biochar stability

Aside from renowned conventional metrics, two other stability indices were adopted in an attempt to evaluate the biochars produced from in-house pyrolysis experiments.

2.1.1.1 Thermostable fraction (TSF): Category 1 or alpha

TSF is represented through the ratio of FC to the cumulative value of VC and FC derived from proximate analysis of biochar. Equation 1 is adapted from Adhikari et al 2024 to replace VC in place of VM since the biochar sample is already pre-dried to eliminate as much moisture as possible.

$$\text{TSF}\ (\%) = \left(\frac{\text{FC}}{\text{VC} + \text{FC}}\right) \times 100$$

Equation 1

2.1.1.2 TGA R50: Category 2 or beta

Oxidation resistance of biochar was calculated using a low-cost assessment via thermogravimetric analysis (TGA) and by incorporating an index of recalcitrance called R50 (Yang et al 2018). It is a quantitative screening tool to predict biochar's mineralization tendency. A higher R50 value is an indication for greater stability and recalcitrance (Li and Chen, 2018). Pyrolysis parameters, mainly temperature, along with heat treatment duration, and nature of feedstock are directly proportional to this R50 value (Wang et al 2021, Harvey et al 2012). The aforementioned authors classify R50 values into three types: Class A (R50≥0.7) suggesting least biodegradation; Class B (0.5≤R50<7) with moderate degradation; and Class C (R50<0.5), showing highest susceptibility to degradation. From the raw thermogram, R50 is calculated using Equation 2:

$$R50 = \left(\frac{T_{50\%\text{ weight loss for biochar}}}{T_{50\%\text{ weight loss for graphite}}}\right)$$

Equation 2

Here, $T_{50\%\text{ weight loss for biochar}}$ was the temperature in °C obtained from the raw thermogram of a biochar sample where it experienced exactly 50% of its weight loss. Likewise, $T_{50\%\text{ weight loss for graphite}}$ was the theoretical temperature in °C obtained for 50% weight loss of a reference graphite material. Different values for $T_{50\%\text{ weight loss for graphite}}$ were used such as 844 °C in Wang et al 2021 and 886 °C as in Chen et al 2021. In this article, 886 °C was used for calculating the R50 value because it is more common amidst literatures that try to compute biochar carbon stability using this method. However, before the respective temperatures where 50% weight loss of biochar were recorded, the thermograms were first corrected for moisture and ash content using the method discussed in Harvey et al 2012. This ensures that the weight loss was only occurring in the carbonaceous fraction of biochar. To correct the thermogram, Equation 3 is used:

$$W_{i,corrected} = 100 + \left[100 \times \left[\frac{W_{i,uncorrected} - W_{200,ucorrected}}{W_{200,uncorrected} - W_{cutoff,uncorrected}}\right]\right]$$

Equation 3

Here, $W_{i,corrected}$ was the final corrected weight of biochar in the thermogram, $W_{i,uncorrected}$ was the initial uncorrected weight of biochar sample during the initiation of the TGA process, $W_{200,uncorrected}$ was the weight of biochar at 200 °C at which free and non-structural water was believed to be lost or the point after which weight loss was largely attributed to organic carbon decomposition (Yaashikaa et al 2020), and $W_{cutoff,uncorrected}$ was the final weight of biochar in the TGA process where it faced no additional oxidation or further loss of weight. All $W_{uncorrected}$ values were obtained as percentage weights of the sample at that particular temperature from the raw thermogram.

Predicting biochar stability indices still remains challenging due to inconsistencies in available methods, requiring further research to establish robust evaluation criteria. Some methods available to examine stable biochar and the methods that will be used in this work are discussed in **Supplementary table 1**.

2.2 Biomass preparation for pyrolysis

2.2.1 Size separation

As in Figure 3, a mix of CRD wood of varying particle sizes was sourced from "BRQ Fibre et Broyure", Trois-Rivières, Québec, Canada (A). It was collected and brought to the Innofibre's Thermobiom premises at Trois-Rivières in buckets (B). Then, the mix was size separated (C) in a mechanically vibrated sieve of pore sizes >45 mm (E), >7 mm (F), >5 mm (G), and >3 mm (H) with the last tray allotted for any fines. Any contaminants found in the wood mix like glass, plastic, nylon, rubber, and rocks were retrieved and segregated (D).

Figure 3: CRD wood sorting, size-separation, and contaminant removal

2.2.2 Milling

A Retsch SM300 with a 3kW motor, coupled with a high-speed tungsten carbide rotor of variable speeds of 100-3000 rpm, was used for fines generation through milling. The pore size of screens can go down to as low as 500 µm for the apparatus. This equipment was used to produce powder-like material of both, biomass and biochar for their individual characterizations.

2.3 Biochar characterization

2.3.1 Proximate analysis

For proximate analysis, the percentage of ash was quantified using a muffle furnace as per ISO 1171 (McLaughlin, 2018). 1 g of powdered and dry biochar was taken in an open ceramic crucible and heated at a rate of 5 K/min from ambient temperature to 106 °C, where it was held for 60 min. Then the temperature was ramped up to 550 °C with the same heating rate and once again, held for 120 min. Finally, the crucible was removed from the oven and cooled in a dessicator for 15-20 min before the residual weight of biochar was measured for ash determination. For VC, 1 g of powdered and dry biochar was taken in a quartz sealed quartz crucible. Once the temperature of the muffle furnace was set at 900 °C, the crucible was placed inside for exactly 7 min. Following this, the crucible was cooled down in a dessicator for 15-20 min before weighing to determine the labile carbon lost (ISO 562). FC was calculated by using the formula: 100-(VC+ash), on a weight percent dry basis (wt%DB). This formula was adopted from Tu et al 2022 for VC in place of VM since our sample was already dried and moisture-deprived.

2.3.2 Ultimate analysis

To compute the percentage of elements like C, H, N, S, an Elementar Vario Macro Cube was used that has an add on Cl detector too. About 60 samples with varying sample weights of 1-200 mg can be loaded under the influence of helium (purity>99.996%) as carrier gas. Combustion in the presence of >99.996% oxygen till a temperature of 1200 °C can achieved with the instrumentation. With the value of ash from proximate analysis, O was calculated by difference as [100-(C+H+N+S+ash)] suggested by Chen et al 2022.

2.3.3 TGA

To study the variation in weight loss with temperature, a PerkinElmer TGA 8000 analyzer was used. It can also measure proximate analysis metrics like moisture, VM, and ash. About 48 samples can be processed at once with just 8 mg of powdered biochar as is (without drying) in each vial. About 1200 °C can be accurately reached with this set-up with varying heating rates. For our analysis, compressed air was preferred to study the oxidation behaviour of biomass and biochars at a heating rate of 10 °C/min till a maximum temperature of 900 °C.

2.3.4 FTIR

Agilent Technologies' Cary 630 spectroscope equipped with a Microlab PC software was used to analyze the surface functional group distribution on biochar. About 1 g of dry biochar powder, was placed on the surface of a diamond or germanium crystal after periodic cleaning with ethanol, for the determination of chemical bonds that make up the solid material, using the transmittance function with a spectral range of 1000-4000 cm^{-1}. No normalization or baseline peak correction were performed for the spectral peaks. Assigning peaks to their associated functionalities was carried out following a library as mentioned in Johnston et al 2017.

2.3.5 Raman spectroscopy

To analyse the amorphous and highly stable/graphitic carbon make-up in powdered dry biochar, a ThermoScientific DXR3 Raman Spectroscope with a laser power of 7 mW, collection exposure time of 60 s, and a laser excitation wavelength of 532 nm for carbonaceous materials, was used. The diameter which the laser spot could cover can be as low as 1 µm that aided a wider coverage of biochar crystallites. Recorded spectra were under the wavenumber range of 800-1800 cm^{-1}. The ratio of D and G band as I_D/I_G, was used to represent the evolution of biochar's microstructure or degree of graphitization as pyrolysis temperature increased from 500 °C to 800 °C.

2.3.6 BET

Micrometrics Tristar II with a deaerator system to remove impurities, was used to measure the specific surface area and pore volume of dry biochar powder through nitrogen or helium gas physisorption. Pore sizes varying from 0.35-100 nm can be detected using this instrumentation, beginning from 0.01 m^2/g.

2.3.7 Metals

For the detection of metals and other sensitive elements in dry biochar powder, Agilent Technologies' 4210 Microwave Plasma Atomic Emission Spectrometer (MP-AES) operating with nitrogen as fuel source and a SPS 4 autosampler, was used. It allows simultaneous multi-element analysis by nebulizing the biochar sample into a nitrogen plasma to form monoatomic ions. To precisely measure the inorganic content, organic matter in biochar was digested completely by the instrumentation.

2.3.8 pH

Dry biochar powder, at a 1:10 weight ratio with demineralized water (DMW), was mixed with a magnetic stirring plate for 60 min. Post shaking, a bench-top pH analyser was used to measure the pH of the biochar suspension.

2.3.9 Bulk density of biomass

The bulk density of CRD wood to figure out the type of wood it harbored, was carried out according to a method discussed in Pahnila et al 2024. A steel container of a known mass and volume was filled with the heterogeneous CRD wood (before size separation). The surface of the wood mix was evenly levelled to take away excess material and the mass of the container was re-weighed. With the difference in mass of container with and without the CRD wood and its known volume, the bulk density is calculated using Equation 4:

$$\text{Bulk density } \left(\frac{\text{kg}}{\text{m3}}\right) = \frac{(\text{Mass of container with CRD biomass} - \text{Mass of empty container})}{\text{Volume of container}}$$

Equation 4

2.3.10 Biochar yield

The extent of biomass conversion to carbonaceous biochar was indicated by the mass yield that is given by Equation 5, as reported by Khater et al 2024.

$$\text{Biochar yield (\%)} = \left(\frac{\text{Mass of biochar from pyrolysis}}{\text{Mass of CRD biomass taken for pyrolysis}}\right) \times 100$$

Equation 5

2.3.11 Higher heating value (HHV)

The HHV of CRD wood biomass and biochars were calculated using the method described in Channiwala and Parikh, 2002 and Khatibi et al 2023. This method correlated elemental analysis to determine fuel-like properties of the materials.

2.3.12 SEM-EDX

All 4 PR:2 biochars were submitted internally to the microscopy laboratory at I^2E^3, UQTR for the SEM-EDX analysis using a Hitachi electron microscope SU-70 attached to an X-ray analyzer. Magnifications of 500X and 1000X with a 15 kV acceleration voltage under vacuum were adopted for this characterization.

2.4 Statistical analysis

To evaluate the impact of a pyrolysis parameter on key biochar properties such as carbon, hydrogen, oxygen, H/C, O/C, surface area, biochar yield, VC, FC, ash, and TSF, a one-way analysis of variance or ANOVA statistical test using Design Expert software and Origin was applied. Here, differences across the aforesaid dependent variables w.r.t an independent variable like pyrolysis temperature are quantitively analyzed. The data was initially prepared to include replicate information for calculating mean and standard deviation. The p-value was then calculated to check the level of significance ($p \leq 0.05$ – the influence is significant) for the ANOVA test. The meaning for errors were also given to understand the cause of outliers.

2.5 Slow pyrolysis of CRD wood residues

2.5.1 Laboratory-scale horizontal tube furnace - 105 min cycle with 60 min BRT

Initially, 15 g of CRD wood waste not cleaned for AAEM and consisting of a heterogeneous mixture of bark-less hardwood and softwood of varying particle sizes (3 mm to 2.5 cm), were loaded into a cylindrical quartz column (length of 12-inch, diameter of 1 inch, and volume of 0.15 L) of a Thermo Scientific Lindberg Blue M™ 1100 °C mini horizontal tubular fluidized reactor, with a heater wattage of 800 W, power 50/60 Hz and 120 V. The unit and its functions are shown in Supplementary figure 2.

It was verified via a Mettler Toledo analyzer that the moisture content of biomass was less than 10% to minimize a delay in the onset of pyrolysis and to attenuate excessive thermal inertia between the feed and the furnace. Successively, the tube was purged with nitrogen gas (0.1-1 l/min) to flush out oxygen and other reactive gases surrounding biomass, to maintain an inert atmosphere before and after the heating function was turned on. As in Table 1, pyrolysis temperature (300-700 °C) and heating rate (20-50 °C/min) were the variable parameters taken into consideration. In all, 5 experimental runs were conducted to understand the behaviour of the tube furnace on biomass as well as biochar's yield and characteristics. A total cycle time of 105 min was followed during pyrolysis that comprised of a ramp-up phase in the first 15 min, followed by a stationary phase (at set temperature) for 60 min, and a final dwelling/cooling phase for 30 min. The pyrolysis gases generated were condensed in a cold trap and the NCGs were let out.

Table 1: Pyrolysis parameters for laboratory-scale horizontal tube furnace (105 min and 165 min cycles)

Parameters varied during the first round of laboratory trials with constant mass (15 g) of feedstock	Range				
	lowest	low	mid-point	high	highest
Pyrolysis temperature (°C)	300	400	500	600	700
Biomass heating rate (°C/min)	20	26.7	33.3	40	46.7

2.5.2 Laboratory-scale horizontal tube furnace - 165 min cycle with 120 min BRT

For the next series of experiments, the same process conditions as before were adopted except the BRT parameter which was increased to 120 min from 60 min.

2.5.3 AAEM reduction in CRD wood

The sourced CRD wood biomass while classified as low-ash (<5%), contains significant intrinsic AAEM that could pose challenges in biochar production by increasing ash content, catalyzing carbon cracking, and reducing fixed carbon, particularly at high pyrolysis temperatures. Initial experiments with untreated CRD wood revealed issues such as residue buildup that required labour-intensive cleaning. Sometimes, it led to equipment damage and operational downtime in both laboratory and scaled-up reactors. Albeit, a mild acid pre-treatment leached some AAEM content and enabled smoother pyrolysis operations with improved equipment longevity. Given the scarcity of research on CRD wood pyrolysis in Québec and Canada, future work linked to this article will also focus on uncleaned feedstock processed in tube furnaces and pilot-scale equipment (15–25 kg batches) to further investigate the role of pyrolysis parameters, feedstock composition, kinetics, and the operational impact of AAEM-laden wood on biochar properties.

Pre-treatment of CRD wood biomass to lower AAEM and unstable metal content in ash could increase efficiency of pyrolysis (Mazerolle et al 2019). To evaluate if AAEM can be reduced in CRD wood residues prior to pyrolysis, solvent-based lixiviation was followed. This washing of biomass involves a systematic approach using specific reagents and methods to ensure effective inorganic contaminant removal. The protocol mentioned in Québec, 2023 was adopted and modified according to our objectives to be assessed. In Supplementary figure 3, CRD wood blocks (base case) and their chipped/milled residues were taken as two different samples just to compare the change in leaching efficiency with particle size and solvent medium. DMW of a neutral pH at 7.00, served as the primary washing solvent. For acid treatment, a solution was prepared by mixing 14 mL nitric acid (HNO_3) and 16 mL of sulfuric acid (H_2SO_4) in a beaker. This stock solution was then diluted by adding it dropwise to 950 mL of DMW in a 2 L beaker, ensuring a final pH range of 3-4 to mimic a moderately acidic leaching (used interchangeably here with lixiviation) atmosphere. Firstly, for DMW as the leaching solvent, 40 g of undried CRD wood as blocks and chips, were loaded into a lixiviation bottle where a solid-to-liquid ratio of 1:4 was maintained. The mixture was stirred vigorously and subjected to a lixiviation roller treatment at 30 rpm for either 16 or 24 h, depending on the experimental conditions designed. Post-lixiviation treatment, vacuum filtration via a 0.45 µm pore size filter paper proceeded to collect the leached filtrate for analysis. Secondly, for acid leaching, the same procedure was followed by substituting DMW with the prepared acid buffer solution as a new lixiviation solvent. For the entirety of experiments, critical parameters including solid-liquid ratio, lixiviation time, rpm, and the weight of CRD chips/blocks, were maintained as constant parameters to ensure reliable results.

2.5.4 Scaled-up horizontal tube furnace

Acid-washed and chipped CRD wood of varying particle sizes (till 2.5 cm) was loaded into a scaled-up horizontal fluidized bed reactor depicted in Supplementary figure 4. A BRT of 120 min and pyrolysis temperatures between 300 °C and 800 °C were tested, with heating rates varying from 20-55 °C/min to resemble prior conditions. Pyrolysis gas release was monitored as in Supplementary figure 5 to check the reaction's progress.

A Thermo Scientific Lindberg Blue M™ 1100 °C horizontal tube furnace was utilized as a scaled-up configuration for slow pyrolysis under fluidized conditions. A cylindrical heat-resistant steel reactor column of diameter 2.5-inch, length 69 inch, and a combined volume of approximately 5.55 L, was designed and constructed. It could accept up to 500 g of feedstock for pyrolysis at once considering limitations circumventing heat distribution, inert gas passage, and the circulation time of pyrolytic gases. Heating rate for pyrolysis was calculated based on the fact that the reactor was pre-programmed to achieve the set point temperature (SPT) in 15 min. This instrumentation was equipped with 3 temperature controllers, connected by individual K-type thermocouples that measured the furnace temperature supplied to 3 different zones of the quartz tube reactor. This enabled us to comprehend the actual temperature imbibed by the pyrolysis feedstock keeping in mind, any thermal inertia that may have occurred. Supplementarily, another K-type thermocouple was lodged into the quartz column to monitor real time temperature within the reaction zone and to understand how thermal inertia affected the efficiency of pyrolysis. This was the first amendment to our process design. To subdue the settling of hydrocarbon-rich volatiles on biochar surface and also to improve the Van-Krevelen parameters, carefully increased nitrogen flow rates (between 1-5 L/min) to sweep through the reactor to flush out any reactive atmospheres and fixing a vacuum pump as in Supplementary figure 6 with heating a high suction capacity towards the exit gas zone, were two other measures considered.

A problem via accumulation of condensed volatiles in the vacuum suction unit's hose was encountered as pyrolysis gas temperature reduces. A heating tape set at 300 °C and that was attached to the outer body of the vacuum pump's hose, ensured a drastic reduction of tar accumulation inside it or the pump's core. In other words, the pyrolysis gases were transported to the combustion chamber as is with negligible condensation. Usually, if the condensable pyrolysis gases are not removed immediately from the hot reactor, their extended residence time could also result in the formation of more gaseous components thereby leading to carbon loss in biooil or char. The product gases were actually fed into the combustion chamber of a pilot pyrolyzer that catered to a part of its energy demand for pyrolysis operations in the factory. A series of steel meshes with different pore sizes were capped to the end of the reactor column where pyrolysis gases passed through to the vacuum pump. These ensured that firstly, any solid particles were retained within the reactor and did not clog the suction apparatus. Secondly, the meshes also came in handy to prevent solid particulates in the pyrolysis gas mixture from depositing within the condenser train in case they are to be liquified for analyzing the biooil product quality and characteristics.

As the first step to test the column's functions, understand thermal inertia, and acclimatise/train it to pyrolysis cycles, a few redundant test runs were conducted on the CRD wood feedstock as aforesaid earlier, with a diverse range of temperatures (300-800 °C), BRT (30-120 min), and mass of loaded CRD wood (100-500 g). Once the equipment functionalities and process are standardized, further repeatability and reproducibility (R&R) runs will be performed.

3. Results and discussion

3.1 Slow pyrolysis in laboratory-scale horizontal tube furnace - 105 min cycle with 60 min BRT

The three phases of CRD wood pyrolysis, *i.e*, ramp-up, stationary, dwelling, and their experimental progress were recorded as shared in

Supplementary figure **7**. The ultimate analysis and biochar yield data in Table 2 show a clear increase in carbon content with rising pyrolysis temperatures from 300 °C to 600 °C, consistent with observations by Babu et al 2024. However, at 700°C, carbon content decreases slightly below 80%, potentially due to the onset of carbon cracking, resulting in the loss of carbon as light gases. This phenomenon aligns with findings by Aktas et al 2024, which indicate a 39% reduction in biochar yield—from 39.13% at 300 °C to 23.93% at 700 °C. The presence of AAEM in the biomass could have contributed to greater catalytic activity, promoting gas-phase reactions that remove carbon during volatile-char interactions (Li et al 2023). Conversely, AAEM may also increase secondary char yield under certain conditions, highlighting the complexity of its dual effects (Anca-Couce et al 2017). Further research is necessary to fully understand these mechanisms.

The density and diversity of oxygen-containing volatile functional groups decrease with rising pyrolysis temperatures. However, at 700 °C, the oxygen content in biochar contradicts this trend, showing an unexpected increase compared to the biochar at 600 °C. This anomaly may result from the deposition of oxygen-rich pyrolytic volatiles on biochar or their interaction during volatile evolution within the reaction zone (Huang et al 2020). Without proper removal of pyrolytic volatiles—either by increasing the inert carrier gas flow rate or employing vacuum suction—oxygenic volatiles might condense within cooler reactor zones, particularly at the tube's ends where heating is less effective. Additional factors contributing to the observed carbon loss and oxygen increase include: air infiltration during pyrolysis (Supplementary figure 10); air infiltration during the cooling phase; or secondary reactions between volatiles and char, leading to carbon loss as gaseous products.

Proposed solutions to mitigate these challenges are discussed in subsequent sections, which focus on scaled-up experiments using a horizontal tube furnace.

Table 2: Elemental analysis and biochar yields from the 105 min cycle

Sample (Biomass or biochar)	N (%)	C (%)	H (%)	S (%)	Ash (%)	O (%)	H/C	O/C	Biochar yield (g)	Biochar yield (%)
CRD wood feed	0.99	49.88	6.12	0.10	1.17	41.74	1.47	0.63	---	---
Biochar at 300 °C	0.30	69.97	3.87	0.17	4.82	20.87	0.66	0.22	5.87	39.13

Biochar at 400 °C	0.38	75.16	3.45	0.09	5.99	14.93	0.55	0.15	4.59	30.60
Biochar at 500 °C	0.39	79.28	2.97	0.05	6.80	10.51	0.45	0.10	4.19	27.93
Biochar at 600 °C	0.34	82.86	2.22	0.03	6.32	8.23	0.32	0.07	3.90	26.00
Biochar at 700 °C	0.57	79.18	1.40	0.02	6.96	11.87	0.21	0.11	3.59	23.93

The removal of heat-labile functional groups (hydrogen, oxygen, and decomposable carbon) increases with higher pyrolysis temperatures and BRT that can be represented by a Van Krevelen diagram. This indicates a reduction in volatile functionalities and progress in carbon structural ordering (C–C, C=C). Low H/C and O/C ratios are critical for oxidative stability, though they require further validation for accurately predicting biochar's structural framework (Zhu et al 2023). Optimization of pyrolysis conditions and biomass pre-treatment (*e.g.,* acid washing to reduce catalytically active AAEM) can improve biochar quality. Higher temperatures and longer BRT enhance intra-particle heat distribution, aided by external convective heating. This promotes more efficient biomass decomposition, increasing carbon content while reducing oxygen, hydrogen, and overall biochar yield.

To study the effect of longer biomass residence time (BRT), it was increased from 60 to 120 min, keeping the ramp-up and dwelling times constant. The stationary phase (SPT) was extended by 60 min, while the temperature range (300–700 °C) and heating rates remained unchanged. Increasing the nitrogen gas flow is recommended to prevent condensation of pyrolytic volatiles on biochar. However, excessive nitrogen flow may cool the reactor, reduce heat distribution, and accelerate volatile condensation.

3.2 Slow pyrolysis in laboratory-scale horizontal tube furnace - 165 min cycle with 120 min BRT

Similar to the 105 min pyrolysis cycle, the three phases of CRD wood pyrolysis in the 165 min cycle with their temperature profiles were recorded as shared in Supplementary figure 8. During the 165 min cycle, biochar at 700 °C showed higher carbon content (83–84%) with reduced oxygenates and improved Van Krevelen parameters of H/C and O/C (Table 3), compared to minor discrepancies in the 105 min cycle. Carbon content increased from 62.16% at 300 °C to 83.51% at 700 °C. While increased BRT theoretically reduces yields due to prolonged heating, yields were consistent between cycles at 400–700 °C. However, at 300 °C, yield increased significantly (70.60%, 10.59 g), likely due to unconverted CRD wood fractions from uneven heating or temperature gradients (Marti-Rossello et al 2019). The BET surface area at 700 °C was 139.88 m^2/g, indicating micropore formation from volatile decomposition, compared to a lower surface area (2.67 m^2/g) at 300 °C (Barszcz et al 2024). Pyrolysis gases (CO, CO_2, and C_1–C_3) released intrinsic carbon, forming structurally ordered microporous networks.

Table 3: Elemental analysis and biochar yields from the 165 min cycle

Sample (Biomass or biochar)	N (%)	C (%)	H (%)	S (%)	Ash (%)	O (%)	H/C	O/C	Biochar yield (g)	Biochar yield (%)	S.Area (m^2/g)
CRD wood feed	0.99	49.88	6.12	0.10	1.17	41.74	1.47	0.63	---	---	---
Biochar at 300 °C	0.23	62.16	5.37	0.00	4.8	27.39	1.04	0.33	10.59	70.60	2.67
Biochar at 400 °C	0.43	73.14	3.46	0.00	8.8	14.19	0.57	0.15	4.86	32.40	2.76
Biochar at 500 °C	0.36	78.38	2.77	0.00	9.0	9.48	0.42	0.09	3.97	26.47	99.16
Biochar at 600 °C	0.43	79.98	2.27	0.06	10.1	7.19	0.34	0.07	3.75	25.00	104.5
Biochar at 700 °C	0.54	83.51	1.62	0.00	9.6	4.70	0.23	0.04	3.51	23.40	139.88

A high nitrogen carrier gas flow rate likely reduced reactive species by quickly removing pyrolytic volatiles, preventing their premature settling on biochar or biomass surfaces and reducing secondary charring. Secondary charring can block micropores and active sites, impairing adsorptive properties (Anca-Couce et al 2017). Retrofitting a vacuum suction pump to extract pyrolytic gases during production is a potential solution for scaled-up systems to mitigate this issue.

High thermal inertia between the refractory bricks and the tube reactor was observed at higher pyrolysis temperatures (≥500 °C), affecting biochar appearance. At lower temperatures (300–400 °C), unconverted biomass fractions persisted suggesting incomplete biomass breakdown and insufficient pyrolysis. To address these issues, additional tests were conducted using equipment with temperature monitoring (via a probe) under the same 120 min BRT. Results confirmed a thermal inertia of approximately 300 °C (Supplementary figure 9), which adversely impacts biomass carbonization and biochar physiochemical properties. Despite significant thermal inertia, ash content in biochar increased with temperatures from 300–700 °C when BRT was extended by 60 min. Pre-treating biomass with H_2SO_4, HNO_3, or water washing could reduce initial metal content, potentially improving biochar quality. Using a gas analyzer during the initial phase of the 120 min BRT cycle (Supplementary figure 10) revealed oxygen levels of 15–20 vol%, likely from unnoticed air infiltration due to sealing issues. This could lead to mild combustion, contributing to increased ash and reduced carbon in biochar. Gaseous products like CO and CO_2 were detected, likely from typical decarbonylation and decarboxylation reactions but warrant differentiation from oxygen infiltration. Proper reactor sealing and inert gas use are essential to maintain an oxygen-limited environment (<1 vol% oxygen) and prevent combustion-like reactions, ensuring optimal biochar composition and stability.

Examining the results from 105 min and 165 min cycles, minor discrepancies can be observed with respect to heat loss, heat transfer between biomass particles, and partial settling of volatile matter. On the other hand, elemental analysis and yields of biochar implied that the effect of feedstock composition, optimization of pyrolysis parameters, and modifying reactor/working design can boost the reliability of experimentations. Due to the undependability of obtained results from laboratory-scale horizontal tube furnace linked to unevenness of equipment functions, the next phase of trials was conducted in a scaled-up horizontal tube furnace, but this time, using CRD wood treated for inherent metals like AAEM.

3.3 Impact of CRD wood acid washing

Acid washing of CRD wood was performed to assess its ability to leach metals and its impact on subsequent pyrolysis (Bindar et al 2024). The leaching efficiencies for Ca, K, Ba, Mg, and Na were significantly higher in acidic media than in DMW, regardless of particle size. The formation of soluble metal complexes through proton displacement in the acid might explain this trend (Usino et al 2023). The pH of lixiviated acidic filtrates increased over time due to rising metal concentrations, neutralizing the acid's effect. As tabulated in Supplementary table 2, with CRD wood blocks, metal concentrations rose substantially between DMW (16 h lixiviation) and acid (24 h lixiviation): Na from 18.07 to 69.83 mg/L, K from 2.12 to 28.99 mg/L, Ca from 4.50 to 104.11 mg/L, Mg from 5.58 to 52.55 mg/L, and Ba from 0.011 to 0.125 mg/L. For CRD wood chips, similar trends were observed: Na from 86.56 to 240.09 mg/L, K from 20.87 to 239.39 mg/L, Ca from 80.14 to 719.31 mg/L, Mg from 51.01 to 258.03 mg/L, and Ba from 10.096 to 191.242 mg/L. These results confirm the effectiveness of acid washing in reducing metal content, enhancing its potential for improved pyrolysis outcomes.

Ca was the most leached AAEM across both biomass particle sizes (Figure 4). Mild acid pre-treatment proved effective in reducing AAEM content in CRD wood with stronger acids likely to enhance this reduction further. Acid treatment destabilized and hydrolyzed biomass polymers like hemicellulose and cellulose, weakening covalent bonds with lignin and AAEM which may improve pyrolysis efficiency (Usino et al 2023). An unusual trend was noted with Fe levels which increased significantly in CRD wood blocks from 0.82 mg/L (16 h DMW) to 100.77 mg/L (24 h acid). This was likely due to residual nails or metal traces in the blocks, contrasting with lower Fe levels in CRD chips, where particle size reduction helped separate contaminants. Chips also showed higher leaching efficiency, as finer samples provided greater surface area and solution contact.

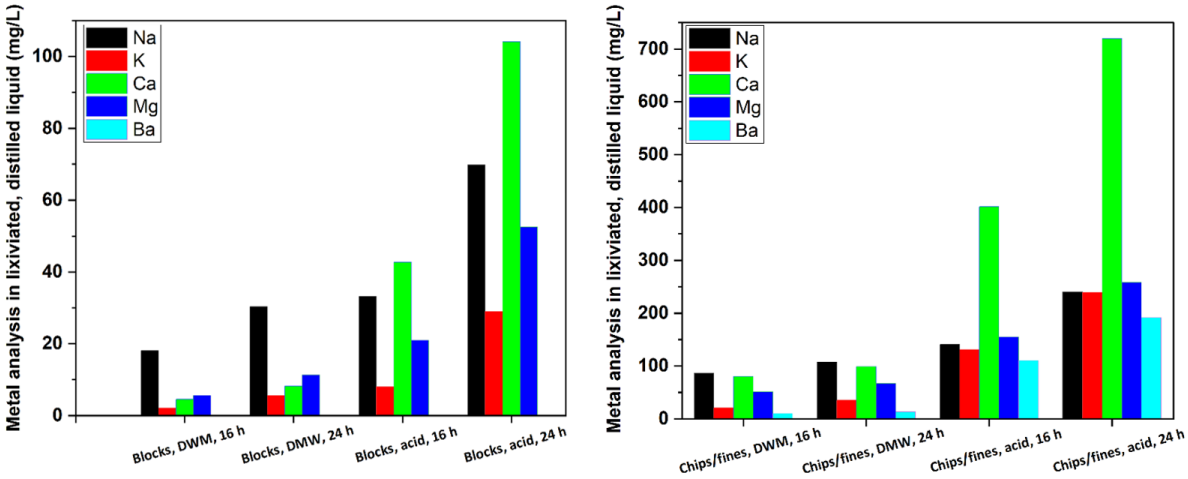

Figure 4: Variation in concentration of leached AAEM with time, solvent type, and particle size

As described in Zadeh et al 2020, when the mild acid treated and untreated CRD wood chips were compared, there was an increase in carbon (7.92%), and a reduction in nitrogen, sulfur, hydrogen, and oxygen heteroatoms as interpreted from Table 4. Implicitly, H/C and O/C were also lowered suggesting that acid treatment solubilized some biomass volatiles. Ash content in the treated fraction concomitantly reduced by 27.35%.

Table 4: Difference in composition of CRD wood before and after washing

Sample (Biomass or biochar)	N (%)	C (%)	H (%)	S (%)	Ash (%)	O (%)	H/C	O/C
CRD wood feed before washing	0.99	49.88	6.12	0.10	1.17	41.74	1.47	0.63
CRD wood feed after washing	0.49	53.83	5.84	0.04	0.85	38.95	1.30	0.54

This experiment, hence, proves that AAEM and other metals in CRD wood can be reduced prior to pyrolysis for eliminating any unnecessary side reactions and inflicting mechanical stress over the unit's instrumentation (mainly the reactor). However, it is important to remember that treating CRD wood for any metal removal will generate metal-laden wastewater that has to be treated via biological or chemical means eventually adding to process costs.

3.4 Slow pyrolysis in scaled-up horizontal tube furnace

It was examined from Supplementary figure 11 that the temperatures of 300 °C and 400 °C yielded low carbon in the biochar and also resulted in incomplete conversion of biomass. In other words, it was increasingly complex to achieve high degree of carbonization below 500 °C. From 500 °C, the conversion and char morphology were appreciable. Higher temperatures of 600, 700, and 800 °C yielded chars with subsided yields, but with superior properties. Subsided yields can be attributed to high heat treatment temperature (HTT) and due to leached/gradual devolatilization of AAEM as inferred from Xu and Sheng, 2012. Thermal inertia between the refractory bricks and reaction column was minimal (15–20°C) up to 500°C but increased to 50–125 °C at 500–800 °C (Supplementary figure 12). To address this, SPTs were adjusted for each trial. A 120 min BRT was maintained to replicate conditions from the smaller laboratory-scale setup. At the larger scale, 400 g of feedstock was identified as the optimal biomass load per run, ensuring efficient heat transfer, minimal pyrolytic condensate trapping, and effective inert gas sweeping for vacuum suction. Further experiments are needed to confirm the repeatability and reproducibility (R&R) of this setup.

As a second step, two different conditions were chosen based on the observations from preliminary test runs. For the first condition, a moderate pyrolysis temperature of 500 °C, BRT of 120 min, and 400 g of CRD wood feedstock was adopted. The second condition was executed at a high pyrolysis temperature of 800 °C while the other two parameters remained the same. The elemental analysis and yields of biochar are tabulated in Table 5.

Table 5: Biochar properties and conversion from test runs at 500 °C and 800 °C in scaled-up tube furnace

Sample	N (%)	C (%)	H (%)	S (%)	Ash (%)	O (%)	H/C	O/C	Biochar yield (g)	Biochar yield (%)
CRD wood feed	0.49	53.83	5.84	0.04	0.85	38.95	1.30	0.54	---	---
Biochar 500°C	0.45	86.26	2.90	0.06	2.66	7.67	0.40	0.07	106.8	26.7
Biochar 800°C	1.04	90.78	0.72	0.05	6.62	0.79	0.10	0.01	78.0	19.5

The results in Figure 5 revealed that CRD wood pyrolysis in the scaled-up horizontal tubular furnace supported lower H/C, O/C, higher carbon, and better temperature control (low heat loss – biomass in the reaction zone received sufficient heat) relative to the laboratory-scale horizontal tubular furnace. So, the next set of trials will be carried forward in this set-up. A comparison of Van-Krevelen performances of CRD wood biochars produced in-house versus some reference biochars, anthracites, and cokes (described in Supplementary table 3) was derived to understand the effect of pyrolysis process conditions on biochar properties.

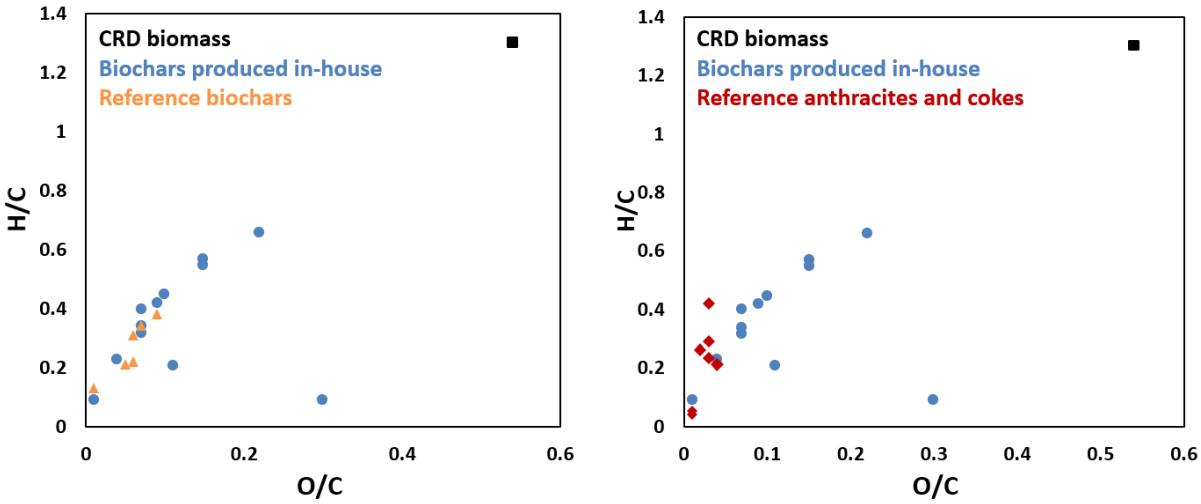

Figure 5: Comparative Van-Krevelen performance of carbonaceous materials. {12 tests in total: (5 tests) - 105 min pyrolysis; (5 tests) - 165 min pyrolysis; and (2 tests) - scaled-up horizontal tube furnace pyrolysis trial runs}

VC in biochar was estimated as wt%DB to assess the proportion of easily decomposable carbon. Unlike volatile matter (VM), VC excludes moisture and other labile components. Using ash content values, FC was calculated to better understand carbon stability (Moisture + VC + FC + Ash = 100 wt%DB). To evaluate the repeatability and reproducibility (R&R) of the scaled-up horizontal tube furnace, two additional pyrolysis rounds (PR:1 and PR:2) were conducted using CRD wood residues from the same bale. Identical biomass pre-treatment and pyrolysis parameters were applied by different operators. The properties of the resulting biochars, detailed in Table 6, were analyzed to validate the system's performance.

Table 6: Physiochemical properties of biochars produced in the scaled-up horizontal tubular furnace as part of R&R testing.

Sample	N (%)	C (%)	H (%)	S (%)	Ash (%)	O (%)	H/C	O/C	S.Area (m^2/g)	Pore volume (cm^3/g)	Yield (%)
Treated CRD wood feed	0.49	53.83	5.84	0.04	0.85	38.95	1.30	0.54	---	---	---
Pyrolysis Round 1: (PR:1)											

Biochar 500 °C	0.56	85.42	3.63	0.25	3.88	6.27	0.51	0.06	88.335	0.092	25.7
Biochar 600 °C	0.41	85.46	2.18	1.01	4.94	6.01	0.31	0.05	198.151	0.096	22.4
Biochar 700 °C	0.18	87.82	0.89	0.25	5.88	4.98	0.12	0.04	251.276	0.111	21.1
Biochar 800 °C	0.16	89.54	0.67	0.10	7.27	2.27	0.09	0.02	270.004	0.122	16.6
Pyrolysis Round 2 (PR:2)											
Biochar 500 °C	0.51	84.02	3.11	1.01	2.11	9.24	0.44	0.08	71.354	0.090	26.9
Biochar 600 °C	0.46	85.87	2.64	0.25	3.76	7.02	0.37	0.06	187.516	0.092	21.9
Biochar 700 °C	0.38	87.09	1.59	0.25	5.65	5.04	0.22	0.04	223.703	0.102	19.6
Biochar 800 °C	0.25	89.47	0.91	0.10	6.52	2.76	0.12	0.02	238.88	0.116	15.1

3.5 Biochar characterization

3.5.1 Ultimate analysis for PR:1 and PR:2 biochars

Heteroatom composition in PR:1 and PR:2 biochars was consistent. The carbon content increased while oxygen and acidic functionality decreased with higher pyrolysis temperatures, promoting aromatic condensation and hydrophobicity. High temperature biochars exhibited alkaline pH due to the decomposition of surface protons and the concentration of residual ash including AAEM salts and minerals which contribute to basicity (Sun et al 2017). This alkaline range is beneficial for remediating acidic soils through extractable nitrates, Mg, and Ca (Premalatha et al 2023). Traces of sulfur from gypsum drywall composites in CRD wood were detected as intrinsic sulfur in biochars at 400–500 °C. After 600 °C, sulfur could have been released as SO_2 and H_2S due to progressive carbon lattice cleavage. Surface area increased significantly with temperature: for PR:1, from 88 m^2/g at 500 °C to 270 m^2/g at 800 °C (206% rise), and for PR:2, from 71 m^2/g to 238 m^2/g. These enhancements, along with tunable active sites and porosity, make biochar suitable for agricultural applications, improving moisture retention, erosion control, aeration, and microbial development (Sharma, 2024).

3.5.1.1 H/C and O/C indices to determine biochar stability

Biochars produced at 600–800 °C align with stability standards set by global organizations such as the European Biochar Industry (EBI), International Biochar Initiative (IBI), and Australia New Zealand Biochar Industry Group (ANZBIG) (Adhikari et al 2024). As shown in the Van Krevelen plots, biochar at 800 °C exhibits properties similar to green coke, with potential for further heat treatment to enhance stability akin to metallurgical or calcined coke. High pyrolysis temperatures increased carbon content while reducing H/C and O/C ratios, consistent with findings by Sanei et al 2024 and validated in this study. As depicted in Figure 6, H/C values for biochars above 500 °C dropped to 0.1 or lower, with PR:1 biochar at 800 °C achieving an H/C of 0.09, classifying it under the "inertinite benchmark" (Bier and Lerchenmuller, 2024). These biochars hold potential for long-term carbon sequestration, with inertinite fractions offering resistance to degradation for up to 10,000 years (Bier and Lerchenmuller, 2024). Although most commercial biochars meet these inertinite criteria, further research is needed to confirm their resistance to microbial degradation through realistic incubation studies (Azzi et al 2024).

In the black carbon continuum, biochars with O/C < 0.2 are less sensitive to oxidative atmospheres and may have a half-life exceeding 1000 years, compared to 100–1000 years for O/C between 0.2–0.6, and ~100 years for O/C > 0.6 (Spokas, 2010). This makes O/C < 0.2 ideal for applications like soil carbon sequestration and metallurgy, which require resistance to mineralization. Mineralization, as defined in this context, refers to the decay of organic matter to CO_2 via biotic or abiotic interactions (Chiaramonti et al 2024). For biochars produced in the scaled-up horizontal tube furnace, O/C values < 0.1 (Figure 6) suggest a minimum half-life of 1000 years and progression toward a turbostratic structure of condensed heterocyclic aromatics. However, confirming this requires molecular analyses such as Raman spectroscopy, XRD, ^{13}C-NMR, or FTIR. O/C is an indicator of stability but can be influenced by post-production factors like cooling method, rate, and storage. For instance, while nitrogen-purged cooling and airtight storage in this study ensured O/C < 0.2, air or water cooling and open storage could increase

O/C, regardless of pyrolysis temperature. Thus, O/C (and H/C) may reflect not just volatile content but also inherent structure and post-production effects, emphasizing the need for controlled pyrolysis, activation (if necessary), and storage practices.

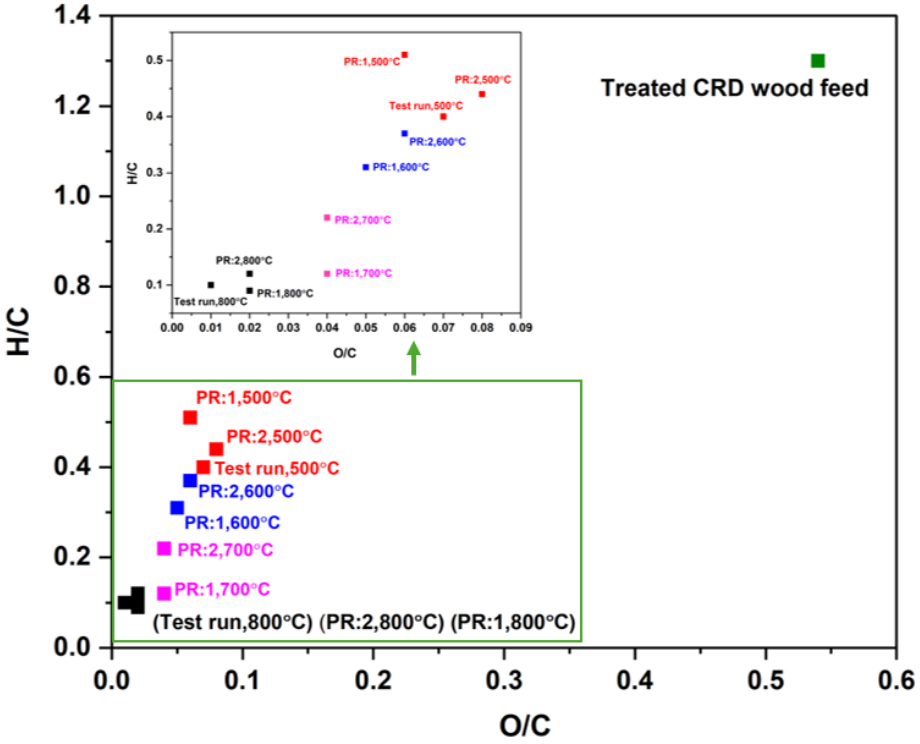

Figure 6: H/C and O/C indicators of biochars produced in pyrolysis rounds 1 and 2 for projecting stability. The two test runs at 500 °C and 800 °C from laboratory scaled-up horizontal tube furnace are also included

3.5.2 Proximate analysis for PR:1 and PR:2 biochars

In Table 7, increase in pyrolysis temperature from 500 °C to 800 °C, led to a reduction in VC by 64% among the PR:1 biochars (also described in Supplementary figure 13). A similar trend was observed for the PR:2 biochars where it decreased by 60%. Heat treatment releases most functional groups from the biochar's surface into the pyrolysis gas phase and concentrates carbon with inorganics. This statement can be confirmed by the increase in ash content by 87% and 209% for PR:1 and PR:2 biochars respectively. FC concomitantly rose by approximately 19% and 14% too.

Table 7: Proximate analysis parameters and HHV for biochars produced in pyrolysis rounds 1 and 2. TGA thermal stability index and Raman index for biochars produced in pyrolysis round 1 only

Char sample	VC (wt%DB)	Ash (wt%DB)	FC (wt%DB)	TSF (%)	HHV (MJ/kg)	TGA R50	I_D/I_G
PR:1, 500 °C	25.74	3.88	70.38	73.22	33.38	---	---
PR:2, 500 °C	24.86	2.11	73.03	74.60	32.09	0.544	0.787
PR:1, 600 °C	15.55	4.94	79.51	83.64	31.77	---	---
PR:2, 600 °C	16.04	3.76	80.20	83.33	32.30	0.577	0.812
PR:1, 700 °C	12.23	5.88	81.89	87.01	31.09	---	---
PR:2, 700 °C	13.60	5.65	80.75	85.59	31.66	0.588	0.928
PR:1, 800 °C	9.27	7.27	83.46	90.00	31.67	---	---
PR:2, 800 °C	10.06	6.52	83.42	89.24	31.89	0.647	0.972

TSF is a proxy for biochar FC and VC which are in turn surrogate indices for the overall biochar stability. TSF for biochars in PR:1 and PR:2 are comparable and vary from 73-75% when the pyrolysis temperature is 500 °C, to 89-90% when produced at 800 °C. This could prove that biochars derived at high temperatures can retain a

remarkable amount of carbon by resisting thermal decomposition and could have a high permeance when applied to soils or used for carbon credits projects. HHV of CRD wood biomass was calculated to be 21.62 MJ/kg. As pyrolysis temperature was increased, the HHV ranged from 31-34 MJ/kg which signifies a jump in calorific value. To summarize, the properties of biochar from the above trials (test runs, PR:1, and PR:2) do not differ drastically thereby, bypassing the need for the triplicate runs. There is plausible precision with the results from the two trials in addition to the test runs at 500 and 800 °C. Hence, this equipment is suitable for biochar production.

The following characterizations inclusive of TGA/DTG, SEM-EDX, TGA R50, FTIR, and Raman analysis were performed only on PR:2 biochars as an example to evaluate their stability.

3.5.3 TGA/DTG

Thermal decomposition and stability of biomass and biochars was analyzed using TGA and TGA R50 respectively, at a heating rate of 10 °C/min (Figure 7). Biomass thermograms exhibited a three-phase weight loss pattern (Sarkar et al 2024): a) water evaporation; b) decomposition of holocellulose (hemicellulose and cellulose); and decay of lignin along with high molecular weight compounds. Maximum biomass weight loss (>90%) occurred between 150–550 °C, while biochars decomposed primarily between 500–700 °C, beyond which inorganic content acted as a heat dissipation barrier, halting further weight loss (Anand et al 2023).

For CRD wood, the DTG plot revealed three degradation phases, similar to pine wood and sawdust (Mishra and Mohanty, 2018). The first phase (150–200 °C) involved moisture and surface volatile removal. The second phase (200–400 °C) with a sharp weight loss and peaking at 346 °C indicated hemicellulose and cellulose decomposition, accompanied by reactions such as decarbonylation, depolymerization, and decarboxylation, releasing carbon, oxygen, and hydrogen as gas-phase products. This stage marked a significant reduction in char yields and the release of pyrolytic volatiles (condensible as biooil), mostly from cellulose. Progression of pyrolysis is very obvious in this zone where dissociation of the relatively tough lignin framework also begins. The third phase (beyond 400 °C) involved slow lignin decomposition, peaking at 483 °C. Endothermic reactions such as dehydration, cracking, demethylation, condensation, isomerization, and aromatization formed aromatics and higher hydrocarbons. This phase also promoted char formation and residual ash accumulation.

For PR:2 biochars produced at 500–700 °C, the DTG plot showed a single peak mass loss at 515 °C, 539 °C, and 556 °C, reflecting increased thermal stability and higher energy required to break condensed aromatic structures as pyrolysis temperature rose. These biochars exhibited high energy content due to strong C–C, C=C, and C≡C bonds. At these temperatures, diminished H/C and O/C ratios confirm the volatilization of heat labile compounds during carbonization (Babinszki et al 2024). Slow pyrolysis heating rates promoted VM melting, aiding micropore structure development and surface area increase. Conversely, biochars at lower temperatures retained higher VM, aligning with our findings. For biochar at 800 °C, peak mass loss shifted to ~600 °C, indicating expanded FC and ash content. The flatter DTG curve suggested the absence of easily degradable organics.

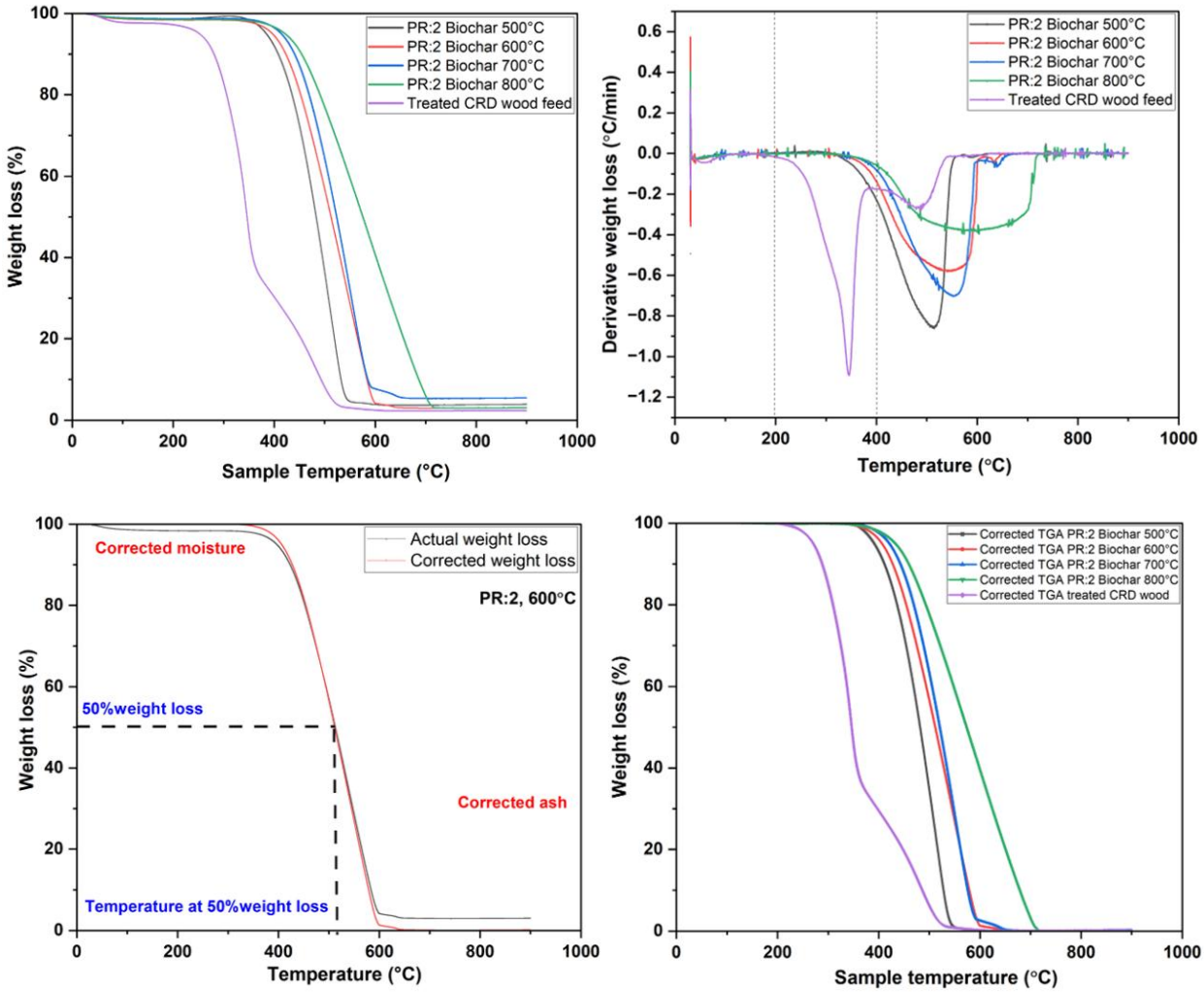

Figure 7: <u>Top left and right</u>: TGA; and DTG thermal decomposition profiles - for CRD wood biomass and biochars under varying pyrolysis temperatures. <u>Bottom left and right</u>: Sample of a corrected thermogram for calculating the TGA R50 recalcitrance index; and all moisture, ash-corrected thermograms

3.5.4 SEM-EDX

Through the EDX spectra, the presence of high carbon and resolute AAEM in ash were shown to be predominant contenders in these stable biochars produced at 600-800 °C which is explainable by increase in alkalinity up to a pH of 11.09. Carbon content in the cross-sections of biochar under analysis as in Figure 8, was about 95%, 95.5%, and 96.6% respectively iterating to the formation of large aromatic carbons via condensation of small aromatic units. Oxygen decreased from 4.6% to 3.8%, and 2.8% respectively, specifying that high temperatures showed a reduction in oxygenic functional groups (*e.g.:* -OH, SO_3H, -COOH). Oxygen may also be bonded to AAEM, as concluded in Chiaramonti et al 2024. AAEM content in ash at this point was mainly seen as Na, K, and Ca making up to 0.4-0.5% only, due to their eventual devolatilization. Pre-treatment of CRD wood might have also led to a decrease in inorganics detected in the EDX spectra. Sulfur was detected due to the presence of gypsum fines from dry wall residues in the initial CRD wood feedstock.

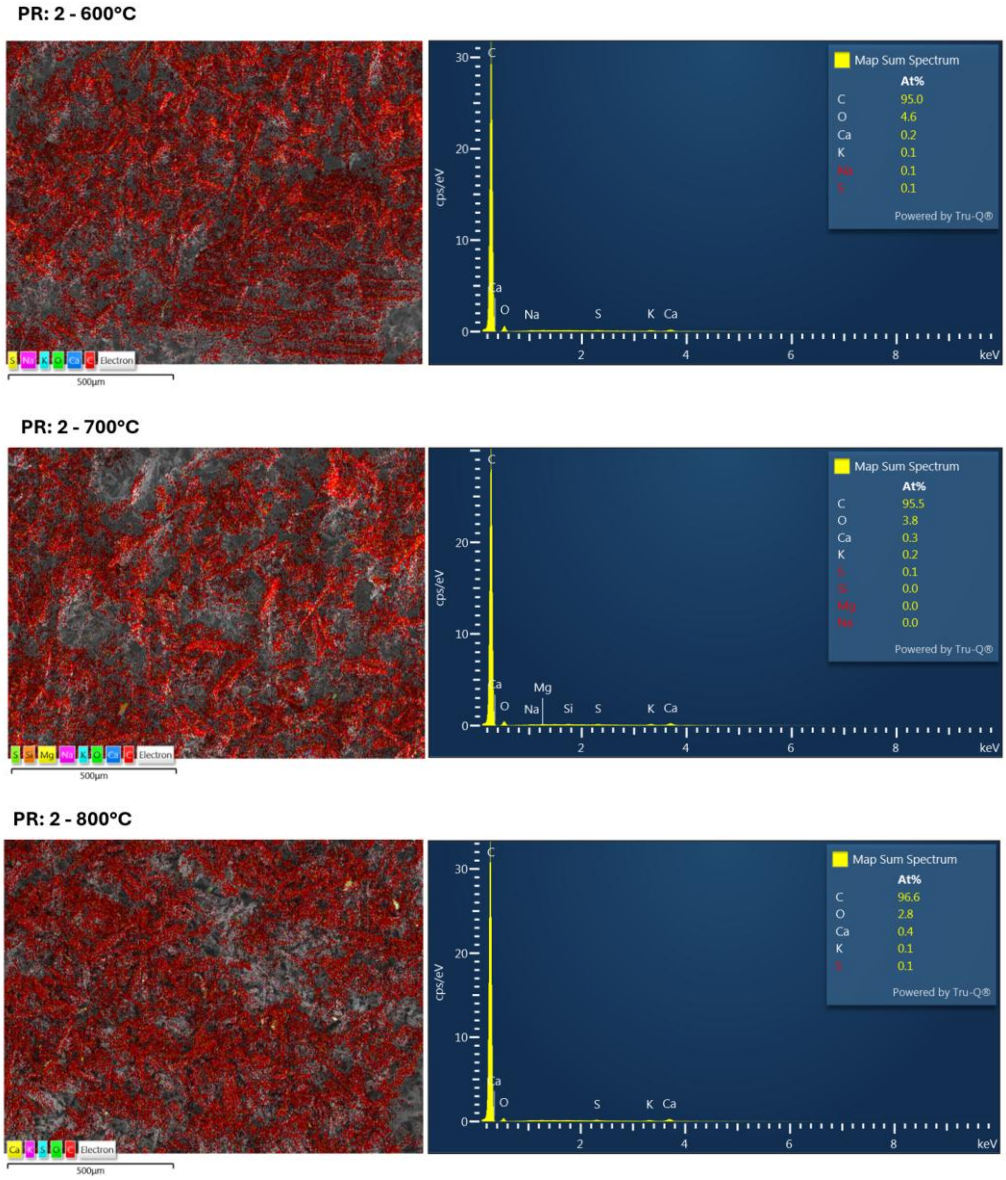

Figure 8: EDX spectral distribution of biochars with concentrated carbon and reduced volatile content: From the top: 600-800 °C

3.5.5 TGA R50

The TGA R50 plots and corrected thermograms (Figure 7) showed improved biochar thermal stability as pyrolysis temperature increased from 500 °C to 800 °C during PR:2. The R50 index rose from 0.54 to 0.65, indicating enhanced stability. Since CRD wood biomass has a R50 of only 0.39, biochar at even a lower temperature can alleviate major stability concerns. As appended in Supplementary figure 14, R50 strongly correlates with O/C ratios, where O/C decreases from 0.08 to 0.02 across biochars with increasing HTT, reducing oxidative sensitivity, promoting the degree of recalcitrance, and minimizing carbon loss to degradative reactions. These findings align with Leng and Huang 2018, who described a black-carbon continuum where O/C decreases from raw biomass charcoal, combustion soot, and finally to graphite (1 to 0: decreasing order). Biochar, being heterogeneous, overlaps with the other carbonaceous materials in composition and stability. R50 also directly relates to ash, FC, TSF, I_D/I_G, and inversely to VC. However, limitations exist in using R50 as a stability index. Nair et al 2020 noted that correcting raw thermograms for ash might overlook catalytic inorganics' role in stability. Additionally, R50 for graphite is not constant and varies with experimental conditions, including graphite type, oxygen flow rate, heating rate, and equipment thermal inertia. Measuring graphite R50 alongside biochar samples is essential for consistency. Gomez et al 2016 proposed refining the R50 scale as T50% weight loss for graphite (886 °C) may not necessarily replicate the exact structural changes happening in biochars, especially at lower or moderate temperatures.

3.5.6 FTIR

Generally, an inverse relation is construed between pyrolysis temperature and the presence of functional groups where increase in temperatures exhibit biochar with limited functional groups. From the FTIR spectrum of PR:2 biochar at 500-800 °C, it is clear that low pyrolysis temperatures conserve oxygenic functionalities that provide biochar surfaces with an overall negative charge. More the deprotonation of biochar surface, higher the pH, greater the negativity, and higher the cation exchange capacity (CEC) (Sarfaraz et al 2020). CEC is evident for soil (*e.g.:* minerals) and adsorption (*e.g.:* heavy metals and cationic dyes) applications mainly. At high temperatures, these surface groups are eliminated which could decrease the conferred CEC. As concluded from the EDX analysis, AAEM and their salts present as part of the ash fraction in high temperature-biochars, may geometrically shield some oxygen functional groups via AAEM-O-C linkages which ameliorate their retention concerns. In this case, an intrinsic CEC may persist till the melting of AAEM at very high temperatures after which CEC is highly negligible.

By fitting the data on assignment of FTIR spectral bands in Johnston, 2017 to Figure 9, from the range of 900-700 cm-^{1}, biochars produced at 500 °C and 600 °C undergo O-H stretch (812-868 cm^{-1} and 807-868 cm^{-1}, respectively) that may result from a mass loss due to the onset of dehydration reactions. For biochar at 700 °C, the O-H stretch lies slightly farther at 935 cm^{-1} that signifies metal-O-H vibrations and bending associated to minerals in biochar (eg: AAEM-O-H). This may highlight the effect of temperature on mineral degradation that detaches O-H and eventually exposes these labile functionalities. Next, C-O stretch for biochars at 500 °C and 600 °C is seen uniquely in the regions of 1164 cm^{-1} and 1153 cm^{-1}. These intense peaks can correlate with the vibrations amidst pyrolyzed carbohydrate fractions in the form of aldehydes, alcohols, ethers, and furfurals. COO^{-} activation as in amides from proteins and esters is showcased only for biochars at 500 °C and 600 °C along 1578 cm-^{1} and 1550 cm^{-1} and can be attributed to decarboxylation pathways that reject CO_2. In both phenomena, transformations of oxychemicals are apparent where oxygen rejection reactions are being favored. Also, these peaks within 1650-1550 cm^{-1}, may be due to the vibration of C=C that could relate to skeletal vibrations in lignin aromatics as reported by Chiaramonti et al 2024. Strong C=O striations in ketones and carboxylic acids are common to all four biochars in 1701 cm^{-1}, 1701 cm^{-1}, 1735 cm^{-1}, and 1696 cm^{-1}, respectively. Albeit, the intensity decreases for biochars at 700 °C and 800 °C as they may have already started experiencing decomposition of the aforesaid groups due to increase in HTT.

Between 3000-2000 cm^{-1}, C-H stretching vibrations with deformations in terminal CH_2 or CH_3 aliphatic hydrocarbons increase for lower temperature biochars. Rising distortions of H-bearing syndicates can hint at the formation of aromatics from these aliphatic by dehydrogenation, condensation (*e.g.:* Diels-Alder), and cyclization which leads to a decrease in H/C as justified from the ultimate analysis results. Between 3100-3000 cm^{-1}, C-H stretching vibrations in nascent aromatic systems appear as medium-to-low intensity bands in lower temperature biochars pointing out that a stable arrangement of carbon resulting from high degrees of disorder in amorphous carbon, is in progress as soon as the material witnesses sustained heat treatment. For biochars at 700 °C and 800 °C, these bands are not present that could mean a significant portion of carbon in these biochars do not exhibit defects (McCall et al 2024). However, this do not mean that such C-H contractions are the only qualifying criteria to identify aromaticity in high temperature-biochars (McCall et al 2024). Even the presence of any substituents in the aromatic rings structure may also lead to vibrations of the C-H planes. Next, within spectroscopic bands in the range of 3670-3200 cm^{-1}, presence of polar -OH groups that are hydrogen-bonded to biochar mostly via moisture sorption, are seen for temperatures of 500 °C and 600 °C making them hydrophilic. Due to large pore sizes, there could also be sufficient diffusion of ambient humidity and its further interaction with biochar carbon. At higher temperatures, the polar -OH groups diminish, and this is in agreement with Sahoo et al 2021. Simultaneously, a diffusion limitation comes into play due to disappearance of meso and macropores and the origination of micropores. Despite micropores being limiting factors for the entry of surrounding moisture, their surface availability (increase in surface area) could also lead to sorption and contribute to clear spectral bands in this region.

An interesting observation from the FTIR spectra is the absence of bands below 600 cm^{-1} which may usually arise due to vibrational bending of inorganics like Cl, P, and Si according to Nair et al 2020. Despite ash content between 5-8% for PR:2 biochars at 700 °C and 800 °C, the absence of spectral bands could be due to devolatilization of some of its endogenous components at high pyrolysis temperatures. Therefore, investigating the exact composition of ash at this stage might be necessary to understand which constituents are amplified and become recalcitrant at high temperatures.

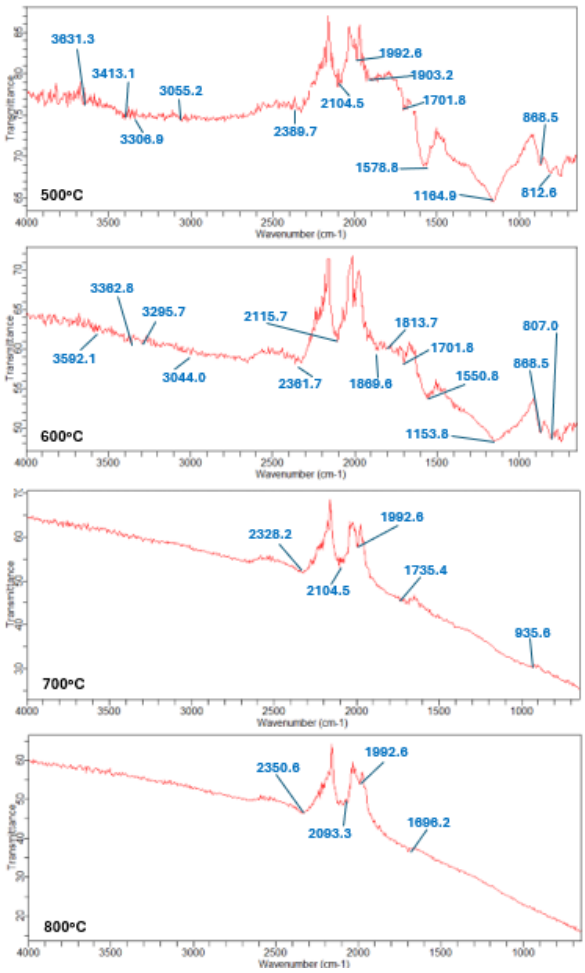

Figure 9: FTIR spectra and their variations with pyrolysis temperature: Top to bottom - 500-800 °C

3.5.7 Raman spectroscopy

The I_D/I_G ratio from Figure 10, captures the structural evolution of biochars during pyrolysis. The D band reflects disorder in amorphous carbon caused by edges, vacancies, or functionalities during its transformation to a turbostratic configuration, while the G band indicates sp^2-bonded crystalline carbon, typical of graphite (Xu et al 2020). The carbon arrangement in turbostratic crystallites, however, does not perfectly resemble stacked carbon as in graphite (Amdani et al 2020). As pyrolysis temperature increased from 500 °C, PR:2 biochars showed a rise in the D band intensity (higher I_D/I_G), indicating increased faultiness in amorphous carbon (Sarkar et al 2024). This deformity keeps growing proportionally with pyrolysis temperature or any post-production heat treatment till a point where all defect-borne amorphous carbon is converted to large, stable, condensed aromatics that develop inherent chemical and biological recalcitrance during the transformation process (Pusceddu et al 2017). At 800 °C, PR:2 biochars reached an I_D/I_G of 0.972, suggesting further pyrolysis at ≥900 °C could yield values >1, signalling structural inconsistencies prior to crystalline carbon formation.

Biochars, however, typically exhibit limited graphitization and may remain mildly non-graphitized even with higher heat treatment (Wood et al 2024). Unlike TGA R50, the I_D/I_G ratio provides insights into the structural makeup and stability of biochar carbon. Results may vary with sample preparation, biochar particle size, and environmental conditions.

A low H/C can also be analogized with high aromaticity and stable biochar carbon as pyrolysis temperature increases (Xiao et al 2016) (represented in Supplementary figure 15). For example, hydrogen elimination reactions inclusive of dehydration, oxidation, and condensation of cyclic hydrocarbons lower H/C suggesting the formation of monoaromatic and polyaromatic hydrocarbon (MAH/PAH) clusters. This theory is ideally validated by the properties of PR:2 biochars where H/C lowered from 0.44 to 0.12, and I_D/I_G graphitization degree increased from 0.787 to 0.972.

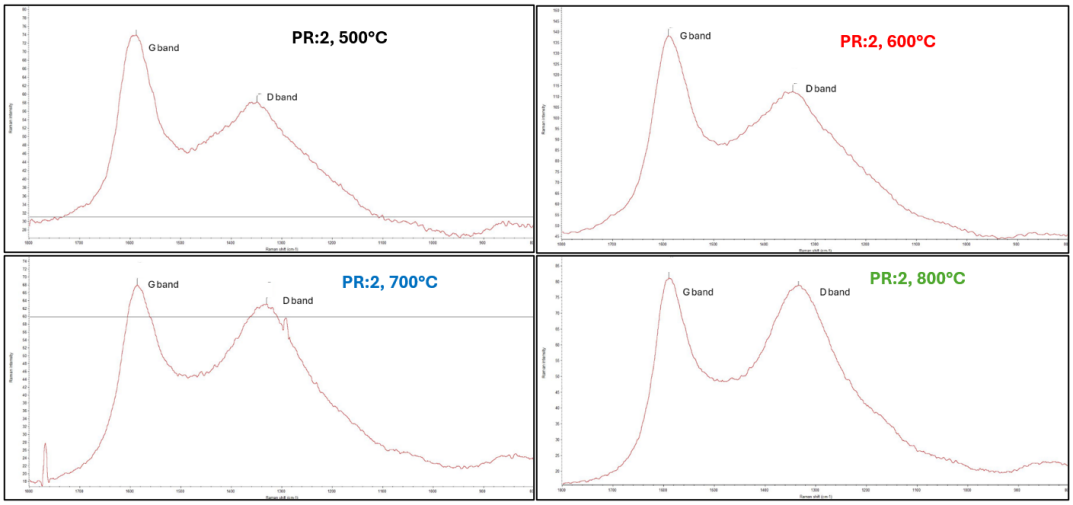

Figure 10: Defects in biochar carbon with increase in pyrolysis temperature realized via the Raman I_D/I_G index. Progress of D band towards G band is from right to left due to inverted x-axis scale. For 500 °C – D band at 1348 cm^{-1} and G band at 1587 cm^{-1}. For 600 °C – D band at 1344 cm^{-1} and G band at 1590 cm^{-1}. For 700 °C – D band at 1330 cm^{-1} and G band at 1586 cm^{-1}. For 800 °C – D band at 1333 cm^{-1} and G band at 1589 cm^{-1}

3.6 Statistical analysis

The statistical analysis was performed only for biochars from PR:1 and PR:2 produced using the scaled-up horizontal tubular furnace with reference to the most influencing process parameter, *i.e*, temperature, since other parameters such as BRT, heating rate, equipment, feedstock type, and mass of feedstock processed are unvaried. For a replicate count of two (N=2), a descriptive statistical analysis for biochar properties at each temperature was carried out. The computed values of standard deviations for parameters like C%, H%, O%, H/C, O/C, yield, VC, FC, ash, and TSF of biochar are ≤ 2 (in most cases ≤ 1), which indicates a lower degree of variability among these dependent variables. However, the standard deviation of surface area is > 2 that may be due to differences in cross-section of biochar and particle size whilst BET analysis. From the ANOVA analysis, it can be concluded that temperature definitely influenced all dependent variables since p-value was ≤ 0.05. With an increase of pyrolysis temperature, a significant elevation of carbon content (p=0.004) especially at 800 °C, decrease in hydrogen (p=0.006) and oxygen content (p=0.036) conferring greater stability and aromaticity, decrease in Van-Krevelen parameters of H/C (p=0.005) and O/C (p=0.013) interspersing resistance towards oxidative reactivity, an increase of surface area (p=0.001) specifically at 800°C due to micropore development, and a reduction in yield (p=0.001) favoring efficient depolymerization of the CRD wood biomass, were observed. For the proximate analysis parameters, an increase in temperature aided a drop in VC (p=0.0001), increase in FC (p=0.001), increase in ash (p=0.030), and promotion of TSF (p=0.0001). These replicates also showed very minimal perturbation indicating relatively consistent experimental and characterization conditions.

Any errors in this analysis may have stemmed from minor inconsistencies among CRD wood biomass constituents taken for pyrolysis mainly at low temperatures, like particle size, composition, and residual inherent contaminants. Sometimes variabilities could arise due to uneven heating patterns encountered in the furnace assembly. Measurement inaccuracies during characterization may be yet another error source. Mitigation strategies to address potential outliers can include increasing the number of replicates and advanced standardization of experimental conditions to enhance data reliability and interpretation. These findings emphasize the importance of optimizing different pyrolysis conditions aside from temperature for desired biochar characteristics.

3.7 Effect of feedstock composition and pyrolysis parameters on biochar properties

To lock in as much stable carbon as possible, the erosion resistance of biochar needs to be remediated such that it does not get oxidised or degraded quickly under harsh environments (natural – *e.g*.: soil, and artificial: power plants). The properties of biochar governing the aforesaid characteristics in general, are greatly influenced by both the type of feedstock, and the conditions appropriated during pyrolysis.

3.7.1 Feedstock composition

3.7.1.1 Biochemical framework

CRD wood residues, a mix of hardwood and softwood, consist of cellulose, hemicellulose, and lignin, with bulk density varying from 200 to 800 kg/m³, reflecting compositional variability. Their lignin content varied from 24-31% which proves this heterogeneity factor. Softwoods contain 22–40% hemicellulose, 33–42% cellulose, and 27–32% lignin, while hardwoods have 17–38% hemicellulose, 38–51% cellulose, and 21–31% lignin (Tarasov et al 2018). Hemicellulose, an amorphous polymer of short-chain sugars, decomposes at 190–350 °C, producing non-condensable gases (Wang et al 2022). Its degradation produces biochar with high volatile content and poor properties (Chen et al 2022). Cellulose, with β-1,4-glycosidic-linked glucose, degrades at 260–400 °C. Amorphous cellulose decomposes first, yielding anhydrosugars like levoglucosan (LGA) and levoglucone (LGO) along with light oxygenates from pyranose ring collapse (Leng et al 2018). Cellulose contributes to biochar porosity, CEC, and pH, suitable for soil enrichment (Santos et al 2023). Lignin, a complex aromatic polymer with hydroxyphenyl, syringyl, and guaiacyl units, begins depolymerization at 160–330 °C and undergoes significant mass loss at 400–600 °C due to stable C=C, C-O, and aromatic bonds (Li et al 2020). Lignin's aromatic content enhances char yield and stability, with optimal pyrolysis temperatures between 300–600 °C. Softwoods, with higher lignin content, favor recalcitrant char formation.

3.7.1.2 Extractives

Additionally, biomass is also embodied of extractive materials such as pigments, sugars, fats, proteins, resins, gums, oils, and waxes that can either effect the reactivity of feedstock during pyrolysis reactions or can block biochar pores thereby reducing its surface area and reactivity (Shadangi et al 2023). This is implicit for CRD residues that is bearing painted, varnished or resin-rich wood.

3.7.1.3 Inorganics and minerals

Biomass for pyrolysis contains inorganic minerals, including AAEM (*e.g.*, Ca, K, Na, Mg, Ba) and their salts (chlorides, carbonates, sulfates, nitrates), which influence biochar's ash content, porosity, and reactivity (Mourant et al 2011). AAEMs, acting as cross-linkers in biomass polymers, sever, and reform organometallic bonds (*e.g.*, Ca-O-C) during pyrolysis, altering reaction pathways (Mourant et al 2011). While AAEMs can enhance secondary char production (Anca-Couce et al 2017), they also concentrate ash at high temperatures, reducing carbon content (Hu et al 2015). Additionally, AAEMs promote reactions such as the water-gas-shift (WGS) and Boudouard reactions, increasing CO_2, H_2, and CO in the gas fraction (Hu et al 2015). Pyrolysis temperature significantly affects biochar pH and surface functionality. At low temperatures, volatiles with protonic functional groups are retained, resulting in acidic biochar (pH < 7). Higher temperatures eliminate H-containing volatiles and concentrate inorganic salts (*e.g.*, $CaCO_3$, KOH, NaCl), leading to negatively charged surfaces and alkaline biochar (pH > 7). This trend was observed in PR:1 and PR:2 biochars, where pH increased from 7.27 to 11.09 as pyrolysis temperature rose from 500 °C to 800 °C.

3.7.2 Pyrolysis parameters: Interdependence between biomass particle size, temperature, heating rate, and BRT to assess potential applications

The CRD wood sized between a few mm and 2.5 cm, showed minimal heat transfer limitations at high pyrolysis temperatures. However, biochars produced at 300 °C and 400 °C in both laboratory-scale and scaled-up horizontal tube furnaces could have faced intra-particle thermal gradient issues particularly at 300 °C, leading to poor conversion. To address this, subsequent trials were conducted starting at 500 °C, ensuring complete carbonization. BET characterization revealed that smaller CRD wood particle sizes increased biochar surface area due to reduced macro- or mesoporosity and enhanced micropore formation (Maziarka et al 2024). Biochars produced at 700 °C and 800 °C achieved surface areas between 200–300 m²/g without additional activation.

At high pyrolysis temperatures, aromatic compounds fuse, increasing stability as labile functionalities are rejected, and carbon becomes concentrated. Fused aromatic rings stack into carbon sheets, transitioning from amorphous to composite, turbostratic, and ultimately annealed structures with maximum order (Zou et al 2024; Makowska and Dziosa, 2024). This progression is reflected in the I_D/I_G ratio from Raman spectra (PR:2 biochar), exceeding 0.9 at 800 °C, indicating deformations in the carbon lattice en route to a graphitic structure. High-temperature biochars (700–800 °C) exhibit enhanced mechanical integrity, carbon content, microporosity, and surface area, making them suitable for metallurgy, pollutant adsorption, capacitive energy storage, soil salinization mitigation, and long-term carbon sequestration (Xu et al 2024). However, at these temperatures, CRD wood particle yields are lower due to rapid thermal degradation and charring. Achieving a balance between solids yield and carbon composition is critical for effective conversion. For soil amendment applications aiming to reduce nutrient run-off and improve water retention, biochars with greater porosity and surface functionality are preferred. These

properties are best achieved at lower pyrolysis temperatures, promoting hydrophilicity and uniform surface features (Tang et al 2023).

A low heating rate (~50°C/min or lower) enables gradual phase transformations, balancing biochar yield and gas evolution (Mukherjee et al 2020). Combined with high BRT, it enhances carbon conservation, FC, low VM, and calorific value, making biochar ideal for metallurgical reductants and power plants (Makavana et al 2020). From Table 7, biochar produced at 500 °C had the highest HHV, while higher temperatures reduced HHV by 1–2 MJ/kg due to increased ash and reduced hydrogen content (Rahmat et al 2023). The resulting hydrophobic and stable biochar is suitable for polymer composites, enhancing thermal stability, tensile strength, and impact resistance (Hoang et al 2024). Hydrophobic biochar has also been applied for oil spill sorption (Sun et al 2022). Heating rate also influences porosity. Low heating rates, prolonged BRT, and high temperatures for small CRD wood particles result in micropores with high adsorptive properties. For PR:2 biochar at 600 °C, 40 °C/min, and 120 min BRT, adsorption capacity for methyl orange (MO) ranged from 0.8 mg/g to 15 mg/g, achieving >90% dye removal for wastewater concentrations of 8–164 ppm (Tomczyk et al 2020). Conversely, higher heating rates with low BRT cause rapid devolatilization, creating macropores suited for agricultural applications but with reduced surface area (Hosseinzaei et al 2022).

4. Conclusion

The nature of biomass feedstock and pyrolysis conditions penultimately decide biochar's physiochemical properties and potential applications. Slow pyrolysis characterized by low heating rate, high residence time, and high pyrolysis temperature produced highly stable biochar that can be evaluated by different categories of stability indicators. Proximate analysis can be used to derive a conclusion on the chemical make-up of biochar whereas ultimate analysis with the support of Van-Krevelen indices, can predict both the chemical composition and stability of biochar at appreciable levels and moreover, cost-effectively within a short time frame. Structural analysis tools like Raman I_D/I_G, despite being a rapid technique, is expensive. FTIR is very beneficial to identify functional groups of interest on biochar surfaces that gives an overall idea of biochar carbon forms. TGA coupled with DTG and R50 recalcitrance index, are sound methods to evaluate biochar thermal stability but encompass nuances related to the apt heating rates employed during non-isothermal analysis. SEM-EDX can be used as an auxiliary method to proximate and ultimate analysis for assessing ash and carbon concentration in biochar which communicate a proverbial inertness factor, *i.e.,* resistance to biotic and abiotic degradation. Standardizing these metrics and understanding that no single indicator can be exploited to assess biochar permeance are key as part of further investigations especially in the area of CDR technologies. As for future work on CRD wood waste valorization, scaled-up pilot pyrolysis trials to produce biochar followed by its characterization, kinetic analysis of pyrolytic decomposition via non-isothermal TGA/DTG under different heating rates, and the propensity for biochar to undergo self-ignition during post-production stages, will be studied.

Author Contributions: Conceptualization, methodology, validation, formal analysis, investigation, data curation, writing—original draft preparation, editing, visualization - **Aravind Ganesan**. Supervision, review, mentorship - **Olivier Rezazgui**. Project administration – **Cyrine Boussabbeh.** Supervision, review, mentorship – **Simon Langlois**. Supervision, review, mentorship – **Simon Barnabé**. Supervision, review, mentorship – **Patrice Mangin**. All authors have read and agreed to the published version of the manuscript.

Funding: This research was funded by MITACS, through Escouade Energie, Citeq, and supported by Innofibre, and I^2E^3 – UQTR, Québec, Canada. The work was conducted at Innofibre – Centre d'Innovation des Produits Cellulosiques, Trois-Rivières and at the Institute for Innovation in Ecomaterials, Ecoproducts, and Ecoenergies (I^2E^3), University of Québec Trois-Rivières (UQTR), Québec, Canada.

Conflicts of Interest: The authors declare no conflict of interest. The funders had no role in the design of the study; in the collection, analyses, or interpretation of data; in the writing of the manuscript; or in the decision to publish the results.

5. References

Adhikari, S., Moon, E., Paz-Ferreiro, J., & Timms, W. (2024). Comparative analysis of biochar carbon stability methods and implications for carbon credits. Science of the Total Environment, 914, 169607.

Amdani, R. Z., Ossler, F., & Brackmann, C. (2020, June). Raman spectroscopy for characterizing porous carbon. In Laser Applications to Chemical, Security and Environmental Analysis (pp. LTh4F-3). Optica Publishing Group.

Anand, A., Gautam, S., & Ram, L. C. (2023). Feedstock and pyrolysis conditions affect suitability of biochar for various sustainable energy and environmental applications. Journal of Analytical and Applied Pyrolysis, 170, 105881.

Anca-Couce, A., Dieguez-Alonso, A., Zobel, N., Berger, A., Kienzl, N., & Behrendt, F. (2017). Influence of heterogeneous secondary reactions during slow pyrolysis on char oxidation reactivity of woody biomass. Energy & fuels, 31(3), 2335-2344.

Azzi, E. S., Li, H., Cederlund, H., Karltun, E., & Sundberg, C. (2024). Modelling biochar long-term carbon storage in soil with harmonized analysis of decomposition data. Geoderma, 441, 116761.

Babinszki, B., Czirok, I. S., Johnson, R., Sebestyén, Z., Jakab, E., Wang, L., ... & Czégény, Z. (2024). Volatile matter characterization of birch biochar produced under pressurized conditions. Journal of Thermal Analysis and Calorimetry, 1-12.

Babu, K. K. B. S., Nataraj, M., Tayappa, M., Vyas, Y., Mishra, R. K., & Acharya, B. (2024). Production of biochar from waste biomass using slow pyrolysis: Studies of the effect of pyrolysis temperature and holding time on biochar yield and properties. Materials Science for Energy Technologies, 7, 318-334.

Barszcz, W., Łożyńska, M., & Molenda, J. (2024). Impact of pyrolysis process conditions on the structure of biochar obtained from apple waste. Scientific Reports, 14(1), 10501.

Bier, H., Lerchenmüller, H. (2024). European Biochar Industry (EBI). Report on permeance of biochar: Perspectives from two recent publications and EBI conclusions.

Bindar, Y., Ramli, Y., Steven, S., & Restiawaty, E. (2024). Optimization of purity and yield of amorphous bio-silica nanoparticles synthesized from bamboo leaves. The Canadian Journal of Chemical Engineering, 102(4), 1419-1430.

Bindar, Y., Steven, S., Kresno, S. W., Hernowo, P., Restiawaty, E., Purwadi, R., & Prakoso, T. (2024). Large-scale pyrolysis of oil palm frond using two-box chamber pyrolyzer for cleaner biochar production. Biomass Conversion and Biorefinery, 14(5), 6421-6434.

Budai, A., Zimmerman, A. R., Cowie, A. L., Webber, J. B. W., Singh, B. P., Glaser, B., ... & Joseph, S. (2013). Biochar Carbon Stability Test Method: An assessment of methods to determine biochar carbon stability. International biochar initiative, 1, 1-20.

Channiwala, S. A., & Parikh, P. P. (2002). A unified correlation for estimating HHV of solid, liquid and gaseous fuels. Fuel, 81(8), 1051-1063.

Chen, D., Cen, K., Zhuang, X., Gan, Z., Zhou, J., Zhang, Y., & Zhang, H. (2022). Insight into biomass pyrolysis mechanism based on cellulose, hemicellulose, and lignin: Evolution of volatiles and kinetics, elucidation of reaction pathways, and characterization of gas, biochar and bio-oil. Combustion and Flame, 242, 112142.

Chen, J., Ding, L., Wang, P., Zhang, W., Li, J., Mohamed, B. A., ... & Zhou, W. (2022). The estimation of the higher heating value of biochar by data-driven modelling. J. Renew. Mater, 10, 1555-1574.

Chen, J., Wang, P., Ding, L., Yu, T., Leng, S., Chen, J., ... & Zhou, W. (2021). The comparison study of multiple biochar stability assessment methods. Journal of Analytical and Applied Pyrolysis, 156, 105070.

Chiaramonti, D., Lehmann, J., Berruti, F., Giudicianni, P., Sanei, H., & Masek, O. (2024). Biochar is a long-lived form of carbon removal, making evidence-based CDR projects possible. Biochar, 6(1), 81.

Chiaramonti, D., Lotti, G., Vaccari, F. P., & Sanei, H. (2024). Assessment of long-lived Carbon permanence in agricultural soil: Unearthing 15 years-old biochar from long-term field experiment in vineyard. Biomass and Bioenergy, 191, 107484.McLaughlin, H. (2018). Biochar Standards and Characterization Schemes.

Cross, A., & Sohi, S. P. (2013). A method for screening the relative long-term stability of biochar. Gcb Bioenergy, 5(2), 215-220.

Dada, T. K., Sheehan, M., Murugavelh, S., & Antunes, E. (2021). A review on catalytic pyrolysis for high-quality bio-oil production from biomass. Biomass Conversion and Biorefinery, 1-20.

Dieguez-Alonso, A., Anca-Couce, A., Zobel, N., & Behrendt, F. (2015). Understanding the primary and secondary slow pyrolysis mechanisms of holocellulose, lignin and wood with laser-induced fluorescence. Fuel, 153, 102-109.

Fawaz, M., Avery, A., Onasch, T. B., Williams, L. R., & Bond, T. C. (2021). Pyrolysis principles explain time-resolved organic aerosol release from biomass burning. Atmospheric Chemistry and Physics, 21(20), 15605-15618.

Gómez, N., Rosas, J. G., Singh, S., Ross, A. B., Sánchez, M. E., & Cara, J. (2016). Development of a gained stability index for describing biochar stability: Relation of high recalcitrance index (R50) with accelerated ageing tests. Journal of Analytical and Applied Pyrolysis, 120, 37-44.

Harvey, O. R., Kuo, L. J., Zimmerman, A. R., Louchouarn, P., Amonette, J. E., & Herbert, B. E. (2012). An index-based approach to assessing recalcitrance and soil carbon sequestration potential of engineered black carbons (biochars). Environmental science & technology, 46(3), 1415-1421.

Hasan, M. M., Rasul, M. G., & Khan, M. M. K. (2022, November). The effects of slow and fast pyrolysis on the yields and properties of produced bio-oils from macadamia nutshell. In AIP Conference Proceedings (Vol. 2681, No. 1). AIP Publishing.

Heo, H. S., Park, H. J., Park, Y. K., Ryu, C., Suh, D. J., Suh, Y. W., ... & Kim, S. S. (2010). Bio-oil production from fast pyrolysis of waste furniture sawdust in a fluidized bed. Bioresource technology, 101(1), S91-S96.

Hoang, P., Zhang, Z., Ren, J., Peng, Y., & Cao, J. (2024). Versatile biochar for wood-plastic composites: Improving mechanical properties, dimensional and thermal stability. Polymer Composites.

Hosseinzaei, B., Hadianfard, M. J., Ruiz-Rosas, R., Rosas, J. M., Rodríguez-Mirasol, J., & Cordero, T. (2022). Effect of heating rate and H3PO4 as catalyst on the pyrolysis of agricultural residues. Journal of Analytical and Applied Pyrolysis, 168, 105724.

Hu, S., Jiang, L., Wang, Y., Su, S., Sun, L., Xu, B., ... & Xiang, J. (2015). Effects of inherent alkali and alkaline earth metallic species on biomass pyrolysis at different temperatures. Bioresource technology, 192, 23-30.

Huang, Y., Liu, S., Akhtar, M. A., Li, B., Zhou, J., Zhang, S., & Zhang, H. (2020). Volatile–char interactions during biomass pyrolysis: Understanding the potential origin of char activity. Bioresource Technology, 316, 123938.

J.W. Kim, H.W. Lee, I.G. Lee, J.K. Jeon, C. Ryu, S.H. Park, et al., Influence of reaction conditions on bio-oil production from pyrolysis of construction waste wood, Renew Energy 65 (2014) 41–48, http://dx.doi.org/10.1016/j.renene.2013.07.009.

Jiang, W., Nadeau, G., Zaghib, K., & Kinoshita, K. (2000). Thermal analysis of the oxidation of natural graphite—effect of particle size. Thermochimica Acta, 351(1-2), 85-93.

Johnston, C. T. (2017). 18 Biochar analysis by Fourier-transform infra-red spectroscopy. Biochar: a guide to analytical methods, 199.

Jung, S. H., Kim, S. J., & Kim, J. S. (2012). Characteristics of products from fast pyrolysis of fractions of waste square timber and ordinary plywood using a fluidized bed reactor. Bioresource Technology, 114, 670-676.

Kasmiarno, L. D., Panannangan, J. K., Steven, S., Rizkiana, J., Hernowo, P., Achmad, F., ... & Bindar, Y. (2024). Exploration of bio-hydrocarbon gases production via pyrolysis of fresh natural rubber: experimental and volatile state kinetic modeling studies. Journal of Analytical and Applied Pyrolysis, 177, 106275.

Kern, S., Halwachs, M., Kampichler, G., Pfeifer, C., Pröll, T., & Hofbauer, H. (2012). Rotary kiln pyrolysis of straw and fermentation residues in a 3 MW pilot plant–Influence of pyrolysis temperature on pyrolysis product performance. Journal of Analytical and Applied Pyrolysis, 97, 1-10.

Khater, E. S., Bahnasawy, A., Hamouda, R., Sabahy, A., Abbas, W., & Morsy, O. M. (2024). Biochar production under different pyrolysis temperatures with different types of agricultural wastes. Scientific Reports, 14(1), 2625.

Khatibi, M., Nahil, M. A., & Williams, P. T. (2023). Improving the Quality of Bio-oil Using the Interaction of Plastics and Biomass through Copyrolysis Coupled with Nonthermal Plasma Processing. Energy & Fuels, 38(2), 1240-1257.

Klasson, K. T. (2017). Biochar characterization and a method for estimating biochar quality from proximate analysis results. Biomass and Bioenergy, 96, 50-58.

Leng, E., Zhang, Y., Peng, Y., Gong, X., Mao, M., Li, X., & Yu, Y. (2018). In situ structural changes of crystalline and amorphous cellulose during slow pyrolysis at low temperatures. Fuel, 216, 313-321.

Leng, L., & Huang, H. (2018). An overview of the effect of pyrolysis process parameters on biochar stability. Bioresource technology, 270, 627-642.

Li, B., Huang, H., Xie, X., Wei, J., Zhang, S., Hu, X., ... & Liu, D. (2023). Volatile-char interactions during biomass pyrolysis: Effects of AAEMs removal and KOH addition in char. Renewable Energy, 219, 119459.

Li, J., Bai, X., Fang, Y., Chen, Y., Wang, X., Chen, H., & Yang, H. (2020). Comprehensive mechanism of initial stage for lignin pyrolysis. Combustion and Flame, 215, 1-9.

Li, S., & Chen, G. (2018). Thermogravimetric, thermochemical, and infrared spectral characterization of feedstocks and biochar derived at different pyrolysis temperatures. Waste Management, 78, 198-207.

Makavana, J. M., Sarsavadia, P. N., & Chauhan, P. M. (2020). Effect of pyrolysis temperature and residence time on biochar obtained from pyrolysis of shredded cotton stalk. International Research Journal of Pure and Applied Chemistry, 21(13), 10-28.

Makowska, M., & Dziosa, K. (2024). Influence of different pyrolysis temperatures on chemical composition and graphite-like structure of biochar produced from biomass of green microalgae Chlorella sp. Environmental Technology & Innovation, 35, 103667.

Martí-Rosselló, T., Li, J., Lue, L., Kärlstrom, O., & Brink, A. (2019, June). Heat transfer behaviour of a wheat straw pellet undergoing pyrolysis. In ICAE2019: The 11th International Conference on Applied Energy.

Mazerolle, D., Rezaei, H., Bronson, B., Nguyen, L., & Preto, F. (2019). Sieving and acid washing as a pretreatment to fast pyrolysis of a high ash hog fuel. Energy & Fuels, 33(6), 5352-5359.

Maziarka, P., Kienzl, N., Dieguez-Alonso, A., Fierro, V., Celzard, A., Arauzo, P. J., ... & Ronsse, F. (2024). Part 1─ Impact of pyrolysis temperature and wood particle length on vapor cracking and char porous texture in relation to the tailoring of char properties. Energy & Fuels.

McCall, M. A., Watson, J. S., & Sephton, M. A. (2024). Predicting Stability of Barley Straw-Derived Biochars Using Fourier Transform Infrared Spectroscopy. ACS Sustainable Resource Management, 1(9), 1975-1983.

Ministry of the Environment, the Fight against Climate Change, Wildlife and Parks, Quebec. 2023. Analysis Method: Lixiviation Protocol for inorganic species. www.environnement.gouv.qc.ca.

Mishra, R. K., & Mohanty, K. (2018). Pyrolysis kinetics and thermal behavior of waste sawdust biomass using thermogravimetric analysis. Bioresource technology, 251, 63-74.

Mourant, D., Wang, Z., He, M., Wang, X. S., Garcia-Perez, M., Ling, K., & Li, C. Z. (2011). Mallee wood fast pyrolysis: Effects of alkali and alkaline earth metallic species on the yield and composition of bio-oil. Fuel, 90(9), 2915-2922.

Muema, F. M., Richardson, Y., Keita, A., Sawadogo, M. (2024). An interdisciplinary overview on biochar production engineering and its agronomic applications. Biomass and Bioenergy. 190 (2024) 107416.

Mukherjee, A., Patra, B. R., Podder, J., & Dalai, A. K. (2022). Synthesis of biochar from lignocellulosic biomass for diverse industrial applications and energy harvesting: effects of pyrolysis conditions on the physicochemical properties of biochar. Frontiers in Materials, 9, 870184.

Nair, R. R., Mondal, M. M., & Weichgrebe, D. (2020). Biochar from co-pyrolysis of urban organic wastes—investigation of carbon sink potential using ATR-FTIR and TGA. Biomass Conversion and Biorefinery, 1-15.

Oktavia, F. D., Steven, S., Putri, A. H. I., Hernowo, P., Restiawaty, E., & Bindar, Y. (2024). Vacuum distillation of raw bio-crude oil (RBCO) from empty fruit bunches (EFB) pyrolysis to produce light distillate containing acetic acid and phenol for sustainable chemical purposes. Brazilian Journal of Chemical Engineering, 1-18.

Pahnila, M., Koskela, A., Sulasalmi, P., & Fabritius, T. (2024). Biocarbon production using three-stage pyrolysis and its preliminary suitability to the iron and steel industry. Energies, 17(13), 3131.

Panwar, N. L. (2024). Pyrolysis technologies for biochar production in waste management: a review. Clean Energy, 8(4), 61-78.

Paradela, F., Pinto, F., Gulyurtlu, I., Cabrita, I., & Lapa, N. (2009). Study of the co-pyrolysis of biomass and plastic wastes. Clean Technologies and Environmental Policy, 11, 115-122.

Premalatha, R. P., Poorna Bindu, J., Nivetha, E., Malarvizhi, P., Manorama, K., Parameswari, E., & Davamani, V. (2023). A review on biochar's effect on soil properties and crop growth. Frontiers in Energy Research, 11, 1092637.

Pusceddu, E., Montanaro, A., Fioravanti, G., Santilli, S. F., Foscolo, P. U., Criscuoli, I., ... & Miglietta, F. (2017). Comparison between ancient and fresh biochar samples, a study on the recalcitrance of carbonaceous structures during soil incubation. Int. J. New Technol. Res, 3, 39-46.

Rahmat, A., Nissa, R. C., Nuraini, L., Nurtanto, M., & Ramadhani, W. S. (2023, June). Analysis of rice husk biochar characteristics under different pyrolysis temperature. In IOP Conference Series: Earth and Environmental Science (Vol. 1201, No. 1, p. 012095). IOP Publishing.

Recyc-Québec, 2018. Construction, Renovation, and Demolition Residues (CRD). https://www.recyc-quebec.gouv.qc.ca/sites/default/files/documents/Fiche-info-crd.pdf. Accessed on 1 November 2024.

Recyc-Québec, 2021. Construction and Demolition Waste. https://www.recyc-quebec.gouv.qc.ca/sites/default/files/documents/bilan-gmr-2021-crd-english.pdf. Accessed on 1 November 2024.

Sahoo, S. S., Vijay, V. K., Chandra, R., & Kumar, H. (2021). Production and characterization of biochar produced from slow pyrolysis of pigeon pea stalk and bamboo. Cleaner engineering and technology, 3, 100101.

Sanei, H., Rudra, A., Przyswitt, Z. M. M., Kousted, S., Sindlev, M. B., Zheng, X., ... & Petersen, H. I. (2024). Assessing biochar's permanence: An inertinite benchmark. International Journal of Coal Geology, 281, 104409.

Santos, J. L., Centeno, M. A., & Odriozola, J. A. (2023). Biochar production from cellulose under reductant atmosphere: influence of the total pyrolysis time. RSC advances, 13(30), 21071-21079.

Sarfaraz, Q., Silva, L. S. D., Drescher, G. L., Zafar, M., Severo, F. F., Kokkonen, A., ... & Solaiman, Z. M. (2020). Characterization and carbon mineralization of biochars produced from different animal manures and plant residues. Scientific Reports, 10(1), 955.

Sarkar, D., Panicker, T. F., Mishra, R. K., & Kini, M. S. (2024). A comprehensive review of production and characterization of biochar for removal of organic pollutants from water and wastewater. Water-Energy Nexus.

Schorr, D., Boivin, G., 2023. Overview of Canadian CRD wood waste recycling and valorization ecosystem. FP Innovations.

Shadangi, K. P., Sarangi, P. K., & Behera, A. K. (2023). Characterization techniques of biomass: physico-chemical, elemental, and biological. In Bioenergy Engineering (pp. 51-66). Woodhead Publishing.

Sharma, P. (2024). Biochar application for sustainable soil erosion control: a review of current research and future perspectives. Frontiers in Environmental Science, 12, 1373287.

Spokas, K. A. (2010). Review of the stability of biochar in soils: predictability of O: C molar ratios.

Steven, S., Nugraha, P. Z., Hernowo, P., Oktavia, F. D., Putri, A. H. I., & Bindar, Y. (2024). Investigation of high water content in bio-crude oil (BCO) produced from empty oil palm fruit bunches pyrolysis. Biomass Conversion and Biorefinery, 1-17.

Sun, J., He, F., Pan, Y., & Zhang, Z. (2017). Effects of pyrolysis temperature and residence time on physicochemical properties of different biochar types. Acta Agriculturae Scandinavica, Section B—Soil & Plant Science, 67(1), 12-22.

Sun, X., Fu, H., Bao, M., Liu, W., Luo, C., Li, Y., ... & Lu, J. (2022). Development of a new hydrophobic magnetic biochar for removing oil spills on the water surface. Biochar, 4(1), 60.

Tang, E., Liao, W., & Thomas, S. C. (2023). Optimizing biochar particle size for plant growth and mitigation of soil salinization. Agronomy, 13(5), 1394.

Tarasov, D., Leitch, M., & Fatehi, P. (2018). Lignin–carbohydrate complexes: properties, applications, analyses, and methods of extraction: a review. Biotechnology for biofuels, 11, 1-28.

Tian, Y., Wang, F., Djandja, J. O., Zhang, S. L., Xu, Y. P., & Duan, P. G. (2020). Hydrothermal liquefaction of crop straws: Effect of feedstock composition. Fuel, 265, 116946.

Tomczyk, A., Sokołowska, Z., & Boguta, P. (2020). Biochar physicochemical properties: pyrolysis temperature and feedstock kind effects. Reviews in Environmental Science and Bio/Technology, 19(1), 191-215.

Turkan Aktas, I. Savas Dalmis, Levent Taseri, and Tolga Batur, “A Comprehensive Characterization of Biochar Derived from Grape Pomace via Fast Pyrolysis”, Int J Sci Res Sci Eng Technol, vol. 11, no. 4, pp. 218–227, Aug. 2024, doi: 10.32628/IJSRSET24114125.

Usino, D. O., Sar, T., Ylitervo, P., & Richards, T. (2023). Effect of acid pretreatment on the primary products of biomass fast pyrolysis. Energies, 16(5), 2377.

Wang, W., Bai, J., Lu, Q., Zhang, G., Wang, D., Jia, J., ... & Yu, L. (2021). Pyrolysis temperature and feedstock alter the functional groups and carbon sequestration potential of Phragmites australis-and Spartina alterniflora-derived biochars. GCB Bioenergy, 13(3), 493-506.

Wang, W., Lemaire, R., Bensakhria, A., & Luart, D. (2022). Review on the catalytic effects of alkali and alkaline earth metals (AAEMs) including sodium, potassium, calcium and magnesium on the pyrolysis of lignocellulosic biomass and on the co-pyrolysis of coal with biomass. Journal of Analytical and Applied Pyrolysis, 163, 105479.

Wood, R., Mašek, O., & Erastova, V. (2024). Developing a molecular-level understanding of biochar materials using public characterization data. Cell Reports Physical Science, 5(7).

Xiao, X., Chen, Z., & Chen, B. (2016). H/C atomic ratio as a smart linkage between pyrolytic temperatures, aromatic clusters and sorption properties of biochars derived from diverse precursory materials. Scientific reports, 6(1), 22644.

Xu, C., Wei, K., Du, Z., & Ma, W. (2024). Effect of particle size on the properties of biomass gasification residue pellets used as a metallurgical-grade silicon reducing agent. Powder Technology, 435, 119406.

Xu, J., Liu, J., Ling, P., Zhang, X., Xu, K., He, L., ... & Xiang, J. (2020). Raman spectroscopy of biochar from the pyrolysis of three typical Chinese biomasses: A novel method for rapidly evaluating the biochar property. Energy, 202, 117644.

Xu, M., & Sheng, C. (2012). Influences of the heat-treatment temperature and inorganic matter on combustion characteristics of cornstalk biochars. Energy & fuels, 26(1), 209-218.

Yaashikaa, P. R., Kumar, P. S., Varjani, S., & Saravanan, A. J. B. R. (2020). A critical review on the biochar production techniques, characterization, stability and applications for circular bioeconomy. Biotechnology reports, 28, e00570.

Yang, K., Huang, J., Dong, B., Liu, P., Chen, L., Wang, Z., & Jia, L. (2021). Secondary reactions of primary tar from biomass pyrolysis: characterization of heavy products by FT-ICR MS. Energy & Fuels, 35(16), 13191-13199.

Yang, Y., Sun, K., Han, L., Jin, J., Sun, H., Yang, Y., & Xing, B. (2018). Effect of minerals on the stability of biochar. Chemosphere, 204, 310-317.

Ye, L., Peng, Z., Wang, L., Anzulevich, A., Bychkov, I., Kalganov, D., ... & Jiang, T. (2019). Use of biocarbon for sustainable ferrous metallurgy. Jom, 71, 3931-3940.

Zadeh, Z. E., Abdulkhani, A., Aboelazayem, O., & Saha, B. (2020). Recent insights into lignocellulosic biomass pyrolysis: a critical review on pretreatment, characterization, and products upgrading. Processes, 8(7), 799.

Zhou, D., Zhang, L., Zhang, S., Fu, H., & Chen, J. (2010). Hydrothermal liquefaction of macroalgae Enteromorpha prolifera to bio-oil. Energy & Fuels, 24(7), 4054-4061.

Zhu, Z., Duan, W., Chang, Z., Du, W., Chen, F., Li, F., & Oleszczuk, P. (2023). Stability of Functionally Modified Biochar: The Role of Surface Charges and Surface Homogeneity. Sustainability, 15(10), 7745.

Zou, X., Debiagi, P., Amjed, M. A., Zhai, M., & Faravelli, T. (2024). Impact of high-temperature biomass pyrolysis on biochar formation and composition. Journal of Analytical and Applied Pyrolysis, 179, 106463.

6. Supplementary information

The caption for every illustration is added above.

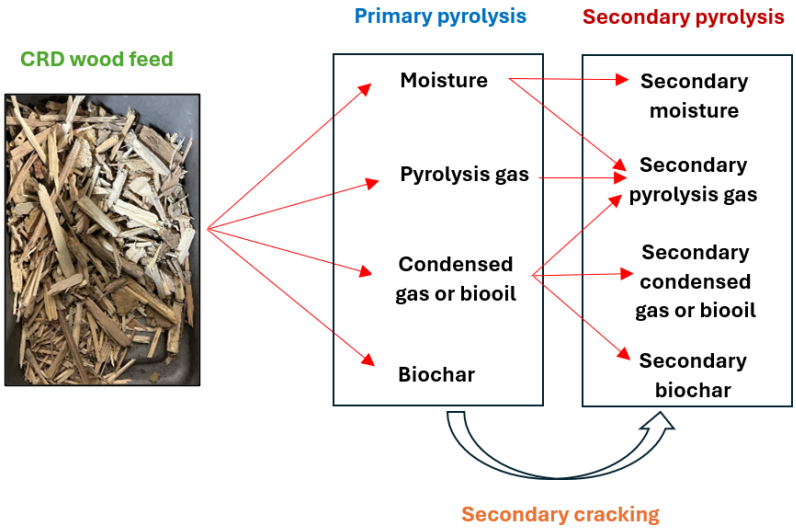

Supplementary figure 1: Pyrolysis mechanisms potentially undergone by CRD wood

Supplementary table 1: Three categories of biochar stability tools (non-exhaustive). Metrics used in this article are highlighted in grey

Category 1 or alpha	Category 2 or beta	Category 3 or gamma
Biochar carbon makeup and its aromaticity	**Biochar oxidation resistance**	**Biochar persistance**
Elemental analysis: 1. Proximate analysis: VC, FC, ash, TSF 2. Ultimate analysis: CHNSO, H/C, O/C (Van-Krevelen)	**Thermostability methods:** 1. TGA and DTG 2. R50 recalcitrance index 3. Edinburgh stability tool and chemical incubation experiments	**Structural analysis:** 1. ^{13}C-NMR 2. FTIR 3. Raman spectroscopy and I_D/I_G indices 4. XRD 5. SEM-EDX

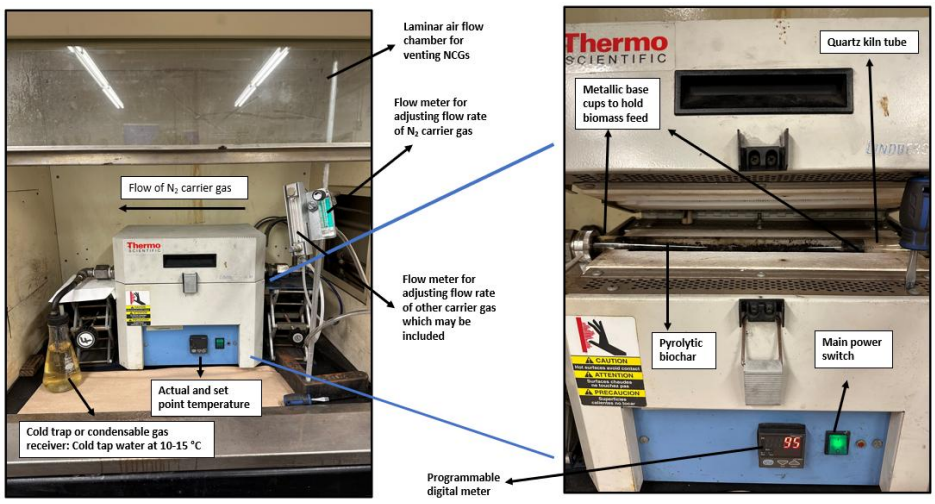

Supplementary figure 2: Laboratory-scale horizontal tube furnace and associated parts

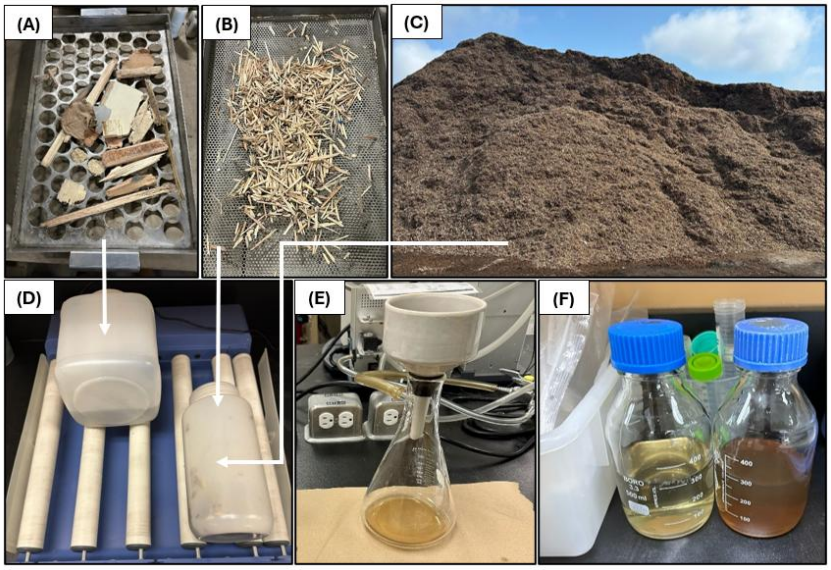

Supplementary figure 3: Washing of CRD residues to treat the AAEM content. From top left: Size-separated CRD wood A), B); CRD fines C); Lixiviation in DMW and acid D); Filtration and storage of leachate from CRD residues for metals analysis E), F) – change in color of lixiviation medium due to efficient leaching

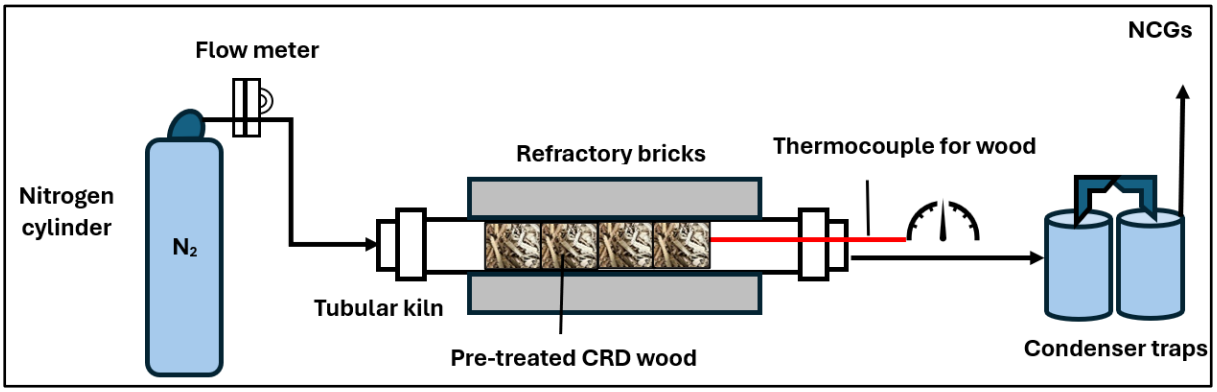

Supplementary figure 4: Scaled-up horizontal tube furnace set-up: Equipment and functionalities

Supplementary figure 5: On-set and termination of CRD wood pyrolysis according to the color of gas under suction. From the left: Evaporation of moisture (colorless); Hemicellulose, extractives, and initiation of cellulose degradation (pale-yellow); Condensation of volatiles and resulting biooil flaming when in contact with ambient air; Ceasing of flaming and gas production

Supplementary figure 6: Vacuum suction of pyrolytic gases to minimize the accumulation of condensed volatiles on biochar

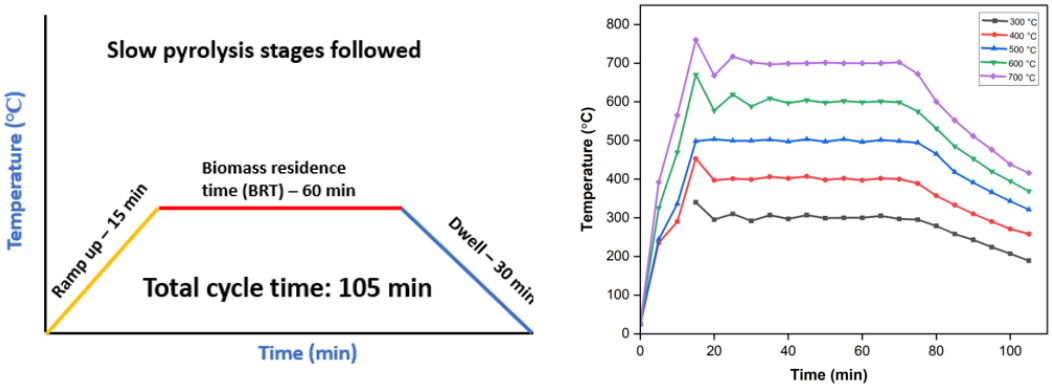

Supplementary figure 7: Stages of slow pyrolysis and associated temperature profile for the 105 min cycle

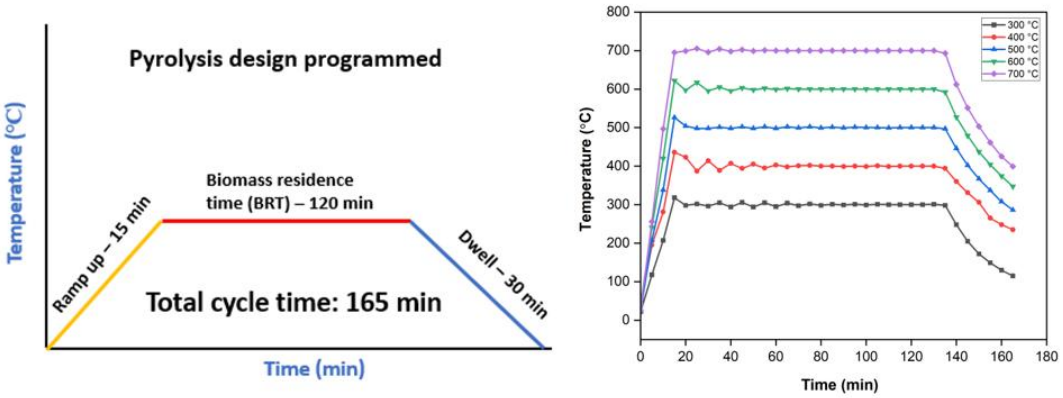

Supplementary figure 8: Stages of slow pyrolysis and associated temperature profile for the 165 min cycle

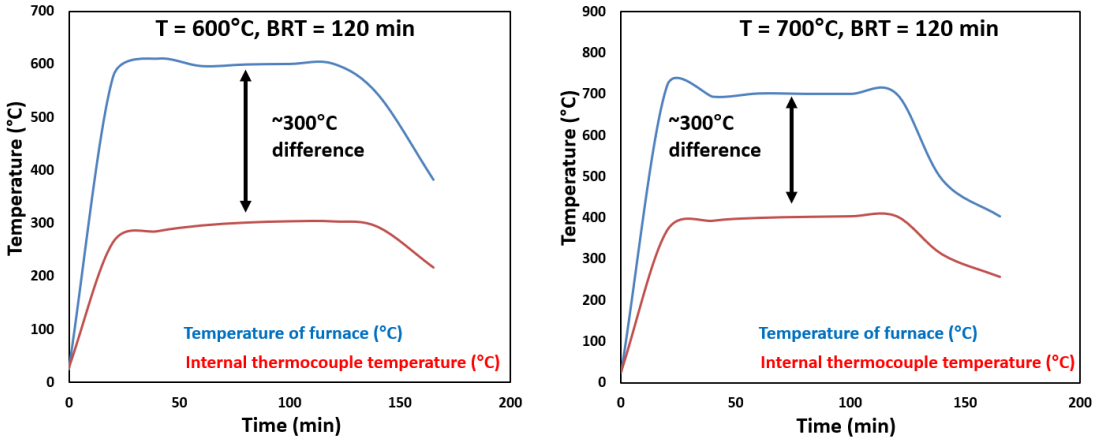

Supplementary figure 9: Temperature difference due to thermal inertia in the laboratory-scale horizontal tube furnace

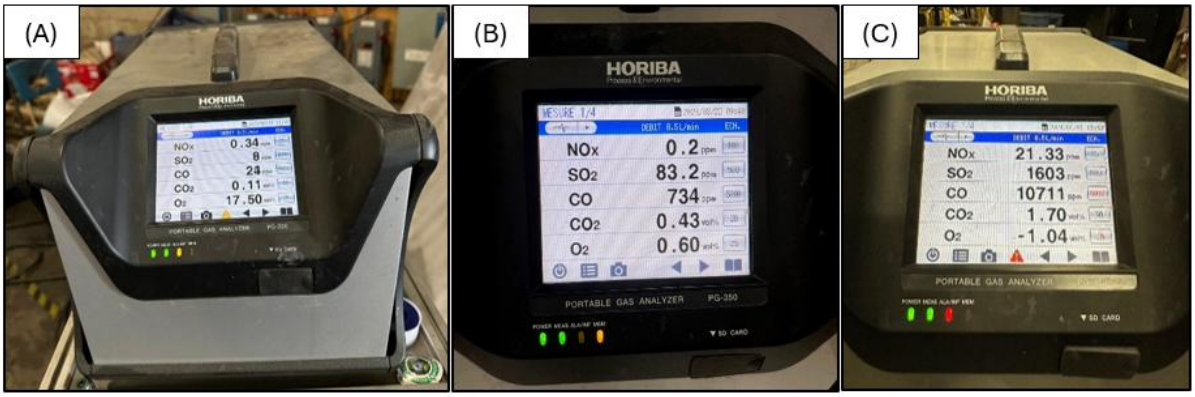

Supplementary figure 10: A gas analyzer monitoring the level of oxygen during pyrolysis. From the left: A) oxygen or air infiltration into the tube furnace; B) C) areas with leaks detected and sealed tight which decreases oxygen concentration

Supplementary table 2: Leaching efficiency of AAEM with CRD wood blocks and chips

CRD wood size	Lixiviation medium	Time of lixiviation (h)	Na (mg/L)	K (mg/L)	Ca (mg/L)	Mg (mg/L)	Ba (mg/L)
Blocks	DMW	16	18.07	2.12	4.50	5.58	0.011
Blocks	DMW	24	30.37	5.57	8.21	11.32	0.013
Increase in leached metal concentrations (%)			**68.07**	**162.74**	**82.44**	**102.87**	**18.18**
Blocks	Acid	16	33.20	8.01	42.66	20.95	0.104
Blocks	Acid	24	69.83	28.99	104.11	52.55	0.125
Increase in leached metal concentrations (%)			**110.33**	**261.92**	**144.05**	**150.84**	**20.19**
Chips	DMW	16	86.56	20.87	80.14	51.01	10.096
Chips	DMW	24	107.81	35.14	98.65	66.96	13.132
Increase in leached metal concentrations (%)			**24.55**	**68.38**	**23.10**	**31.27**	**30.07**
Chips	Acid	16	140.86	131.09	401.35	154.88	110.164
Chips	Acid	24	240.09	239.39	719.31	258.03	191.242
Increase in leached metal concentrations (%)			**70.45**	**82.61**	**79.22**	**66.60**	**73.60**

Supplementary figure 11: Extent of carbonization with increase in pyrolysis temperature from 300-500 °C

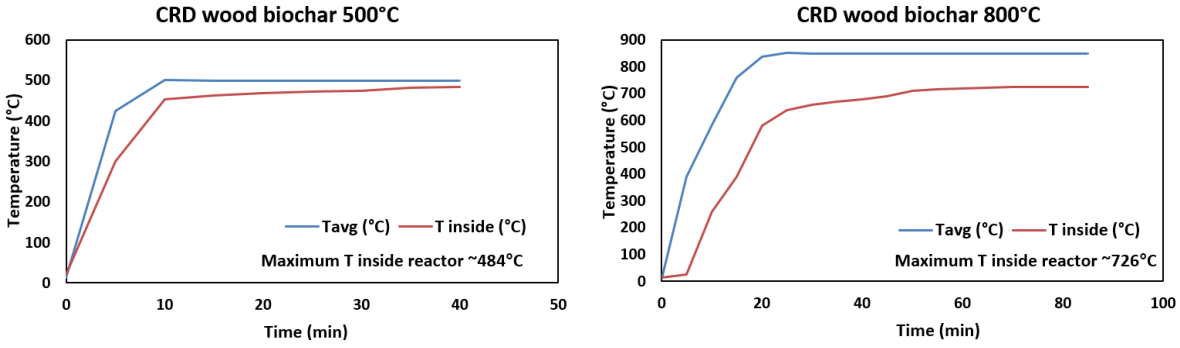

Supplementary figure 12: Thermal inertia recorded in scaled-up horizontal tube furnace

Supplementary table 3: Elemental properties of conventional anthracites, cokes, and biochars

Reference sample	C [%]	H [%]	N [%]	S [%]	Ash (%)	O (%)	O:C	H:C
Anthracite 1	86.28	1.68	0.86	0.347	7.5	3.31	0.03	0.23
Anthracite 2	80.16	1.43	0.62	0.648	13.3	3.85	0.04	0.21
Anthracite 3	84.45	1.83	0.81	0.563	10.1	2.23	0.02	0.26
Green or raw coke	91.06	3.18	0.46	0.128	1.2	3.94	0.03	0.42
Metallurgical grade coke 1	95.51	0.30	1.33	1.887	0.2	0.73	0.01	0.04
Metallurgical grade coke 2	95.42	0.37	1.50	1.498	0.3	0.94	0.01	0.05
Biochar 1	93.45	1.02	0.47	0.053	3.3	1.68	0.01	0.13
Biochar 2	82.96	2.37	0.55	0.059	6.2	7.83	0.07	0.34
Biochar 3	86.60	2.22	0.47	0.012	3.9	6.76	0.06	0.31
Biochar 4	87.14	1.51	0.60	0.005	5.1	5.66	0.05	0.21
Biochar 5	84.66	2.70	0.72	0.002	2.3	9.66	0.09	0.38
Biochar 6	86.00	1.58	0.63	0	5.0	6.81	0.06	0.22

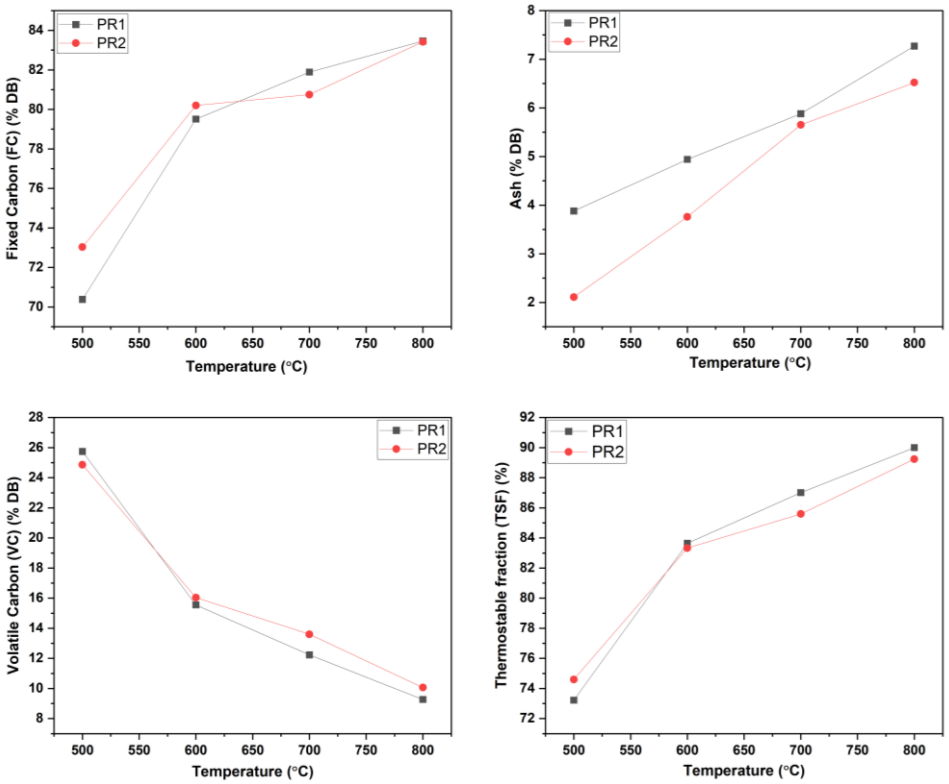

Supplementary figure 13: Variation of biochar FC, VC, ash, and TSF with temperature

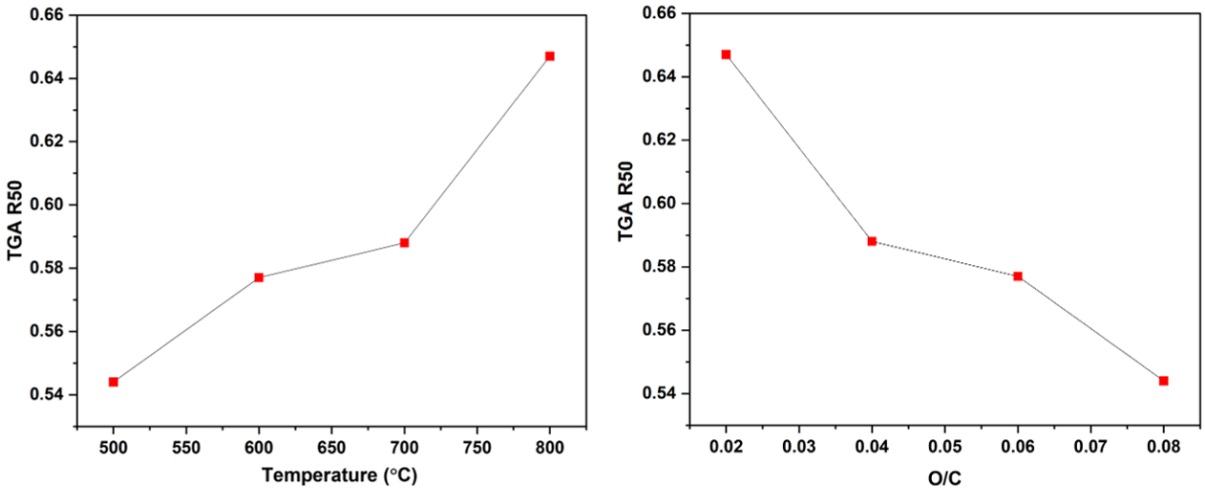

Supplementary figure 14: Interdependence between pyrolysis temperature, R50 recalcitrance index, and O/C

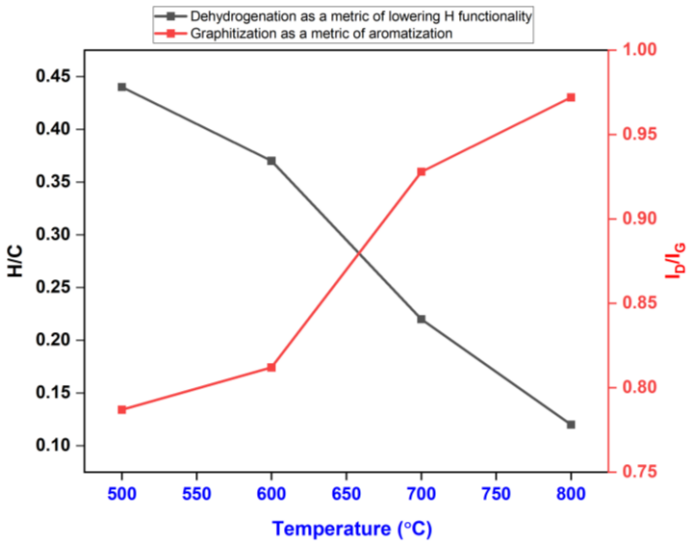

Supplementary figure 15: H/C and I_D/I_G serving a dual purpose: Indices for both, biochar carbon structure and stability

CHAPTER 3 – SCIENTIFIC ARTICLE (2)

Turning Construction, Renovation, and Demolition (CRD) Wood Waste into Biochar: A Scalable and Sustainable Solution for Energy and Environmental Applications

Aravind Ganesan[1,2,*], Simon Barnabé[1*], Younès Bareha[1], Simon Langlois[2], Olivier Rezazgui[2], Cyrine Boussabbeh[2]

[1] Institut d'Innovations en Écomatériaux, Écoproduits et Écoénergies, Pavillon CIPP, Université du Québec à Trois-Rivières, boul. des Forges, Trois-Rivières G8Z 4M3, Québec, Canada

[2] Cégep de Trois-Rivières, Pavillon des Sciences, 3500 Rue de Courval, Trois-Rivières, G8Z 1T2, Québec, Canada
Innofibre – Centre d'Innovation des Produits Cellulosiques, 3351, boul. des Forges C.P.97. Trois-Rivières G9A 5E6, Québec, Canada

***** Correspondence: Aravind.Ganesan@uqtr.ca / Simon.Barnabe@uqtr.ca

Abstract

Diversion routes for construction, renovation, and demolition (CRD) wood wastes is largely minimal. Landfilling is currently being viewed as the easiest of these routes but is getting increasingly complex and harder due to stringent governmental regulations on land-use, emissions, soil and groundwater contamination from the leachates since CRD wood is severely treated beforehand to be fit for construction purposes. As an effective waste management tool, pyrolysis could be viewed as a potential thermochemical valorization path for CRD wood to both reduce the volumes of waste and also to produce energy-dense products like biochar. An elaborate design of experiments (DOE) involving different process conditions like pyrolysis temperature, biomass residence time (BRT), and mass of feedstock were followed to evaluate their combined effect on biochar's physicochemical and morphological characteristics. A horizontal tube furnace and a horizontal rotary retort-furnace reactor were used for validating these robustness trials by changing process variables between each run. Post-production, biochars were analyzed for their composition and aromaticity (proximate and elemental analysis), thermal and oxidative resistance (TGA and TGA R50), surface properties and permeance (BET, SEM-EDX, Raman spectroscopy). Four biochar properties were studied in detail as examples using response surface methodology (RSM) modelling and statistical analysis to project their dependence on pyrolysis conditions. Proximate analysis revealed that high temperature biochars as in B800 showed highest FC (87%), TSF (96%), and lowest VC (9%) proving a positive relation with pyrolysis temperature and BRT. The same goes for high carbon content (92%), BET surface area (300 m^2/g), and micropore volume (0.146 cm^3/g). But there was a sharp decline in hydrogen (0.9%), oxygen (2.2%), Van-Krevelen parameters (H/C: 0.1, O/C: 0.02), and biochar yield (21%) implying a strongly negative relation for these indices mainly with pyrolysis temperature. Metal/trace element content in CRD wood was also under permissible limits. All these properties underscore biochar's potential in metallurgy and carbon sequestration applications. For CRD wood pyrolysis to gain attention, scalability is a prominent requisite. In our work, the horizontal rotary retort-furnace reactor showed tremendous potential with a higher mass of feedstock (3 kg) processed, to almost match biochar properties derived out of a tube furnace where only 50-250 g could be treated at once. Moderate temperature biochars like B600 showed a great balance of physicochemical, morphological, surface functionality, and yield characteristics that qualified its use as an adsorbent material for dye removal batch adsorption experiments with colored water. Since methyl orange is an anionic azo dye and B600 was a biochar with a pH_{PZC} of 9.02, optimization of adsorption conditions, especially pH, was key to evaluate its performance via the metrics like removal percentage and adsorption capacity. Maximum removal of over 90% for methyl orange dye were under low pH, high adsorbent dose, long duration, and lower initial concentration of dye in the test solution. From the derived adsorption parameters, B600 agreed well with the Freundlich isotherm model (R^2=0.97, 1/n=0.5) and pseudo-second order kinetic model (R^2=1) suggesting favorable, multilayer heterogeneous adsorption that is affected by the concentration of dye (8-164 ppm) and the available active binding sites. Comparison of these results with similar studies confirmed that our work related well with existing data.

Key words: biomass, pyrolysis, biochar, adsorption, environment, metallurgy, carbon

1. Introduction

Large volumes of refused construction, renovation, and demolition (CRD) wood poses challenges to the environment due to its variable chemical composition and inherent metal content (Robey et al., 2018). The quantity of CRD wood waste generation is largely variable and depends upon the percentage of wood used in construction according to government legislations, specific CRD practices, and geography under consideration. Conventional disposal methods such as landfilling and incineration lead to burden on spatial requirements, groundwater pollution, odour issues, and release of (global greenhouse gas) GHG into the surrounding atmosphere. Pyrolysis, a controlled thermal decomposition pathway to treat organic residues in an oxygen-deficient atmosphere, serves as an efficient thermochemical conversion technology that could be employed as an alternative waste management tool (Al-Rumaihi et al., 2022). Its effectiveness in generating multiple products (biooil, pyrolysis gas, and biochar) of various end-uses, ability to be optimized as slow, fast or flash pyrolysis to maximize the yield of solids, liquids or non-condensable gases (NCGs), permanent immobilization of pollutants once part of the initial biomass into the pores of biochar product, and overall shrinkage in waste volumes puts this method under limelight nowadays as a sustainable and circular solution (Li et al., 2017).

Biochar, the solid carbonaceous material derived from pyrolysis of biomass, has garnered immense attention for its versatile applications in soil remediation, carbon sequestration, wastewater treatment, metallurgy, automotive, and construction, where it could potentially substitute the use of fossil fuels like coal and commercial activated carbon (Sivaranjanee et al., 2024). Although, current scenarios favour only partial substitution, further research in biochar engineering is expected to boost its usage at higher percentages. Nowadays, the use of biochar has progressed and is finding scopes within sustainable agriculture businesses (Ayaz et al., 2021), filler materials of biopolymers (Malińska et al., 2024), and even in energy storage materials like supercapacitors (Ahuja et al., 2024). Tailoring biochar, however, depends on the nature of biomass feedstock dealt with and the pyrolysis conditions such as temperature, biomass residence time (BRT), heating rate, feedstock mass, and particle size (Anand et al., 2023). Pyrolysis temperature, however, was supposed to have the most prominent influence on biochar's nature (Ghorbani et al., 2022). On the feedstock choice, woody biomass like CRD wood waste, forest residues, yard waste, manure, and organic fraction of municipal solid waste differ noticeably w.r.t biochemical composition, heteroatom make-up, and presence of inorganics. Amidst the ash fraction, alkali and alkaline earth metal (AAEM) components like Na, K, Ca, Mg, Ba, their salts and oxides interfere in biomass breakdown reactions during pyrolysis resulting in the loss of structural carbon as CO_2 that could alter biochar yield (Nan et al., 2021). This may be held true for high ash feedstock like agriculture residues. As for production parameters, high pyrolysis temperatures (over 600 °C) yield biochar with high stability (graphitized, aromatic carbon), molecular integrity, low volatiles, and subtle reactivity, making them strong contenders for carbon sequestration applications (Nan et al., 2021). Biochar produced at milder temperatures show diverse surface functionalities, cation exchange capacity (CEC), tunable surface area and pore volume, enabling their utilization for agriculture and adsorption applications. Bolan et al., 2023 stated that such reactive surface groups may be eliminated gradually as heat treatment severity rises over 500 °C due to decarbonylation, decarboxylation, dehydration, dehydrogenation, and/or dehydroxylation reactions. Chemical (acid, alkali) and physical (steam, CO_2) activation conditions of biochar/biomass is yet another topic of discussion circumventing adsorption applications to increase available surface area for facile entrapment of pollutants in water and air (Beljin et al., 2024). Although, not all biochars in this case need to undergo secondary treatments to achieve satisfactory surface area. Thus, customizing biochar characteristics w.r.t its intended applications become key (Buffi et al., 2024). For a rejected residue like CRD wood, which would have been subjected to landfill disposal anyway, optimization of pyrolysis parameters can by itself be beneficial for tuning necessary adsorption properties like surface area, pore volume, and hydrophilic functionalities containing hydrogen and oxygen that interact well with the pollutant.

Methyl orange, an organic anionic dye, used widely in the textile, leather, paper, chemical, and packaging industrial sectors, for coloring and tinting, is an azo dye (with the functional group -N=N- bonded to aromatic or aryl species) which is synthetic and polluting (Iwuozor et al., 2021). Process wastewater from these industries that is ridden with methyl orange could lead to ecotoxicity and health complexities due to its carcinogenic nature and resistance against degradation (Serban et al., 2023). Activated carbons derived from fossil fuels like coal are usually the predominant adsorbent choices as far as adsorption, filtration, or purification applications are concerned due to their non-destructive adsorption nature and superior material properties, but their emissions-intensive production and/or activation involving chemicals coupled with geographically isolated manufacturing hubs (energy-intensive transportation for exports) necessitate alternative, environmentally benign options (Lee et al., 2024). On this note, pyrolytic biochar has been tested as a versatile carbonaceous adsorbent to remove dyes

(Jian et al., 2018). Albeit, the use of CRD wood biochar has not been tested to the best of our knowledge as a dye removal material. Adjustable porosity, surface area, surface functional groups, and carbon stability are four important properties necessary for biochar to be an effective adsorbent in water treatment, to remove organic/inorganic pollutants (Cano et al., 2025). The nature of biomass feedstock, pyrolysis parameters, and any chemical, thermal or physical activation techniques govern these properties (Hama Aziz et al., 2024). Although, if activation is carried out, post-adsorption recycling or reusability potential becomes a pre-requisite since secondary treatment of biochar is a rigorous and resource intensive process that contradicts one-time usage circumventing environmental and economic viability. Thus, efforts to use industrial downstream products which are discarded and cheap to source, are nowadays, being researched for use in adsorbent materials as stated in Ramath et al., 2023. Additionally, adsorption parameters such as pollutant's initial concentration, adsorbent dosage, temperature, pH, effect of co-ions, and time have notable effects on the performance of biochar (Issaka et al., 2022). These are in a way, interdependent with its physicochemical and morphological attributes. Together, they are responsible for various adsorption mechanisms such as electrostatic forces, π-π interactions, covalent bonding, hydrogen bonding, surface complex formation, and pore adsorption (Zhao et al., 2024; Hama Aziz et al., 2024). Thermodynamically, biochar-based dye adsorption processes are endothermic, i.e, requiring external energy, and are spontaneous (Behera et al., 2024). In this work, CRD wood biochar will be exploited as is, for methyl orange adsorption application. No reusability studies will be conducted since the biomass source is largely cheap, abundantly available, and already non-recyclable/end-of-life/refused material. After usage, this biochar can be readily used in carbon sequestration applications (*e.g.:* concrete, building materials, asphalt co-component in pavements or roads), thereby, allowing long-term entrapment of the pollutant. However, questions on biochar's capability to leach the pollutants back to its surrounding environment needs to be thought about in case of soil-based carbon sequestration efforts that would not be an ideal post-adsorption step. Ironic to other relevant studies, biochar activation is also not followed to avoid the use of reactive gases, chemicals, and any downstream pollution from the process. This could facilitate on-spot production, usage, and immediate disposal minimizing overall energy and costs. The best engineered biochar w.r.t adsorption properties, only from our range of experiments, will be chosen for this application.

Till now, a comprehensive analysis involving a robust design of experiments (DOE) framework to specifically study the influence of CRD wood pyrolysis parameters on the characteristics of biochar product is underexplored. So, the current work aims to bridge this gap by analyzing the influence of key process variables like pyrolysis temperature, BRT, and biomass feed mass via slow pyrolysis in a horizontal tube furnace reactor– an extension of previous work completed in Ganesan et al., 2025. Following this, slow pyrolysis tests of the same CRD wood material are conducted in a semi-pilot horizontal rotary retort-furnace reactor under five identical conditions chosen, to assess the scalability potential. Based on the physicochemical and/or morphological properties, CRD wood biochar applications in carbon sequestration, soil amendments, and metallurgy are discussed wherever applicable.

Its adsorption performance circumventing an industrial dye, methyl orange, is also studied in detail through batch adsorption experiments. Optimization of adsorption conditions along with performing kinetic, isotherm, and thermodynamic model calculations will be yet another objective. To be precise, biochar that is non-activated, will only be used in this work for wastewater dye adsorption tests. Through this multi-faceted approach, critical insights on the feasibility of CRD wood biochar production and its utilization under industrial and environmental settings will be derived.

2. Materials and methods

2.1 Sample preparation

The CRD wood residues sourced from BRQ Fibre et Broyure, Trois-Rivières, Quebec, Canada, with an initial moisture content of 18%, were brought in cartons Figure 11 (A) and dried in a drying oven overnight at 105 °C till the moisture was reduced to less than 1 wt% (0.18 wt% in our case). At this low level, moisture reduction may hasten pyrolysis and heat transfer within the feedstock particles. It also could result in a lower energy consumption in the reactor. Then, dried CRD wood of a known mass was subjected to a vibrational sieving treatment (LABTECH unit) for at least 5 min to analyze the particle size distribution of the feedstock. Non-wood contaminants of varying sizes were hand-sorted continuously and the treatment progressed for the remaining wood residues. The mass collected in each sieve was then calculated and mapped to determine the average particle size of the wood mix. If the average particle size of CRD wood was greater than 2.5 cm, this biomass was subjected

to a milling treatment with a Retsch SM-300 to ensure a manageable/optimal size of 3 mm - 2.5 cm for pyrolysis in the two reactors Figure 11 (B). For characterization, the same mill Figure 11 (C) with a screen of least pore size was used to generate fines of both, biomass Figure 11 (D) and pyrolytic biochar Figure 11 (E).

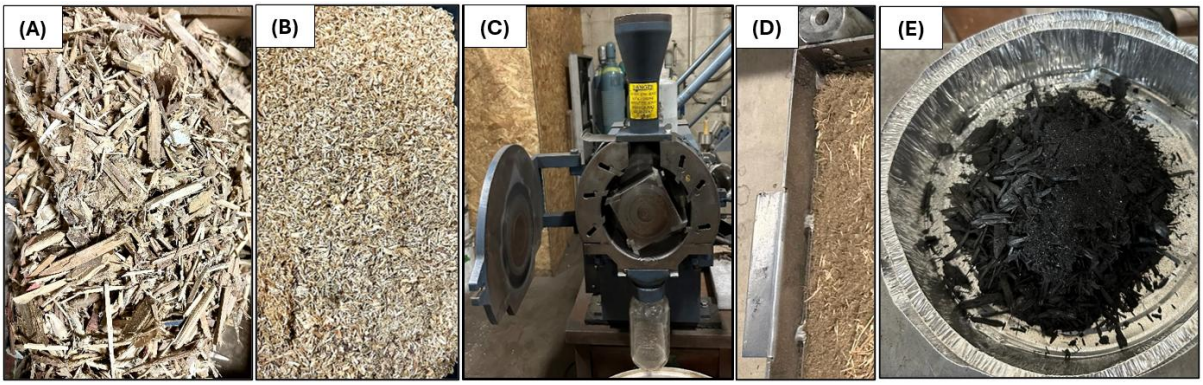

Figure 11: Sample preparation for pyrolysis and characterization. (A) CRD wood as is received from source site; (B) size separation and selection of suitable particle size (3 mm to 2.5 cm); (C) Thomas Wiley mill model 4; (D) CRD wood fines; and (E) biochar fines

2.2 Slow pyrolysis set up and design of experiments

The conditions for pyrolysis are tabulated as in **Table 8**. Slow pyrolysis was carried out following a robust DOE modelled using Stat-Ease's response surface methodology (RSM) tool and adopting the central composite design (CCD) method. Three independent pyrolysis variables namely: temperature, BRT, and mass of feedstock were varied continuously across each experimental run to determine their individual and synchronous effect on different response variables that describe biochar properties (*e.g.:* BET surface area, micropore volume, H/C, O/C). Theory behind the derived DOE model design and the list of conditions to be validated are explained with Supplementary figure 16 and Supplementary table 4. Statistical analysis via model significance (p-value), model fit (R^2), and independent variable coefficients along with surface, contour, perturbation, and predicted versus actual value plots are key performance indicators (KPI) for each model that is evaluated.

Table 8: Experimental conditions chosen for pyrolysis

Coded independent variable	Actual Independent variable	Coded and actual values for the five levels				
		-α (lowest)	**-1 (low)**	**0 (mid-point)**	**1 (high)**	**α (highest)**
A	Pyrolysis temperature (°C)	400	500	600	700	800
B	BRT (min)	30	45	60	75	90
C	Mass of feedstock (g)	50	100	150	200	250

Two reactors as shown in Figure 12 (left) were chosen for performing pyrolysis experiments. Firstly, the scaled-up horizontal tube furnace reactor ("Thermo Scientific Lindberg Blue M™ 1100 °C") as in Ganesan et al., 2025 was used in this work for slow pyrolysis of CRD wood. The exact instrumentation design was adopted here with no changes. A custom-made temperature-resistant steel tube reactor of a 2.5-inch diameter, 69-inch length, and combined volume of 5.55 L, that is deemed to accept a maximum optimal CRD wood feedstock mass of 400 g, is placed inside a hollow provision allotted within the furnace's ceramic bricks. This reactor was capable to reach the set point pyrolysis temperature with 15 min and encompassed three K-type thermocouples connected to each of the three furnace zones. Additionally, another K-type thermocouple was inserted into the reaction zone containing the CRD wood biomass to gauge heat transfer occurrences. For eliminating reactive atmospheres and to prevent the settling of pyrolysis volatiles over biomass/biochar surfaces, a nitrogen flow rate of 1-5 L/min along with a vacuum pump of high suction capacity is fitted to the exit gas zone. The drawn-out gases are fed directly

to a combustion chamber of the in-house pilot pyrolyzer for catering to a minor portion of its energy demand in tandem with natural gas and pilot pyrolysis gas. To prevent the carry-over of dusts and other particulates from the reaction zone, a steel mesh filter is used.

Secondly, for scale up trials, a horizontal rotary retort-furnace reactor was used. Its configuration is depicted in Figure 12 (right). The furnace body was connected to three individual K-type thermocouples to monitor temperatures across different zones. An additional temperature probe is inserted directly into the reaction zone of the retort to observe any abnormal thermal inertia patterns as a result of convective or radiative heat losses. Thermal inertia could be defined as the reactor's resistance towards increase in temperature caused by non-uniform heating patterns and loss of heat via the reactor walls due to inefficient insulation. As a result, the refractory bricks of the furnace heat up to the set point temperature, but this heat is not transferred adequately to the retort and thus, the biomass inside sees a delayed heat transfer. In fact, the influence of thermal inertia on material energy balance during pyrolytic thermal decomposition in both these reactor configurations, has also been addressed in Supplementary table 7 and Supplementary table 8. Quartz wool was used as an insulation material to sheath the extremities of the retort and avoid its contact with cool ambient air that could otherwise lead to premature condensation of pyrolytic volatiles. To avoid this, additionally, a vacuum pump with high suction capacity just like what was used for the scaled-up horizontal tube furnace reactor earlier, is retrofitted here. It transports all the gases swiftly to the in-house pilot pyrolyzer's combustion chamber for contributing to a minor part of its energy requirements. Nitrogen as carrier gas with flow rates up to 1-5 L/min sweeps through the retort during the process and minimizes the influence of unstable reactive atmospheres. Controlled flow rates of nitrogen also help to eliminate dust or fine particles in the reaction chamber via a joint action with the vacuum pump. About 3 kg of CRD wood could be treated at once in this retort allowing for sufficient mixing of biomass through the unit's rotational function. This mass is also optimal without causing any restrictions for inert gas flow and helps the volatiles to elutriate quickly to avoid condensation on biochar surface that could otherwise lead to secondary reactions like cracking and polymerization.

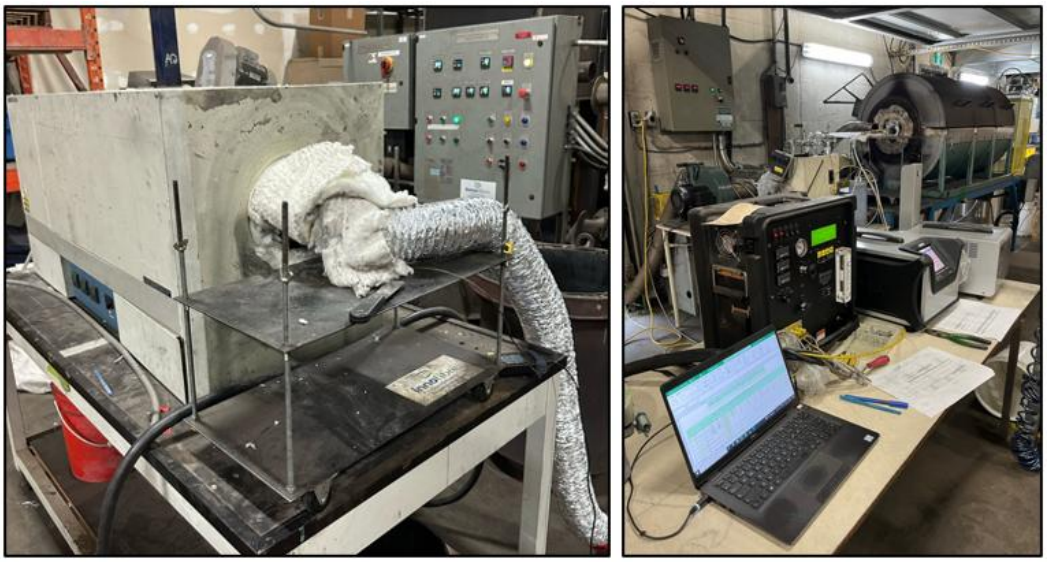

Figure 12: Left - Horizontal tube furnace reactor; and Right – Horizontal rotary retort-furnace reactor

2.3 Physicochemical and morphological characterization of biochar

All characterizations were carried out by the same technician, with the same initial CRD biomass feedstock, and instrumentation as in Ganesan et al., 2025. The list of equipment for analyzing biochar's carbon make up with aromatization degree, thermal or oxidative stability, and permeance are described in this section. Some of these characterizations were also performed for the CRD wood biomass.

Proximate analysis for biochar was carried out in a muffle furnace according to ISO 1171. Here, 1 g of dried biochar fines was heated stepwise with a 5 °C/min heating rate till 550 °C where it was held for 2 h after which ash content was measured. Volatile carbon (VC) analysis involved taking 1 g of dried biochar fines in a covered quartz crucible and heating it at 900 °C for 7 min (ISO 562). Fixed carbon (FC) was then calculated by difference [VC+FC+ash=100], all three weights represented on a dry weight basis (wt%DB) to not account for any other

volatiles aside from carbon. Elemental/ultimate analysis of dried biochar fines was performed using an Elementar Vario Macro Cube equipped with an inert carrier gas supply like helium. Oxygen is the carrier gas for combustion at a high temperature of 1200 °C. Percentage of oxygen is then calculated as [O=100-(C+H+N+S+ash)]. Thermogravimetric analysis (TGA) was employed using a PerkinElmer TGA 8000 analyzer which used only 8 mg of biochar as is (without drying) and heated it at a 10 °C/min ramp till 900 °C in the presence of compressed air as carrier gas for analyzing biochar's decomposition behaviour in thermally and oxidatively stressful conditions. Correcting the thermograms for moisture and ash is key to calculate the TGA R50 recalcitrance index, *i.e*, the ratio of temperatures at which 50% weight loss in a biochar material happens to that of a reference graphite material. Biochar's surface functionalities were detected using the Agilent Cary 630 Fourier Transform Infrared (FTIR) spectrometer. Here, dried biochar fines were placed on a crystal, either diamond or germanium. The transmittance spectral distribution method within the range of 500–4000 cm^{-1} was chosen and raw data from the spectra was collected. Following baseline correction and smoothening using the ORIGIN software, a stacked spectra was obtained to easily compare one biochar sample with another and identify structural transformations occurring with changes in pyrolysis conditions. The degree of amorphous to crystalline carbon transitions in dried biochar fines was examined with a ThermoScientific DXR3 Raman Spectrometer with a 532 nm laser, 7 mW power, and an exposure time of 60 s, covering a range of 800–1800 cm^{-1}. The intensity of amorphous D band and graphitic G band were measured, and this I_D/I_G index was leveraged to predict disorderliness or defects in biochars at different temperatures until its graphitization is nearing.

Brunauer-Emmett-Teller (BET) surface area and micropore volume of dried biochar fines were measured using a Micromeritics Tristar II BET analyzer using helium or nitrogen adsorption. Metal content was analyzed with an Agilent 4210 Microwave Plasma Atomic Emission Spectrometer (MP-AES), where dried biochar fines were hydrolyzed using an acid and nebulized into a nitrogen plasma for multi-element detection. The pH was determined by mixing biochar fines as is with demineralized water in a ratio of 1:10 and allowed to shake in a temperature controlled orbital shaker. Once mixing was over, the biochar suspension was let to rest at ambient conditions for about 30 min after which its pH was tested with a bench-top pH analyzer. Bulk densities were assessed by weighing a known mass of biochar after pyrolysis with surface levelling in a pre-weighted steel container of a known volume, and calculating density based on mass to volume ratio. Biochar yield was expressed as the percentage ratio of total biochar weight as is obtained from pyrolysis to the initial biomass weight taken for the process. Higher heating value (HHV) of biochar fines as were estimated using elemental composition data from Channiwala and Parikh 2002 and Khatibi et al. 2023. Lastly, SEM-EDX analysis was performed to investigate the surface presence of various biochar (dry fines) elements using a Hitachi SU-70 electron microscope with an appended X-ray analyzer at 15 kV electron voltage under vacuum, capturing images at 100X, 250X, 500X, and 1000X magnifications. The elements under utmost consideration were carbon, oxygen, Fe, and AAEM.

3. Results and discussion

3.1 CRD wood pyrolysis in horizontal tube furnace reactor

Five biochar samples from the DOE, produced at temperatures spanning from 400-800°C (B400-B800), are chosen randomly for further characterizations and scalability tests to study pyrolysis parametric influence more precisely. However, characterization results from **Table 9** are firstly fed to the DOE model for statistical evaluations to take precedence.

3.1.1 Physicochemical characterization

A detailed tabulation of the results from all 16 slow pyrolysis runs in the horizontal tube furnace reactor are drafted in Table 9. Carbon content increased by 40-41% from B400-B800 exerting a direct influence on pyrolysis temperature (Pearson's coefficient, r = 0.92; DOE model p-value = 0.0002). Simultaneously declining oxygen and hydrogen content with low O/C (Pearson's coefficient, r = -0.88; DOE model p-value = <0.0001) and H/C (Pearson's coefficient, r = -0.95; DOE model p-value = <0.0001) qualifies biochar as mature and with stable aromatics. However, for soil amendment applications such as alleviation of acid-ridden soils and heavy metal remediation, presence of negatively charged volatile oxygenic functionalities on biochar's surface is key to increase its CEC (Huff et al., 2018). Therefore, for this application, biochars like B400 and B500 are adaptable where their relatively higher O/C can be linked to higher surface negative charge and in turn, higher CEC (Lehmann et al., 2011). BET surface area increased till 600 °C after which it drops below 300 m^2/g (Pearson's coefficient, r = 0.83; DOE model p-value = 0.001). This may be due to collapsing of walls between adjacent micropores and the formation of mesopores that can be seen from the SEM micrographs of B800 in **Figure 18**

(G)(H)(I). This is in agreement with the findings in Nartey & Zhao et al., 2014 where high pyrolysis temperature and BRT caused an increase in pore size. A high surface area (320-340 m^2/g) and micropore volume (0.112-0.149 cm^3/g) as achieved for biochars produced at 600 °C, harbor more active sites with adsorption properties. Soil fertility enhancements and replenishments in arid areas with biochar having similar properties, can be productive to retain water and other nutrients due to the formation of dense porous networks according to Khater et al., 2024. FC increased by 360% from CRD wood to B400 enunciating the positive role of even the slightest of carbonization in carbon arrangements. As pyrolysis temperature increased from B400-B800, FC climbed by 23% to 86.73% reinforcing its applications in carbon sequestration and metallurgy (Pearson's coefficient, r = 0.95; DOE model p-value = 0.0099). This is possible only due to the decomposition of volatile and reactive organics. This finding can be validated by a decrease in VC by 65% from B400-B800 (Pearson's coefficient, r = -0.96; DOE model p-value = <0.0001).

Other properties of biochar also showed significant influence with pyrolysis temperature. Ash in CRD wood biochar is comparable with ash in other woody biomass like pinewood (0.40-1.80 wt%), poplar (3.45 wt%), and softwood pellets (0.61 wt%) as mentioned in Li et al., 2024. This suggests that CRD wood waste falls under the low ash feedstock category. Maximum ash was seen for B700 at 6.13% after which there was a decline to 4.10% probably due to melting and volatilization of unstable inorganics. This finding can be supported from the AAEM content in biochars listed in **Table 11**. Yield of biochar experienced a downward trend from B400-B800 at 57.8-21.1%, respectively (Pearson's coefficient, r = -0.78). At 400 °C, there was unconverted biomass left over from a woody appearance in some portions of the product, which contributed to a yield above 50%. As soon as the temperature was increased to 500 °C, there was a steep decline in yield by 53% confirming an overestimation for B400 due to incomplete pyrolysis. HHV rose from 20.28 MJ/kg for CRD wood to 32.74 MJ/kg for B800 suggesting that growing carbon and reducing volatiles content improved calorific value (Pearson's coefficient, r = 0.87). Loss of moisture and oxygen functional groups at such levels also means that more energy retention per unit mass of fuel could be achieved during combustion as in power plants and energy/high temperature reduction applications as in metallurgy. An increase in bulk density from 270-451 kg/m^3 was observed with pyrolysis temperature from B400-B800 (Pearson's coefficient, r = 0.99), adequately matching the conceptual finding from Khater et al., 2024. Due to higher degrees of heat treatment, structural compaction in biochar with more ordered crystallites and volume shrinkage is prevalent (Dufourny et al., 2019). However, the opposite trend was proposed in He et al., 2024. Here, the authors also state that ion exchange and reactivity of biochar decreases with increasing temperatures which may be due to volatilization of surface charges and localization of carbon. This means that growing structural and layered FC can increase heat conductivity and/or electrical conductivity, *i.e*, the somewhat graphitic behaviour is serendipitous for applications in metallurgy as well as charge storage devices.

According to Greco et al., 2021, polyaromatic hydrocarbons (PAHs) in biochar produced at higher temperatures could also experience a decline especially if carrier gas flow rates were higher that could prevent settling of pyrolytic volatiles on the biochar surface and their uncontrolled polymerization. Instead of tweaking flow rates of inert nitrogen, our process utilized a vacuum pump of high suction capacity to draw out gases as fast as possible to reduce their residence time. Although, Alharbi et al., 2023 stated that biochars produced at lower temperatures, rather focussed more on char yields with only few PAHs that reduces the product's ecotoxicity-related ramifications. The author also stated that ecotoxicity risk increases with higher desorption tendencies of pollutants trapped in biochar. Some priority PAHs to be tested in biochars as part of future works will be Phenanthrene, Naphthalene, Pyrenes and their benzo-derivatives (International Biochar Initiative, 2015).

Table 9: Results of slow pyrolysis runs from the DOE model. Bulk density and HHV are discussed separately as plots (Figure 13 (E)(F)). Five biochars at five different pyrolysis temperatures of 400, 500, 600, 700, and 800 °C with mixed BRT/mass of feedstock conditions are considered for future characterizations. These are labelled as B400, B500, B600, B700, and B800 (highlighted in grey)

Run	Independent variables for RSM			Elemental parameters					Porosity		Biochar output	Proximate parameters			Thermal and chemical stability indices			
															TGA	Van-Krevelen		Carbon strength
	A: Temperature (°C)	B: BRT (min)	C: Mass of feedstock (g)	N (wt%)	C (wt%)	H (wt%)	S (wt%)	O (wt%)	BET surface area (m^2/g)	Micropore volume (cm^3/g)	Yield (%)	VC (wt%DB)	FC (wt%DB)	Ash (wt%DB)	R50	H/C	O/C	TSF (%)
CRD biomass	**N.A**	**N.A**	**N.A**	**0.990**	**49.880**	**6.123**	**0.101**	**41.736**	**N.A**	**N.A**	**N.A**	**83.480**	**15.350**	**1.170**	**0.391**	**1.473**	**0.628**	**15.534**
1 (B400)	**400**	**60**	**100**	**0.780**	**65.320**	**4.293**	**0.442**	**26.145**	**4.238**	**0.002**	**57.800**	**26.384**	**70.596**	**3.020**	**0.513**	**0.789**	**0.300**	**73.271**
2	600	90	200	0.670	86.180	2.193	0.210	7.417	308.703	0.139	21.800	15.748	80.922	3.330	0.570	0.305	0.065	86.061
3	600	30	200	1.070	83.660	2.329	0.213	6.288	309.032	0.132	20.700	17.427	76.133	6.440	0.568	0.334	0.056	80.501
4 (B500)	**500**	**75**	**200**	**0.630**	**79.430**	**2.933**	**0.177**	**13.110**	**195.278**	**0.095**	**26.900**	**25.837**	**70.443**	**3.720**	**0.544**	**0.443**	**0.124**	**73.169**
5	600	60	100	0.910	82.370	2.391	0.241	8.578	255.854	0.123	21.300	18.473	76.017	5.510	0.603	0.348	0.078	80.132
6	500	75	150	0.870	78.340	2.910	0.180	13.840	179.077	0.090	26.400	24.312	71.828	3.860	0.561	0.446	0.132	74.783
7	500	90	150	0.720	77.600	2.746	0.218	12.546	260.562	0.114	26.500	24.247	69.583	6.170	0.545	0.425	0.121	72.452
8	600	45	50	0.700	86.720	2.034	0.123	5.613	334.887	0.149	19.200	14.132	81.058	4.810	0.632	0.281	0.049	86.794
9	700	90	200	0.940	88.760	1.379	0.205	4.026	315.809	0.148	23.300	12.151	83.159	4.690	0.587	0.186	0.034	90.002
10 (B800)	**800**	**75**	**200**	**0.890**	**91.740**	**0.870**	**0.168**	**2.232**	**299.554**	**0.146**	**21.100**	**9.169**	**86.731**	**4.100**	**0.647**	**0.114**	**0.018**	**96.191**
11 (B700)	**700**	**75**	**200**	**0.950**	**88.340**	**1.413**	**0.253**	**2.914**	**293.195**	**0.138**	**23.600**	**11.640**	**82.230**	**6.130**	**0.588**	**0.192**	**0.025**	**89.295**
12	500	90	250	0.510	82.000	2.825	0.151	11.344	229.033	0.108	26.600	23.857	72.973	3.170	0.546	0.413	0.104	76.032
13 (B600)	**600**	**90**	**250**	**0.430**	**87.510**	**2.209**	**0.123**	**6.168**	**323.776**	**0.145**	**21.900**	**15.037**	**81.403**	**3.560**	**0.577**	**0.303**	**0.053**	**86.817**
14	700	45	150	1.630	85.880	1.352	0.332	2.136	217.947	0.118	25.200	13.903	77.427	8.670	0.638	0.189	0.019	82.996
15	400	90	200	1.000	73.770	3.351	0.151	17.598	4.034	0.002	31.200	32.542	63.328	4.130	0.534	0.545	0.179	65.274
16	600	60	150	1.140	72.180	1.786	0.215	2.649	247.457	0.112	25.600	22.723	55.247	22.030	0.647	0.297	0.028	57.678

N.A: Not Analyzed

Figurative descriptions of these data are provided as in Figure 13 (A)-(D)

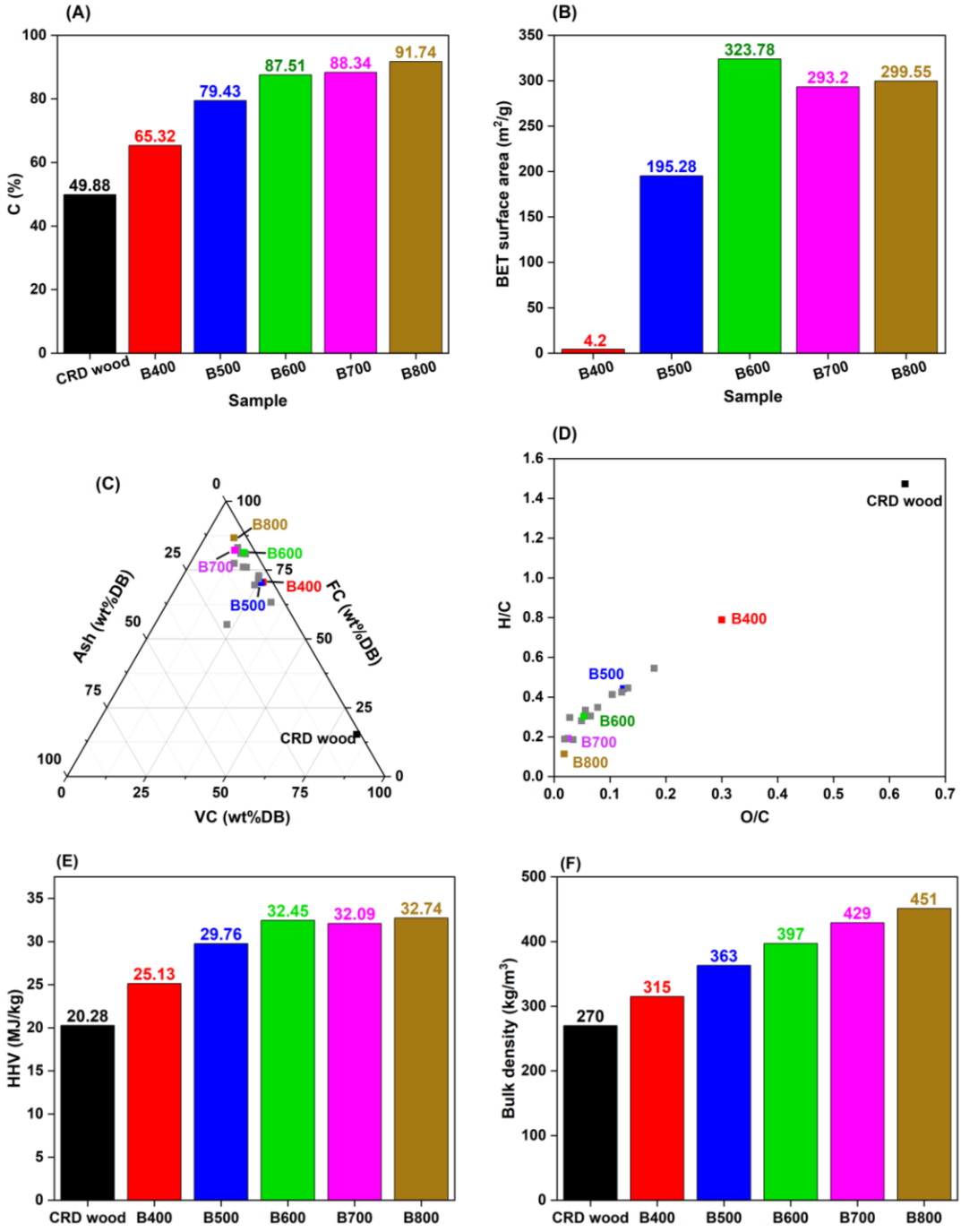

Figure 13: (A) carbon content; (B) BET surface area; (C) proximate analysis; (D) Van-Krevelen plot; (E) HHV; and (F) bulk density: for B400-B800.

3.1.1.1 Effect of particle size on biomass thermal decomposition

Usually in pyrolysis, the size of biomass particles also determines the degree of conversion to biochar, its reactivity, surface area, and chemical composition. In our case, the size of CRD wood particles taken for pyrolysis in the horizontal tube furnace reactor is over 3 mm but less than 2.5 cm. Smaller particle sizes enabled complete volatilization of biomass organics under slow heating rate making sure the heat was pervasive from the boundary layer towards the core of each particle. In fact, Patel and Panwar, 2024 mentioned that small to intermediate biomass particle size with low initial moisture witnessed quick heat transfer and reasonable biochar yields. Our work has shown a 20-30% average yield of biochar that is comparable to studies which adopted similar pyrolysis temperatures, indicating an apt particle size range was chosen. Successful conversion was confirmed by the visual appearance of biochar and its crisp nature. This uniform pyrolysis supports the development of micro and

mesopores (Maziarka et al., 2024). Xu et al., 2024 stated that biochar, if densified and retrieved in small particle sizes, it could be useful as a metallurgical reductant where smaller particle sizes promoted strength, reduced porosity (increasing particle and bulk density), and controlled reactivity under thermally degrading atmospheres, all of which reinforce its applications in smelting processes. There existed some biochar particles showing lower surface area owing to their micro-to-mesoporous nature which could be useful for wastewater treatment and recovery of nutrients (Bian et al., 2024). Sometimes, bigger pores also facilitate heavy metal entrapments within biochar. For carbon sequestration, the porosity of biochar particles is not the major deciding factor, rather, it is the physicochemical properties like FC, VC, carbon content, and other stability indices. However, high pyrolysis temperature CRD chars showed both, *i.e*, good stability indices as well as increased surface area and pore volume. Here, the large surface availability for oxygen, air, moisture or other reactive matter to be adsorbed over biochar can be balanced by its low reactivity (low H/C and O/C) and hydrophobicity. But from another perspective, many applications under industrial settings could probably benefit from larger particle size due to their structural stability in shear-intensive dynamic systems (Bian et al., 2024).

3.1.2 Evaluating the robustness of RSM model – statistical analysis, contour/3-D plots, and predicted versus actual value distribution

As examples for evaluating the robustness of the DOE, four biochar properties were chosen. Following the 16 experimental runs, estimating an interdependence between different pyrolysis parameters and their overall influence on exemplar biochar's properties like surface area, micropore volume, H/C, and O/C (indicating surface functionalities/polarities), was satiated through the polynomial equation with coefficients, ANOVA's p-value model significance analysis, and model fit. A summary of statistical results is tabulated in Table 10. Although, an elaborate perspective of these coefficients and statistical results have also been shared in Supplementary table 5 and Supplementary table 6. Next, surface and contour plots of two response variables - BET surface area and Van-Krevelen H/C index, are described also as examples with reference to the influence of independent pyrolysis variables. Finally, for all four aforesaid response or dependent variables, a comparison of theoretical and actual experimental results were evaluated to validate the predictability of the model.

For BET surface area and micropore volume, the RSM's CCD tool recommended quadratic models whereas for the other two response variables of H/C and O/C, it recommended the two-factor interaction models, to conduct statistical evaluation. In both cases, a synergistic influence of independent pyrolysis process variables is plausible. In all cases, a model's significance is determined using the 'p-value' parameter. If it is <0.05, the model is significant and the pyrolysis parameters, also referred here as independent variables, largely influence the responses either as single or combined entities. On that note, pyrolysis temperature shows a p-value <0.05 for all responses. Hence, it can be concluded that it is the most influential parameter. Whereas, BRT is significant only for the BET surface area and micropore volume and does not seem to significantly change the Van-Krevelen molar ratio. When BRT was increased beyond a certain point, we also observed a reduction in surface area and pore volume that could be due to pore rupturing and coalescence. Mass of feedstock does not affect any response variable singularly which is shown by insignificant p-values (>0.05). However, it manifests a combinatory effect along with BRT and also as a squared entity, on BET surface area and micropore volume (evident from the curvature of contour plots in Figure 14 (iv). It explains that when the mass of feedstock is higher or multiplied, the model detects an influential behaviour. Under higher loads, the model advises to prolong the BRT for complete pyrolysis and to maintain yields of biochar. For H/C and O/C, mass of feedstock along with pyrolysis temperature control the rate of volatilization and rearrangement of reactive surface groups on biochar (evident from the curvature of contour plots in Figure 14 (xii). Smaller biomass samples at higher temperatures experience homogeneous heat transfer without any restrictions under a thorough purge of inert gas to promote oxygen and hydrogen rejection reactions coupled with carbon retention. At higher feed mass, there is mass and heat transfer limitation which hinders pyrolysis reactions leading to longer volatiles residence time, inability for reactive volatiles to quickly escape the reaction chamber and finally, its settling or condensation over biochar that increases surface oxygen and hydrogen. This could form C-O-C and C=O species on char (Hu et al., 2024) raising its reactivity faster that is detrimental for carbon sequestration and metallurgical applications. This could lead to secondary reactions that may cause carbon loss as light gases via cracking (Saleem & Baig, 2018). So, a higher flow rate of inert gas with longer BRT and higher temperature will be necessary to bypass these externalities.

The model fit or model correlation, R^2, was over 0.90 for all chosen response variables and suggested that every regression model mapped out the outcomes precisely and with utmost desirability, rendering the analysis acceptable. This can also be observed from the "predicted versus actual" values plotted in Figure 15. Here, all points are scattered around extremely close to the reference line through origin with a R^2>0.90 suggesting

sufficient interaction between independent variables and an apt polynomial model chosen for representation. The equation for each regression model is as follows. In the following DOE model equations, a (-) sign displays an antagonistic influence and a (+) sign displays a synergistic influence.

BET surface area

$$= 84.6827A + 57.4696B - 23.4390C + 4.2486AB - 12.0859AC - 125.5880BC - 46.6398A^2 + 10.6473B^2 + 209.0550C^2 + 230.5000$$

Slow pyrolysis DOE model equation 1

Micropore volume

$$= 0.0425A + 0.0240B - 0.0086C - 0.0006AB - 0.0061AC - 0.0478BC - 0.0203A^2 + 0.0016B^2 + 0.0806C^2 + 0.1130$$

Slow pyrolysis DOE model equation 2

$$\frac{\mathbf{H}}{\mathbf{C}} = -0.2017A - 0.0224B + 0.0303C - 0.0075AB + 0.1497AC + 0.0153BC + 0.3136$$

Slow pyrolysis DOE model equation 3

$$\frac{\mathbf{O}}{\mathbf{C}} = -0.0829A - 0.0040B + 0.0121C - 0.0162AB + 0.1069AC + 0.0112BC + 0.0613$$

Slow pyrolysis DOE model equation 4

Choosing the best or optimum biochar production conditions is ultimately dependent upon the application under focus. Based on our findings, temperature can be underscored as the deciding pyrolysis parameter to have the most drastic influence on biochar properties. This can be confirmed by the Pearson's coefficient of correlation, p-value, and perturbation analysis (relatively steeper slopes observed for pyrolysis temperature) obtained from the DOE model. As a result, five biochar samples from the DOE, produced at temperatures spanning from 400-800 °C (B400-B800), are chosen randomly for further characterizations and scalability tests to study this parametric influence more precisely.

Table 10: Statistical significance results – Equation coefficients, significance of each independent variable (p-values – marked in bold green) on the nature of chosen response variables, and model-fit data are shared. Cells shaded in color grey are not accounted due to the type of applicable model

Response variable	A	B	C	AB	AC	BC	A^2	B^2	C^2	Intercept	Model type	Fit (R^2)	Lack of fit
BET surface area (m^2/g)	84.6827	57.4696	-23.4390	4.2486	-12.0859	-125.5880	-46.6398	10.6473	209.0550	230.5000	**Quadratic**	0.9724	Insignificant
p-values	**0.0010**	**0.0194**	0.3150	0.8474	0.7916	**0.0230**	**0.0034**	0.2764	**0.0119**				
Micropore volume (cm^3/g)	0.0425	0.0240	-0.0086	-0.0006	-0.0061	-0.0478	-0.0203	0.0016	0.0806	0.1130	**Quadratic**	0.9753	Insignificant
p-values	**0.0004**	**0.0214**	0.3844	0.9532	0.7546	**0.0358**	**0.0031**	0.6873	**0.0184**				
H/C	-0.2017	-0.0224	0.0303	-0.0075	0.1497	0.0153				0.3136	**Two-factor interaction**	0.9769	Insignificant
p-values	**<0.0001**	0.1099	0.1850	0.7145	**0.0038**	0.4522							
O/C	-0.0829	-0.0040	0.0121	-0.0162	0.1069	0.0112				0.0613	**Two-factor interaction**	0.9326	Insignificant
p-values	**<0.0001**	0.6894	0.4763	0.3198	**0.0059**	0.4779							

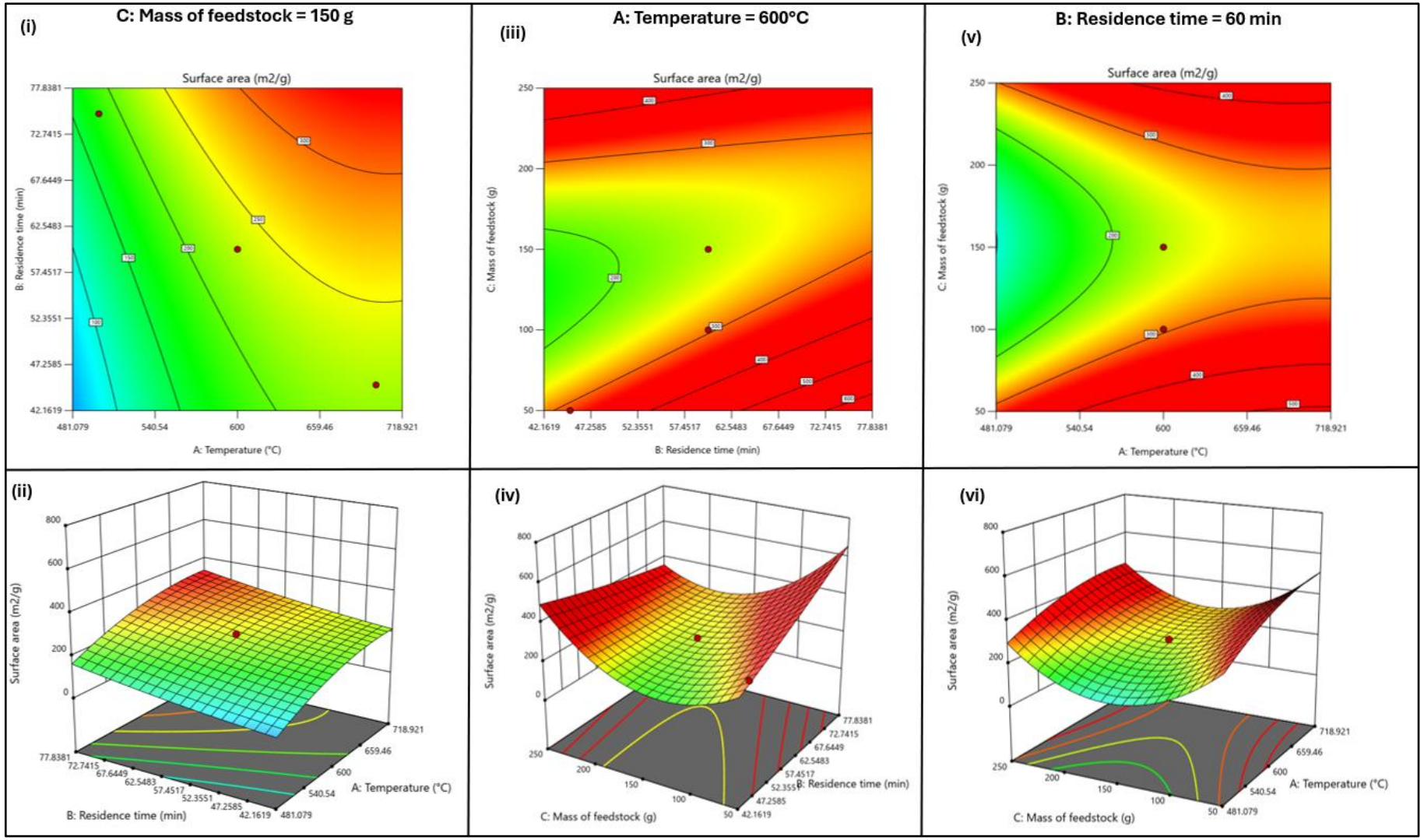
(i)
C: Mass of feedstock = 150 g
Surface area (m2/g)
B: Residence time (min)
A: Temperature (°C)
(iii)
A: Temperature = 600°C
Surface area (m2/g)
C: Mass of feedstock (g)
B: Residence time (min)
(v)
B: Residence time = 60 min
Surface area (m2/g)
C: Mass of feedstock (g)
A: Temperature (°C)
(ii)
Surface area (m2/g)
B: Residence time (min)
A: Temperature (°C)
(iv)
Surface area (m2/g)
C: Mass of feedstock (g)
B: Residence time (min)
(vi)
Surface area (m2/g)
C: Mass of feedstock (g)
A: Temperature (°C)

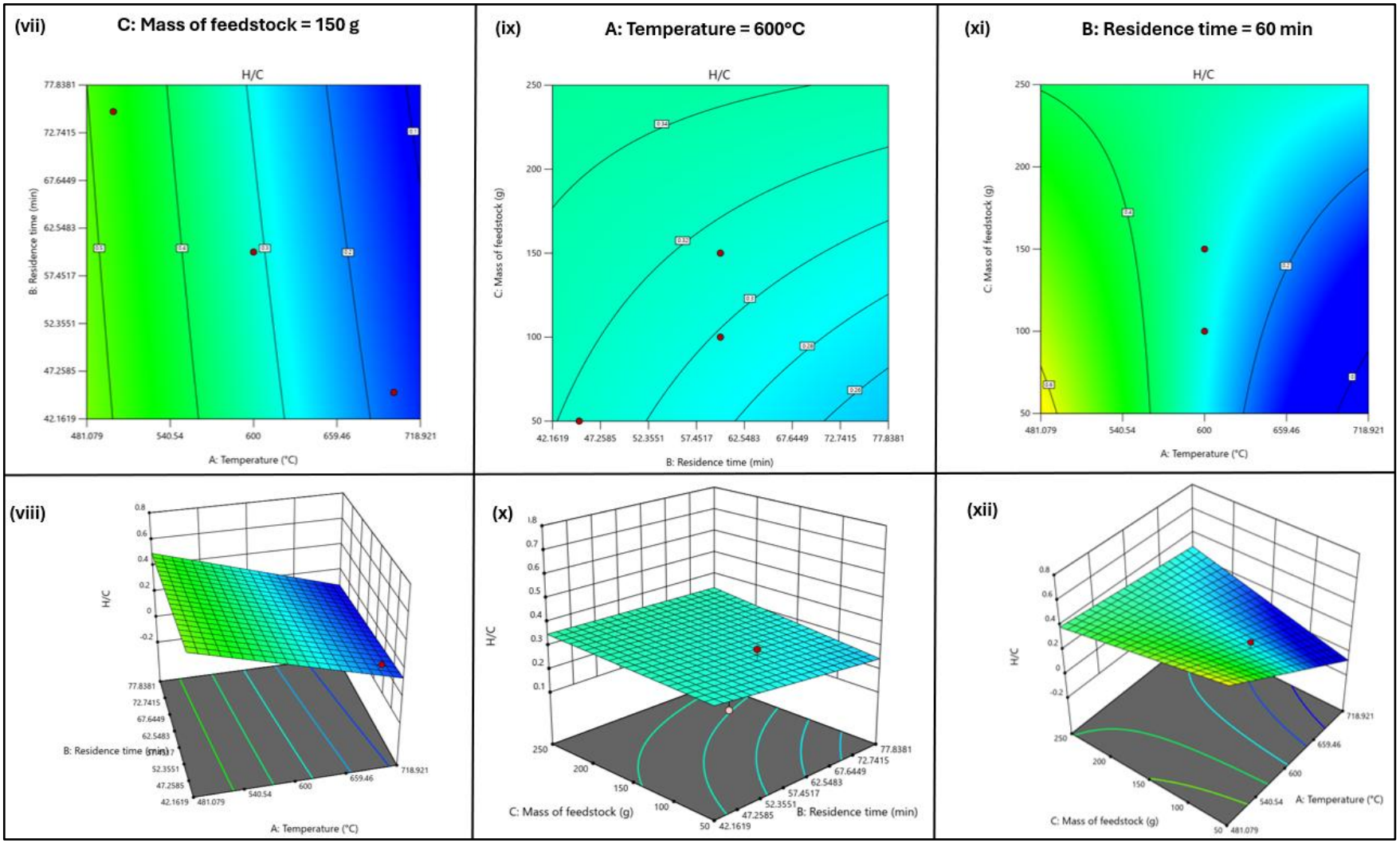

Figure 14: Surface and contour plots delineating the effect of temperature, residence time (BRT), and mass of feedstock on biochar properties. BET surface area (i-vi) and H/C (vii-xii). The 'red dots' represent experimental data points. The lowest to highest of values spread out from color blue to color red

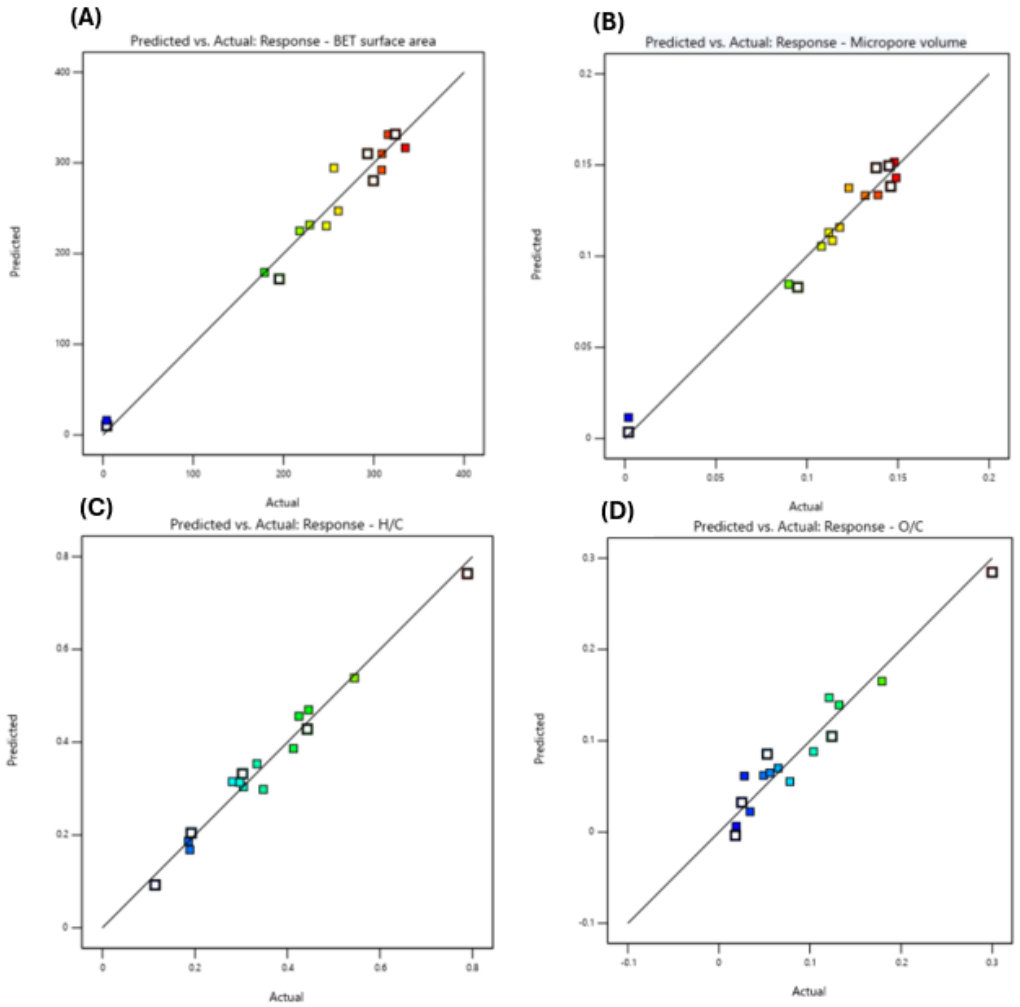

Figure 15: Predicted (y-axis) vs experimental/actual (x-axis) values for – (A) BET surface area; (B) Micropore volume; (C) H/C; and (D) O/C. Squares outlined in dark black represent B400-B800, spread across the reference line

3.1.3 Other characterizations for B400-B800 horizontal tube furnace reactor biochars

3.1.3.1 Thermogravimetric analysis (TGA)

The different patterns in weight loss observed during TGA of CRD wood and its biochars are influenced by pyrolysis conditions and feedstock composition. TGA (Figure 16 (A)) and DTG (Figure 16 (B)) curves offer insights on their thermal decomposition behaviour involving a cascade of intrinsic biopolymer (cellulose, hemicellulose, and lignin) degradation steps at specific ranges of temperature (Panizio et al., 2024). CRD wood has 70-75% holocellulose and 20-30% lignin just like most woody biomass. Overall, there are three distinct phases of weight loss expressed by the samples. The first phase between 0-150°C indicates highest weight loss of 2.38% for CRD wood and varied between 1.29-1.64% for B400-B800. This phase primarily involves dehydration reactions that remove moisture, light volatiles, and some extractives. B600-B800 typically showed some perturbations here that may have resulted due to adsorption of moisture and other labile surface species upon post-production cooling or storage. In the second phase, raw wood sample exhibited maximum weight loss of 66.95% due to hemicellulose and cellulose breakdown resulting in the loss of CO, CO_2, CH_4, and other lights gases that strip some biomass carbon. Release of these gases was observed when internal reactor temperature was between 200-325 °C and 325-400 °C. Significant weight loss in this second phase between 200-400 °C could be due to the release of carboxylic acids, furfural, volatile light oxygenates from hemicellulose, and levoglucosan, aldehydes, ketones, esters from cellulose. Here, pyrolysis oil and gas are produced. These findings can be validated by the first peak melting temperature for CRD wood in this band at 344.28 °C. A decreasing trend in weight loss from 27.53-1.87% from B400-B800 respectively, may mean that as charring intensified with heat treatment severity, the biochar product harbored less of these volatile organic compounds. Thus, only amorphous biochars like B400 with dense surface reactive species inclusive of oxy-radicals, showed a minor breakdown peak in this phase at

337.44 °C whereas the melting of other biochar structures with superior degrees of graphitization was pushed further to higher temperatures amidst the third phase. This finding can be projected from a concept discussed in Pei et al., 2023.

The third phase from 400-600 °C led to weight loss that could be due to lignin breakdown yielding several phenolic intermediates, simple aromatic hydrocarbons, and release of stable/entrapped volatiles over a wide range of temperatures. CRD wood decomposition showed a second peak here in its total curve at 481.76 °C with an additional 27.80% loss in weight. B400 also had its second breakdown peak here at 502.74 °C owing to greater ordered lignin presence, contributing to a 66.81% weight loss. From B500-B800, majority of decomposition took place between 513.91-597.13 °C that could be due to growing presence of condensed aromatics resistant towards collapsing. B500, B600, and B700 showed a weight loss between 88.17-90.39% whereas B800 underwent only 56.10% of breakdown due its rigid, non-breakable C-C, C=C, and C≡C bonds from dehydrogenation, cyclization, and aromatization reactions. It is between 600-900 °C where the rest of progressively graphitized B800 disintegrates causing a fresh 37.46% loss due to excess energy supplied to cleave the aforementioned linkages by overcoming activation energy barriers (Kim et al., 2024, Gonnella et al., 2022). From efficient pyrolysis, partly turbostratic transformations of in-bound carbon from an amorphous arrangement once seen at lower pyrolysis temperatures, could be a driving force behind this hyperstability. A similar concept was verified in Kim et al., 2024 and Gonnella et al., 2022. Whereas other biochars experienced weight loss of lower than 2.5% due to substantial conversion already accomplished in the earlier stages. Any residual weight around 900 °C is relayed to the relatively recalcitrant ash/inorganic constituents of biochars and biomass. From TGA, it is conclusive that higher temperature biochars display favourable properties for carbon sequestration and metallurgical applications.

3.1.3.2 TGA R50

Before calculating the R50 recalcitrance index, TGA curves are corrected for moisture and ash as shown in **Figure 16 (C)**. Based on these findings, the TGA R50 index increased proportionally from 0.39 for CRD wood, and 0.51 for B400 to 0.65 for B800 as in **Figure 16 (D)**, proffering its direct relationship with pyrolysis conditions (especially temperature) and also Van-Krevelen molar ratios. B800 showed the highest thermal stability due to maximum carbonization, FC, and low VC when pyrolyzed at 800 °C as observed from Babu et al., 2024. From Windeatt et al., 2014, looking at the R50 index, B400-B800 can be categorized among the minimally degradable biochars ($0.5 \leq R50 < 0.70$) that could have a longer lifespan in the environment if employed for soil-based carbon sequestration applications. Metallurgical applications could also benefit from this stability where biochar's shear/compressive/breakage resistance is key due to largely dynamic operations in smelters. Chen et al., 2025 showed higher R50 values with increase in pyrolysis temperatures due to the tendency of lignocellulose feedstock to form 'organo-metal/mineral' complexes (*e.g.:* Al_2O_3-O-C) that increases stability. CRD wood biochars possess Al and could very well show the same behaviour at higher treatment temperatures. On the other hand, high R50 values could mean low reactivity, unsuitable for soil amendments where biochar's interaction capabilities are valued more. Although, it is important to take note that R50 does not accurately specify how the arrangement or configuration of biochar organic carbon is but turns out to be just an auxiliary indicator of its overall degradation resistance.

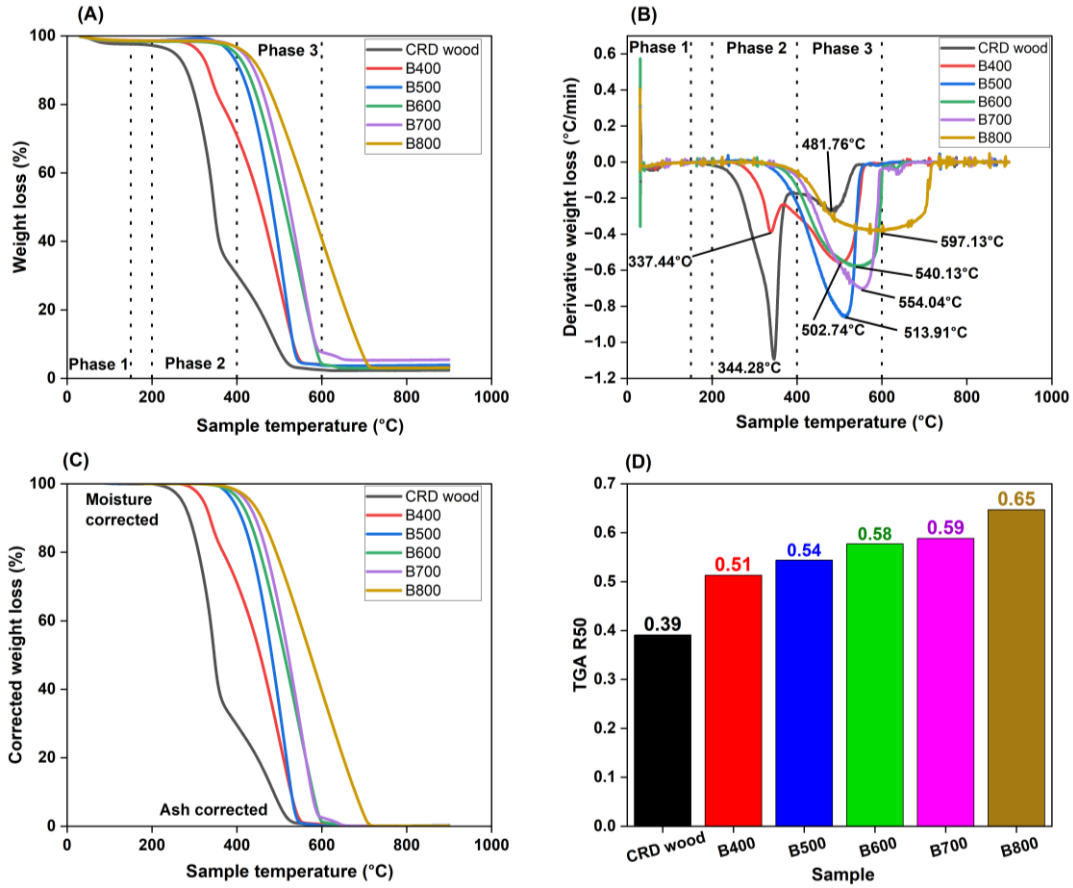

Figure 16: (A) TGA and (B) DTG curves; (C) moisture and ash corrected TGA curves; and (D) TGA R50 index variation with pyrolysis temperature: for B400-B800

3.1.3.3 Fourier transform infrared (FTIR) spectroscopy

FTIR analysis of CRD wood and B400-B800 revealed if there are any detectable changes to their chemical make-up through different functional group placements and their transformations as pyrolysis conditions differed. The intensity of these functionalities also described biochar's structural evolution and the associated implications on its properties. Peaks between 500-4000 cm^{-1} as in Figure 17 were matched and studied with the spectral database provide in Handiso et al., 2024 and Nicholas et al., 2022.

The hydrogen-bonded -OH group vibrations between 3200-3600 cm^{-1} showed the presence of moisture in CRD wood with intensities decreasing from CRD wood to B800 as a result of dehydration at higher temperatures. Next, a similar trend in perturbations across the band 3020-3080 cm^{-1} show C-H vibrations associated to aromatics. Maximum disturbance is for CRD wood with the highest amorphous carbon content available to undergo aromatic transformations. Then, B400-B600 manifest minor ramps indicating gradual cyclization of inherent organics. At higher temperatures, when aromatization is being soundly established, these vibrations disappear. However, McCall et al., 2024 stated that these vibrations are not the only deciding factor for qualifying the extent of crystallinity/graphitization in biochar. Between 2840-3020 cm^{-1}, C-H vibrations in aliphatic monomers take over and embrace intensity reduction from CRD wood towards B800 (Matin & Aydin, 2022). Such vibrations are common when simple hydrocarbon chains experience dehydration, demethylation, and condensation reactions originating from the terminal methyl ($-CH_3$) and methylene ($-CH_2$) groups of less stable holocellulose undergoing depolymerization. This is in line with the findings in Nicholas et al., 2022. It also means, the biochars like B400 and B500 witnessed incomplete decomposition and may still hold significant volatiles (can be seen from their high VC, O/C, and H/C).

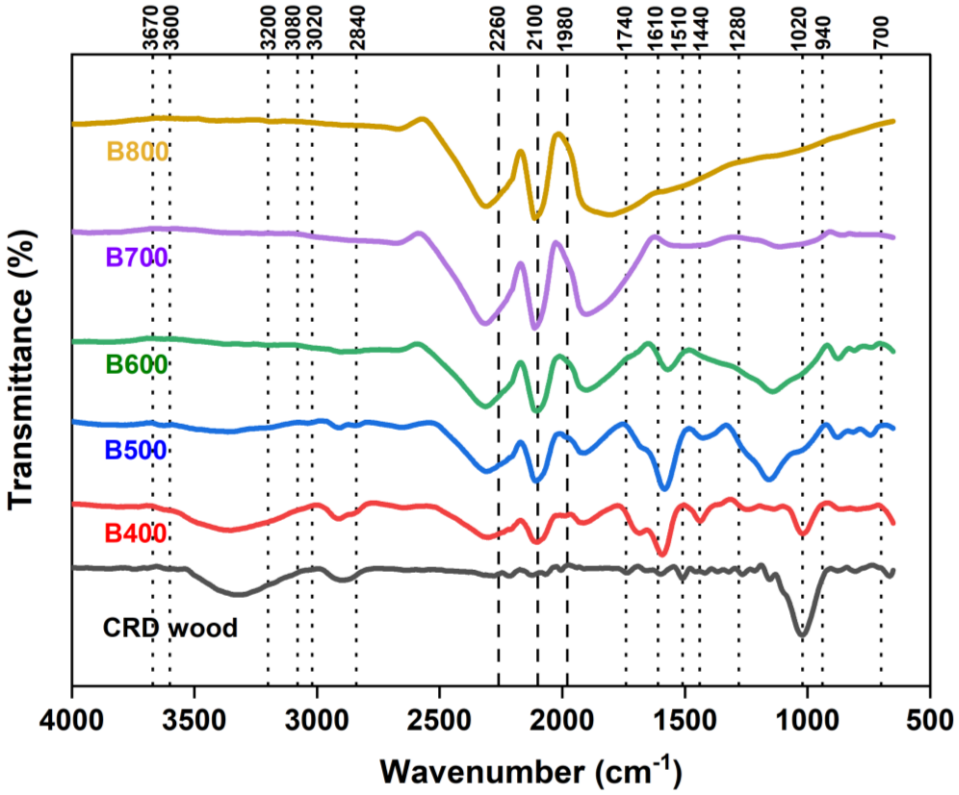

Figure 17: FTIR spectra for B400-B800

The region between 2100-2260 cm^{-1} depicts C≡C alkyne stretching vibrations as in condensed polyaromatics that is positively correlated with pyrolysis temperature (Handiso et al., 2024). The increasing trend of this structural transformation is thus, seen from B400-B800 when aromatic ring clusters also increase. Around 2250 cm^{-1} is also where C≡N stretches appear that grows from CRD wood to B800 suggesting the presence of polar nitrile groups which contribute to structural rigidity. Amidst 1740-2100 cm^{-1}, firstly the C=C=C allene functionality is clearly seen with increasing appearance from B400-B800 signifying strain propagation in certain carbons during graphitization, due to the localized unnatural adjacent dienes. This stretching vibration was also seen in Handiso et al., 2024. Then, C=O stretching vibrations increasing with temperatures due to breakdown of lignin, is more prominent due to high energy supplied during pyrolysis. Lignin carbonyls between 1610-1740 cm^{-1} (McCall et al., 2024) faded from B400-B800 due to prior breakdown in higher temperature chars. This carbonyl group can be found in decomposition products such as aldehydes, carboxylic acids, ketones, and esters (Nicholas et al., 2022, Handiso et al., 2024).

The band 1510-1610 cm^{-1} saw C=C stretching which is a sign of carbon ring formation. B400-B600 showing holocellulose breakdown have the maximum intensities where deprotonation of the structure is taking its due course and is truncating biochar hydrophilicity whilst increasing its hydrophobicity. The region in 1440-1510 cm^{-1} depicts aromatic skeletal vibrations during the earlier stages of pyrolysis where oxygen and hydrogen are lost as gases. The C-OH stretching and O-H bending vibrations in 1280-1440 cm^{-1} relate as a foundation for the formation of biochar's aromatic backbone. Decreasing intensities from CRD wood to B800 between 1020-1280 cm^{-1} show C-O/C-OH/C-H stretching and C-O-C skeletal vibrations in polysaccharides hinting at distortions within amides and esters upon decomposition of hemicellulose and unstable cellulose fractions in lower biochars (Zou et al., 2024, Matin & Aydin, 2022). Such volatile groups in B400 and B500 are reasons for their high CEC, as shared in Roshan et al., 2023. Lastly, 700-840 cm^{-1} is linked to volatile surface acidic functionalities that are removed upon increasing temperature.

3.1.3.4 Scanning electron microscope – energy dispersive x-ray (SEM-EDX) spectroscopy

Surface morphology analysis for B400 [Figure 18 (A)(B)(C)], B600 [Figure 18 (D)(E)(F)], and B800 [Figure 18 (G)(H)(I)] was carried out with SEM at three different maginifications of 250X, 500X and 1000X, without any gold sputtering procedure for conductivity enhancements.

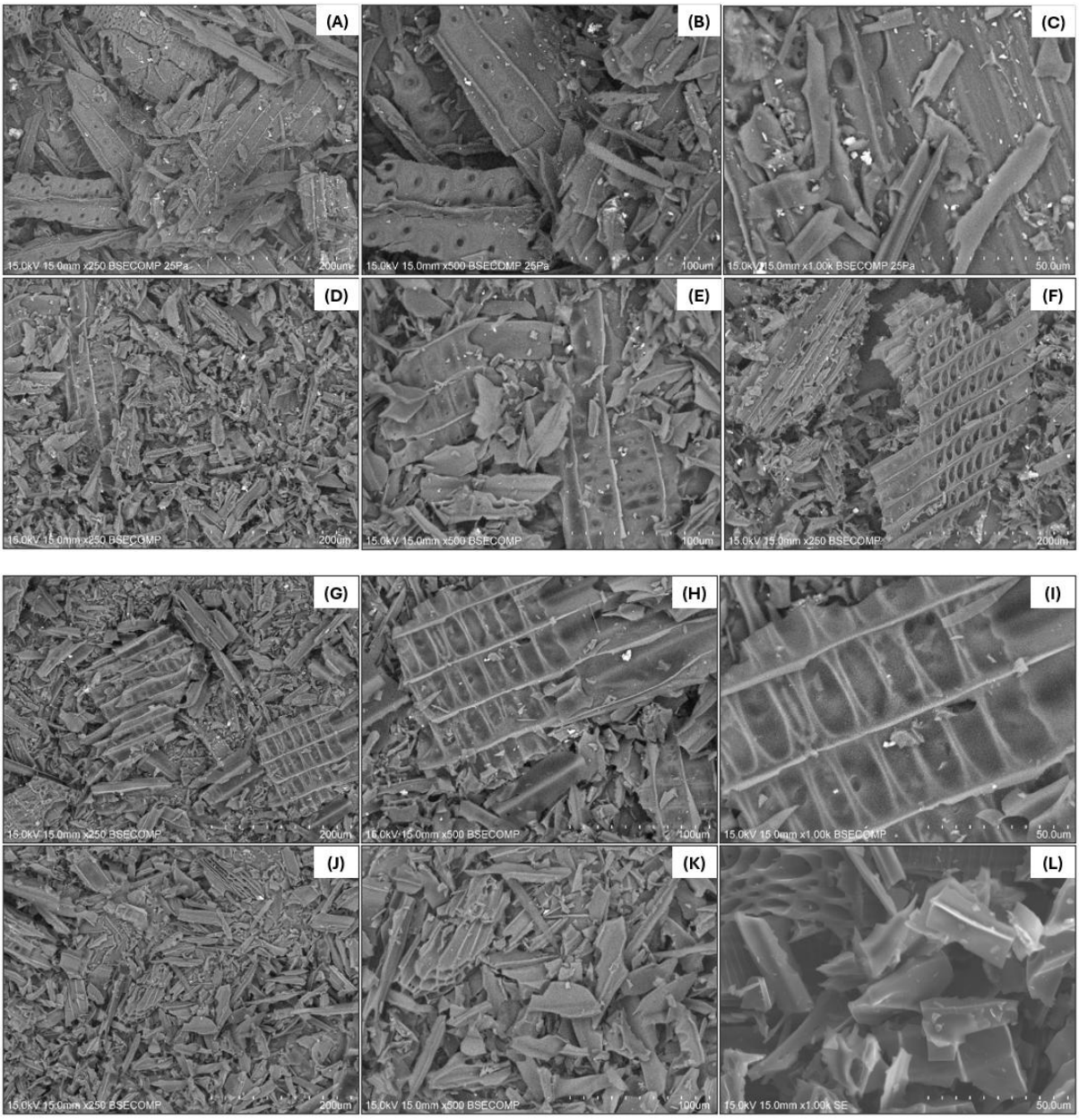

Figure 18: SEM micrographs of B400 (A)(B)(C); B600 (D)(E)(F); B800 (G)(H)(I); B600 in dye adsorption application (J)(K)(L) at 250X, 500X, and 1000X magnifications

Partly smooth surfaces were seen only at higher pyrolysis temperatures whereas lower temperatures showed severe roughness with scales and bumps that are uneven leftovers from partially altered biomass structures like cell walls and fibres. Micrographs for B400 show the creation of very minimal porosities since at this temperature, only hemicellulose and parts of cellulose could have been fractured, decomposed, and released intermittently as volatiles with most or all of lignin remaining intact. This may be contributing to a few sporadic macropores in biochars as stated in Patel & Panwar, 2024 and hence, could be deemed fit for use in soil amendment applications ascribed to the water-holding and aeration capacities supplemented by its favorable atmosphere towards microbial growth (Shaaban et al., 2014). There have been cases of using lower temperature chars as additives in anaerobic digestion experiments to increase methane yields (Świechowski et al., 2022). Oxidative remnants will still be present over the biochar surface that contribute to its reactivity. Dhar et al., 2022 underscored that such biochars will make good solid fuels too, for energy purposes.

At an intermediate pyrolysis temperature, B600 developed more defined pores as in Figure 18 (F) where lignin softening, melting, and breakdown is in due course after biomass's native holocelulose decomposition (Salinas-Farran et al., 2024). Some depolymerization steps here, could witness cross-linking of monomers that increase

solid char yield (Das et al., 2021). Faster release of volatiles with collapsing cell walls resulted in expansion of uniform, ordered porosities causing shrinkage in structure and growth of FC-dense layers, especially with increase in BRT (Dhar et al., 2022). Thus, as pyrolysis temperatures approached 600 °C, pore sizes diminshed (Clarke & Olea, 2024). Surface area and thermal maturity of this biochar makes it suitable for carbon sequestration, metallurgical, and adsorption applications (*e.g.*: dyes, heavy metals). Since acidic functionalities are also being lost, the pH becomes alkaline and the biochar can then be used to treat acidic soils (Dhar et al., 2022). Lastly, at higher temperatures as for B800, smooth honeycomb-like frameworks Figure 18 (I) appear due to complete carbonization and elimination of surface volatiles under low heating rates. High carbon content, TSF (low VC/FC ratio) and low H/C, O/C form thermally and oxidatively recalcitrant graphitic carbon sheets making this biochar ideal for use in energy materials (*e.g.:* supercapacitors, electrodes) and once again for carbon sequestration with even higher permeance this time. The same trend with increasing pyrolysis temperature was affirmed by Ma et al., 2016. From Nkomo et al., 2021, an expansion in pore size is possible, probably due to cracking of micropore walls to conjointly form mesopores (heterogeneous porosity) upon coalescing, reducing surface area and micropore volume as recorded in our case for B700 and B800.

Pore blockage could also be a possibility with increasing concentrations of ash inorganics including AAEM that reduce active site surface availability till a specific range of temperature prior to their volatilization (for less stable, monovalent AAEM like Na and K) at even higher temperatures due to pore reaming. The surface elemental analysis using SEM-EDX spectra is depicted in Figure 19, that could confirm presence of such AAEM on the biochar surface.

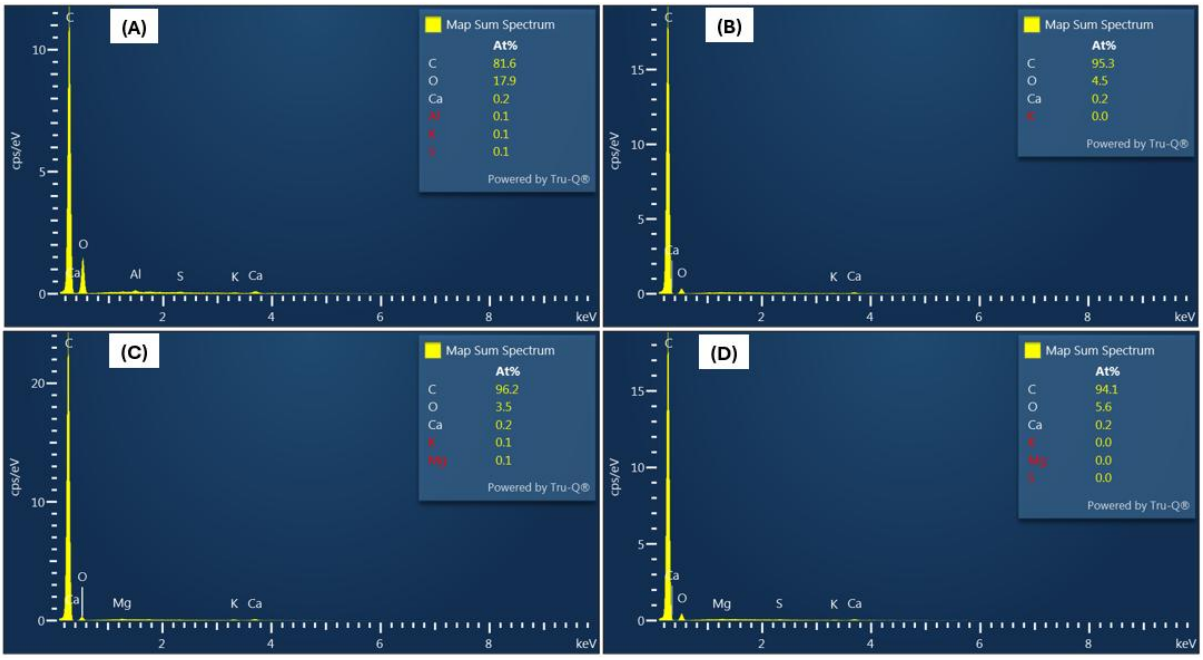

Figure 19: SEM-EDX surface elemental analysis: (A) B400; (B) B600; (C) B800; and (D) B600 in dye adsorption application

From Figure 19 (A)(B)(C), B400, B600, and B800 showed an increase in surface carbon content from 81.6%, 95.3%, to 96.2%, respectively (Ma et al., 2016). Surface oxygen content dropped by about 80%, thus showing a negative relation with pyrolysis temperature. EDX peaks also confirmed the surface presence of AAEM like Ca, K, Na (0.2-0.4% totally) with higher pyrolysis temperatures that could form inorganic metals salts (carbonates, oxides, chlorides) raising the overall pH of biochar and improving its CEC that could support electrostatic attractions (Suárez-Hernández & Barrera-Zapata, 2017). These were distributed across the biochar surface, near, and over the pores (Sharma & Ratner, 2021). Presence of sulfur, part of gypsum dry walls in CRD wood residues, is seen initially for B400 at 0.1%, that in later cases would have been volatilized as SO_x. To conclude, morphology of biochar is highly variable and can be tuned w.r.t biomass feedstock composition (with pre-treatment too) and pyrolysis conditions adopted that directly impact its end-uses in environmental, energy, and agricultural applications.

3.1.3.5 Raman spectroscopy

Raman spectroscopy was used to identify any transformations from amorphous carbon to crystallinity within biochars via deformations experienced during variations in pyrolysis temperatures from 400-800 °C. The spectral bands for biochars are shared in Figure 20.

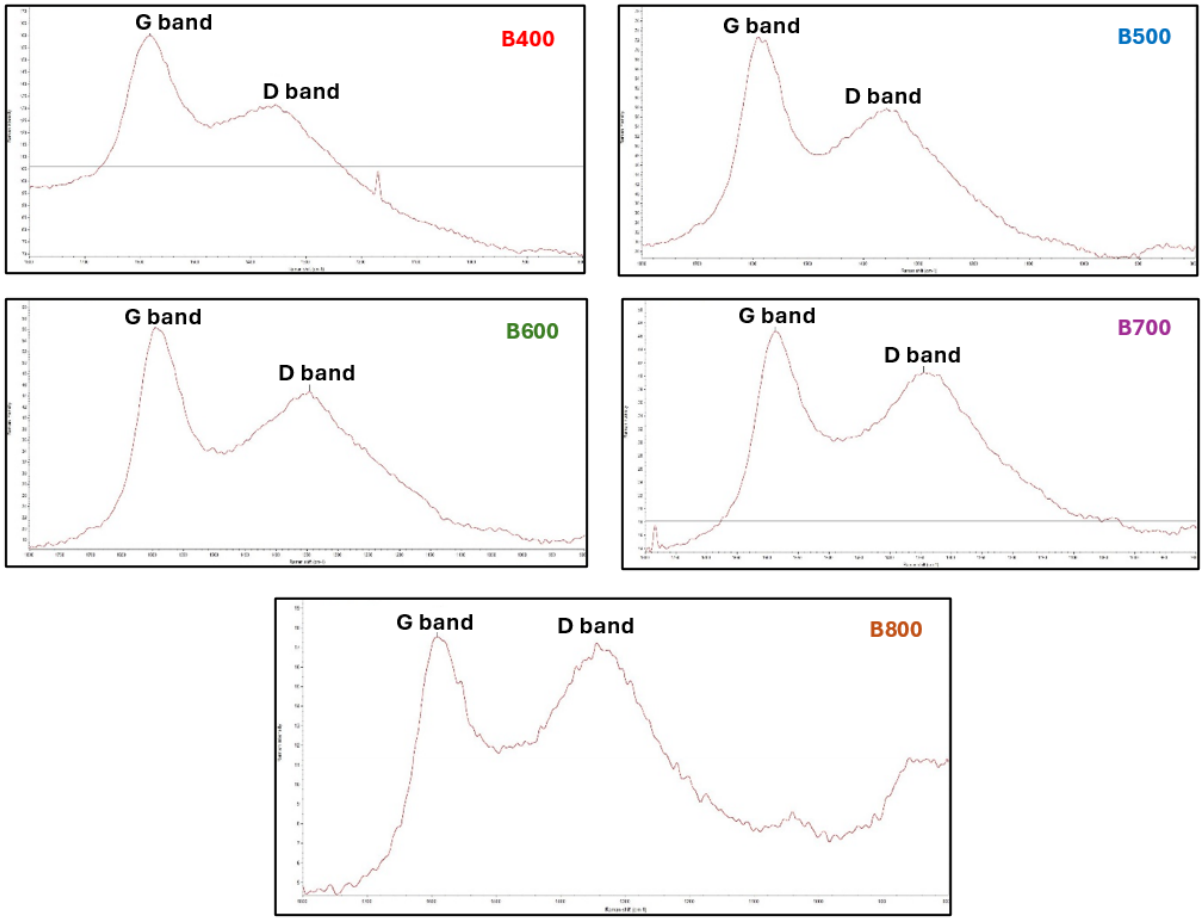

Figure 20: Raman spectra for B400-B800. Peak positioning from right-to-left on x-axis (800-1800 cm^{-1}): B400: D band: 1355.63 cm^{-1} and G band: 1581.92 cm^{-1}; B500: D band: 1358.55 cm^{-1} and G band: 1590.43 cm^{-1}; B600: D band: 1345.67 cm^{-1} and G band: 1595.96 cm^{-1}; B700: D band: 1345.52 cm^{-1} and G band: 1587.93 cm^{-1}; B800: D band: 1344.82 cm^{-1} and G band: 1592.10 cm^{-1}

The degree of graphitization achieved is quantitatively communicated via the I_D/I_G index, *i.e*, the ratio of intensity in deformations or disorderliness in amorphous carbon (D-band) to that of quantity of graphitic carbon structures (G-band). Higher this ratio, higher the deformations experienced by amorphous structural carbon during pyrolysis, to witness a shift towards turbostratic carbon arrangement (Grimm et al., 2025). Largely stable carbonaceous materials like graphite or graphene have very low I_D/I_G suggesting that they possess a well-developed crystalline framework already in place, and only negligible or weak defects lingering about its lattice (Makowska & Dziosa, 2024). From the peak intensities for D-bands and G-bands, I_D/I_G indices were calculated to be between 0.78-0.97 for B400-B800. Thus, increasing heat treatment increases defects that point towards the degree of unstable amorphous carbon presence or incomplete graphitization in biochar, a trend also observed in Makowska & Dziosa, 2024. In fact, Senapati et al., 2025 stated that such profound defected areas in amorphous carbons, common in biochars from lower pyrolysis temperatures, are due to functional groups like hydroxyls and carboxylic acids that tend to harbor good adsorption properties. I_D/I_G actually increases till all loosely-arranged carbon in biochar is ordered similar to the sp^2-hybridized/bonded structural carbons as in graphite. In other words, until complete decomposition of biomass polymers ceases, I_D/I_G will show positive relation with pyrolysis temperature. This is where Grimm et al., 2025 tested the presence of chemical activators like sulfur and boron with biochar which have the tendency to localize interstitially within biochar and reduce the activation energy barrier required for the transformation of its unstable lattice to a crystalline lattice, even at temperatures below 1000 °C (that would otherwise, be possible only above 2000 °C).

There may come a point where I_D/I_G would not increase further followed by a downward trend suggesting that almost all carbon in biochar is graphitized with aromatic ring clusters (Pei et al., 2023). At this stage, biochar could be perfectly suitable for carbon sequestration even in highly-sensitive biotic and abiotic environments. Due to dense carbon, they could be suitable as catalysts too, possessing electron transfer capabilities (Pei et al., 2023). With such high thermal stability, they could be used in ultra-high temperature settings as in blast furnaces as a partial coke substitute due to high mechanical strength, controlled reactivity, and low oxygen content (premature reactivity avoided). Here, heat-labile inorganics in biochars can also be eliminated gradually at very high pyrolysis temperatures thereby, reducing ash content and volatiles. In fact, coal wastes like gangue resulting from mining operations have also been used as co-substrates for lignocellulosic biomass pyrolysis as in Chen et al., 2025, to boost Raman I_D/I_G between 0.5-0.8 with increasing pyrolytic temperatures.

3.1.3.6 Metal content

AAEM in biochars were concentrated till 600 °C at 92.28% after which it may have decreased due to volatilization. Relative to CRD wood, AAEM is higher in all biochars due to shrinkage in biomass volume (loss of volatiles) and breakdown of organo-metallic linkages with increasing temperatures (Marmiroli et al., 2018). Non-volatile trace metals like Fe, Cu, Cr, Zn, Ni, Pb, Co, and Cd are present in varying percentages that could be explained by advanced treatments that these CRD wood residues were subjected to initially (*e.g.*: chromated copper arsenates or ACC) during their applications in regional construction projects such as houses, electricity poles, piers, and bridge components. That is why treated wood as in CRD wood waste, if openly burnt for energy purposes, will be classified hazardous in nature according to the United States Environment Protection Agency (USEPA) (Robey et al., 2018). From Lin et al., 2025, the upper and lower limits of some metallic constituents in biochar are mentioned in **Table 11**. In B400-B800 evaluated here, it is conclusive that hazardous metal content is within the prescribed range and meets the stipulations set forth by renowned biochar standards like that of International Biochar Initiative (IBI), European Biochar Certificate (EBC), Australia New Zealand Biochar Industry Group (ANZBIG), Biochar Quality Mandate (BQM), and Singapore standard SGS). Metals below detection limits in the CRD wood and its biochars were Hg, As, and Se. Also, Fe was the most present metal (non-AAEM entity) in CRD wood (16086 mg/kg) and its biochars (B400: 15546 mg/kg to B800: 16699 mg/kg) due to the presence of embedded remnants of nuts, bolts, nails, and joints, once part of the feedstock before disassembly or demolition.

3.1.4 Qualifying B600 as an adsorbent material for dye removal tests from contaminated water

B600 was chosen as the adsorbent for adsorption of methyl orange-borne water. Despite another biochar produced at the same temperature range (**Run 8**) that harbors relatively higher surface area and micropore volume, B600 is superior in terms of carbon, hydrogen, and oxygen content, FC, H/C, and O/C, which are also important adsorption properties suggesting hydrophilicity, chemical/thermal stability, and capability to form electrostatic, covalent, and/or hydrogen bonds via surface functional groups, that are necessary for water-based applications under varying temperatures and pH. A similar finding was seen from Teweldebrihan & Dinka, 2024, who stated that biochar surface area is not the only deciding factor for its adsorption performance. Moreover, methyl orange is a polar dye that could dissolve in polar solvents such as water. Hence, biochar's reactivity towards water needs to be enhanced and will be leveraged using its hydrophilic nature. Additionally, since methyl orange is anionic, biochar's positive surface charge indicated by at least satisfactory H/C could be beneficial to faintly minimize repulsive forces between negatively charged biochar functional groups and methyl orange. Further other biochar candidates, higher pyrolysis temperatures in the case of B700 and B800, reduced H/C and O/C making these more hydrophobic that may be effective in the adsorption of hydrophobic pollutants in wastewater. As a matter of fact, B600 does not compromise on surface area either, since it displays the second highest value (only second to Run 8 at 334.89 m^2/g) across the DOE, recorded at 323.78 m^2/g, that too, even without any chemical, physical, thermal or mechanical activation process. Related to activated biochars, its surface area is still low and a borderline-micromolecule like methyl orange (lower than 10 nm in size) may depend on dense micro-mesoporous channels for adsorption as in some minerals too (Wu et al., 2021). There is a possibility that if a pore-filling mechanism during adsorption takes place, and if the porosity of biochar is too high, desorption of the dye molecules may occur!

Table 11: Metal content in B400-B800 and the permissible limit set by IBI

Sample	Al	Ba	Ca	Cd	Co	Cr	Cu	Fe	K	Mg	Mn	Mo	Na	Ni	Pb	V	Zn	Total	AAEM	AAEM
	mg/kg	mg/kg	mg/kg	mg/kg	mg/kg	mg/kg	mg/kg	mg/kg	mg/kg	mg/kg	mg/kg	mg/kg	mg/kg	mg/kg	mg/kg	mg/kg	mg/kg	mg/kg	mg/kg	%
CRD wood	**12043**	**1165**	**149284**	**2**	**69**	**86**	**613**	**16086**	**38043**	**17566**	**5587**	**24**	**37685**	**5**	**561**	**21**	**1389**	**280229**	**243742**	**86.98**
B400	7707	1949	163961	2	58	79	5777	15546	49507	17794	6799	21	37901	41	381	17	1484	309026	271113	87.73
B500	4273	1554	143017	4	57	112	300	8861	36641	15503	7649	<2	44478	17	450	11	1924	264852	241194	91.07
B600	3505	1834	165480	11	51	179	237	11898	68529	20299	7576	<2	41471	92	296	13	1038	322507	297612	92.28
B700	8856	1900	161627	9	39	179	231	10387	38942	15529	3883	11	23800	104	210	24	1316	268940	241797	89.91
B800	9680	3889	167379	14	60	318	2297	16699	44660	20019	8303	19	26990	82	225	27	76	300738	262938	87.43
IBI (low)				**0.3**		**15**	**40**					**10**		**10**	**10**		**150**			
IBI (high)				**39**		**1200**	**6000**					**75**		**600**	**500**		**7400**			

3.2 CRD wood pyrolysis in horizontal rotary retort-furnace reactor – A scale-up from horizontal tube furnace reactor

The same batch of contaminants-separated, dried, and size reduced CRD wood, from 3 mm to 2.5 cm particle size, were also subjected to scaled-up pyrolysis rounds in the horizontal rotary retort-furnace reactor. The exact conditions of temperature and BRT listed in the DOE for B400, B500, B600, B700 and B800 were followed for an approximate comparison against the tests conducted in the horizontal tube furnace. Since biochar properties were greatly influenced by pyrolysis temperature, the basis behind selection of these samples is to have an extended range covered w.r.t this parameter.

Note: Proximate and elemental analysis results for B400-B800 are tabulated in **Table 12**. It is to be noted that no other characterizations will be performed for scaled-up biochars. Advanced characterizations are performed only for biochars chosen from the horizontal tube furnace reactor.

Relative to the previous set of experiments, yields were more reliable this time, especially for B400 since biomass underwent complete pyrolysis. In fact, Altıkat et al., 2024 reported very similar biochar yields for pyrolysis temperatures of 400 °C (B400: 37.7%) and 600 °C (B600: 29.5%). The carbon content of B600-B800 here is about 5-7% lower, even though it showed positive relation with temperature (Pearson's coefficient, r = 0.99). This could be attributed to more feedstock mass processed in the rotary retort (3 kg) whereas only 50-250 g was pyrolyzed in the tube furnace, clearly pointing at a heat transfer limitation even with the rotations in place to avoid 'surface-only' heating. There could be two other reasons for this turn of events: a) carbon loss due to secondary cracking reactions originated from condensed volatiles (even with a vacuum suction unit fixed at the exit gas zone) due to low sweeping flow rate of inert carrier gas; b) infiltration of ambient air into the reactor due to improper sealing causing mild combustion. But there was no alarming rise in ash levels since they were found to be similar with the tube furnace tests at higher temperatures. Although, H/C and O/C are slightly higher for B600-B800 suggesting some presence of hydrogen and oxygen-rich superfacial volatiles. Nevertheless, these indices are well under the prescribed limits and show excellent carbonization with aromaticity in these biochars, *i.e.,* a negative relation with temperature (Pearson's coefficient, r, for O/C: -0.99 & H/C: -0.98).

From Lin et al., 2025, O/C<0.2 and H/C<0.4 for CRD wood biochars here, obtained at higher pyrolysis temperatures, rank them as superior grades with less VC and other volatiles, high FC, good aromatization, and longer persistence in soil and carbon sequestration applications if used appropriately. Resistance to oxidation, hydrophilic interactions, and microbial degradation may also be achieved since the Van-Krevelen parameters for CRD wood biochars obey the above criteria. The IBI states that it is now better to use the index H/C_{org} in place of H/C since carbon content as a whole will also include inorganics like carbonates in the ash fraction and not be selectively describing the organic carbon aromatics of interest in biochar which is the baseline condition for any thermochemical conversions to have taken place relative to the original biomass feedstock (International Biochar Initiative, 2015). Next, the proximate parameters of FC (up by 15% from B400-B800) and VC (down by 53% from B400-B800) also improved drastically with temperature and follow the same trajectory as previous tests. Pearson's coefficient, r, for FC and VC showed a positive and a negative relation with pyrolysis temperature at 0.98 and -0.99, respectively. TSF is boosted as well (by 19%), thereby, showing signs of carbonaceous biochars gaining thermally stability (Pearson's coefficient, r = 0.99). HHV for B400-B800 also was in the path of the previous tests ranging from 29-32 MJ/kg underscoring its applications in energy and metallurgy.

Table 12: Yield, proximate, and elemental analysis results for B400-B800 in the horizontal rotary retort-furnace reactor. The prefix 'R' indicates 'rotary retort-furnace' unit

Sample	N (wt%)	C (wt%)	H (wt%)	S (wt%)	Ash (wt%DB)	O (wt%)	H/C	O/C	VC (wt%DB)	FC (wt%DB)	TSF (%)	Yield (%)
RB400	0.650	78.380	2.887	0.184	2.640	15.259	0.442	0.146	26.739	70.621	72.536	37.700
RB500	0.380	80.580	2.489	0.089	4.120	12.342	0.371	0.115	23.451	72.429	75.541	32.100
RB600	1.150	81.690	2.410	0.372	4.050	10.328	0.354	0.095	17.992	77.958	81.249	29.500
RB700	0.580	83.790	2.149	0.114	5.970	7.397	0.308	0.066	14.858	79.172	84.199	27.900
RB800	0.740	85.610	2.042	0.133	5.820	5.655	0.286	0.050	12.613	81.567	86.608	26.200

Overall, B400-B800 and RB400-RB800 showed good relatability in terms of proximate, elemental properties, and a similar dominant effect from pyrolysis temperature. Future studies entailing pilot-scale conversions can thus, be recommended, where at least 15-20 kg of CRD wood can be treated at once via batch pyrolysis.

3.3 The effect of feedstock composition and pyrolysis process parameters on biochar properties - comparison to similar works

The physicochemical properties of biochar are mostly determined by the composition of biomass and pyrolysis conditions employed. Understanding their relationships is necessary to optimize biochar for different applications as in carbon sequestration, metallurgical reductants, pollutants removal or adsorption. Lignocellulosic biomass feedstock like forest wood (even in CRD wood) and crop residues give rise to biochars with good carbon content and improved stability owing to their lignin, cellulose, and hemicellulose distribution that vary in molecular weight and decompose steadily over a wide temperature window (Conz et al., 2017). For example, Choudhary et al., 2019 discussed that biochars which are derived from cellulose-based feedstock tend to possess higher volatiles and lower carbon compared to lignin-rich feedstock, that could reach a carbon content of 80% and even greater. Other feedstock like algae yield less stable, low-quality biochar with irregular porous frameworks, low surface area and carbon content due to their inherent nitrogen, phosphorous, sulfur, trace elements, and inorganics (Yu et al., 2017). That is why co-pyrolysis methods can attenuate limitations from single-source feed materials. Blending poorly-performing feedstock like biosolids, with superior feedstock like lignocellulose, have improved elemental composition, surface area (300-400 m^2/g), porosity, and entrapment of vital minerals in biochar (Rathnayake et al., 2023).

Among pyrolysis conditions, temperatures over 500 °C reduce biochar yields, increase stable aromatics, carbon content, hydrophobicity, and also surface area (Crombie et al., 2013). This was observed in our case with B600, B700, and B800, respectively. Temperatures even close to 700 °C with surface treatments (*e.g.*: amination) derive heterogenous porosity (from some ruptures) that is advantageous for the adsorption of different pollutant gases (Chatterjee et al., 2020). Whereas lower temperature (below 400 °C) biochars gain nutrient retention capabilities as well as low/slightly acidic pH (Antonangelo et al., 2019). Also, at these temperatures, presence of hydrophilic domains inclusive of oxygenated functional groups may increase water retention capacities of biochar (Ferraro et al., 2021). The latter property is also supported when there is good porosity in biochar at higher temperatures. An increase in surface area from 150 m^2/g at 300 °C to over 500 m^2/g at 700 °C was seen according to Tomczyk et al., 2020 and Mukherjee et al., 2022. But identical to our findings related to CRD wood pyrolysis, Venkatesh et al., 2022 stated that temperatures between 450-600 °C could contribute to maximum microporosity and temperatures more than 600 °C showed bulk removal of volatile organics forming mesopores that could be useful in water filtration applications and as catalysts in chemical reactions entailing larger molecules. A decline in surface area was seen for biochars at 700 °C and 800 °C relative to 600 °C which validates this statement. Still, applications like metallurgical coal substitutes should fit well with such biochars considering their above par FC, low VC, high stability, and controlled ash levels.

Next, long BRT can lead to gradual heat transfer and complete carbonization of biomass that increase carbon content, yield, and develops uniform porosity without any drastic intra-particle explosions (Cimò et al., 2014). Here, the aromaticity index H/C decreased (below 0.3) indicating concentration of structurally stable carbon. A similar value of H/C was seen in Chatterjee et al., 2020 where carbon content reached 85% and over at temperatures of about 700 °C under long BRT. Kumar et al., 2024 demonstrated that lignin-rich feedstock, when pyrolyzed at higher temperatures, can yield a H/C below 0.2 and surface areas of about 500 m^2/g. Likewise, another Van-Krevelen stability index O/C reduced from approximately 0.5 at 350 °C to less than 0.2 at 700 °C signifying higher degrees of carbonization and removal of heat labile functionalities in the biochar product making it more resistant to chemical, thermal or microbial degradation (Chatterjee et al., 2020). Mariyam et al., 2023 found that long BRT of over 60 min also reduces H/C and O/C contributing to long-term sequestration of carbon. Proximate analysis of biochars from woody biomass produced at the same temperature revealed an increased in FC and reduction in volatiles (Ronsse et al., 2013). Conversely, shorter BRT of under 30 min resulted in high volatiles and low FC turning biochar only slightly stable but more reactive. Building on Antonangelo et al., 2019, high pyrolysis temperatures confer alkaline pH in biochars due to the volatilization of organic acids, protonic functionalities, and increased mineral salts content which may prove effective in treating acidified soils. High pyrolytic BRT with a slow heating rate especially in fluidized bed reactors with enhanced solid-gas contact, mixing, negligible temperature hot-spots, and tar/volatiles elutriation, can aid in biochar with superior morphological properties (Patel et al., 2019). Thus, whenever choosing the conditions for pyrolysis, there always exists a trade-off between different characteristics.

Thirdly, the amount of biomass fed to a pyrolysis reactor plays an important role in determining the properties of biochar. From our experimental investigations, it directly influences the intra and interparticle heat transfer efficiency and judges whether carbonization is achieved to fruition. Smaller mass of feedstock showed great

conversion and effective release of gases and volatiles (Nair at al., 2023). Smaller mass also leads to biochar with better porous frameworks under low heating rates, long BRT, and milder pyrolysis temperatures favoring moisture preservation, pollutant adsorption, and soil amendment properties (Zhang et al., 2023, Xiong et al., 2021, Kalina et al., 2022). Whereas larger particle size could lead to poor penetration and uneven heat transfer that could retain volatiles in biochar with underdeveloped carbon backbone. Thus, a comprehensive understanding of all these independent variables (pyrolysis temperature, BRT, heating rate, and mass of feedstock) and how they interplay is vital for optimizing biochar characteristics for specific applications under focus.

3.4 Methyl orange batch adsorption experiments – An application for CRD wood biochar from the DOE

As an application concerning a biochar from the DOE runs, adsorption experiments of an industrial dye methyl orange, from contaminated water, were carried out. Since B600 exhibited a balanced manifestation of both morphological and surface properties, along with adequate stability, it was used as the adsorbent at varying doses throughout these experiments.

3.4.1 Adsorption standard determination

To begin with, methyl orange indicator of a concentration 0.05 w/v, *i.e,* 0.05 g/100mL or 0.5g/L, was sourced from the institute's pulp and paper analytical laboratory. Using its molar mass as 327.33 g/mol, the molarity was found to be 1.5 mM. To make reference solutions totalling 10mL of varying concentrations for plotting the standard curve, the formula: $C_1V_1=C_2V_2$ was used. Here, C_1 is the concentration of methyl orange in the reagent bottle (mM), V_1 is the volume of methyl orange to be taken from this bottle to prepare the reference stocks (mL), C_2 is the concentration of the reference stock (mM), and V_2 is the total volume of the stock solution to be prepared (mL). Five stock concentrations of 0.001, 0.01, 0.0175, 0.025, and 0.0375 mM, were prepared followed by UV-visible-spectrophotometer (HACH – DR 6000) absorbance measurements at 464 nm (alkaline, pH≥4.4, indicated by orange color) or 506 nm (acidic, pH≤3.2, indicated by pink color). By fitting these data with Beer-Lambert's law, the intercept and molar absorptivity coefficient were calculated along with the model's correlation (R^2=0.9995).

3.4.2 Batch adsorption experiments

For the adsorption experiments (notable steps represented in Figure 21), 50 mL test solutions with different initial concentrations of the model pollutant dye (methyl orange) were prepared with deionized water as the solvent to rule out the effect of competing ions. All experiments were conducted in 250 mL reaction flasks, placed over a magnetic stirrer set at 300 rpm with the temperature controller. The 0.025 mM or 8 ppm and 0.5 mM or 164 ppm stocks, were two chosen (from similar studies) concentrations tested. Thereafter, other process parameters like adsorption pH (1-9), temperature (20-50 °C or 293-323 K), time (till 24 h), and adsorbent (B600) dosage (1-10 mg/mL test solution), were varied to analyze the dye removal efficiency and narrow down on optimal conditions. On the pH forefront, 0.1M H_2SO_4 and 0.1M NaOH were used as buffering agents. Before absorbance measurements, the test solutions were filtered at appropriate time intervals through a 0.45 µm syringe filter to separate B600 particles. Optionally, vacuum filtration with filter papers of similar porosity can be used. Upon coupling absorbance measurements from all experiments to the data computed from the absorbance standard, unknown (residual) concentrations of methyl orange in the test solutions followed by removal percentage, and the adsorption capacity were validated. Each adsorption experiment was carried out thrice and the mean values were reported.

The fundamental equations for removal percentage, adsorption capacity, kinetics, equilibrium models, and thermodynamics, can be referred from Supplementary equation 13 to Supplementary equation 34.

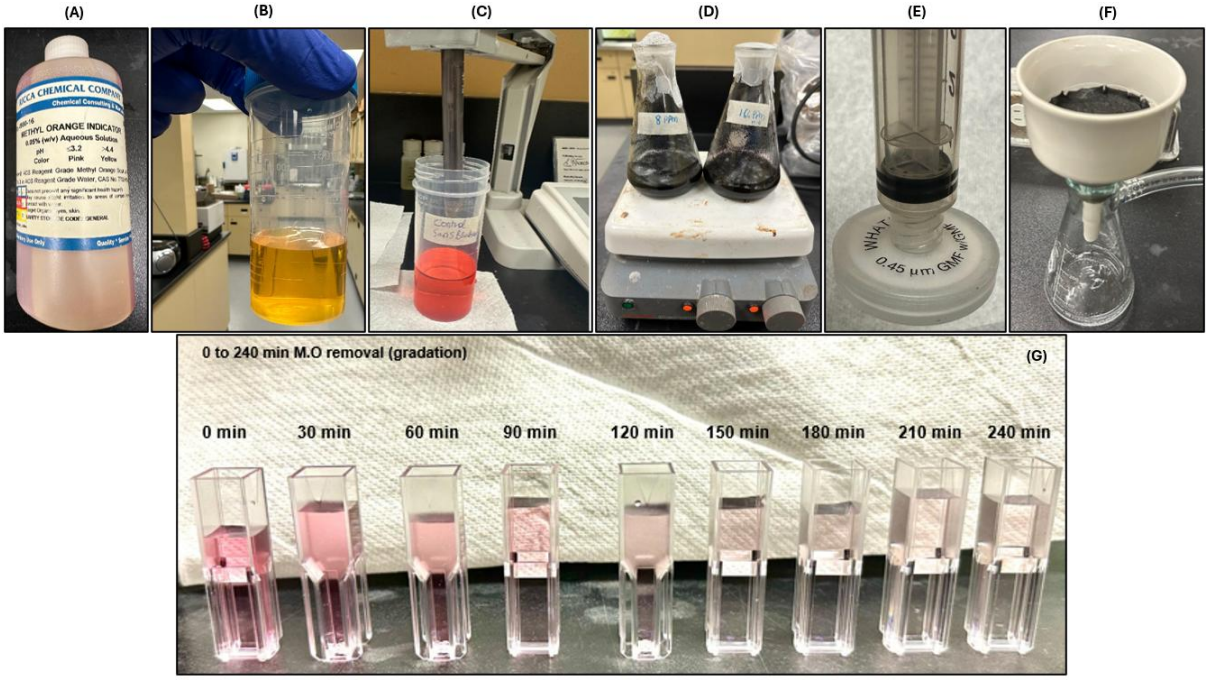

Figure 21: Methyl orange batch adsorption experiments with B600. (A) methyl orange dye; (B) yellowish-orange color before changing pH; (C) pink color after pH alteration; (D) adsorption tests on temperature controlled magnetic stirrer plate; (E) 0.45 µm syringe filter and (F) vacuum filtration set up - for separation of B600 from treated water during kinetic and isotherm tests; (G) effect of B600 on test solution with increase in duration (0-240 min). Here, M.O represents methyl orange

3.4.3 Optimization of adsorption parameters and results

Before adsorption isotherm and kinetic experiments, two other parameters have to be optimized, *i.e*, pH and B600 dosage. Here, based on data referred to as in Supplementary table 10, the probable initial concentration of methyl orange tested was around 150 ppm. In fact, 150 ppm of methyl orange concentration was also seen in Aichour et al., 2022. Hence, from the initial set of calculations for deciding adsorption standard stock concentrations, 164 ppm was chosen for the test solution due to the range proximity. Likewise, the maximum temperature (50 °C/323 K) and duration (24 h) were chosen after reviewing similar studies (Supplementary table 10) that dealt with biochar adsorbents produced from pyrolysis of different biomass feedstock, for methyl orange removal in polluted water. In fact, the contact time of 24 h was also preferred to prolong the analysis time just so if any saturation patterns might be observed.

3.4.3.1 Effect of pH

The pH was varied from 1-9 (1, 3, 5, 7, and 9) to investigate the percentage of dye removal depending on the affinity of methyl orange to biochar. Since biochars produced under increasing temperatures display alkaline pH and an overall negative surface charge, anionic dyes like methyl orange largely benefit from only a positively charged adsorbent surface to subdue electrostatic repulsion. From Muema et al., 2024, a high AAEM content in CRD wood could also have aided a basic B600 (pH: 9.7) since salts of Ca, Mg, K, and Na including carbonates and oxides, their role in ash concentration, and volatilization of heat-labile acidic surface groups are prominent as pyrolysis temperature increases. Performance of B600 in terms of surface area, micropore volume, Van-Krevelen molar ratio, FC, and overall stability were appreciable characteristics that bolstered its candidacy to be used for adsorption experiments, that too, under above normal room temperatures and in acidic conditions. For this reason, B600 should be complemented by a low pH (acidic conditions) to maintain protonation and anion exchange capacity (AEC) of the biochar surface during adsorption (Ghani et al., 2022). In other cases, biochar may be treated using acid activators to modify its surface charges towards the positive horizon as in Islam et al., 2022. It also signifies the role of electrostatic forces of attraction between the dye and biochar. Another reason for a low ambient pH to hasten methyl orange adsorption is the pH_{pzc} of B600 at 9.02 (Figure 22 (A)), which means that if the solution's pH is below pH_{pzc}, the surface of B600 will favour positive charges that could attract negatively charged methyl orange dye molecules. If the solution's pH is above pH_{pzc}, the surface of B600 is negative that

will repel the dye and delay or slow down adsorption. Despite a higher pH_{pzc}, maximum dye removal was seen only when the solution's pH was between 1-3.

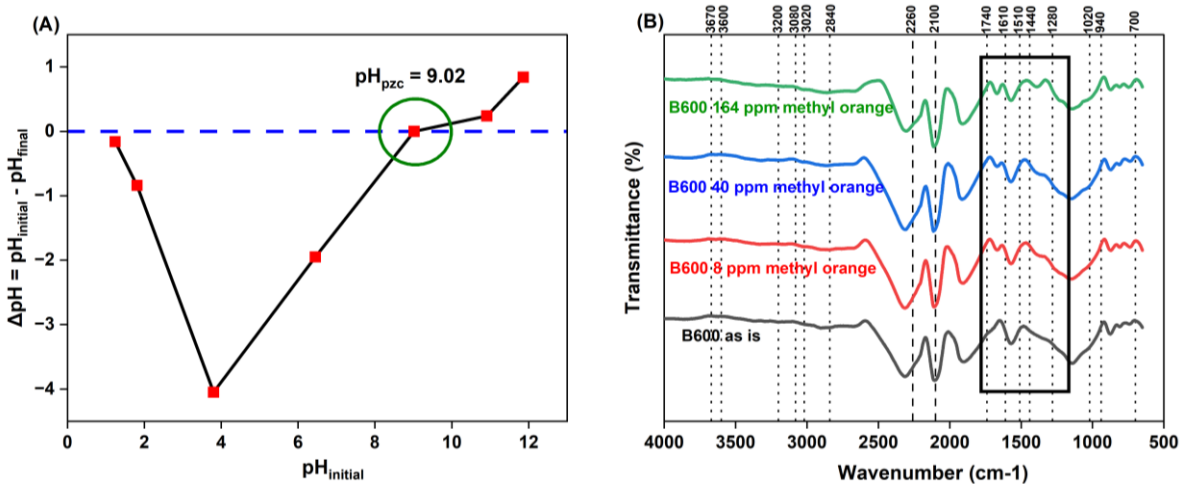

Figure 22: (A) B600 pH_{PZC}; and (B) FTIR spectra of B600 with varying concentrations of methyl orange (8-164 ppm) to detect spectral differences before and after adsorption

This theory was implicit from Figure 23 (A) where methyl orange removal efficiency was maximum at the lowest pH of 1 (93.53%), and decreased gradually to 88.64%, 60.56%, 48.09%, and 33.72%, for the pH of 3, 5, 7, and 9, respectively. A similar trend was followed in Lu et al., 2019. It highlights that the best mass transfer happens in these conditions and q_e will be superior in acid media. If the structure of methyl orange molecule is closely examined, it harbors a positive charge from Na+ and sometimes, a second positive charge from sulfonic acid, HSO_3^+, especially in low pH conditions (otherwise existing as sulfonate: SO_3^-) (Lee et al., 2024). Thus, if a charge transfer mechanism is exhibited from methyl orange over to B600, protonation of the biochar surface is more pronounced here that results in the adsorption of this anionic dye effectively.

Since a pH of 1 is realistically adverse, the second-best pH of 3 is considered for all future adsorption tests.

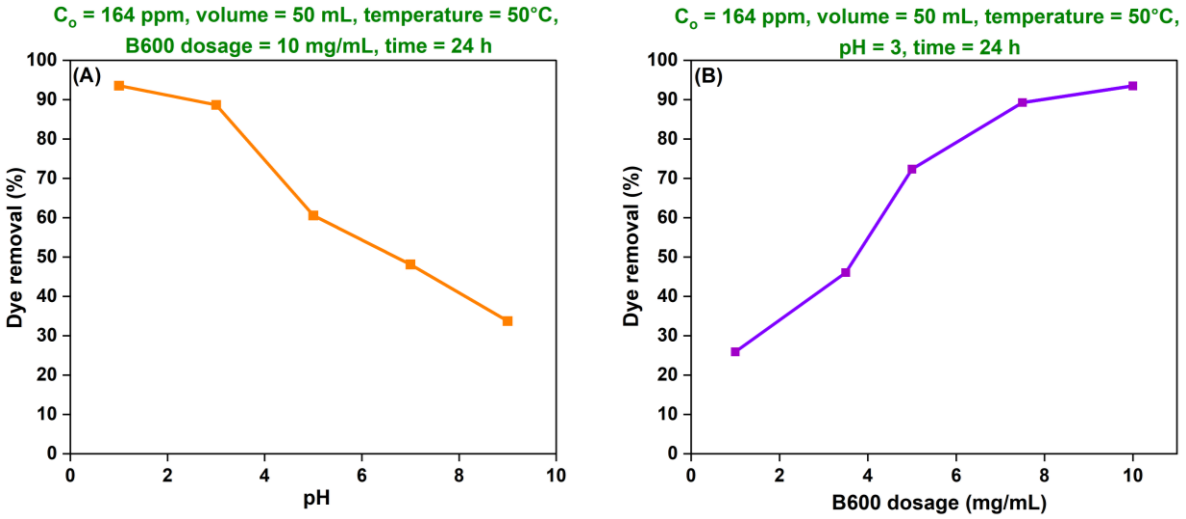

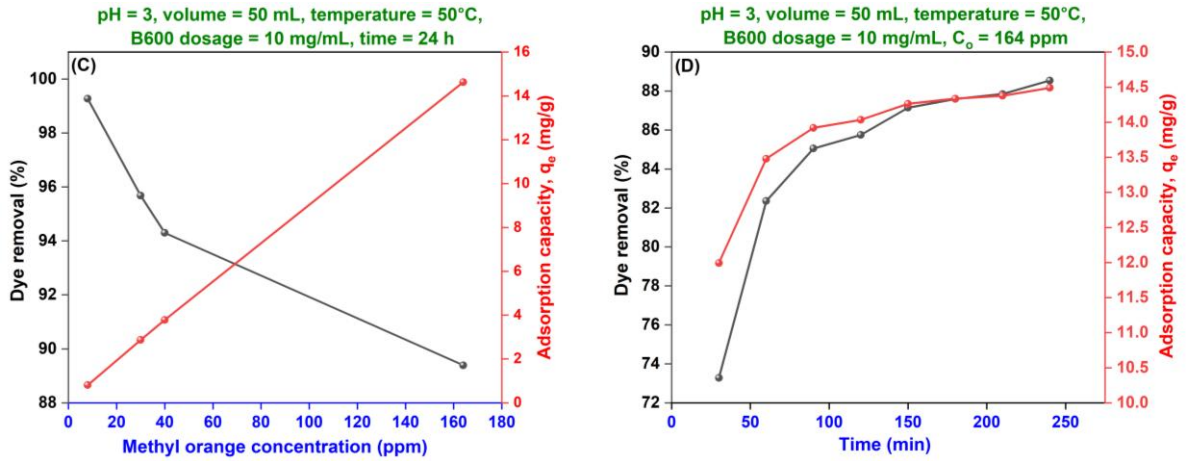

Figure 23: Optimization of adsorption parameters w.r.t dye removal percentage and adsorption capacity of B600: (A) pH; (B) adsorbent dosage; (C) initial dye concentration; and (D) duration

3.4.3.1.1 Confirming changes to B600 surface chemical composition

To validate if any surface-based adsorption occurs post-pH alteration for varying concentrations of methyl orange (8-164 ppm), FTIR spectra of the B600 adsorbent with the dye are recorded. As in Figure 22 (B), the spectra of B600 after adsorption experiments in test solutions containing 8, 40, and 164 ppm methyl orange conserved most of the signals as in native B600. Although three faintly noticeable changes can be listed: a) A slight decrease in peak intensity between 1020-1280 cm^{-1} may indicate masking of negatively charged oxygen-bearing groups like C-O and C-O-C, that could provide a favourable site of anchorage for positively charged sulfonic acid moieties of methyl orange under low pH; b) Development of minor peaking between 1280-1440 cm^{-1} with rise in dye concentrations could be due to O-H bending vibrations from alcohols and phenols resulting from heteroatom abstraction by methyl orange; and c) C=C stretching vibrations and amide-based C=O stretching vibrations between 1610-1740 cm^{-1} pointing at the probable role of nascent biochar aromatics in π-π interactions with benzene rings of methyl orange (no peaking for native B600). Loc et al., 2022 and Chen et al., 2024 also stated that in acidic conditions, aside from electrostatic interactions, π-π bonding (aromatic or benzene rings) and hydrogen bonding may also originate. On the flip side, at higher pH, hydroxyl groups occupy the surface of B600 and sometimes even compete with methyl orange for the active binding sites, leading to worsening of repulsion and suppressed dye adsorption on the now, negatively charged biochar surface (Akl et al., 2024).

3.4.3.2 Effect of adsorbent dosage

Methyl orange removal was tested at different B600 loadings: 1-10 mg/mL (1, 3.5, 5, 7.5, and 10 mg/mL). Because of unrestricted access to a greater number of adsorption sites available, 10 mg/mL showed the highest dye removal at 93.48%, and a decreasing trend was observed then onwards, to 89.24%, 72.33%, 46.04%, and 25.89% at an adsorbent dosage of 7.5, 5, 3.5, and 1 mg/mL, respectively (Figure 23 (B)). A similar concept was seen for an anionic dye like Congo red on biochar as in Akl et al., 2024. However, the q_e of B600 reduces due to an excessive number of binding sites available that leads to a drop in concentration gradient, hindering rapid migration of the adsorbate molecules at the solid-liquid interphase. In other words, for an unwavering initial dye concentration, due to less spatial constraints, its distribution per unit mass of adsorbent is limited where some adsorption sites will not even witness any adsorption due to compromised low binding energies and stay non-utilized (Nizam et al., 2021). This finding was also concluded from Praveen et al., 2022 who postulated that high q_e can be achieved at low adsorbent dosages only. Other binding sites on the adsorbent may also experience overlapping that could block porosity, reduce the surface area accessibility, and obstruct diffusion (Bassareh et al., 2023). Ideally, compared to some studies in Supplementary table 10, this work uses biochar with a 100-fold jump in loading rate which explains the far lower q_e values obtained. One recommendation to counteract is to increase the adsorbate:adsorbent ratio that could supply the necessary mass transfer driving force by reducing biochar overloads. Synchronously, the second way is to load B600 with appreciable properties (with or without activation) at a low dosage to increase q_e. In this case, exposed sites of high binding energies could quicken the process of adsorption. For example, if a relatively lower dosage of 1 g/L is followed instead of the very high dosage of 10 g/L as in our original case, for the same concentration of 164 ppm, q_e could reach 146 mg/g. For an even lower loading rate at 0.5 g/L, q_e may reach 293 mg/g. These numbers will then be comparable to other studies in

consideration with a similar or lower surface area. Thus, adsorbent loading rate is inversely proportional to q_e and directly proportional to dye removal efficiency.

3.4.3.3 Effect of initial dye concentration - adsorption isotherms

As methyl orange concentrations increased between 8-164 ppm in the test solution, the removal witnessed a drop from over 99% to 89% (Figure 23 (C)). This was seen in Jameel et al., 2024 where increasing the initial concentration of an azo dye called 'Acid Orange 7', from 25 ppm to 200 ppm reduced its removal at the end of adsorption. A low removal at high concentration (*e.g.:* 164 ppm), despite an elevated adsorbent dosage, could indicate that not all binding sites on B600 possess the greatest of affinity towards the dye. This finding could be extrapolated from Eleryan et al., 2024 where the authors concluded that a maximum removal can be reached only at a specific concentration of the pollutant dye where most binding sites might be accessible. Above this, dye molecules may start aggregating on top of each other with increasing distances from the adsorbent layer and also with weak bonding forces. So, only a few adsorption sites that contain high energies may be favorable, and only with those, methyl orange embraces electrostatic attraction. Binding constituents in these sites could also display hydrophilicity, hydrogen bonding, or even aromatic interactions. Henceforth, methyl orange molecules dissolved in the solution initially at low concentrations can only find a few of these sites in a short span of time resulting from supportive driving forces, before resulting in saturation or plateauing due to which this solution retains some non-adsorbed dye components that lowers removal rates. A similar finding for cationic and anionic dye adsorption using biochar was derived in Nirmaladevi & Palanisamy, 2020. Moreover, as discussed under the effect of adsorbent dosage section, a concentration gradient is vital for fast and efficient adsorption processes. When there is a high concentration of methyl orange with high adsorbent dosage, driving forces for the dye to reach B600 surface may be affected due to growing resistive forces and mass transfer limitations in the solution and in turn, slower collisions between adsorbent and adsorbate. Therefore, in spite of increase in q_e, it is still only very low. A reduction in molecular transfer resistance, good adsorption dynamics, and high q_e may be achieved by lowering biochar dosage for high dye concentrations as observed from Kaya et al., 2022.

Adsorption isotherm studies conducted using Langmuir, Freundlich, and Temkin models describe how the interaction between methyl orange and B600 unfold at equilibrium (Priyanka et al., 2024). As observed in Figure 24 (B)(A), Freundlich and Langmuir isotherms produce the best correlation of 0.97 and 0.94, respectively. All calculated adsorption parameters are shared in **Table 13**.

In Freundlich isotherm, the high correlation reveals that methyl orange adsorption over B600 is multi-layered, especially at high concentrations. So, both physisorption and chemisorption could be possible depending upon the requisite energies offered by the heterogeneous binding sites on B600 (Nirmaladevi & Palanisamy, 2020). Additionally, a non-linear trend would be witnessed when compared to the concentration of adsorbate left in the solution as concurred in Kaya et al., 2022. The Freundlich isotherm parameter 1/n = 0.5 indicates that adsorption is favorable since it satisfies the condition $0<1/n<1$. This finding is consistent with Lee et al., 2024. A K_F of 2.92 and low q_e is attributable to the high dosage level of 10 g/L in our process and also due to simultaneous increase in methyl orange concentration. Nevertheless, $q_{e,cal}$ is close to $q_{e,exp}$ which means the reliability of this model is good. This is implicit from the error estimations which provide an approximation in the degree of closeness between observed and expected values of q_e, where the model showed very low deviations (RMSE = 0.216, $\chi^2 = 0.03$).

Secondly, under Langmuir isotherm, since $0<R_L<1$, the adsorption is favorable and also exhibits monolayer-like patterns (Jadhav & Thorat, 2022). Hence, favourable adsorbate-adsorbent bonding mainly due to negligible or no aggregation of dye molecules (and their inter-molecular interactions) are possible, resembling chemisorption. A homogeneous, fixed number of active sites with similar binding energies and affinity (K_L = 3.33), aid in this process and act as a rate-limiting condition (Senapati et al., 2025, Eleryan et al., 2024). Along with a very good model fit, errors between $q_{e,exp}$ and $q_{e,cal}$ were also low (RMSE = 1.133, $\chi^2 = 1.08$) but relatively higher than for Freundlich model. Yet, a lower q_m (than $q_{e,exp}$) could be due to competing adsorption sites, adsorbate presence, and adsorption experimental conditions.

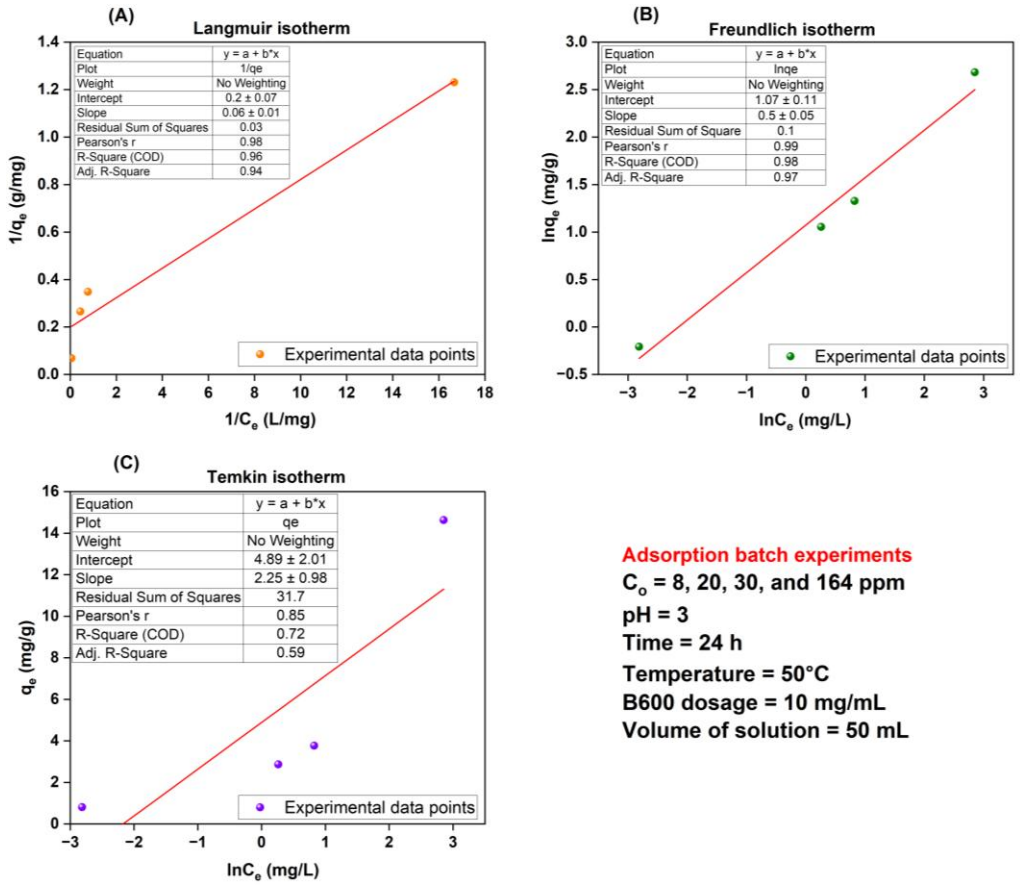

Figure 24: Adsorption isotherm models: (A) Langmuir isotherm; (B) Freundlich isotherm; and (C) Temkin isotherm, with the conditions for experimentation

Lastly, the Temkin isotherm model manifested a lower data fit (R^2 = 0.59) but at the same time, very low errors too (RMSE =0.002, $\chi^2 = 0$), still suggesting partial dependability. It could also mean that overall binding energy variations along with an increase in active site coverage over the non-uniform B600 layer are far more complex to be evaluated with precision as a result of dominance from the other two isotherm models, *i.e.,* a convergence of different mechanisms. The model predicts that affinity between methyl orange and B600 is low according to the Temkin isotherm from a low B of 2.25 J/mol that could hint at low heat of adsorption. As methyl orange concentrations escalated from 8 ppm to 164 ppm in the test solution with all other independent variables unchanged, there is an obvious linear increase in q_e. But due to the inverse relation with adsorbate concentration and q_e, the heat of adsorption should ideally decrease as more and more binding sites get occupied, paving the way for subsequent adsorbate molecules to face repulsive forces from the already initially adsorbed entities (when heat of adsorption would have been maximum for fresh sites with high binding energies). Therefore, from the calculated model parameters, physisorption may be deemed to influence the mechanism forefront, mainly at high adsorbate concentrations (Wei et al., 2022). Despite being "less contrary" to the theoretical understanding, Temkin isotherm is ranked last here only due to the low model correlation.

Table 13: Adsorption isotherm parameters

Average	Langmuir isotherm					Freundlich isotherm				Temkin isotherm			
$q_{e,exp}$ (mg/g)	q_m (mg/g)	$q_{e,cal}$ (mg/g)	K_L (L/mg)	R_L	R^2	K_F [(mg/g)(L/mg)$^{1/n}$]	1/n	$q_{e,cal}$ (mg/g)	R^2	B (J/mol)	K_T (L/mg)	$q_{e,cal}$ (mg/g)	R^2
5.52	5.00	3.56	3.33	0.002-0.036 from 164-8 mg/L	0.94	2.92	0.50	5.15	0.97	2.25	8.79	5.52	0.59

To summarize, Freundlich, followed by Langmuir isotherm models indicate favourable methyl orange adsorption over B600, where both monolayer and multilayer interactions can be deducted. Despite being less contrary to the theory, Temkin isotherm is ranked last here only due to the low model correlation factor.

3.4.3.4 Effect of adsorption duration - adsorption kinetics

As contact time increased from 0-240 min, complete stability in the system was not observed yet (Figure 23 (D)). The q_t and removal increased for both concentrations of 8 ppm (0.64-0.73 mg/g, and 77-89%) and 164 ppm (11.99-14.49 mg/g, and 73-89%) with more than 50% activity occurring rapidly within the first 30 min suggesting that the first phase of this adsorption process is fast (Priyanka et al., 2024). The difference in the shape of curves between 8 ppm and 164 ppm suggests that increase in adsorbate presence does not significantly alter removal rates. Another observation was that with the same availability of active binding sites on B600, competition between dye molecules increases q_t even with the high loading rate of B600 and without any drastic concentration gradient to drive rampant mass transfer. Next, an increase in contact time over 240 min may have probably achieved equilibrium and noticeable saturation in adsorption. This is because when contact time was 24 h during the isotherm experiments, q_e and removal percentages reached a maximum of 14.63 mg/g and 89.39%, respectively. Although, the difference in both these parameters was just 0.14 mg/g and 0.85%. So, an increase in duration would not have necessarily led to a promising difference in results anyway since almost all adsorption sites on B600 are already occupied by the dye. Nearing equilibrium, electrostatic repulsion between aggregating methyl orange molecules, their inaccessibility to high energy binding sites (already saturated), and slow diffusion in the pores, could have dominated the overall process preventing any further increase in dye removal and q_e.

As for kinetics involving initial methyl orange concentrations of 8 ppm and 164 ppm, pseudo-first order, pseudo-second order, and intra-particle diffusion models were used to calculate adsorption parameters (Table 14) like in Loc et al., 2022. Both linear (Figure 25 (A-C)) and non-linear (Figure 25 (D-E)) fitting plus regression methods were evaluated and compared as in Ghani et al., 2022. All error estimations for analyzing the closeness between $q_{e,exp}$ and $q_{e,cal}$ for both linear and non-linear kinetic modelling are computed separately in Table 15.

Table 14: Adsorption kinetic parameters

Dye concentration	Pseudo first order kinetics			Pseudo second order kinetics			Intra-particle diffusion kinetics		
	q_e (mg/g)	k_1 (min^{-1})	R^2	q_e (mg/g)	k_2 (g/mg.min)	R^2	k_3 ($mg/g.min^{1/2}$)	C (mg/g)	R^2
Linear fitting with linear regression									
8 ppm	0.194	0.004	0.978	0.748	0.158	1.000	0.010	0.583	0.983
164 ppm	2.752	0.012	0.951	14.872	0.010	1.000	0.214	11.473	0.772
Non-linear fitting with non-linear regression									
8 ppm	0.700	0.059	0.495	0.726	0.254	0.879	0.010	0.583	0.983
164 ppm	14.107	0.056	0.517	14.716	0.011	0.890	0.214	11.473	0.772

For pseudo-second order model, linear fitting and regression analysis suggested that R^2 is 1 for both concentrations indicating slow, but strong and dominant chemical interactions of methyl orange with B600 via chemisorption (Wang et al., 2024). A similar observation was seen for the adsorption of methyl orange and malachite green dyes over Zn activated sawdust biochar as in Maiti et al., 2024. Since formation of chemical bonds is a slow process, adsorption duration/contact time could play a key role here (Chen et al., 2024, Maiti et al., 2024). This can be facilitated by the surface functional groups over partly-hydrophilic B600, containing hydrogen and oxygen to which sulfonic acid groups of methyl orange can attach to (Diaz-Uribe et al., 2023). The ease with which B600 and methyl orange molecules interact, governs the overall adsorption capacity resulting from sharing of lone pair of electrons in addition to diffusion phenomenon (Cano et al., 2025). For this, the active site availability and methyl orange concentration in the solution are the major rate limiting factors. This can be supported by the fact that a high adsorption site availability persists due to a high loading rate of B600. The values of $q_{e,cal}$ were 0.75 mg/g and 14.87 mg/g for 8 ppm and 164 ppm respectively, that is found to be close to their $q_{e,exp}$ counterparts via a 0.02-0.09 RMSE. For non-linear fitting and regression analysis, $q_{e,cal}$ for 8 ppm and 164 ppm methyl orange concentrations were found to be similar to linear regression method, at 0.73 mg/g and 14.72 mg/g, with a RMSE of only 0.03 for both concentrations relative to $q_{e,exp}$. This supports model validity. The rate constant k_2 ($1<k_2<1$) also showed similar values that could manifest the existence of appreciable adsorbate-adsorbent surface interactions. However, a marked difference in R^2 existed for the non-linear method, where it dropped to 0.88 and 0.89 for 8 ppm and 164 ppm, respectively. Nevertheless, pseudo-second order model is said to have played its part in methyl orange adsorption over B600. Especially at 8 ppm, $k_2>k_1$ that supports our interpretation.

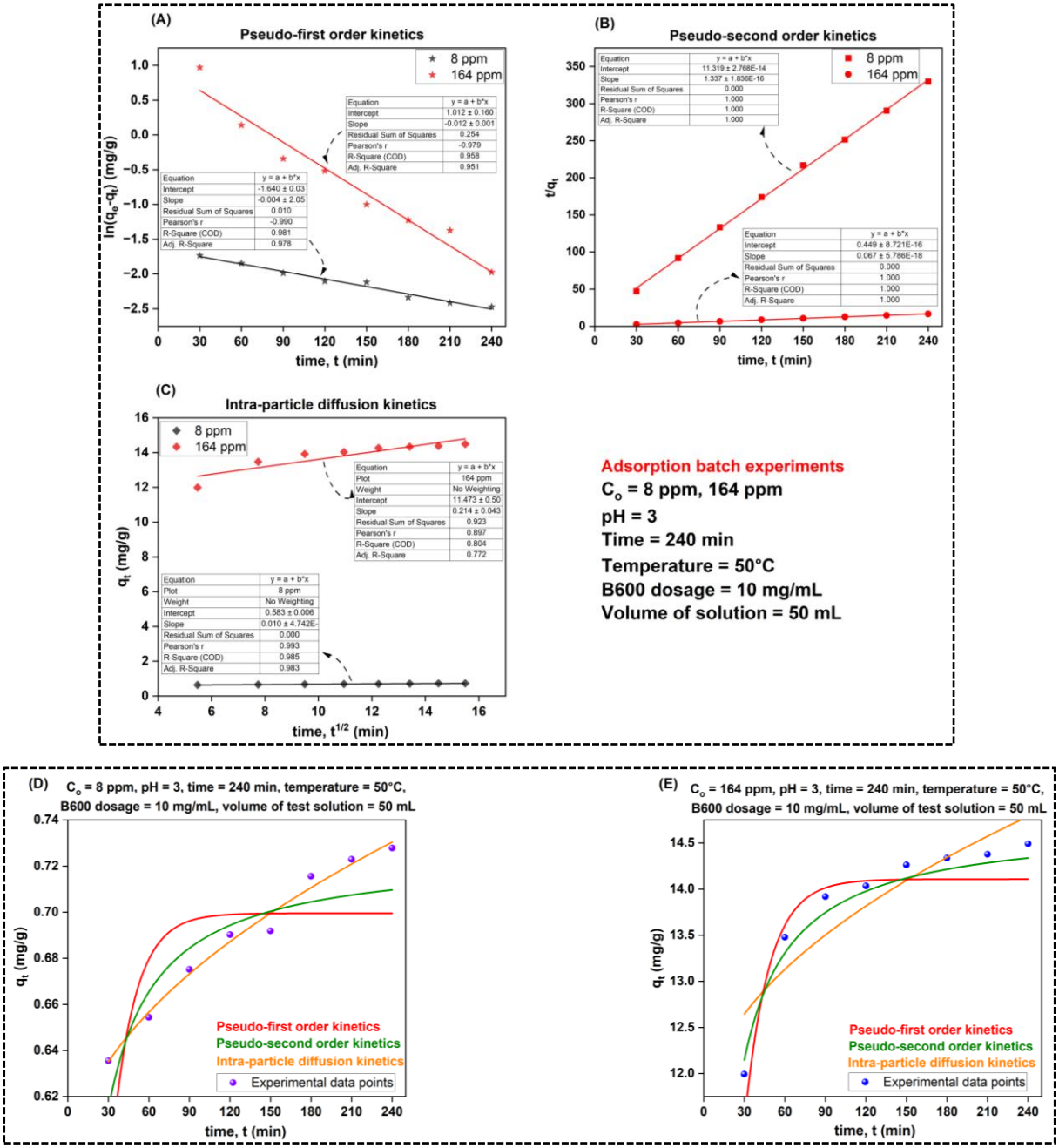

Figure 25: Adsorption kinetic models: Linear (A-C) and non-linear (D-E) fitting methods

Next, for pseudo-first order model, bound by the effectiveness in diffusion of methyl orange molecules at the solid-liquid interphase, linear fitting and regression analysis yielded a high R^2 of 0.98 and 0.95 for 8 ppm and 164 ppm, respectively, bolstering the intervention of subdued physisorption mechanism. This can be explained by high concentrations of methyl orange in the test solution, albeit the transmigration driving forces during adsorbate-adsorbent interactions differs between low and high concentrations. For instance, a low concentration of 8 ppm contributed to unified interactions of methyl orange with the open binding sites of B600 leading to their controlled coverage. Towards 164 ppm, there is pooling of more molecules, competing non-unified interactions, and rejection by the already engaged sites. It is also at this concentration where there is a drastic variation between $q_{e,cal}$ (2.75 mg/g) and $q_{e,exp}$ (14.63 mg/g) by a high RMSE of 4.49 (versus 0.23 for 8 ppm). Due to a good model fit, it could conclude that pseudo-first order model may predict the adsorption mechanism of methyl orange much better at mainly low concentrations. However, for the other method, very low R^2 of 0.50 and 0.52 question the ability of non-linear pseudo first order data fitting to judge the adsorption mechanism, despite very good precision between $q_{e,cal}$ (14.11 mg/g) and $q_{e,exp}$ (14.63 mg/g) at 164 ppm (RMSE = 0.20). The rate constant k_1 in both fitting methods is less than 0.1 min^{-1} which could mean that adsorption could be controlled by weak forces and adsorbate diffusion.

Lastly, for the intra-particle diffusion kinetic model, common for linear and non-linear fitting and regression analysis, supported a great R^2 (0.98) for low concentrations of methyl orange. Whereas a R^2 of 0.77 for 164 ppm indicated three findings: a) The pores of B600 with a specified number of active sites with high binding energies begin to show intolerance towards adsorption as adsorbate concentration increases; b) increasing adsorbate concentrations suffer from a diffusion barrier; and c) the molecules of B600 may agglomerate and would form a larger geometry, thereby, not being able to access the small pores. This may be derived from $q_{e,cal}$ (8 ppm: 0.58 mg/g, 164 ppm: 11.47 mg/g) that shows increase in RMSE from 0.09-1.19, respectively. In fact, at 8 ppm, $k_3 > k_1$, highlighting its importance over pseudo-first order reactions. At 164 ppm, $k_3 > k_1$ and k_2, meaning that once surface-active sites are occupied, further increase in adsorbate concentration will insinuate diffusion and filling of porous channels until mass transfer impedes the process along with saturation of all internal binding sites (Senapati et al., 2025). Therefore, movement of adsorbate molecules from the solution's bulk to the boundary layer of the adsorbent along with active site binding efficacy and porosity (surface area and pore volume) of B600 play an important role in adsorption processes.

Table 15: RMSE derived upon comparison of qe,exp and qe,cal for two initial methyl orange concentrations, Co: 8 ppm and 164 ppm, during adsorption kinetic model evaluation

Kinetic model	C_o (ppm)	Average $q_{e,exp}$ (mg/g)	$q_{e,cal}$ (mg/g)	RMSE
Linear fitting with linear regression				
Pseudo-first order	8	0.812	0.194	0.234
Pseudo-first order	164	14.630	2.752	4.489
Pseudo-second order	8	0.812	0.748	0.024
Pseudo-second order	164	14.630	14.872	0.091
Intra-particle diffusion	8	0.812	0.583	0.087
Intra-particle diffusion	164	14.630	11.473	1.193
Non-linear fitting with non-linear regression				
Pseudo-first order	8	0.812	0.700	0.042
Pseudo-first order	164	14.630	14.107	0.198
Pseudo-second order	8	0.812	0.726	0.033
Pseudo-second order	164	14.630	14.716	0.033
Intra-particle diffusion	8	0.812	0.583	0.087
Intra-particle diffusion	164	14.630	11.473	1.193

To sum up, physisorption, chemisorption, and molecular diffusion within pores of the adsorbent are the key adsorption mechanisms underscored each of which harbors one or multiple rate-limiting steps w.r.t concentration of adsorbate, adsorption sites, binding interactions, and finally, pore diffusion.

3.4.3.5 Effect of temperature – adsorption thermodynamics

Thermodynamic parameters of the adsorption process are given in Table 16. Upon increasing the temperature for adsorption from 20-50 °C or 293-323 K, q_e generally experienced an increase from 0.20-0.81 mg/g along with the removal percentage in the range of 24-99%, for an initial methyl orange concentration of 8 ppm. This pattern was also seen in Hanoon & Ahmed, 2019. Since a temperature dependence is expected here, thermodynamic analysis of this adsorption process is necessary. From the $\ln k_d$ versus 1/T plot, ΔH was calculated to be 144.15 KJ/mol which could mean very strong chemisorption owing to a high magnitude of endothermicity. Adsorption here will then be dictated by covalent, hydrogen and π-π bonding. Increased energy requirements may also mean that kinetic energy of dye molecules could increase that leads to collisions with B600 (Lu et al., 2019). Positive ΔS also means that disorderliness or randomness builds up within the adsorption system where methyl orange has the molecular freedom for migrating from the bulk of the solution to attach on to the B600 surface and further participate in dispersive interfacial diffusion reactions before active site binding (Hanoon & Ahmed, 2019). On the other hand, as adsorption ceases, entropy has to decrease since the movement of dye molecules is now, tremendously restricted once affixed. Overall, ΔS was calculated to be 0.46 KJ/mol.K. Finally, ΔG calculated ranged from 8.38 KJ/mol at 20 °C to -6.21 KJ/mol at 50 °C, suggesting growing spontaneity in adsorption with increase in temperature and gradually phasing out external energy requirements to render the process favourable (Azim et al., 2024).

Table 16: Adsorption thermodynamic parameters and the influence of temperature

Enthalpy	Entropy	Gibbs free energy		
ΔH (KJ/mol)	ΔS (KJ/mol.K)	Temperature (K)	ΔG (KJ/mol) = ΔH-TΔS	ΔG (KJ/mol) = -RTlnk_d
144.153	0.460	293	9.419	8.376
		303	4.823	5.437
		313	0.227	2.488
		323	-4.369	-6.207

3.4.4 Adsorption mechanism and theory

Being surface-driven, methyl orange dye molecules traversed from the bulk of contaminated aqueous solution to the surface of B600. This is when B600's surface charge, functional groups, inventory of adsorption sites with a myriad of energy levels, porous framework (micro to meso), and binding sites in the pores could have dictated adsorption. Other factors that governed the process are ambient pH, temperature, contact time, adsorbent dosage, and initial methyl orange concentration in the solution. Electrostatic interactions between B600 and methyl orange were prominent, where modifying the pH to acidic conditions may have created positively charged moieties on the biochar that attracted the anionic azo dye (Ding et al., 2022). At this stage, repulsive forces could have been kept out. Next, as FTIR suggested, the presence of residual hydroxyl, carboxyl, amides on the surface of B600 opened opportunities for covalent and hydrogen bond formations with methyl orange's sulfonate group under low pH conditions. Upon observing Figure 19 (D), adsorption of methyl orange affected the surface elemental composition of B600 that is evident from a drop in surface carbon from 95.3% to 94.1% and an increase in surface oxygen from 4.5% to 5.6% after adsorption. Such strong chemical interactions resulted in chemisorption that was affirmed by the pseudo-second order kinetic model where adsorption efficiency increased and showed signs of irreversibility. This may be evident from the Langmuir isotherm parameter R_L, that was close to 0 (still>0 and favourable). Langmuir isotherm's monolayer adsorption with a fixed number of active binding sites with high energies and Freundlich isotherm's heterogeneous multilayer interactions (0<1/n<1), are both explainable. Pseudo-first order kinetics also fitted well as a supportive mechanism with the adsorption data showing the dominance of weak physical forces via physisorption as discussed in Shi et al., 2019. Since B600 showed the presence of C=C and C≡C linkages in FTIR along with good stability indices from the physicochemical characterization, aromatic condensation may have been possible that could have resulted in π-π stacking interactions with the aromatic rings of methyl orange (Zubair et al., 2020). Others like Aladeokin & Fletcher, 2024 describe a mechanism called π-π electron-donor-acceptor (EDA) reaction taking its course. Next, a BET surface area of about 323 m^2/g with a high correlation for the intra-particle diffusion model at low concentrations of methyl orange, also suggested molecular diffusion and pore-filling in B600. Figure 18 (J)(K)(L) shows the sudden disappearance of porosities in B600 and surface clusters that may have been due to interactions with the dye.

4. Conclusion

Sustainable management of CRD wood waste is an area of concern due to widespread landfilling practices owing to its non-recyclable tag. A major research problem with CRD wood is a hesitation to convert this material into usable forms due to its worn-out nature as a result of wilting, irresponsible demolition, and excessive surface chemical treatments. Albeit, heat treatment technologies can disprove this notion by creating valuable products that could aid some hard-to-abate industrial sectors towards decarbonization pathways. On that note, alternative waste management technologies like pyrolysis not only shrink the vast volumes of CRD wood waste but also generate energy dense products of environmental and industrial importance. The objectives of this work were to delve deeper into this thermochemical conversion technique channelling biochar production, analyzing the influence of pyrolysis conditions on its yield and properties, and validate its potential to be a relevant substitute for fossil coal or its derivatives in applications concerning metallurgical, carbon sequestration, and pollutant adsorption processes.

Proximate and ultimate analysis revealed that biochar carbon content, FC, TSF, TGA R50, and Raman I_D/I_G indices correlate positively with pyrolysis temperature, BRT, and mixed responses with mass of feedstock, both in the horizontal tube furnace and rotary retort-furnace scale-up experiments indicating the biochar's strong contention towards carbon sequestration and metallurgical uses (either directly in proportions within smelting or as a co-substrate with metallurgical-grade coal to produce petroleum coke reductant). Biochars produced under moderate

temperatures (B600) somewhat strike a balance between surface area, pore volume, and surface functionalities that deemed it suitable for soil amendments and also for pollutant adsorption (*e.g.:* dyes) from contaminated water. An industrial grade dye, methyl orange, was effectively adsorbed with high removal rates by optimizing adsorption conditions such as time, pH, adsorbent dosage, and the initial concentration of the dye. However, a key note here is that no pre- or post-pyrolysis activation was carried out using chemicals or reactive atmospheres at extreme conditions due to possible externalities from chemical usage, downstream contamination (wastewater generation), and excessive energy requirements. Comparison of pyrolysis and adsorption experiment results with similar studies that could be found, confirmed relatable projections with existing data. Since CRD wood is already an end-of-life heterogenous material having low purpose, it could be viewed as a single-use entity in the form of biochar where its application like adsorption could be followed by a responsible but creative post-use fate such as being an additive to concrete (building materials) or tar/asphalt (roads, pavements). In this way, even a problem like pollutant desorption that seldom occurs can be overcome via long-term sequestration of biochar: a win-win situation. Although, in case of activated CRD wood biochar, regeneration and reuse of adsorbent has to be considered.

Despite benefits of CRD wood pyrolysis that can bring out its untapped potential, drawbacks do exist. These include establishing a consistent supply of the wood from demolition sites, efficient inherent contaminant removal, utilization of co-products such as biooil and pyrolysis gas, and most importantly an economically and environmentally feasible reactor and process design according to the applications under focus. Since pyrolysis of lignocellulose biomass is already widespread, integrating a feedstock like CRD wood should not be a big problem if procuring and handling the material is mastered along the supply chain. It could also be used as a co-feedstock with other forest wood residues, agricultural wastes, and organic municipal solid wastes in local mobile pyrolysis units that can be stationed near all these source sites to subdue logistical issues. Future work entails carrying out even larger scalability tests within a pilot pyrolyzer at different conditions to tailor biochar properties for the same applications, exploring an understated biochar post-production treatment in the form of thermal activation, and also conducting self-ignition examinations of CRD wood biochars to find probable underlying causes for this "less-spoken about" problem.

Author Contributions: Conceptualization, methodology, validation, formal analysis, investigation, data curation, writing—original draft preparation, editing, visualization - **Aravind Ganesan**. Supervision, review, mentorship – **Simon Langlois**. Supervision, review, editing, mentorship - **Olivier Rezazgui**. Supervision, review, editing, mentorship - **Younès Bareha**. Project administration – **Cyrine Boussabbeh**. Supervision, mentorship – **Simon Barnabé**. Supervision, review, mentorship – **Patrice Mangin**. All authors have read and agreed to the published version of the manuscript.

Funding: This research was funded by MITACS, through Escouade Energie, Citeq, and supported by Innofibre, and I^2E^3 – UQTR, Québec, Canada. The work was conducted at Innofibre – Centre d'Innovation des Produits Cellulosiques, Trois-Rivières and at the Institute for Innovation in Ecomaterials, Ecoproducts, and Ecoenergies (I^2E^3), University of Québec Trois-Rivières (UQTR), Québec, Canada.

Conflicts of Interest: The authors declare no conflict of interest. The funders had no role in the design of the study; in the collection, analyses, or interpretation of data; in the writing of the manuscript; or in the decision to publish the results.

5. References

Abdu, M., Babaee, S., Worku, A., Msagati, T. A., & Nure, J. F. (2024). The development of Giant reed biochar for adsorption of Basic Blue 41 and Eriochrome Black T. azo dyes from wastewater. *Scientific Reports*, *14*(1), 18320. Abdu, M., Babaee, S., Worku, A., Msagati, T. A., & Nure, J. F. (2024). The development of Giant reed biochar for adsorption of Basic Blue 41 and Eriochrome Black T. azo dyes from wastewater. *Scientific Reports*, *14*(1), 18320.

Acharya, A., Jeppu, G., Girish, C. R., Prabhu, B., Murty, V. R., Martis, A. S., & Ramesh, S. (2024). Adsorption of arsenic and fluoride: Modeling of single and competitive adsorption systems. *Heliyon*, *10*(11).

Agboola, O. D., & Benson, N. U. (2021). Physisorption and chemisorption mechanisms influencing micro (nano) plastics-organic chemical contaminants interactions: a review. *Frontiers in Environmental Science*, *9*, 678574.

Ahuja, V., Palai, A. K., Kumar, A., Patel, A. K., Farooque, A. A., Yang, Y. H., & Bhatia, S. K. (2024). Biochar: Empowering the future of energy production and storage. *Journal of Analytical and Applied Pyrolysis*, *177*, 106370.

Aichour, A., Zaghouane-Boudiaf, H., & Khodja, H. D. (2022). Highly removal of anionic dye from aqueous medium using a promising biochar derived from date palm petioles: Characterization, adsorption properties and reuse studies. *Arabian Journal of Chemistry*, *15*(1), 103542.

Akl, M. A., & Serage, A. A. (2024). Chitosan impregnated sugarcane bagasse biochar for removal of anionic dyes from wastewater. *Scientific Reports*, *14*(1), 27097.

Aladeokin, O., & Fletcher, A. (2024). A novel activated carbon material from peanut shells for the removal of methyl orange and methylene blue dyes from wastewater: kinetics, isotherms and mechanism. *Adsorption Science & Technology*, *42*, 02636174241256843.

Alharbi, H. A., Alotaibi, K. D., El-Saeid, M. H., & Giesy, J. P. (2023). Polycyclic aromatic hydrocarbons (PAHs) and metals in diverse biochar products: Effect of feedstock type and pyrolysis temperature. *Toxics*, *11*(2), 96.

Al-Rumaihi, A., Shahbaz, M., Mckay, G., Mackey, H., & Al-Ansari, T. (2022). A review of pyrolysis technologies and feedstock: A blending approach for plastic and biomass towards optimum biochar yield. *Renewable and Sustainable Energy Reviews*, *167*, 112715.

Altıkat, A., Alma, M. H., Altıkat, A., Bilgili, M. E., & Altıkat, S. (2024). A comprehensive study of biochar yield and quality concerning pyrolysis conditions: a multifaceted approach. *Sustainability*, *16*(2), 937.

Anand, A., Gautam, S., & Ram, L. C. (2023). Feedstock and pyrolysis conditions affect suitability of biochar for various sustainable energy and environmental applications. *Journal of Analytical and Applied Pyrolysis*, *170*, 105881.

Antonangelo, J. A., Zhang, H., Sun, X., & Kumar, A. (2019). Physicochemical properties and morphology of biochars as affected by feedstock sources and pyrolysis temperatures. *Biochar*, *1*, 325-336.

Ayaz, M., Feizienė, D., Tilvikienė, V., Akhtar, K., Stulpinaitė, U., & Iqbal, R. (2021). Biochar role in the sustainability of agriculture and environment. *Sustainability*, *13*(3), 1330. Ayaz, M., Feizienė, D., Tilvikienė, V., Akhtar, K., Stulpinaitė, U., & Iqbal, R. (2021). Biochar role in the sustainability of agriculture and environment. *Sustainability*, *13*(3), 1330.

Azim, E. A., Samy, M., Hanafy, M., & Mahanna, H. (2024). Novel mint-stalks derived biochar for the adsorption of methylene blue dye: Effect of operating parameters, adsorption mechanism, kinetics, isotherms, and thermodynamics. *Journal of Environmental Management*, *357*, 120738.

Babu, K. K. B. S., Nataraj, M., Tayappa, M., Vyas, Y., Mishra, R. K., & Acharya, B. (2024). Production of biochar from waste biomass using slow pyrolysis: Studies of the effect of pyrolysis temperature and holding time on biochar yield and properties. *Materials Science for Energy Technologies*, *7*, 318-334.

Bassareh, H., Karamzadeh, M., & Movahedirad, S. (2023). Synthesis and characterization of cost-effective and high-efficiency biochar for the adsorption of Pb2+ from wastewater. *Scientific Reports*, *13*(1), 15608.

Behera, A. K., Shadangi, K. P., & Sarangi, P. K. (2024). Efficient removal of Rhodamine B dye using biochar as an adsorbent: Study the performance, kinetics, thermodynamics, adsorption isotherms and its reusability. *Chemosphere*, *354*, 141702.

Beljin, J., Đukanović, N., Anojčić, J., Simetić, T., Apostolović, T., Mutić, S., & Maletić, S. (2024). Biochar in the Remediation of Organic Pollutants in Water: A Review of Polycyclic Aromatic Hydrocarbon and Pesticide Removal. *Nanomaterials*, *15*(1), 26.

Bian, H., Wang, M., Huang, J., Liang, R., Du, J., Fang, C., ... & Zhang, J. (2024). Large particle size boosting the engineering application potential of functional biochar in ammonia nitrogen and phosphorus removal from biogas slurry. *Journal of Water Process Engineering*, *57*, 104640.

Bolan, S., Hou, D., Wang, L., Hale, L., Egamberdieva, D., Tammeorg, P., ... & Bolan, N. (2023). The potential of biochar as a microbial carrier for agricultural and environmental applications. *Science of the Total Environment*, *886*, 163968.

Buffi, M., Hurtig, O., Prussi, M., Scarlat, N., & Chiaramonti, D. (2024). Energy and GHG emissions assessment for biochar-enhanced advanced biofuels value chains. *Energy Conversion and Management*, *309*, 118450.

Cano, F. J., Reyes-Vallejo, O., Sánchez-Albores, R. M., Sebastian, P. J., Cruz-Salomón, A., Hernández-Cruz, M. D. C., ... & Torres-Ventura, H. H. (2025). Activated Biochar from Pineapple Crown Biomass: A High-Efficiency Adsorbent for Organic Dye Removal. *Sustainability*, *17*(1), 99.

Channiwala, S. A., & Parikh, P. P. (2002). A unified correlation for estimating HHV of solid, liquid and gaseous fuels. *Fuel*, *81*(8), 1051-1063.

Chatterjee, R., Sajjadi, B., Chen, W. Y., Mattern, D. L., Hammer, N., Raman, V., & Dorris, A. (2020). Effect of pyrolysis temperature on physicochemical properties and acoustic-based amination of biochar for efficient CO2 adsorption. *Frontiers in Energy Research*, *8*, 85.

Chen, G., Yin, Y., Zhang, X., Qian, A., Pan, X., Liu, F., & Li, R. (2024). Enhanced Adsorption of Methyl Orange from Aqueous Phase Using Chitosan–Palmer Amaranth Biochar Composite Microspheres. *Molecules*, *29*(8), 1836.

Chen, M., Sun, Y., Peng, Y., Han, Z., Chen, G., Chen, X., & Lu, S. (2025). Effect of low-carbon coal gangue on the stability and dissolved organic matter characteristics of co-pyrolysis biochar: insights on pyrolysis temperatures and minerals. *Carbon Research*, *4*(1), 19.

Choudhary, T. K., Khan, K. S., Hussain, Q., Ahmad, M., & Ashfaq, M. (2019). Feedstock-induced changes in composition and stability of biochar derived from different agricultural wastes. *Arabian Journal of Geosciences*, *12*, 1-13.

Cimò, G., Kucerik, J., Berns, A. E., Schaumann, G. E., Alonzo, G., & Conte, P. (2014). Effect of heating time and temperature on the chemical characteristics of biochar from poultry manure. *Journal of agricultural and food chemistry*, *62*(8), 1912-1918.

Clarke, J., & Olea, M. (2024). The effect of temperature and treatment regime on the physical, chemical, and biological properties of poultry litter biochar. *Reactions*, *5*(3), 379-418.

Conz, R. F., Abbruzzini, T. F., de Andrade, C. A., Milori, D. M., & Cerri, C. E. (2017). Effect of pyrolysis temperature and feedstock type on agricultural properties and stability of biochars. *Agricultural Sciences*, *8*(09), 914.

Crombie, K., Mašek, O., Sohi, S. P., Brownsort, P., & Cross, A. (2013). The effect of pyrolysis conditions on biochar stability as determined by three methods. *Gcb Bioenergy*, *5*(2), 122-131.

Daffalla, S., Da'na, E., Taha, A., & El-Aassar, M. R. (2024). Synthesis of a Novel Magnetic Biochar from Lemon Peels via Impregnation-Pyrolysis for the Removal of Methyl Orange from Wastewater. *Magnetochemistry*, *10*(12), 95.

Das, O., Mensah, R. A., George, G., Jiang, L., Xu, Q., Neisiany, R. E., ... & Berto, F. (2021). Flammability and mechanical properties of biochars made in different pyrolysis reactors. *Biomass and Bioenergy*, *152*, 106197.

Dhar, S. A., Sakib, T. U., & Hilary, L. N. (2022). Effects of pyrolysis temperature on production and physicochemical characterization of biochar derived from coconut fiber biomass through slow pyrolysis process. *Biomass Conversion and Biorefinery*, *12*(7), 2631-2647.

Diaz-Uribe, C., Ortiz, J., Duran, F., Vallejo, W., & Fals, J. (2023). Methyl Orange Adsorption on Biochar Obtained from Prosopis juliflora Waste: Thermodynamic and Kinetic Study. *ChemEngineering*, *7*(6), 114.

Ding, W., Habineza, A., Zeng, X., Yan, Z., Yan, J., & Yang, G. (2022). Adsorption of Methylene blue and Methyl orange on nano zero-valent iron (nZVI) coated biochar: column adsorption experiments. *Desalination and Water Treatment*, *260*, 169-178.

Dufourny, A., Van De Steene, L., Humbert, G., Guibal, D., Martin, L., & Blin, J. (2019). Influence of pyrolysis conditions and the nature of the wood on the quality of charcoal as a reducing agent. *Journal of Analytical and Applied Pyrolysis*, *137*, 1-13.

Eleryan, A., Güner, E. K., Hassaan, M., El-Nemr, M. A., Ragab, S., & El Nemr, A. (2024). Mandarin biochar-CO-TETA was utilized for Acid Red 73 dye adsorption from water, and its isotherm and kinetic studies were investigated. *Scientific Reports*, *14*(1), 13021.

Eleryan, A., Hassaan, M., Nazir, M. A., Shah, S. S., Ragab, S., & El Nemr, A. (2024). Isothermal and kinetic screening of methyl red and methyl orange dyes adsorption from water by Delonix regia biochar-sulfur oxide (DRB-SO). *Scientific Reports*, *14*(1), 13585.

Ferraro, G., Pecori, G., Rosi, L., Bettucci, L., Fratini, E., Casini, D., ... & Chiaramonti, D. (2021). Biochar from lab-scale pyrolysis: influence of feedstock and operational temperature. *Biomass Conversion and Biorefinery*, 1-11.

Ganesan, A., Rezazgui, O., Burgos, J. B., Mangin, P. J., & Barnabé, S. (2025). Valorization of lignocellulosic biomass forest residues in quebec via the integrated hydropyrolysis and hydroconversion (IH2) technology: A review. *Biomass and Bioenergy*, *193*, 107516.

Ganesan, A., Rezazgui, O., Langlois, S., Boussabbeh, C., & Barnabé, S. (2025). Pyrolytic conversion of construction, renovation, and demolition (CRD) wood wastes in Québec to biochar: Production, characterization, and identifying relevant stability indices for carbon sequestration. *Science of The Total Environment*, *965*, 178650.

Ghani, U., Jiang, W., Hina, K., Idrees, A., Iqbal, M., Ibrahim, M., ... & Aslam, I. (2022). Adsorption of methyl orange and Cr (VI) onto poultry manure-derived biochar from aqueous solution. *Frontiers in Environmental Science*, *10*, 887425.

Ghorbani, M., Amirahmadi, E., Neugschwandtner, R. W., Konvalina, P., Kopecký, M., Moudrý, J., ... & Murindangabo, Y. T. (2022). The impact of pyrolysis temperature on biochar properties and its effects on soil hydrological properties. *Sustainability*, *14*(22), 14722.

Gonnella, G., Ischia, G., Fambri, L., & Fiori, L. (2022). Thermal analysis and kinetic modeling of pyrolysis and oxidation of hydrochars. *Energies*, *15*(3), 950.

Greco, G., Videgain, M., Di Stasi, C., Pires, E., & Manyà, J. J. (2021). Importance of pyrolysis temperature and pressure in the concentration of polycyclic aromatic hydrocarbons in wood waste-derived biochars. *Journal of Analytical and Applied Pyrolysis*, *159*, 105337.

Grimm, A., Conrad, S., Gentili, F. G., Mikkola, J. P., Hu, T., Lassi, U., ... & dos Reis, G. S. (2025). Highly efficient boron/sulfur-modified activated biochar for removal of reactive dyes from water: Kinetics, isotherms, thermodynamics, and regeneration studies. *Colloids and Surfaces A: Physicochemical and Engineering Aspects*, 136486.

Güleç, F., Williams, O., Kostas, E. T., Samson, A., Stevens, L. A., & Lester, E. (2022). A comprehensive comparative study on methylene blue removal from aqueous solution using biochars produced from rapeseed, whitewood, and seaweed via different thermal conversion technologies. *Fuel*, *330*, 125428.

Guo, X., Liu, A., Lu, J., Niu, X., Jiang, M., Ma, Y., ... & Li, M. (2020). Adsorption mechanism of hexavalent chromium on biochar: kinetic, thermodynamic, and characterization studies. *ACS omega*, *5*(42), 27323-27331.

Hama Aziz, K. H., Fatah, N. M., & Muhammad, K. T. (2024). Advancements in application of modified biochar as a green and low-cost adsorbent for wastewater remediation from organic dyes. *Royal Society Open Science*, *11*(5), 232033.

Handiso, B., Pääkkönen, T., & Wilson, B. P. (2024). Effect of pyrolysis temperature on the physical and chemical characteristics of pine wood biochar. *Waste Management Bulletin*, *2*(4), 281-287.

Hanoon, M. A., & Ahmed, M. J. (2019). Adsorption of methyl orange from wastewater by using biochar. *Iraqi Journal of Chemical and Petroleum Engineering*, *20*(3), 23-29.

Hassaan, M. A., Yılmaz, M., Helal, M., El-Nemr, M. A., Ragab, S., & El Nemr, A. (2023). Isotherm and kinetic investigations of sawdust-based biochar modified by ammonia to remove methylene blue from water. *Scientific Reports*, *13*(1), 12724.

He, D., Luo, Y., & Zhu, B. (2024). Feedstock and pyrolysis temperature influence biochar properties and its interactions with soil substances: insights from a DFT calculation. *Science of the Total Environment*, *922*, 171259.

Hou, Y., Liang, Y., Hu, H., Tao, Y., Zhou, J., & Cai, J. (2021). Facile preparation of multi-porous biochar from lotus biomass for methyl orange removal: Kinetics, isotherms, and regeneration studies. *Bioresource Technology*, *329*, 124877.

Hu, R., Li, C., Hu, X., & Qiao, Y. (2024). Varied impacts of volatiles from pyrolysis of poplar wood, bark and leaves on property of coal char. *Journal of Analytical and Applied Pyrolysis*, *178*, 106389.

Huff, M. D., Marshall, S., Saeed, H. A., & Lee, J. W. (2018). Surface oxygenation of biochar through ozonization for dramatically enhancing cation exchange capacity. *Bioresources and Bioprocessing*, *5*(1), 1-9.

International Biochar Initiative. (2015). Standardized product definition and product testing guidelines for biochar that is used in soil. *Int. Biochar Initiat*, *23*.

Islam, M. S., Roy, H., & Afrose, S. (2022). Phosphoric acid surface modified Moringa oleifera leaves biochar for the sequestration of methyl orange from aqueous solution: Characterizations, isotherm, and kinetics analysis. *Remediation Journal*, *32*(4), 281-298.

Issaka, E., Fapohunda, F. O., Amu-Darko, J. N. O., Yeboah, L., Yakubu, S., Varjani, S., ... & Bilal, M. (2022). Biochar-based composites for remediation of polluted wastewater and soil environments: Challenges and prospects. *Chemosphere*, *297*, 134163.

Iwuozor, K. O., Ighalo, J. O., Emenike, E. C., Ogunfowora, L. A., & Igwegbe, C. A. (2021). Adsorption of methyl orange: A review on adsorbent performance. *Current Research in Green and Sustainable Chemistry*, *4*, 100179.

Jadhav, S. K., & Thorat, S. R. (2022). Adsorption of azo dyes using biochar prepared from regional crop waste material. *Biosciences Biotechnology Research Asia*, *19*(1), 141-151.

Jain, M., Khan, S. A., Sahoo, A., Dubey, P., Pant, K. K., Ziora, Z. M., & Blaskovich, M. A. (2022). Statistical evaluation of cow-dung derived activated biochar for phenol adsorption: Adsorption isotherms, kinetics, and thermodynamic studies. *Bioresource Technology*, *352*, 127030.

Jameel, R., Lashari, S., Sharif, M. N., Javaid, S., Alam, K., Mahmood, F., ... & Kokab, A. (2024). Effective Sequestration of Acid Orange-7 Dye from Wastewater by using Ricinus Communis Biochar along with Zinc Oxide Nanocomposites. *Indus Journal of Bioscience Research*, *2*(02), 1214-1222.

Jian, X., Zhuang, X., Li, B., Xu, X., Wei, Z., Song, Y., & Jiang, E. (2018). Comparison of characterization and adsorption of biochars produced from hydrothermal carbonization and pyrolysis. *Environmental Technology & Innovation*, *10*, 27-35.

Kalina, M., Sovova, S., Svec, J., Trudicova, M., Hajzler, J., Kubikova, L., & Enev, V. (2022). The effect of pyrolysis temperature and the source biomass on the properties of biochar produced for the agronomical applications as the soil conditioner. *Materials*, *15*(24), 8855.

Kaya, N., Yıldız Uzun, Z., Altuncan, C., & Uzun, H. (2022). Adsorption of Congo red from aqueous solution onto KOH-activated biochar produced via pyrolysis of pine cone and modeling of the process using artificial neural network. *Biomass Conversion and Biorefinery*, 1-23.

Khater, E. S., Bahnasawy, A., Hamouda, R., Sabahy, A., Abbas, W., & Morsy, O. M. (2024). Biochar production under different pyrolysis temperatures with different types of agricultural wastes. *Scientific Reports*, *14*(1), 2625.

Khatibi, M., Nahil, M. A., & Williams, P. T. (2023). Improving the Quality of Bio-oil Using the Interaction of Plastics and Biomass through Copyrolysis Coupled with Nonthermal Plasma Processing. *Energy & Fuels*, *38*(2), 1240-1257.

Kim, D., Hadigheh, S. A., & Wei, Y. (2024). Unlocking biosolid pyrolysis: Towards tailored biochar with different surface properties. *Materials Today Sustainability*, *27*, 100868.

Kumar, N. V., Sawargaonkar, G., Rani, C. S., Pasumarthi, R., Kale, S., Prakash, T. R., ... & Chandra, M. S. (2024). Harnessing the potential of pigeonpea and maize feedstock biochar for carbon sequestration, energy generation, and environmental sustainability. *Bioresources and Bioprocessing*, *11*(1), 5.

Lee, H., Fiore, S., & Berruti, F. (2024). Adsorption of methyl orange and methylene blue on activated biocarbon derived from birchwood pellets. *Biomass and Bioenergy*, *191*, 107446.

Lehmann, J., Rillig, M. C., Thies, J., Masiello, C. A., Hockaday, W. C., & Crowley, D. (2011). Biochar effects on soil biota–a review. *Soil biology and biochemistry*, *43*(9), 1812-1836.

Li, J., Sun, W., Lichtfouse, E., Maurer, C., & Liu, H. (2024). Life cycle assessment of biochar for sustainable agricultural application: A review. *Science of The Total Environment*, 175448.

Li, W., Dang, Q., Brown, R. C., Laird, D., & Wright, M. M. (2017). The impacts of biomass properties on pyrolysis yields, economic and environmental performance of the pyrolysis-bioenergy-biochar platform to carbon negative energy. *Bioresource technology*, *241*, 959-968.

Lin, G., Wang, Y., Wu, X., Meng, J., Ok, Y. S., & Wang, C. H. (2025). Enhancing agricultural productivity with biochar: Evaluating feedstock and quality standards. *Bioresource Technology Reports*, 102059.

Lingamdinne, L. P., Angaru, G. K. R., Pal, C. A., Koduru, J. R., Karri, R. R., Mubarak, N. M., & Chang, Y. Y. (2024). Insights into kinetics, thermodynamics, and mechanisms of chemically activated sunflower stem biochar for removal of phenol and bisphenol-A from wastewater. *Scientific Reports*, *14*(1), 4267.

Loc, N. X., Tuyen, P. T. T., Mai, L. C., & Phuong, D. T. M. (2022). Chitosan-modified biochar and unmodified biochar for methyl orange: Adsorption characteristics and mechanism exploration. *Toxics*, *10*(9), 500.

Lu, Y., Chen, J., Bai, Y., Gao, J., & Peng, M. (2019). Adsorption properties of methyl orange in water by sheep manure biochar. *Pol. J. Environ. Stud*, *28*, 3791-3797.

Ma, X., Zhou, B., Budai, A., Jeng, A., Hao, X., Wei, D., ... & Rasse, D. (2016). Study of biochar properties by scanning electron microscope–energy dispersive X-ray spectroscopy (SEM-EDX). *Communications in soil science and plant analysis*, *47*(5), 593-601.

Mahajan, T., Paikaray, S., & Mahajan, P. (2023, October). Applicability of the equilibrium adsorption isotherms and the statistical tools on to them: a case study for the adsorption of fluoride onto Mg-Fe-CO3 LDH. In *Journal of Physics: Conference Series* (Vol. 2603, No. 1, p. 012056). IOP Publishing.

Maiti, P., Mangsatabam, M., Chatterjee, A., Siddiqi, H., Mishra, A., & Meikap, B. C. (2024). In-situ synthesis of efficient ZnCl2 doped pyrolyzed biochar for adsorptive remediation of organic dyes: performance evaluation, mass transfer and mechanism. *Separation and Purification Technology*, *329*, 125096.

Makowska, M., & Dziosa, K. (2024). Influence of different pyrolysis temperatures on chemical composition and graphite-like structure of biochar produced from biomass of green microalgae Chlorella sp. *Environmental Technology & Innovation*, *35*, 103667.

Malińska, K., Dróżdż, D., Postawa, P., & Stachowiak, T. (2024). Biochar—A Filler in "Bioplastics" for Horticultural Applications. *Materials*, *17*(24), 6208.

Mariyam, S., Alherbawi, M., Pradhan, S., Al-Ansari, T., & McKay, G. (2024). Biochar yield prediction using response surface methodology: effect of fixed carbon and pyrolysis operating conditions. *Biomass Conversion and Biorefinery*, *14*(22), 28879-28892.

Marmiroli, M., Bonas, U., Imperiale, D., Lencioni, G., Mussi, F., Marmiroli, N., & Maestri, E. (2018). Structural and functional features of chars from different biomasses as potential plant amendments. *Frontiers in plant science*, *9*, 1119.

Matin, N. H., & Aydin, E. (2022). Reviewing the effect of pyrolysis temperature on the fourier-transform infrared spectra of biochars. *Acta Horticulturae et Regiotecturae*, *25*(2), 160-173.

Maziarka, P., Kienzl, N., Dieguez-Alonso, A., Fierro, V., Celzard, A., Arauzo, P. J., ... & Ronsse, F. (2024). Part 1─ Impact of pyrolysis temperature and wood particle length on vapor cracking and char porous texture in relation to the tailoring of char properties. *Energy & Fuels*, *38*(11), 9751-9771.

McCall, M. A., Watson, J. S., & Sephton, M. A. (2024). Predicting Stability of Barley Straw-Derived Biochars Using Fourier Transform Infrared Spectroscopy. *ACS Sustainable Resource Management*, *1*(9), 1975-1983.

Meroufel, B., Benali, O., Benyahia, M., Benmoussa, Y., & Zenasni, M. A. (2013). Adsorptive removal of anionic dye from aqueous solutions by Algerian kaolin: Characteristics, isotherm, kinetic and thermodynamic studies. *J. Mater. Environ. Sci*, *4*(3), 482-491.

Mihai, S., Bondarev, A., Călin, C., & Sîrbu, E. E. (2024). Adsorbent biomaterials based on natural clays and orange peel waste for the removal of anionic dyes from water. *Processes*, *12*(5), 1032.

Muema, F. M., Richardson, Y., Keita, A., & Sawadogo, M. (2024). An interdisciplinary overview on biochar production engineering and its agronomic applications. *Biomass and Bioenergy*, *190*, 107416.

Mukherjee, A., Patra, B. R., Podder, J., & Dalai, A. K. (2022). Synthesis of biochar from lignocellulosic biomass for diverse indus applications and energy harvesting: effects of pyrolysis conditions on the physicochemical properties of biochar. *Frontiers in Materials*, *9*, 870184.

Nair, R. R., Kißling, P. A., Schaate, A., Marchanka, A., Shamsuyeva, M., Behrens, P., & Weichgrebe, D. (2023). The influence of sample mass (scaling effect) on the synthesis and structure of non-graphitizing carbon (biochar) during the analytical pyrolysis of biomass. *RSC advances*, *13*(20), 13526-13539.

Nan, H., Yin, J., Yang, F., Luo, Y., Zhao, L., & Cao, X. (2021). Pyrolysis temperature-dependent carbon retention and stability of biochar with participation of calcium: Implications to carbon sequestration. *Environmental Pollution*, *287*, 117566.

Nartey, O. D., & Zhao, B. (2014). Biochar preparation, characterization, and adsorptive capacity and its effect on bioavailability of contaminants: an overview. *Advances in Materials Science and Engineering*, *2014*(1), 715398.

Nicholas, H. L., Mabbett, I., Apsey, H., & Robertson, I. (2022). Physico-chemical properties of waste derived biochar from community scale faecal sludge treatment plants. *Gates Open Research*, *6*, 96.

Nirmaladevi, S., & Palanisamy, N. (2020). A comparative study of the removal of cationic and anionic dyes from aqueous solutions using biochar as an adsorbent. *Desalination and Water Treatment*, *175*, 282-292.

Nizam, N. U. M., Hanafiah, M. M., Mahmoudi, E., Halim, A. A., & Mohammad, A. W. (2021). The removal of anionic and cationic dyes from an aqueous solution using biomass-based activated carbon. *Scientific Reports*, *11*(1), 1-17.

Nkomo, N., Odindo, A. O., Musazura, W., & Missengue, R. (2021). Optimising pyrolysis conditions for high-quality biochar production using black soldier fly larvae faecal-derived residue as feedstock. *Heliyon*, *7*(5).

Panizio, R., Castro, C., Pacheco, N., Assis, A. C., Longo, A., Vilarinho, C., ... & Nobre, C. (2024). Investigation of biochars derived from waste lignocellulosic biomass and insulation electric cables: A comprehensive TGA and Macro-TGA analysis. *Heliyon*, *10*(18).

Patel, M. R., & Panwar, N. L. (2024). Development, process optimization and assessment of sustainable mobile biochar kiln for agricultural use. *Journal of Cleaner Production*, *477*, 143866.

Patel, S., Kundu, S., Halder, P., Veluswamy, G., Pramanik, B., Paz-Ferreiro, J., ... & Shah, K. (2019). Slow pyrolysis of biosolids in a bubbling fluidised bed reactor using biochar, activated char and lime. *Journal of Analytical and Applied Pyrolysis*, *144*, 104697.

Pei, S., Zhao, Y., Li, W., Qu, C., Ren, Y., Yang, Y., ... & Wu, C. (2023). Critical impact of pyrolysis temperatures on biochars for peroxymonosulfate activation: Structural characteristics, degradation performance and mechanism. *Chemical Engineering Journal*, *477*, 147274.

Praveen, S., Jegan, J., Bhagavathi Pushpa, T., Gokulan, R., & Bulgariu, L. (2022). Biochar for removal of dyes in contaminated water: an overview. *Biochar*, *4*(1), 10.

Priyanka, Vashisht, D., Ibhadon, A. O., Mehta, S. K., & Taylor, M. J. (2024). Enhanced wastewater remediation using mesoporous activated wheat straw biochars: a dye removal perspective. *ACS Sustainable Resource Management*, *1*(2), 355-367.

Ramath, R., Sukumaran, A. M., Ramachandran, A., & Basheer, S. B. (2023). Methyl orange dye adsorption and degradation at low temperature using iron oxide-incorporated biochar derived from industrial by-products. *Bioresource Technology Reports*, *22*, 101470.

Rathnayake, N., Patel, S., Hakeem, I. G., Pazferreiro, J., Sharma, A., Gupta, R., ... & Shah, K. (2023). Co-pyrolysis of biosolids with lignocellulosic biomass: Effect of feedstock on product yield and composition. *Process Safety and Environmental Protection*, *173*, 75-87.

Raza, A., Mahmoud, M., Alafnan, S., Arif, M., Kirmani, F., Kamal, M. S., ... & Rana, A. (2024). Role of high-density brines in reservoir development stages: A review. *Energy Geoscience*, 100304.

Robey, N. M., Solo-Gabriele, H. M., Jones, A. S., Marini, J., & Townsend, T. G. (2018). Metals content of recycled construction and demolition wood before and after implementation of best management practices. *Environmental Pollution*, *242*, 1198-1205.

Ronsse, F., Van Hecke, S., Dickinson, D., & Prins, W. (2013). Production and characterization of slow pyrolysis biochar: influence of feedstock type and pyrolysis conditions. *Gcb Bioenergy*, *5*(2), 104-115.

Roshan, A., Ghosh, D., & Maiti, S. K. (2023). How temperature affects biochar properties for application in coal mine spoils? A meta-analysis. *Carbon Research*, *2*(1), 3.

Saleem, M., & Baig, N. (2018, December). Production of bio-oil and bio-char from different biomass wastes. In *IOP Conference Series: Materials Science and Engineering* (Vol. 458, No. 1, p. 012021). IOP Publishing.

Salinas-Farran, L., Mosonik, M. C. A., Jervis, R., Marathe, S., Rau, C., & Volpe, R. (2024). Tracked evolution of single biochar particle's morphology during pyrolysis in operando x-ray micro-computed tomography. *Biochar*, *6*(1), 86.

Sangsuk, S., Suebsiri, S., & Puakhom, P. (2018). The metal kiln with heat distribution pipes for high quality charcoal and wood vinegar production. *Energy for Sustainable Development*, *47*, 149-157.

Senapati, S., Giri, J., Mallick, L., Singha, D., Bastia, T. K., Rath, P., ... & Panda, A. K. (2025). Rapid adsorption of industrial cationic dye pollutant using base-activated rice straw biochar: performance, isotherm, kinetic and thermodynamic evaluation. *Discover Sustainability*, *6*(1), 46.

Serban, G. V., Iancu, V. I., Dinu, C., Tenea, A., Vasilache, N., Cristea, I., ... & Chiriac, F. L. (2023). Removal efficiency and adsorption kinetics of methyl orange from wastewater by commercial activated carbon. *Sustainability*, *15*(17), 12939.

Shaaban, A., Se, S. M., Dimin, M. F., Juoi, J. M., Husin, M. H. M., & Mitan, N. M. M. (2014). Influence of heating temperature and holding time on biochars derived from rubber wood sawdust via slow pyrolysis. *Journal of Analytical and Applied Pyrolysis*, *107*, 31-39.

Shafiq, M., Alazba, A. A., & Amin, M. T. (2021). Kinetic and isotherm studies of Ni2+ and Pb2+ adsorption from synthetic wastewater using Eucalyptus camdulensis—Derived biochar. *Sustainability*, *13*(7), 3785.

Sharma, T., & Ratner, A. (2021). Analysis and characterization of metallic nodules on biochar from single-stage downdraft gasification. *Processes*, *9*(3), 533.

Shi, Y. Y., Shan, R., & Yuan, H. R. (2019). Effects and mechanisms of methyl orange removal from aqueous solutions by modified rice shell biochar. *Huan Jing ke Xue= Huanjing Kexue*, *40*(6), 2783-2792.

Sivaranjanee, R., Kumar, P. S., Chitra, B., & Rangasamy, G. (2024). A critical review on biochar for the removal of toxic pollutants from water environment. *Chemosphere*, 142382.

Suárez-Hernández, L., & Barrera-Zapata, R. (2017). Morphological and physicochemical characterization of biochar produced by gasification of selected forestry species. *Revista Facultad de Ingeniería*, *26*(46), 123-130.

Świechowski, K., Matyjewicz, B., Telega, P., & Białowiec, A. (2022). The influence of low-temperature food waste biochars on anaerobic digestion of food waste. *Materials*, *15*(3), 945.

Tcheka, C., Conradie, M. M., Assinale, V. A., & Conradie, J. (2024). Mesoporous biochar derived from Egyptian doum palm (Hyphaene thebaica) shells as low-cost and biodegradable adsorbent for the removal of methyl orange dye: Characterization, kinetic and adsorption mechanism. *Chemical Physics Impact*, *8*, 100446.

Teweldebrihan, M. D., & Dinka, M. O. (2024). Methyl red adsorption from aqueous solution using Rumex Abyssinicus-derived biochar: Studies of kinetics and isotherm. *Water*, *16*(16), 2237.

Tomczyk, A., Sokołowska, Z., & Boguta, P. (2020). Biochar physicochemical properties: pyrolysis temperature and feedstock kind effects. *Reviews in Environmental Science and Bio/Technology*, *19*(1), 191-215.

Van Hien, N., Valsami-Jones, E., Vinh, N. C., Phu, T. T., Tam, N. T. T., & Lynch, I. (2020). Effectiveness of different biochar in aqueous zinc removal: Correlation with physicochemical characteristics. *Bioresource Technology Reports*, *11*, 100466.

Venkatesh, G., Gopinath, K. A., Reddy, K. S., Reddy, B. S., Prabhakar, M., Srinivasarao, C., ... & Singh, V. K. (2022). Characterization of biochar derived from crop residues for soil amendment, carbon sequestration and energy use. *Sustainability*, *14*(4), 2295.

Wang, J., & Guo, X. (2020). Adsorption isotherm models: Classification, physical meaning, application and solving method. *Chemosphere*, *258*, 127279.

Wang, Z., Li, J., Liu, G., & Li, C. (2024). Biochar obtained from alkaline earth metal-treated mushroom residue: Thermal behavior and methyl orange adsorption capability. *Journal of Environmental Management*, *351*, 119669.

Wei, X., Miao, J., Lv, Z., Wan, X., Zhang, N., Zhang, R., & Peng, S. (2022). Phosphate adsorption onto an Al-Ti bimetal oxide composite in neutral aqueous solution: performance and thermodynamics. *Applied Sciences*, *12*(5), 2309.

Windeatt, J. H., Ross, A. B., Williams, P. T., Forster, P. M., Nahil, M. A., & Singh, S. (2014). Characteristics of biochars from crop residues: Potential for carbon sequestration and soil amendment. *Journal of environmental management*, *146*, 189-197.

Wu, L., Liu, X., Lv, G., Zhu, R., Tian, L., Liu, M., ... & Liao, L. (2021). Study on the adsorption properties of methyl orange by natural one-dimensional nano-mineral materials with different structures. *Scientific reports*, *11*(1), 10640.

Xiong, Z., Huanhuan, Z., Jing, W., Wei, C., Yingquan, C., Gao, X., ... & Hanping, C. (2021). Physicochemical and adsorption properties of biochar from biomass-based pyrolytic polygeneration: effects of biomass species and temperature. *Biochar*, *3*, 657-670.

Xu, C., Wei, K., Du, Z., & Ma, W. (2024). Effect of particle size on the properties of biomass gasification residue pellets used as a metallurgical-grade silicon reducing agent. *Powder Technology*, *435*, 119406.

Yu, K. L., Lau, B. F., Show, P. L., Ong, H. C., Ling, T. C., Chen, W. H., ... & Chang, J. S. (2017). Recent developments on algal biochar production and characterization. *Bioresource technology*, *246*, 2-11.

Zhang, K., Zhang, K., Li, Y., Kang, Q., Wang, Y., Wang, J., ... & Mao, J. (2023). Easily Pyrolyzable Biomass Components Significantly Affect the Physicochemical Properties and Water-Holding Capacity of the Pyrolyzed Biochar. *Agriculture*, *13*(11), 2053.

Zhao, X., Wang, J., Zhu, G., Zhang, S., Wei, C., Liu, C., ... & Zhang, S. (2024). Efficient removal of high concentration dyes from water by functionalized in-situ N-doped porous biochar derived from waste antibiotic fermentation residue. *Chemosphere*, *364*, 143215.

Zou, X., Debiagi, P., Amjed, M. A., Zhai, M., & Faravelli, T. (2024). Impact of high-temperature biomass pyrolysis on biochar formation and composition. *Journal of Analytical and Applied Pyrolysis*, *179*, 106463.

Zubair, M., Mu'azu, N. D., Jarrah, N., Blaisi, N. I., Aziz, H. A., & A. Al-Harthi, M. (2020). Adsorption behavior and mechanism of methylene blue, crystal violet, eriochrome black T, and methyl orange dyes onto biochar-derived date palm fronds waste produced at different pyrolysis conditions. *Water, Air, & Soil Pollution*, *231*, 1-19

6. Supplementary information

6.1 Process conditions for CRD wood pyrolysis DOE model

For analysing the influence of pyrolysis process conditions on biochar properties using response surface methodology's (RSM) central composite design (CCD), three independent variables or factors coded as A, B, C, with five levels of operation parameters coded as -α, -1, 0, 1, α, were considered as in Supplementary figure 16. These variables were pyrolysis temperature (400-800 °C), BRT (30-90 min), and mass of CRD wood feedstock loaded into the reactor for pyrolysis (50-250 g). To have a robust representation of the design, eight factorial or corner points (p_f), six axial points (p_a), and one to three center points (p_c) could be suitable to derive adequate conclusions for a system. In fact, the number of independent variables can also be increased for a more thorough evaluation but the total number of experimental investigations will proportionally increase, thus, increasing resource utilization w.r.t feedstock, time, money, and energy. Nevertheless, this design efficiently marks important relationships between process parameters to render superior performances of the pyrolysis system.

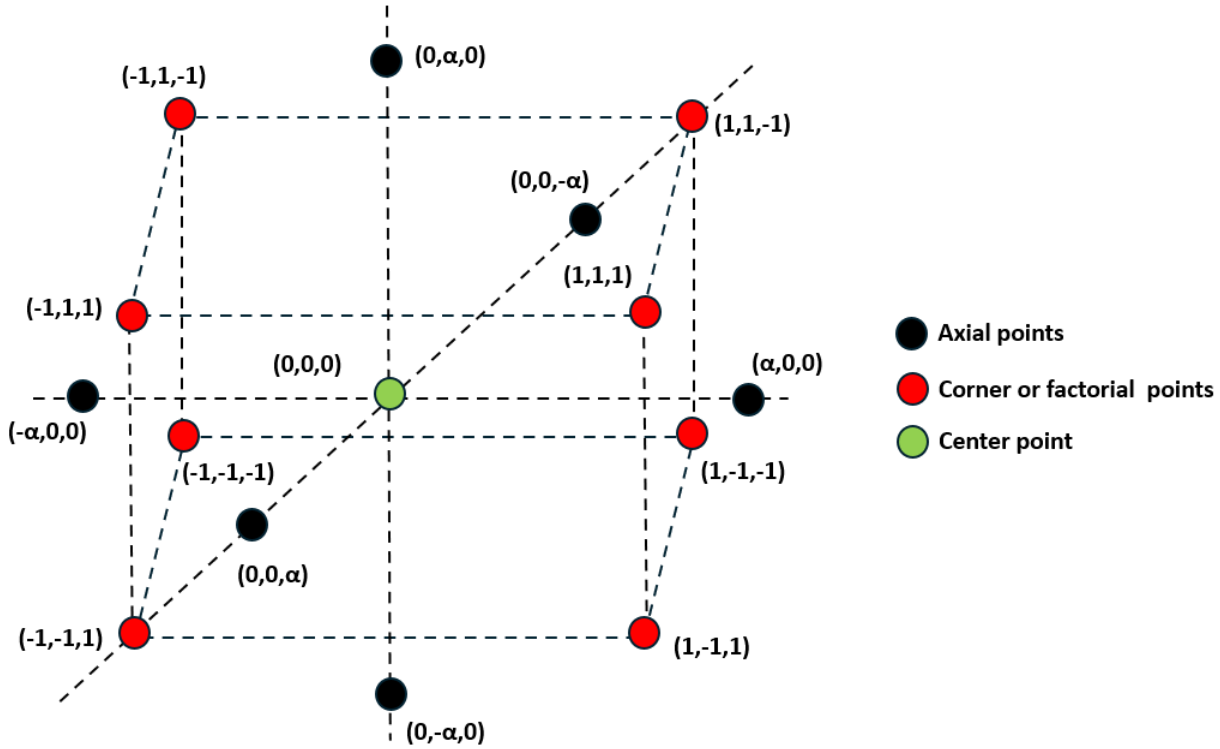

Supplementary figure 16: RSM's CCD design points

The total number of experimental rounds to be carried out, can be determined by Supplementary equation 1,

$$N = p_f + p_a + p_c$$

Supplementary equation 1

This can also be written arithmetically as in Supplementary equation 2:

$$N = 2^k + 2k + 1$$

Supplementary equation 2

Here, 'k' represents total number of independent variables. Here, only one center point has been mentioned. More center point experiments could be run to ensure reliability. In our case, a duplicate experiment was carried out for a non-center point. The equation and total number of experiments now become:

$$N = 2^3 + 2(3) + 1 = 15$$

Supplementary equation 3

The value of axial point, α, is given as in Supplementary equation 4:

$$\alpha = (2^k)^{1/4}$$

Supplementary equation 4

For three independent variables,

$$\alpha = (2^3)^{\frac{1}{4}} = 1.682$$

Supplementary equation 5

An experimental design for the three independent variables can be adopted w.r.t the coded values of all five levels as shown in Supplementary table 4.

Supplementary table 4: Run order with coded and actual values for pyrolysis independent variables

Standard order	Run order	Coded and actual values for independent variables		
		A: Temperature (°C)	B: BRT (min)	C: Mass of feedstock (g)
11	1	400 **(-α)**	60 **(0)**	100 **(-1)**
2	2	600 **(0)**	90 **(+α)**	200 **(+1)**
16	3	600 **(0)**	30 **(-α)**	200 **(+1)**
3	4	500 **(-1)**	75 **(+1)**	200 **(+1)**
1	5	600 **(0)**	60 **(0)**	100 **(-1)**
6	6	500 **(-1)**	75 **(+1)**	150 **(0)**
13	7	500 **(-1)**	90 **(+α)**	150 **(0)**
10	8	600 **(0)**	45 **(-1)**	50 **(-α)**
5	9	700 **(+1)**	90 **(+α)**	200 **(+1)**
4	10	800 **(+α)**	75 **(+1)**	200 **(+1)**
7	11	700 **(+1)**	75 **(+1)**	200 **(+1)**
9	12	500 **(-1)**	90 **(+α)**	250 **(+α)**
8	13	600 **(0)**	90 **(+α)**	250 **(+α)**
15	14	700 **(+1)**	45 **(-1)**	150 **(0)**
14	15	400 **(-α)**	90 **(+α)**	200 **(+1)**
12	16	600 **(0)**	60 **(0)**	150 **(0)**

6.2 Statistical analysis for DOE

Supplementary table 5: Coefficients table for DOE independent variables to evaluate their influence on the different response variables. The p-values for pyrolysis temperature (A) are <0.05 for all response variables suggesting that it has the most dominant influence on biochar properties

	Intercept	A	B	C	AB	AC	BC	A^2	B^2	C^2
Carbon	81.9567	6.2301	0.7381	1.9317						
p-values		0.0002	0.5617	0.4435						
BET surface area	230.5020	84.6827	57.4696	-23.4390	4.2486	-12.0859	-125.5880	-46.6398	10.6473	209.0550
p-values		0.0010	0.0194	0.3150	0.8474	0.7916	0.0230	0.0034	0.2764	0.0119
Volatile carbon (VC)	18.0237	-6.6995	-0.1090	0.9720						
p-values		< 0.0001	0.8912	0.5392						
Fixed carbon (FC)	75.2320	6.0109	1.2705	-0.6543						
p-values		0.0099	0.5398	0.8718						
TGA R50	0.5942	0.0371	-0.0035	-0.0226						
p-values		0.0001	0.6195	0.1190						
H/C	0.3136	-0.2017	-0.0224	0.0303	-0.0075	0.1497	0.0153			
p-values		< 0.0001	0.1099	0.1850	0.7145	0.0038	0.4522			
O/C	0.0613	-0.0829	-0.0040	0.0121	-0.0162	0.1069	0.0112			
p-values		< 0.0001	0.6894	0.4763	0.3198	0.0059	0.4779			
Thermostable fraction (TSF)	79.9473	8.1060	1.5941	-0.9558						
p-values		0.0032	0.4937	0.8336						
Micropore volume	0.1130	0.0426	0.0240	-0.0086	-0.0006	-0.0061	-0.0478	-0.0203	0.0016	0.0806
p-values		0.0004	0.0214	0.3844	0.9532	0.7546	0.0358	0.0031	0.6873	0.0184

Supplementary table 6: Fit statistics for DOE response variables

	Carbon	BET surface area	Volatile carbon (VC)	Fixed carbon (FC)	TGA R50	H/C	O/C	Thermostable fraction (TSF)	Micropore volume
Std. Dev.	4.13	26.79	2.61	6.72	0.03	0.03	0.02	7.54	0.01
Mean	81.86	236.15	19.22	74.94	0.58	0.35	0.09	79.47	0.11
C.V. %	5.05	11.34	13.55	8.97	3.92	9.17	28.68	9.49	10.41
R^2	0.73	0.97	0.88	0.45	0.77	0.98	0.93	0.54	0.98
Adjusted R^2	0.66	0.93	0.84	0.31	0.71	0.96	0.89	0.43	0.94
Predicted R^2	0.46	0.62	0.77	0.12	0.50	0.74	0.52	0.26	0.44
Adeq Precision	11.38	15.19	17.23	6.14	11.22	31.54	17.56	7.33	16.36

6.3 Energy and efficiency calculations for biochar production in different reactor configurations – A thermal decomposition perspective

For estimating the material energy balance and performance efficiency of the two pyrolysis reactors utilized (horizontal tube furnace and rotary retort-furnace units) in which isobaric (all tests at constant atmospheric pressure) thermochemical conversions of CRD wood under the same temperatures, BRT, but different mass of feed (50-250 g versus 3 kg) was carried out, calculation of total energy input, energy output, net energy loss followed by pyrolyzer efficiency are important steps. Energy input is basically derived from the CRD biomass feedstock entering the reactor whereas energy output is the heat spent/lost to volatilize inbound biomass water as steam or superheated steam (gas) along with the energy value of biochar product. Equations for these calculations were referred from Patel and Panwar, 2024 and Sangsuk et al., 2018. Here, energy value of biooil and pyrolysis gas were not considered because of three reasons: a) no instrumentation for gas collection and condensation (so, biooil and gas yield cannot be estimated) was used during the experiments; b) any pyrolysis gas generated was directly fed to the combustion chamber of the in-house pilot pyrolyzer via a vacuum suction pump/hose for contributing to a meagre part of its energy demand; and c) calculation of HHV for non-biochar products from pyrolysis like biooil, dust, fines, and pyrolysis gas was not possible due to absence of appropriate collection units. Since biomass conversion to biochar is mainly reliant on material heat transfer, an external metric like reactor power consumption is also not directly related to this particular thermal decomposition process.

Hence, for material energy balance calculations, only biochar was treated as the product of interest and recovered from the pyrolysis reactor. For CRD wood prior to pyrolysis, its 0.18% moisture post-drying, was considered.

Firstly, energy input is calculated using the expression:

$$Q_{input} = \text{Mass of CRD wood} \times \text{HHV of CRD wood}$$

Supplementary equation 6

where, mass of wood is expressed as kg and its HHV as KJ/kg.

As the next part, energy output can be calculated as three separate steps. This includes loss of energy due to the necessity in evaporation of water to different phases, and energy retention in biochar produced. In the first step, energy required to remove the 0.18% water in biomass as vapor or saturated steam is calculated, i.e, as latent heat:

$$\mathrm{Q_{water,vapor}}\ (\text{or})\ Q_{w,v} = \mathrm{n} \times \mathrm{C_{p,v}} \times (373 - \mathrm{T_{RT}})$$

Supplementary equation 7

Here, n is the number of moles of water in CRD biomass, $C_{p,v}$ is the specific heat capacity (C_p) of water vapor at 100 °C or 373 K expressed as (KJ/mol.K), and T_{RT} is the ambient temperature in K. The final unit of $Q_{water,vapor}$ is KJ. As the second step, energy spent to convert this vapor or steam to gas or superheated steam is calculated as:

$$\mathrm{Q_{water,gas}}\ (\text{or})\ Q_{w,g} = \mathrm{n} \times \mathrm{C_{p,g}} \times (\mathrm{T_{PG}} - 373)$$

Supplementary equation 8

Here, n is the number of moles of water in CRD biomass, $C_{p,g}$ is the specific heat capacity (C_p) of water as gas derived out of the three pyrolysis rounds at 500, 700, and 800 °C expressed as (KJ/mol.K), and T_{PG} is the pyrolysis gas temperature in K. The final unit of $Q_{water,gas}$ is KJ. As the third step, energy content of biochar is calculated as:

$$\mathrm{Q_{biochar}} = \text{Yield of biochar} \times \text{HHV of biochar}$$

Supplementary equation 9

Yield and HHV of biochar are calculated for each of the three pyrolysis rounds resulting in B500, B700, and B800. These three conditions were picked for the horizontal tube furnace reactor since all these conditions harbor the same BRT, mass of feedstock, and only vary across pyrolysis temperatures. This would facilitate easy mapping of the reactor's performance efficiencies as variations in energy requirements exist. Also, the temperature of pyrolysis gas is usually lower than the set point pyrolysis temperature mostly due to convective or radiative heat losses arising from the reactor's design. This was the same set up used in Ganesan et al., 2025 where thermal inertia did not exceed over 150 °C (upper range) for tests conducted even at 800 °C. In the horizontal rotary retort-

furnace reactor set up, a 15-fold higher feed mass was utilized to check the robustness of our experimental design. Here too, thermal inertia has the same 150 °C upper range.

The total energy output was then calculated as:

$$Q_{output} = Q_{water,vapor} + Q_{water,gas} + Q_{biochar}$$

Supplementary equation 10

With this, the net energy loss is calculated using the expression:

$$Q_{net} = Q_{input} - Q_{output}$$

Supplementary equation 11

Pyrolysis efficiency, η_{system}, can then be computed via:

$$\eta_{system} = \frac{Q_{output}}{Q_{input}} \times 100$$

Supplementary equation 12

Variations in Q_{output} and η_{system} are observed with different degrees of thermal inertia.

For determining the pyrolyzer system's energy performance, three scenarios were considered w.r.t thermal inertia: no thermal inertia, 100 °C, and 200 °C. Heat loss through thermal inertia generally means that the set point temperature is not exactly reached by the biomass inside the reaction zone since. So, the temperature of product gas also is lowered and correlates negatively with thermal inertia. From Supplementary table 7, the first observation is that heat loss assumptions did not have any drastic influence over η_{system}. For example, in the horizontal tube furnace and the rotary retort-furnace reactors, η_{system} dropped from about 39% to 34% and 47% to 40% commonly across all three thermal inertia classes, respectively. It is only within each category that efficiency decreased with rise in temperature. As increase in pyrolysis temperatures meant that more energy is spent to convert inherent water from the vapor or steam phase to the gas phase, increments in $Q_{w,g}$ was spotted. On the contrary, an immediate response of decrease in $Q_{w,g}$ and eventually Q_{output} were seen when heat loss faced by the reactor comes into play and superheating water vapor to that specific temperature (to match the new pyrolysis gas temperature) gets complicated – all pointing out at consequences of differences between the internal temperature faced by biomass in the retort during pyrolysis and the external furnace temperature, also termed as thermal gradient. Additionally, if the initial water content was also higher than 0.18%, more energy would be needed to drive it towards boiling point and greater will be the value of $Q_{w,v}$ too, that would belittle the concept of sensible heating. So, drying the biomass feedstock prior to pyrolysis is an unavoidable upstream step that must be followed to reduce energy consumption and overall losses in moisture handling, and prevent any delay in conversion. When calculating $Q_{biochar}$, it decreased from 1.6 MJ to 1.4 MJ and 28.6 MJ to 24.8 MJ along B500, B700, and B800 for both reactors mainly due to a reduction in yield with high pyrolysis temperatures. The yield of biochar from B500-B800 reduced from 26.9% to 21.1% and 32.1% to 26.2% for the horizontal tube furnace and rotary retort-furnace reactors, respectively. This invariably has a direct impact on the amount of energy lost during the process as waste heat (Q_{net}). In fact, for the rotary retort set up, both energy loss and efficiency can reach extremities owing to the relatively larger size of equipment and quantity of material handled.

Supplementary table 7: Material energy balance and pyrolyzer efficiency during biomass thermal decomposition. Case 1: 0.18% internal moisture

Horizontal tube furnace reactor with feeding of CRD wood containing 0.18 wt% initial moisture								
Sample	**Pyrolysis set point temperature (K)**	**Q_{input} (KJ)**	**$Q_{water,vapor}$ (kJ)**	**$Q_{water,gas}$ (kJ)**	**$Q_{biochar}$ (kJ)**	**Q_{output} (kJ)**	**Q_{net} (kJ)**	**η_{system} (%)**
Assuming no thermal inertia during pyrolysis								
B500	**773.00**	4056.00	0.05	0.35	1601.09	1601.49	2454.51	39.48
B700	**973.00**	4056.00	0.05	0.52	1514.65	1515.22	2540.78	37.36
B800	**1073.00**	4056.00	0.05	0.62	1381.63	1382.30	2673.70	34.08
Assuming 100 °C thermal inertia during pyrolysis								
B500	**773.00**	4056.00	0.05	0.27	1601.09	1601.41	2454.59	39.48
B700	**973.00**	4056.00	0.05	0.44	1514.65	1515.14	2540.86	37.36
B800	**1073.00**	4056.00	0.05	0.52	1381.63	1382.20	2673.80	34.08
Assuming 200 °C thermal inertia during pyrolysis								
B500	**773.00**	4056.00	0.05	0.20	1601.09	1601.34	2454.66	39.48
B700	**973.00**	4056.00	0.05	0.35	1514.65	1515.05	2540.95	37.35
B800	**1073.00**	4056.00	0.05	0.44	1381.63	1382.12	2673.88	34.08
Horizontal rotary retort-furnace reactor with feeding of CRD wood containing 0.18 wt% initial moisture								
Sample	**Pyrolysis set point temperature (K)**	**Q_{input} (KJ)**	**$Q_{water,vapor}$ (KJ)**	**$Q_{water,gas}$ (KJ)**	**$Q_{biochar}$ (KJ)**	**Q_{output} (KJ)**	**Q_{net} (KJ)**	**η_{system} (%)**
Assuming no thermal inertia during pyrolysis								
B500	**773.00**	60840.00	0.79	5.32	28604.39	28610.49	32229.51	47.03
B700	**973.00**	60840.00	0.79	7.86	25859.28	25867.93	34972.07	42.52
B800	**1073.00**	60840.00	0.79	9.23	24827.60	24837.62	36002.38	40.82
Assuming 100 °C thermal inertia during pyrolysis								
B500	**773.00**	60840.00	0.79	4.08	28604.39	28609.26	32230.74	47.02
B700	**973.00**	60840.00	0.79	6.57	25859.28	25866.64	34973.36	42.52
B800	**1073.00**	60840.00	0.79	7.86	24827.60	24836.25	36003.75	40.82
Assuming 200 °C thermal inertia during pyrolysis								
B500	**773.00**	60840.00	0.79	2.94	28604.39	28608.12	32231.88	47.02
B700	**973.00**	60840.00	0.79	5.32	25859.28	25865.38	34974.62	42.51
B800	**1073.00**	60840.00	0.79	6.57	24827.60	24834.96	36005.04	40.82

As concurred before, a second case where initial moisture content in CRD wood of 18% (without drying and as received) was also considered, with the assumption of same biochar yields as in the case of pyrolysis with dried CRD wood (Supplementary table 8). Due to 100-fold increase in biomass water content, $Q_{w,g}$ also increases by the 100-fold margin as pyrolysis temperatures increased from 500-800 °C. The same goes for $Q_{w,v}$ since more energy is wasted to volatilize moisture to steam or vapor. Even then, an increase in Q_{output}, decrease in Q_{net}, and increase in η_{system} this time, it is only due to the higher amount of energy spent to vaporize the 18% water in biomass. At a first glance, this finding seems to be counterintuitive but can be validated by simple thermodynamic concepts coming into play. As much as higher internal moisture content before pyrolysis may have a negative influence in thermal decomposition, its presence up to a certain level is beneficial in some ways. Firstly, this 18% moisture could absorb the heat offered during pyrolysis in a gradual manner, allowing reduced overheating, energy losses (under thermal inertia), and increases Q_{output}. Secondly, the moisture also acts as a thermal buffering agent and stabilizes the system from experiencing excessive heat loss via quick release of pyrolysis gases, thereby, reducing Q_{net}. Lastly, there could be a steady heat transfer amidst the feedstock and within the system that results in better heat management and usage till fruition, increasing overall efficiency.

Supplementary table 8: Material energy balance and pyrolyzer efficiency during biomass thermal decomposition. Case 2: 18% internal moisture

Horizontal tube furnace reactor with feeding of CRD wood containing 18 wt% initial moisture								
Sample	**Pyrolysis set point temperature (K)**	**Q_{input} (kJ)**	**$Q_{water,vapor}$ (kJ)**	**$Q_{water,gas}$ (kJ)**	**$Q_{biochar}$ (kJ)**	**Q_{output} (kJ)**	**Q_{net} (kJ)**	**η_{system} (%)**
Assuming no thermal inertia during pyrolysis								
B500	**773.00**	4056.00	5.25	35.45	1601.09	1641.78	2414.22	40.48
B700	**973.00**	4056.00	5.25	52.40	1514.65	1572.30	2483.70	38.76
B800	**1073.00**	4056.00	5.25	61.55	1381.63	1448.42	2607.58	35.71
Assuming 100 °C thermal inertia during pyrolysis								
B500	**773.00**	4056.00	5.25	27.18	1601.09	1633.52	2422.48	40.27
B700	**973.00**	4056.00	5.25	43.81	1514.65	1563.71	2492.29	38.55
B800	**1073.00**	4056.00	5.25	52.40	1381.63	1439.28	2616.72	35.49
Assuming 200 °C thermal inertia during pyrolysis								
B500	**773.00**	4056.00	5.25	19.59	1601.09	1625.92	2430.08	40.09
B700	**973.00**	4056.00	5.25	35.45	1514.65	1555.34	2500.66	38.35
B800	**1073.00**	4056.00	5.25	43.81	1381.63	1430.69	2625.31	35.27
Horizontal rotary retort-furnace reactor with feeding of CRD wood containing 18 wt% initial moisture								
Sample	**Pyrolysis set point temperature (K)**	**Q_{input} (KJ)**	**$Q_{water,vapor}$ (kJ)**	**$Q_{water,gas}$ (kJ)**	**$Q_{biochar}$ (kJ)**	**Q_{output} (kJ)**	**Q_{net} (kJ)**	**η_{system} (%)**
Assuming no thermal inertia during pyrolysis								
B500	**773.00**	60840.00	78.75	531.70	28604.39	29214.84	31625.16	48.02
B700	**973.00**	60840.00	78.75	786.00	25859.28	26724.03	34115.97	43.93
B800	**1073.00**	60840.00	78.75	923.19	24827.60	25829.55	35010.45	42.45
Assuming 100 °C thermal inertia during pyrolysis								
B500	**773.00**	60840.00	78.75	407.76	28604.39	29090.91	31749.09	47.82
B700	**973.00**	60840.00	78.75	657.17	25859.28	26595.21	34244.79	43.71
B800	**1073.00**	60840.00	78.75	786.00	24827.60	25692.35	35147.65	42.23
Assuming 200 °C thermal inertia during pyrolysis								
B500	**773.00**	60840.00	78.75	293.78	28604.39	28976.92	31863.08	47.63
B700	**973.00**	60840.00	78.75	531.70	25859.28	26469.73	34370.27	43.51
B800	**1073.00**	60840.00	78.75	657.17	24827.60	25563.53	35276.47	42.02

To sum up, for increasing the efficiency of a pyrolyzer producing biochar as the main product of interest, it needs to operate with a biomass feedstock of low moisture content, small and uniform particle size to avoid heat transfer limitations, and moderate pyrolysis temperature that could conserve yield (high $Q_{biochar}$) as well as curb excessive energy loss while heating steam to reach set point temperatures. As for design optimization, air-tight sealing of entry and exit ports, pre-heating carrier gas, maneuvering rotation speeds in the case of rotary retorts, sheathing ceramic fibers or quartz wool-like material that can offer good insulation around the reactor's body or extremities, and retrofitting heat/biooil/gas/dust recovery and re-usage equipment are immediate suggestions to taper operational costs and maximize energy quality. On a bigger picture, for calculating overall system efficiency, **reactor power consumption** is also to be included especially when energy integration or re-use (*e.g.:* pyrolysis gas recycling to offset a part of external energy) is under consideration. It is a vital metric for cost analysis and is a huge part of operational expenses determining the system's economic feasibility. Power consumption by auxiliary instrumentation like pumps, cooling, and product recycling systems must also be taken into consideration along with relevant heat losses.

6.4 Methyl orange batch adsorption experiments – An application for CRD wood biochar from the DOE

This section encompasses all theoretical foundations for the adsorption experiments and consists of kinetic, equilibrium, and thermodynamic model equations.

The removal efficiency of B600 adsorbent can be calculated using the expression:

$$\text{Removal efficiency (\%)} = \left(\frac{C_o - C_e}{C_o}\right) \times 100$$

Supplementary equation 13

Where, C_o and C_e are the initial and equilibrium methyl orange (adsorbate) concentrations in the test solution (mg/L (or) ppm), respectively. The equilibrium adsorption capacity (q_e) of B600 can be calculated with the equation:

$$q_e\ (mg/g) = \frac{(C_o - C_e)V}{M}$$

Supplementary equation 14

Where, V is the total volume of the test solution (L) and M is the mass of B600 adsorbent used for the experiment (g).

6.4.1 Adsorption isotherms and effect of initial methyl orange concentrations

Adsorption isotherms typically describe how much of adsorbate is trapped w.r.t to a unit mass of the adsorbent in a given time. For this, 50 mL test solutions with different known concentrations of methyl orange: 8, 30, 40, and 164 ppm, were subjected to adsorption experiments using B600 under the optimal conditions of 50 °C, 24 h (1440 min), pH of 3, and a constant B600 loading of 10 mg/mL (0.5 g/50 mL or 10 g/L). With the resulting C_e and q_e, three models namely, Langmuir, Freundlich, and Temkin isotherms were designed, each highlighting specific adsorption patterns. Upon fitting the experimental adsorption data to these models, adsorption parameters were determined.

6.4.1.1 Langmuir isotherm

Theoretically speaking, Langmuir model states that an adsorbent has specific or finite number of uniform adsorption sites arranged as a single boundary layer with the same binding nature to which the adsorbate firmly attaches to, without any rampant migration from one binding site to another. From Güleç et al., 2022, the parameter q_e derived from this model can be expressed via a non-linear equation as:

$$q_e = \frac{C_e q_m K_L}{1 + C_e K_L}$$

Supplementary equation 15

The above equation can be represented in a straight-line format, y=mx+c.

$$\frac{1}{q_e} = \left(\frac{1}{K_L q_m}\right)\frac{1}{C_e} + \frac{1}{q_m}$$

Supplementary equation 16

Plotting $1/q_e$ versus $1/C_e$ yields a linear plot with an intercept ($1/q_m$) and slope ($1/K_L q_m$) that are used to calculate q_m and K_L. From Tcheka et al., 2024, q_m represents the required adsorbate per unit mass of the adsorbent (mg/g) when monolayer adsorption can be completed to fruition, and K_L denotes the Langmuir isotherm constant describing the affinity between the adsorbate and the adsorbent (L/mg).

In this monolayer adsorption model, a dimensionless separation factor R_L is introduced which is also referred to as the Langmuir isotherm constant (Hou et al., 2021). It determines the favourability of the overall adsorption process. By Meroufel et al., 2013, if the condition $0<R_L<1$ is established, the adsorption process is deemed favorable and successful. Secondly, according to Raza et al., 2024, if $R_L=0$, the adsorption process is strong and

irreversible. Thirdly, if R_L=1, the adsorption is linear where the amount of adsorbate affixed is directly dependent on its initial concentration in the solution (Hou et al., 2021). Lastly, when R_L>1, the process is not suitable or is considered unfavourable (Ramath et al., 2023). R_L can be calculated using the following expression:

$$R_L = \frac{1}{1 + (C_o K_L)}$$

Supplementary equation 17

In this equation, C_o can be varied to check the influence of initial adsorbate concentration on the adsorption favourability (8, 30, 40, and 164 mg/L in our case).

6.4.1.2 Freundlich isotherm

Freundlich model describes adsorption based on heterogeneous surfaces with non-uniform, active binding sites (Teweldebrihan & Dinka, 2024; Agboola & Benson, 2021. In this case, more than one layer (multilayer) of adsorbate molecules could stack up over each other reducing the effective binding strength and proximity of these aggregates with the adsorbent. As a result, adsorption may result from weak forces of attraction like intermolecular and Vanderwaals (physisorption) also, aside from stronger chemisorption phenomena (Wang & Guo, 2020). Hence, q_e may directly depend on the concentration of the adsorbate in the solution that will dictate the nature of molecular collisions with biochar (increases the possibility of occupying the active sites faster). Once again, from Güleç et al., 2022, this model can be viewed non-linearly as:

$$q_e = K_F C_e^{1/n}$$

Supplementary equation 18

Or, can also be represented as a straight-line equation, yielding a linear plot of $\ln q_e$ versus $\ln C_e$.

$$\ln q_e = \ln K_F + \frac{1}{n} \ln C_e$$

Supplementary equation 19

Where, K_F [(mg/g)(L/mg)$^{1/n}$] and n are called Freundlich isotherm constants circumventing the adsorption efficiency (Lee et al., 2024). The intercept ($\ln K_F$) and slope (1/n) derived from the plot are used to calculate K_F and 1/n, respectively. Higher K_F values denote a higher capacity for adsorption (Tcheka et al., 2024). The constant n on the other hand, indicates the intensity of adsorption. If the condition 0<1/n<1 is obeyed, the process is favourable and multilayer sites develop (Mahajan et al., 2023). If 1/n=1, adsorption is fairly linear and simplified with no exceptional interaction observations of adsorbate over the adsorbent, as stated in Acharya et al., 2024. Whereas, if 1/n>1, adsorption becomes unfavourable and the adsorbent's capacity could decline (Mahajan et al., 2023).

6.4.1.3 Temkin isotherm

The Temkin model, unlike Langmuir, and similar to Freundlich, delineates that adsorption is non-uniform mainly with an increase in surface occupancy and simultaneous linear decrease in the heat of adsorption (Hassaan et al., 2023). So, different binding sites could operate at specific energy levels (high versus low) and may be dependent on the temperature of the process as well to reduce any activation energy barriers. Temkin isotherm model also hints at a good possibility of multilayer adsorption. The method can non-linearly be expressed as:

$$q_e = \frac{RT}{b_T} \ln(C_e K_T)$$

Supplementary equation 20

Where, R is the universal gas constant (8.314 J/mol.K), T is the adsorption reaction temperature (323 K), b_T is a Temkin model constant that manifests heat of adsorption process (J/mol) – superimposed by the parameter B, and K_T is an equilibrium constant for binding (L/mg) (Diaz-Uribe et al., 2023).

A linear representation is yielded from the same equation:

$$q_e = \frac{RT}{b_T}[\ln C_e + \ln K_T]$$

Supplementary equation 21

For ease of reporting, substituting $\frac{RT}{b_T}$ as B in the above equation, where B represents the change in adsorption heat generated as the adsorbent's surfaces are gradually occupied by the adsorbate (J/mol),

$$q_e = B[\ln C_e + \ln K_T]$$

Supplementary equation 22

As a straight-line equation, y=mx+c,

$$q_e = B\ln C_e + B\ln K_T$$

Supplementary equation 23

A plot of q_e versus $\ln C_e$ results in a slope (B) and intercept ($B\ln K_T$) which are used to calculate B and K_T.

As advised in Wang & Guo, 2020, adsorption parameter calculation from these isotherms may experience inaccuracies owing to linearizing the model. Thus, non-linear fitting is also suggested to cross-verify any differences that might occur. However, since our isotherms fit better under linearization, non-linear models are not considered here.

6.4.2 Adsorption kinetics and effect of adsorption duration/time

Kinetic models like pseudo-first order, pseudo-second order, and intra-particle diffusion, can describe the reaction rate and mechanisms of an adsorption system (Guo et al., 2020). Pseudo-first and second order models particularly focus on a solid-liquid system where adsorption is directly proportional to the available active adsorption sites along with adsorbate concentration, and the square of these concentrations, respectively. The former supports physisorption due to a weak interactions at the interphase whereas the latter model may also support chemisorption due to strong chemical interactions between molecules of the adsorbate with the adsorbent (Senapati et al., 2025). Hence, there might be a competition possible in this case for the binding sites where the entity with the strongest binding strength is adsorbed. Hence, the pseudo-second order model will indicate a relatively favourable adsorption (Abdu et al., 2024). Intra-particle diffusion model on the other hand, discusses the role of adsorbent's porous channels and voids that support binding aside from boundary layer adsorption (Van Hien et al., 2020). The model fit of these methods, help to determine the mechanism of adsorption, how mass transfer occurs, prevalence of diffusion, and any synchronous patterns of adsorption. Upon fitting batch adsorption experimental data to these models, linear and non-linear fitting followed by regression analysis were used to calculate process parameters like q_e, rate constants, and the model fit, R^2. For this, 50 mL test solutions with two different known concentrations of methyl orange: 8 and 164 ppm, were subjected to adsorption experiments using B600 under the optimal conditions of 50 °C, 4 h (240 min), pH of 3, and a constant B600 loading of 10 mg/mL (0.5 g/50 mL or 10 g/L). From Shafiq et al., 2021, the linearized and non-linearized fitting equations as in Supplementary table 9 can be arrived at!

Supplementary table 9: Non-linear and linear fitting equations for adsorption kinetic models

Adsorption kinetic model	Equation	Parameters and significance	Plot axes
Non-linear fitting			
Pseudo-first order	$q_t = q_e(1 - e^{-k_1 t})$ **Supplementary equation 24**	q_e: equilibrium dye adsorption (mg/g); q_t: dye adsorption at time, t (mg/g); k_1: first order rate constant (min^{-1})	q_t (mg/g) on y-axis versus t (min) on x-axis
Pseudo-second order	$q_t = \frac{q_e^2 k_2 t}{1 + q_e k_2 t}$ **Supplementary equation 25**	q_e: equilibrium dye adsorption (mg/g); q_t: dye adsorption at time, t (mg/g); k_2: second order rate constant (g/mg.min)	q_t (mg/g) on y-axis versus t (min) on x-axis
Linear fitting			

Pseudo-first order	$\ln(q_e - q_t) = \ln q_e - \frac{k_1}{2.303}t$ **Supplementary equation 26**	q_e: equilibrium dye adsorption (mg/g); q_t: dye adsorption at time, t (mg/g); k_1: first order rate constant (min^{-1})	Ln(q_e-q_t) (mg/g) on y-axis versus t (min) on x-axis
Pseudo-second order	$\frac{t}{q_t} = \frac{1}{k_2 q_e^2} + \frac{1}{q_e}t$ **Supplementary equation 27**	q_e: equilibrium dye adsorption (mg/g); q_t: dye adsorption at time, t (mg/g); k_2: second order rate constant (g/mg.min)	$\frac{t}{q_t}$ on y-axis versus t (min) on x-axis
Non-linear/linear fitting			
Intra-particle diffusion	$q_t = k_3 t^{1/2} + C$ **Supplementary equation 28**	q_t: dye adsorption at time, t (mg/g); k_3: intra-particle diffusion constant ($mg/g.min^{1/2}$); C: constant for solid-liquid interphase (mg/g)	q_t (mg/g) on y-axis versus $t^{1/2}$ (min) on x-axis

For both adsorption kinetics and isotherm evaluation, the comparison between experimental and calculated q_e sheds light on the effectiveness of the study. This was accomplished via the root mean square error (RMSE) and chi-square error (χ^2) tests. The equations can be represented as:

$$RMSE = \sqrt{\frac{1}{n-1}\sum_{n=1}^{n}(q_{e,exp} - q_{e,cal})^2}$$

Supplementary equation 29

$$\chi^2 = \sum \frac{(q_{e,exp} - q_{e,cal})^2}{q_{e,cal}}$$

Supplementary equation 30

Where, n is the number of data points considered, $q_{e,exp}$ and $q_{e,cal}$ are the equilibrium adsorption capacities from experimental investigations and from fitting with the theoretical models (calculated), respectively. The closer the values are to '0', the more reliable an adsorption model is!

6.4.3 Adsorption thermodynamics

Thermodynamic parameters indicate if an adsorption phenomenon is occurring with feasibility, hints at the requirements of external energy, and the degree of randomness. Almost the same batch adsorption conditions as followed for kinetics was applied, only difference being the ramping up of temperature from 20-50 °C. The calculations were performed only for the initial methyl orange concentration of 8 ppm as an example. C_e and q_e are calculated once again, which eventually determine the distribution or partition coefficient, k_d (L/g) (Lingamdinne et al., 2024):

$$K_d = \frac{q_e}{C_e}$$

Supplementary equation 31

Then, the thermodynamic parameters such as enthalpy (**ΔH:** KJ/mol), entropy (**ΔS:** KJ/mol), and Gibbs free energy (**ΔG:** KJ/mol.K) were analyzed to seek insights on the nature of adsorption processes and link it with the effect of rising temperatures. These can be quantified as follows (Jain et al., 2022):

$$\ln K_d = \frac{\Delta S}{R} - \frac{\Delta H}{RT}$$

Supplementary equation 32

where, R is the universal gas constant (8.314 J/mol.K) and T is the absolute or reaction temperature (293-323 K). Viewing the aforementioned expression as a straight-line equation, plotting $\ln k_d$ versus 1/T yields a slope (-ΔH/R) and an intercept ΔS/R. With this, ΔG can be calculated from either (Aichour et al., 2022):

$$\Delta G = \Delta H - T\Delta S$$

Supplementary equation 33

Or, from the equation mentioned in Lingamdinne et al., 2024

$$\Delta G = -RT\ln K_d$$

Supplementary equation 34

6.4.4 Other relevant biochar-methyl orange adsorption studies

Supplementary table 10: Comparison of methyl orange removal by biochars from relevant studies

Biomass source for biochar	Surface area (m^2/g)	q_e (mg/g)	Temperature of adsorption (°C)	pH of adsorption	Time of adsorption (min)	Adsorbent dosage (g or g/L)	Dye removal efficiency (%)	Reference
Lemon peel	111.45	17.21	25	4	60	0.025	90.87	Daffalla et al., 2024
Waste antibiotic fermentation residue	1269	521.03	25	3-9	240	0.25-0.50	69.84-90.18	Zhao et al., 2024
Delonix regia seed pods	8.36-15.39	144.9	25	1.01	150	0.75-1	97.95	Eleryan et al., 2024
Wheat straw	747.76-2578.82	93.98-119.76	25	2 (6)[*1]	15-30	0.002-0.014	90-95	Priyanka et al., 2024
Prosopis juliflora	1.28	8.31	25	6	15[*2]	0.1	64	Diaz-Uribe et al., 2023
Palmer Amaranth (invasive weed)	19.6	495.0-554.3	25-45	4	120-240	0.020-0.5	95-100	Chen et al., 2024
Hyphaene thebaica	33.38	264.92	40	2	10-20	0.03	---	Tcheka et al., 2024
Poultry manure	16.09	20.8	25	4	80[*3]	2.5	88.80	Ghani et al., 2022
Rice husk	115.59	31.63	25	3	240	0.2	---	Loc et al., 2022
Date palm fronds	431.82	163.13	25	4	0-1180[*4]	0.002-0.020	---	Zubair et al., 2020
Birch wood	437.34	220	20	2	<1020	0.5-2.5	---	Lee et al., 2024
Ayurvedic waste-iron oxide composite	151.15-398.39	33.90	44	3	60	4	100	Ramath et al., 2023
CRD wood	323.78	14.63	50	3	<1440	10	89-99	**This work**

[*1] – Adsorption of methyl orange was greater than 90% and ideal till a pH of 6. The adsorption behaviour could also be linked to the molar ratio of chemical activation agent since porosity and surface area of resulting biochar increased till an impregnation ratio of 1:1 (biomass:KOH).

[*2] – Saturation was seen around 15 min, methyl orange removal efficiency was tested till 40 min

[*3] – Maximum adsorption seen at or within 120 min after which saturation was observed

[*4] – First phase within 60 min showed maximum adsorption followed by a slow second phase till 360 min, and then saturation

CHAPTER 4 – SCIENTIFIC ARTICLE (3)

Pilot-scale slow pyrolysis, post-production thermal activation, and self-heating performance of biochar fuels derived from construction, renovation, and demolition (CRD) wood waste

Aravind Ganesan[1,2,*], Simon Langlois[2], Olivier Rezazgui[2], Younès Bareha[1], Cyrine Boussabbeh[2], Simon Barnabé[1],

[1] Institut d'Innovations en Écomatériaux, Écoproduits et Écoénergies, Pavillon CIPP, Université du Québec à Trois-Rivières, boul. des Forges, Trois-Rivières G8Z 4M3, Québec, Canada

[2] Cégep de Trois-Rivières, Pavillon des Sciences, 3500 Rue de Courval, Trois-Rivières, G8Z 1T2, Québec, Canada
Innofibre – Centre d'Innovation des Produits Cellulosiques, 3351, boul. des Forges C.P.97. Trois-Rivières G9A 5E6, Québec, Canada

* Correspondence: Aravind.Ganesan@uqtr.ca

Abstract

The increasing accumulation of non-recyclable construction, renovation, and demolition (CRD) wood waste necessitates sustainable valorization strategies. Among thermochemical conversion technologies for refused biomass feedstock, slow pyrolysis is preferred for its superior biochar yield and operational versatility. This study investigates the production and optimization of biochar from CRD wood waste using a pilot-scale retort-kiln system operated at 650°C and 850°C, followed by a secondary thermal activation step for the higher temperature biochar lasting between 30-90 min, in a rotary retort furnace unit. Comprehensive characterization techniques including proximate and elemental analysis, TGA/DTG, TGA R50, FTIR, and SEM-EDX were employed to assess biochar's physicochemical properties and suitability for metallurgical and carbon sequestration applications.

Higher temperature biochar exhibited a carbon content of 85.11% compared to 49.88% in feedstock, with reduced oxygen (5.91%) and hydrogen (1.52%) contents as well. Improved Van-Krevelen ratios (H/C: 0.21; O/C: 0.05) indicated enhanced chemical stability in this biochar. The thermostable fraction (TSF) reached 75.18%, and R50 was measured at 0.57. Fixed carbon (FC) content increased to 70.59%, while volatile carbon (VC) decreased to 23.31%. Surface area expanded to 188.33 m²/g, and pH increased to 8.9, indicating improved cation exchange capacity. Following 30 min of post-heat treatment (PHT) for the higher temperature biochar, further enhancement of carbonization was observed (H/C: 0.18; O/C: 0.02). Extending PHT to 90 min increased FC to 77–78%, TSF to 84–85%, and reduced VC to 13–15%. Surface area peaked between 350–380 m²/g till 75 min of PHT before declining at 90 min due to micropore widening. SEM imaging corroborated these structural changes. Yield losses increased to 20–21% at 90 min PHT. Self-heating assessments further demonstrated that thermal reactivity is influenced by biochar properties, particle size, moisture content, and containment geometry.

Key words: Wood, pyrolysis, biochar, stability, carbon, activation, metallurgical

1. Introduction

The growing global population exerts significant environmental stress, with construction, renovation, and demolition (CRD) activities generating large volumes of waste (Maier, 2021). Only 20% of this waste is recycled, while the rest ends up in landfills, including significant amounts of non-recyclable wood fractions, such as treated, tinted, and adhesive-laden wood, as well as drywall containing gypsum (Hansen & Sadeghian, 2020; Laadila et al., 2021). Furniture waste further contributes to contaminated CRD wood, which, when improperly disposed of together, can harm the environment through greenhouse gas (GHGs) emissions, soil and water pollution (Chen et al., 2022). Landfill leachates containing arsenic, chromium, copper, and polyaromatic hydrocarbons (PAHs) threaten ecosystems and public health, while the economic, social, and legal burdens on municipalities exacerbate the issue. In addition to regulations in place for the segregation of hazardous waste, CRD wood is not properly classified due to its heterogeneous composition owing to differences by location, type of raw material, and storage conditions practiced. The lack of public awareness and limited information slow the exploration of CRD wood's potential for bioenergy and bioproducts, which could create jobs, reduce fossil fuel reliance, and support circular economy applications.

Pyrolysis offers a sustainable waste management path to convert CRD wood into valuable products such as biooil, biochar, pyrolysis gas, and wood vinegar (Basu, 2018). Pyrolysis may also immobilize hazardous substances within the biochar matrix and could sequester carbon without releasing harmful gases or other intermediates into the surroundings. The work here focuses on biochar production through slow pyrolysis only and excludes the options of gasification and combustion due to their lower biochar yield, extreme conditions of operation parameters, and equipment technicalities (Akhtar et al., 2018; Ram & Mondal, 2022). Previous studies, such as Ozbay et al., 2015, have demonstrated the feasibility of producing biochar from furniture wood waste, suggesting its applicability to other CRD wood waste streams. Pyrolysis decomposes organic matter in an oxygen-deficient environment at moderate-to-high temperatures, offering an environmentally responsible alternative to conventional methods like incineration or combustion, which release pollutants (Ganesan et al., 2025, Czajczyńska et al., 2017). Parameters in pyrolysis like temperature, heating rate, particle size, and biomass residence time (BRT) influence biochar's carbon content and reactivity, highlighting their modifications for specific applications (Sakhiya et al., 2020). These parameters, along with post-production/secondary treatments like activation, can enhance biochar quality and physicochemical properties (Sormo et al., 2020). CRD wood contains contaminants like plastics, rubber, glass, metals, insulation materials, and concrete, thereby, requiring pre-sorting followed by size reduction of wood (*e.g.*: chipping or milling) to improve pyrolysis efficiency and heat transfer (Suriapparao & Vinu, 2018). More upstream biomass conditioning steps, such as water or acid washing, may reduce impurities and ash content, that could enhance the final pyrolysis product (Mazerolle et al., 2019). Puri et al., 2024 mentioned that woody biomass from forestry wastes and organic municipal wastes such as furniture waste, paper, and carboard, could fall under the category of low-ash biomass (<5%), whereas agricultural residues like rice husk and straw are considered high-ash feedstock (>10%).

To maximize carbon conservation, biochar must be stable and resistant to chemical and microbial degradation, that are realizable through incubation experiments (Rudra et al., 2024). Physical or chemical incubation studies are often used to predict biochar stability for applications like soil replenishment, but these methods are time and resource intensive. Moreover, they may provide unreliable long-term predictions due to experimental inaccuracies or non-realistic assumptions about biochar's permeance when in real-world situations, open-environmental conditions can act differently on the biochar (Leng et al., 2019). Biochar's thermal and physical stability depends on pyrolysis conditions and feedstock composition. On the stability forefront, carbon in biochar may exist in two pools: (a) persistent; and (b) semi-persistent, depending upon the molecular stability, degradation resistance, and half-life under environmental conditions (Schmidt et al., 2022, Bowring et al., 2022). The Van Krevelen indices (H/C and O/C) calculated from elemental analysis predict the efficiency of pyrolysis, biochar's organic oxygen, environmental stability, and sequestration potential (Bakshi et al., 2020). Biochars with H/C < 0.7 and O/C < 0.6 have a half-life of at least 100 years, while O/C < 0.2 extends the half-life to over 1,000 years (Howell et al., 2022). H/C is influenced by pyrolysis temperature and volatile content, while O/C depends on surface area, pore network, and adsorption properties (Wani et al., 2020). For instance, higher pyrolysis temperatures result in biochar with a larger surface area and well-defined microporosity. These characteristics, along with surface functional groups and pH, enhance adsorption efficiency and are critical for assessing oxidative and self-heating behavior too that will be discussed in later sections of this article.

Biochar reactivity poses challenges for large-scale production, affecting storage, handling, and operational risks (Phounglamcheik et al., 2022). It results from surface oxidation, internal heat build-up, accelerating exothermic

reactions, and eventual thermal runaway. Key contributors include volatiles, surface functionalities, porosity, and secondary modifications like air oxidation or steam/CO_2 activation, which create exothermic zones leading to smoldering (Panahi et al., 2020). Condensed hydrocarbons or tar further catalyze oxidation, forming reactive secondary char (Ba et al., 2023). Reactivity depends on feedstock composition, particularly CRD wood with paint contaminants, which heighten oxidation risks (Mukome et al., 2013; Oliveira et al., 2017). Pre-treatments like washing or torrefaction help reduce volatiles. Pyrolysis temperature is critical where low-temperature biochars have poor oxidative stability due to high volatiles, while high temperatures improve stability but may increase oxygen adsorption and exothermicity due to enhanced microporosity (Pariyar et al., 2020; Phounglamcheik et al., 2022). Aromaticity improves stability, while amorphous structures at low temperatures promote oxidation. Biochar ash may also influence reactivity. Clay and silica could reduce it, while alkali and alkaline earth metals (AAEM) and metal oxides could accelerate oxygen uptake due to their catalytic characteristics. Surface passivation via heat treatment minimizes volatiles, and reactivity while chemical treatments refine porosity, may increase surface reactive groups, and also introduce disposal challenges (Sun et al., 2020). High reactivity also leads to self-heating, limiting biochar's usability.

Biochar self-heating, also known as self-ignition, auto-ignition, or self-combustion, occurs when internal heat from exothermic reactions surpasses dissipation, leading to flammability. This heat can result from microbial oxidation or chemical oxidation triggered by ambient conditions and reactive species (Restuccia et al., 2019; Bluvshtein et al., 2020). Several factors contribute to chemical oxidation, including oxygen diffusion forming reactive functional groups, oxidation of condensed volatiles generating free radicals and heat, low pyrolysis temperatures, fine biochar particles limiting heat dissipation, large stockpile volumes hindering heat loss, increased microporosity from volatile cracking, low moisture content due to excessive drying, and exposure of hot biochar to air post-production (Chaparala & Raj, 2016; Ren et al., 2023; Niu et al., 2021; Locaspi et al., 2021; Fernandez-Anez et al., 2021; Liu et al., 2022; Chen et al., 2023). Industrial-scale stockpiles face additional risks from environmental exposure, where heat loss varies across different regions of the pile, potentially leading to smoldering and combustion. Some universal models are used to study ignition behavior in reactive solids. They are Semenov, Frank-Kamenetskii, and Thomas models (Schwarzer et al., 2021). For a spontaneously heating system, these models consider some assumptions regarding temperature distribution within the material, availability of reactive atmospheres, and its consumption as a reactant. Under a global single-step reaction with undisturbed oxidizer availability (*e.g.:* air, oxygen), the Semenov model assumes uniform heat transfer and negligible reactant consumption, which are unrealistic for large particles or combustion processes with mass loss (Šelešovský, 2010). Secondly, the Frank-Kamenetskii model uses temperature gradients and non-linear thermal behavior but still does not account for reactant consumption during combustion (Janes et al., 2019). Thus, there exists a non-uniform thermal behavior in this case due to exothermic chemical reactions caused by potentially "short-lived" combustible free radicals (Lebelo, 2016). This model also governs the renowned basket self-heating tests in a thermostatic oven for analysing and projecting conductive behaviour within biochar piles. Finally, the Thomas model, built from the Frank-Kamenetskii model, adds convective heat transfer to the existing assumptions, reflecting real-world storage conditions more accurately by considering heat exchange with ambient air properties such as temperature and velocity (Yuan et al., 2019). These models do not accurately account for key factors such as changes in biochar volume within a stockpile of a known geometry, moisture content, and particle size, all of which influence reactivity and self-heating behavior. Despite advancements in biochar production, self-heating remains poorly understood, with limited research available. Literature suggests that post-pyrolysis heat treatment can reduce volatiles, enhance stability, and improve auto-ignition resistance. Here, we aim to correlate biochar production parameters, physicochemical properties, and activation effects with self-heating risks through practical trials, relying on established theories without developing new predictive combustion models.

A promising method to enhance biochar stability and control reactivity is secondary thermal activation at 600–800 °C (Zhu et al., 2018). Unlike physical activation using air, CO_2, or steam at even higher temperatures, thermal activation focuses on eliminating residual volatiles from biochar surfaces and pores (Xiao, 2022). Oxygen-rich functional groups, such as phenols, hydroxyls, carbonyls, and carboxylic acids, if retained, can increase self-ignition risks, especially in biochars with high surface area and porosity. This is particularly relevant for CRD wood biochar, where extractives and organic residues contribute significantly to volatile content. Heat treatment of biochar could enhance its quality by reducing volatile carbon (VC), increasing fixed Carbon (FC), porosity, surface area, and oxidative stability, making it ideal for environmental, energy, and/or soil remediation applications (Tang et al., 2013). Optimizing activation temperature, activation agent type with relevant concentrations/flow rates, and residence time is crucial to maintain biochar's structural and chemical integrity.

The activation atmosphere governs functional groups and porosity. CO_2 activation improves microporosity without expanding pores, making it suitable for energy storage and catalysis (Colomba et al., 2022; Zhu et al., 2018). While steam and CO_2 increase microporosity, air-nitrogen mixtures at moderate temperatures can balance oxygen-bearing surface functionalities and mesoporous channels, aiding adsorption applications (Zhu et al., 2018). Chemical activation using KOH, NaOH, or $ZnCl_2$ intercalates metal salts into biochar, expanding micropores through volatilization, enhancing mesoporosity (Gale et al., 2021). Most studies rely on high activation temperatures, reactive gases, or chemicals. Since moderate-temperature thermal activation without gaseous media remains underexplored, this work investigates biochar passivation at its original pyrolysis temperature under varying time intervals. To align with carbon sequestration and metallurgical applications, reactive atmospheres that introduce charged surface species are avoided to prevent carbon loss. Additionally, no chemicals or water are used, eliminating downstream waste generation.

Biochar generally, can offer significant economic and environmental benefits. Firstly, CRD wood biochar could stabilize organic carbon, otherwise released as CO_2 or CH_4 upon natural decomposition in the environment or in landfills. It may hence, function as a good GHG reduction and carbon sequestration tool. On this note, CRD wood biochar may also be used as landfill covers to adsorb other pollutant gases like H_2S (Sudhakar et al., 2017). Secondly, its high pH, due to concentrated inorganics and metal salts, could increase cation exchange capacity (CEC), making it effective for nutrient, mineral, and water retention, that greatly benefits soil fertility/remediation, especially in dry and arid regions, and reduces reliance on chemical fertilizers or enhancers (Lago et al., 2021). Thirdly, CRD wood biochar with altered physical properties, could adsorb heavy metals and pollutants from wastewater too. For larger molecules, biochar with greater porosity and higher hydrophobicity is usually more effective than microporous biochar mainly due to size constraints (Edeh & Masek, 2022). Fourthly, with increased carbonization at high pyrolysis temperatures and BRT, biochar acquires physicochemical properties like smooth ignitability resembling fossil fuels like bituminous coal or even anthracite in some cases, supporting its potential use to make coke that is generally a reductant in metallurgical processes (Pandit et al., 2020). For clarity, coke is made by further heating coal or anthracite at high temperatures under oxygen-free atmospheres to boost carbon content to >90% with least oxygen and volatiles content. This coke is later used for reduction in blast furnaces to reduce metallic ores. Lastly, pyrolysis of CRD wood generates heat and pyrolysis gas, which could be integrated with biochar production, enhancing energy recovery, resource efficiency, and reducing operation costs, mainly w.r.t external energy requirements.

Addressing technical and regulatory challenges is critical to unlock the full potential of converting CRD wood to biochar via pyrolysis. Rigorous research is required to resolve issues related to scaled-up production, process optimization, biochar characterization with stability indices, effect of combustible volatile matter, secondary treatments, and auto/ignition performance analysis for safety during handling and logistics. Currently, no comprehensive studies on CRD wood valorization across these areas exist to the best of our knowledge. So, this work is based on a myriad of hypotheses regarding CRD wood processing and biochar production. The collected CRD wood is heterogeneous in particle size and contains non-wood materials that require segregation. Pyrolysis temperature is critical in biomass conversion and to produce biochar with appreciable characteristics, regardless of the processing scale. Biochar's post-production activation can be achieved through thermal methods without chemical impregnation or reactive gases, depending on the intended application. Additionally, biochar's flammability is influenced by its properties, particle size, volume, and moisture content.

To address these aspects, this research aims to size-separate, remove inorganic contaminants, and sort the CRD wood waste, pyrolyze the wood in a pilot retort-kiln (following laboratory trials as carried out in Ganesan et al., 2025), analyze the physicochemical and stability properties of biochar across the employed pyrolysis temperatures for satiating applications in the metallurgical and carbon sequestration sectors, conduct post-production thermal activation to reduce volatiles and enhance biochar stability, and investigate its self-heating potential through experimental assessments and underlying theories.

In this study, firstly a clear, theoretical understanding of biochar's oxidative behavior caused by reactive volatiles, the resulting self-heating dangers, and counteracting the root causes via post-pyrolysis/secondary treatment methods, will be provided. Secondly, the methods of isolating the CRD wood fractions from other contaminants will be explained followed by a comprehensive list of characterization techniques for biomass feedstock and biochar product. Thirdly, the instrumentation of slow pyrolysis, secondary heat treatment, and self-heating test equipment will be detailed, along with their functioning method. Fourthly, all characterization results will be analyzed case by case, for biomass, slow pyrolysis biochars, and activated biochars. Lastly, self-heating

experiments will be carried out and compared between pyrolysis biochars and their activated forms. With relevance to studies harboring a similar conceptual basis, these results will be discussed with appropriate reasoning.

2. Materials and methods

All analysis techniques are performed by the same researcher/technician, CRD biomass feedstock, equipment, and methods, as described in Ganesan et al., 2025. They are explained here concisely once again, for providing an overview of all characterization initiatives.

2.1 CRD biomass sample preparation for pyrolysis and characterization

Non-recyclable CRD wood collected from "BRQ Fibre et Broyure", Trois-Rivières, Québec, was transported to Innofibre's factory in pails. Next, as shown in Supplementary figure 17, the collected CRD wood was mechanically sieved (Labtech vibrational sieving unit) into various particle sizes (>4.5 cm, >0.7 cm, >0.5 cm, and >0.3 cm) post-contaminant screening and removal, to provide an overview on technologically facile upstream sample conditioning steps without the necessity for resource-intensive procedures, especially in the case of small-scaled producers of biochar using this grade of feedstock. Even washing was not carried out due to the possibility of generating contaminated wastewater from leaching of CRD wood impurities. CRD wood chips of >0.7 cm and <4.5 cm was chosen for pyrolysis considering the role of particle size in heat transfer and efficient conversion. Since sieving yielded the right particle size, there was no necessity to mill or shred the CRD wood. After size separation, the desired fraction of biomass chips was dried overnight at 105 °C prior to pyrolysis. A Retsch SM300 mill, equipped with a high-speed tungsten carbide rotor and screens as fine as 500 µm or a Thomas Wiley mill with a screen of a similar pore size, was used to produce fines from biomass and also biochar for further characterization.

2.2 Physicochemical characterization

Characterizations of biochars were carried out based on analysis metrics in different categories: 1, 2, and 3, each highlighting a unique objective related to physicochemical composition, stability, and permeance. These methods were exactly followed for biomass too, whenever applicable.

2.2.1 Category 1: Chemical make-up and aromaticity

Analyzing biochar with respect to carbon stability has been challenging in terms of developing globally recognized, standardized methods (Leng et al., 2019). To characterize biochar's chemical make-up and aromaticity, proximate and elemental analysis metrics were explored (Soderqvist, 2019). Their procedure can be briefly described as follows.

2.2.1.1 Proximate analysis

This characterization was used to measure ash, VC, and FC in biochar. For ash, 1 g of dry biochar fines placed in a crucible, was heated in a muffle furnace by adapting to the procedure as in ISO 1171. From room temperature, it was first heated to 106 °C at 5 °C/min and held for 1 h, then ramped-up at the same heating rate from 106 °C to 550 °C, where it was held for 2-4 h. Then, the sample in the crucible was cooled to ambient temperature in a dessicator to avoid any hygroscopic behavior and the ash was later weighed to determine the fraction of biochar left. For VC, 1 g of dry biochar fines was heated to 900 °C for 7 min in a sealed crucible, cooled, and weighed to measure lost carbon. VC is used in some discussions to differentiate just labile carbon, aside from other volatiles. FC was calculated using the formula: 100 − (VC + ash), on a weight percentage dry basis (wt%DB). For this underlying expression, the following Equation 6 is adapted from Weber et al., 2018.

$$\mathrm{VC} + \mathrm{FC} + \mathrm{ash} = 100\ \mathrm{wt\%DB}$$

Equation 6

The same steps were followed to estimate ash, VC, and FC in the biomass sample as well. Using this, a stability index called thermostable fraction (TSF) was calculated for biochar. The equation was adapted from Cely et al., 2015 and John et al., 2024 and can be expressed as in Equation 7:

$$\text{TSF (\%)} = \left(\frac{\text{FC}}{\text{VC} + \text{FC}}\right) \times 100$$

Equation 7

2.2.1.2 Elemental analysis

An Elementar Vario Macro Cube analyzed 1-200 mg of dry biochar fines and biomass for elements like carbon, hydrogen, nitrogen, and sulfur using helium (purity >99.996%) as a carrier gas and oxygen (purity >99.996%) for combustion till 1200 °C. The oxygen content was estimated by difference using the percentages of all individual elements and ash from 100%, as followed in Ali et al., 2022. The expression is given in Equation 8.

$$\text{oxygen} = 100 - (\text{carbon} + \text{hydrogen} + \text{nitrogen} + \text{sulfur} + \text{ash})$$

Equation 8

2.2.2 Category 2: Oxidative and thermal resistance

As means of qualitative and quantitative depiction of biochar's resistance to withstand oxidising and high temperature conditions, the thermogravimetric analysis (TGA), differential thermogram (DTG), and thermogravimetric analysis R50 (TGA R50) recalcitrance index calculation were followed. Here, chemical methods of examining oxidation resistance of biochars via incubation experiments - as in Pereira et al., 2011 - were not tested.

2.2.2.1 TGA/DTG

To investigate weight loss of biochar or biomass as a function of temperature, a PerkinElmer TGA 8000 analyzer was employed. This device was also capable of measuring proximate analysis parameters, including moisture, VC FC, and ash. The analyzer required only 8 mg of biochar or biomass fines per vial in its original, non-dried form. Compressed air with a purity exceeding 99.996% served as the process gas during heating. The system could accurately achieve temperatures up to 1200 °C with adjustable heating rates. A 10 °C/min heating rate up to a maximum temperature of 900 °C was applied to analyze the oxidation behavior of biomass and biochar. DTG curves were arrived at by differentiating weight loss shoulders from the original thermogram with respect to time and plotting against temperature. This resulted in different peaks where maximum weight loss or melting of the sample occurred during TGA and at which temperature, giving insights on its chemical composition and hydrocarbon scaffolding.

2.2.2.2 TGA R50

According to Al-Swadi et al., 2024, the oxidation resistance of biochar could be evaluated through a cost-effective method called TGA R50. This quantitative screening tool aided in predicting the thermal stability of biochar. A higher R50 value indicated appreciable recalcitrance. Factors such as pyrolysis temperature, heat treatment duration, and feedstock type are directly correlated with R50 values (Harvey et al., 2012). Based on R50 values, Wang et al., 2021 classified biochars into three categories: Class A (R50 ≥ 0.7) with least degradation potential; Class B (0.5 ≤ R50 < 0.7) with moderate degradation; and Class C (R50 < 0.5): representing the highest sensitivity towards degradation. Synchronous to this, the carbon sequestration potential also decreased from Class A towards Class C biochars, respectively, according to the authors. The R50 value was calculated from biochar's thermogram corrected for ash and moisture, using the formula and the procedure in Harvey et al., 2012. It can be expressed as in Equation 9.

$$\text{R50} = \left(\frac{\text{T}_{\text{50\% weight loss for biochar}}}{\text{T}_{\text{50\% weight loss for graphite}}}\right)$$

Equation 9

Here, $\text{T}_{\text{50\% weight loss for biochar}}$ is the temperature in (°C) of a biochar sample where it experienced exactly 50% of its weight loss from the corrected thermogram. Likewise, $\text{T}_{\text{50\% weight loss for graphite}}$ is the theoretical temperature in (°C) obtained for 50% weight loss of the reference graphite material's corrected thermogram (886 °C). The same

procedure was followed for the CRD biomass as well, to establish a base value for R50 and compare it with that of biochars.

2.2.3 Category 3: Permeance

To calculate how environmentally persistent biochar is, two methods were adopted.

2.2.3.1 Fourier Transform Infrared Spectroscopy (FTIR)

The surface functional group distribution of biochar was analyzed using an Agilent Technologies Cary 630 spectroscope, operated with Microlab PC software. Approximately 1 g of dry biochar fines was applied to a diamond crystal surface which was periodically cleaned with ethanol. The analysis was conducted in transmittance mode across a spectral range of 500–4000 cm^{-1} to identify the chemical bonds constituting the material. Baseline and peak correction were performed to the derived spectra followed by smoothening the signals.

2.2.3.2 Scanning Electron Microscope – Energy Dispersive X-ray Spectroscopy (SEM-EDX)

The development of porous channels, surface roughness or smoothness, pore clogging, and surface concentration of metallic and non-metallic elements in biochar were analyzed using SEM-EDX. All biochars were tested internally at the microscopy laboratory at I^2E^3, UQTR, using a Hitachi electron microscope SU-70 attached to an X-ray analyzer. Magnifications of 50 X, 100X, 250X, 500x and 1000x with a 15kV acceleration voltage under vacuum were adopted for this characterization.

2.2.4 Other characterizations

2.2.4.1 Brunauer-Emmett-Teller (BET)

The Micromeritics Tristar II, equipped with a deaerator system to eliminate impurities, measured the specific surface area and pore volume of dry biochar fines using nitrogen or helium gas physisorption. It detected pore sizes ranging from 0.35 to 100 nm and surface areas starting from 0.01 m^2/g. If micropore volume was to be specifically computed, the t-plot method was adopted to the BET data.

2.2.4.2 Metals

Metal detection in biomass and biochars was performed using an Agilent Technologies 4210 Microwave Plasma Atomic Emission Spectrometer (MP-AES), equipped with a nitrogen fuel source and an SPS 4 autosampler. This system enabled simultaneous multi-element analysis by nebulizing the biochar sample into a nitrogen plasma to generate monoatomic ions. The instrument ensured precise measurement of inorganic content by completely digesting the organic matter present in the biochar.

2.2.4.3 Higher Heating Value (HHV)

The HHV of CRD biomass and biochars was calculated using the method described in Channiwala & Parikh, 2002 and Khatibi et al., 2023. This method linked calorific value to elemental composition of the samples derived via elemental analysis.

2.2.4.4 pH

The method in Rombola et al., 2023 was adapted to measure the pH of biochars. Dry biochar fines and demineralized water (DMW) at a 1:10 weight ratio, were mixed with a magnetic stirring plate for 60 min. Post shaking, a bench-top pH analyser was used to measure the pH of the biochar suspension.

2.3 Slow pyrolysis in pilot scale

In the pilot-scale retort-kiln assembly, CRD wood with particle sizes ranging from >0.7 cm to <4.5 cm was subjected to pyrolysis. The process was conducted with a BRT of 4 h at furnace temperatures of 650 °C and 850 °C, respectively. Each batch operation accommodated approximately 15–25 kg of biomass feedstock, yielding biochar. For larger-scale testing, the system has the ability to process up to 50 kg of feedstock in a single batch.

2.3.1 Experimental set-up

The experimental set-up is depicted in Figure 26. 20 kg of prepared CRD wood between a particle size range of <4.5 cm and > 0.7 cm, was loaded into a cylindrical retort. The retort was sealed as tight as possible using screws to reduce the infiltration of atmospheric air, and then mechanically placed inside a kiln.

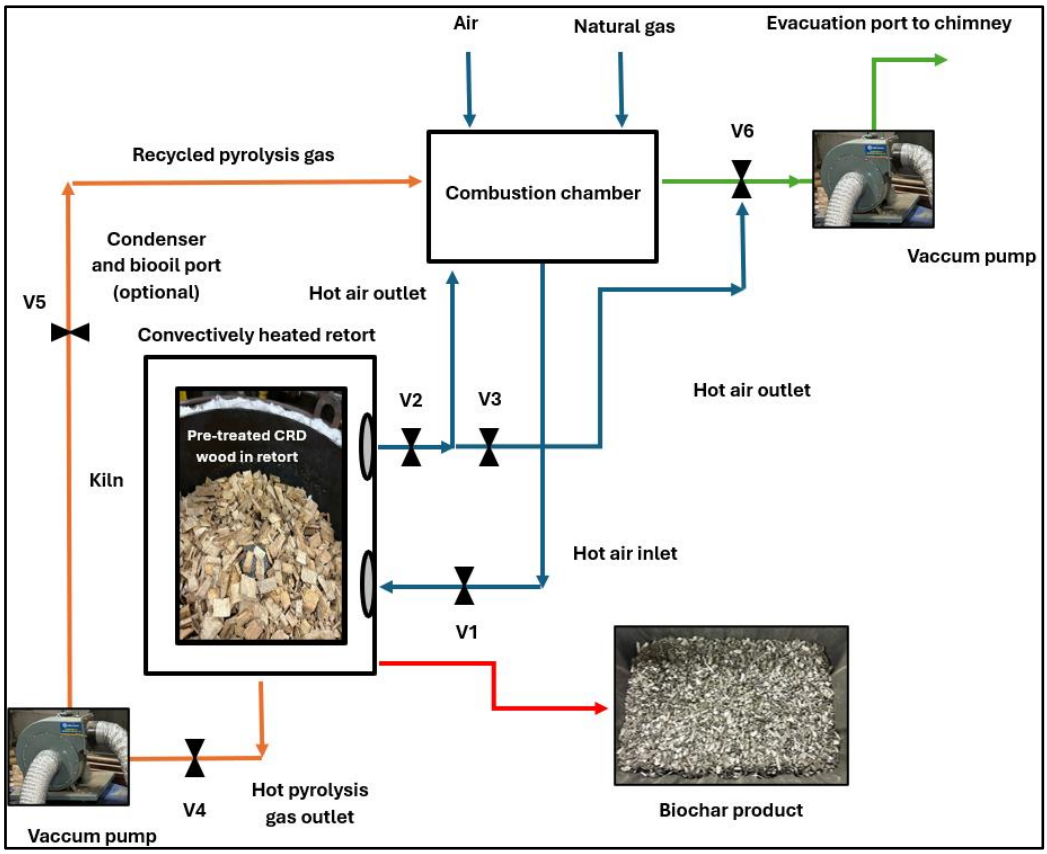

Figure 26: Pilot retort-kiln process flow diagram for CRD wood pyrolysis – an integrated method

The kiln was externally heated via convection by a combustion chamber fuelled with air, natural gas, and recycled pyrolysis gas through valve V1. Hot air then exited the kiln via valve V2, back to the combustion chamber. Alternatively, it was regulated using valve V3 and reached the suction pump that relayed it to the evacuation port and finally to the chimney. The latter step was followed to control rising temperature/pressure and also prior to the start of pyrolysis when the retort was not placed inside the kiln assembly. Hot pyrolysis gases (about 300 °C) from the retort were drawn out and recycled through valve V4 and sent to the combustion chamber for contributing to a part of the energy demand during pyrolysis where it goes back to the retort via V1. Suction of pyrolysis gas is necessary to reduce any settling of tarry volatiles on biochar's surface and minimize their overall residence time within the reactor. This is particularly necessary to limit the PAHs content in biochar product. Optionally, pyrolysis gases could be condensed by installing a portable gas quenching set-up at valve V5 to analyze and work on the biooil product if need be. The system was designed in such a way that recycled pyrolysis gas automatically reduced the input of natural gas to fuel the furnace. In times of emergency, if the furnace temperature shoots drastically, all valves were closed and valve V6 was opened to a suction pump that displaced hot air to the evacuation chamber. Once pyrolysis neared completion (at the end of BRT) and the output of gases seemed to cease, natural gas intake by the furnace increased once again to keep the system running until being switched off for cooling. Then, the retort was mechanically lifted from the kiln and placed on an external bed of cool sand until ambient conditions were reached following which the sealed lid was opened and the biochar was collected for analysis or post-production secondary treatments.

2.4 Secondary heat treatment: Experimental set-up

As depicted in Figure 27, the reactor setup for biochar PHT consisted of a horizontal rotary retort-furnace assembly with an internal diameter of 32 cm, a length of 160 cm, and a total volume of approximately 129 L, capable of processing up to 5 kg of biochar per batch.

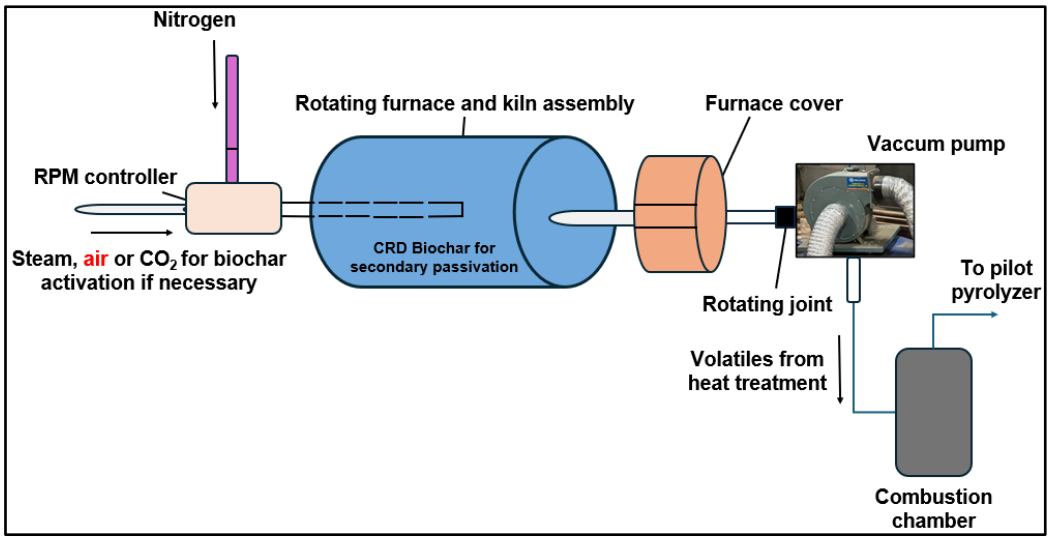

Figure 27: Instrumentation set-up for biochar PHT

The system was equipped with three temperature controllers connected to K-type thermocouples that monitored furnace temperatures at three distinct zones (T1, T2, T3) of the retort. While reporting the results, the average of these three temperatures will be reported and this will be equal to the set point temperature anyway. To prevent volatiles from settling on the biochar surface during PHT, a high-suction vacuum pump was integrated at the exit gas zone. Evacuated volatiles via this suction pump, reached the combustion chamber of the pilot retort-kiln pyrolyzer and was burnt to supply some energy to the process. The rotary motion of the retort ensured uniform heat distribution throughout the biochar framework, including its internal pores, reducing the risk of a surface heating effect. A rotational speed of 10–15 rpm was found to be optimal, as increasing the speed caused excessive shearing, fines release, and eventual entrainment by the vacuum suction unit. A lower rpm was therefore, preferred to maximize passivated biochar yield. For PHT, 2 kg of biochar after pilot pyrolysis, was loaded into the rotary retort, which was then sealed with screws and flushed with nitrogen gas for 5–10 min at about 1-5 L/min, to eliminate reactive atmospheres. Once the nitrogen flow was stopped, the furnace was switched on with the set-point temperature (SPT) logged into the control panel. The retort was designed to prevent air penetration upon proper sealing, ensuring less interference from ambient oxygen. After completion of PHT, the furnace was switched off, allowing biochar in the retort to cool to room temperature. Even during cooling, the rotation of the retort was continued for faster heat dissipation. The vacuum suction unit also remained active until the biochar was fully recovered from the retort for analysis.

2.4.1 PHT trial run for slow pyrolysis biochar

Here, a trial run of PHT was subjected over the slow pyrolysis biochar that had superior characteristics. This step was an effort to justify if PHT, as a secondary activation step, further improved the properties of the best-performing slow pyrolysis biochar. The PHT temperature was chosen to align with the internal pyrolysis temperature recorded during production, for ease in comparison (with versus without PHT). Higher PHT temperatures were not adopted for two other reasons: 1) Due to no inert atmosphere, volatiles cracking could cause any combustion reactions despite the retort being tightly sealed to avoid leaks; 2) High temperature activation has already been achieved by several studies but by different means (chemical and physical). This trial used 2 kg of the slow pyrolysis biochar. Initially, a cycle lasting for 30 min was conducted to verify its effect mainly on VC reduction and increase in FC. Only if this hypothesis was validated, subsequent longer residence times would be tested for PHT at the same temperature, coupled with necessary characterizations to correlate heat treatment duration with biochar properties. Self-heating performance of biochar following the PHT trial was also performed to analyze its effect on biochar's oxidative/reactive stability.

2.5 Preparation of biochar derived from slow pyrolysis and PHT for self-heating tests

For self-heating experiments, biochar lumps and fines (<500 µm) were compared to assess the effect of particle size on combustion behavior. Biochar lumps were collected from the retort post-pyrolysis after it cooled down to ambient temperature, while fines were obtained through vibrational sieving as depicted in Supplementary figure 18. In case very dry biochar (<1% moisture) was required to evaluate the effect of moisture suppression on self-

heating, lumps from the pilot retort were initially dried in the oven for a few hours at 105 °C. The sample was then sieved the same way as before to generate dry fines whereas the dry lumps were used directly as is from the heating oven. It was observed that pre-drying aided in faster generation of fines through the vibrational sieving unit due to thermal stress, moisture loss, brittleness, volume reduction, and mechanical abrasion. For biochar samples which underwent PHT, the same process was repeated, albeit, with biochar collected from the rotary retort instead of the pilot retort-kiln unit.

2.6 Self-heating test for all biochars

Biochar was tested for self-heating propensity using basket heating tests in thermostatically controlled adiabatic ovens as in Supplementary figure 19, following the 33.4.6 UN Manual of Tests and Criteria with a minor adaptation surrounding testing duration. As per the methodology outlined by Restuccia et al., 2019, square steel mesh baskets (0.5 mm diameter, 10.16 cm side length) containing biochar samples were enclosed within steel cages to minimize material loss due to ambient airflow. These baskets were suspended inside oven racks and maintained at fixed temperatures of either 140 °C for a short-to-moderate time frame or 120 °C for a long-time frame. This was done to bring in the effect of heat exposure duration at milder levels. This setup provided an accurate estimation of self-heating behavior in large stockpile geometries, especially when supplemented with additional thermocouples placed in different pile regions. A K-type thermocouple positioned at the center of the biochar sample inside the steel basket was connected to an alarm system to alert users of any abnormal temperature spikes beyond 200 °C (indicating a failed test and flammable biochar). Another K-type thermocouple, also placed centrally, was linked to an OMEGA reader and computer to monitor temperature variations over time. The self-heating experiments were performed for biochars as is from the pilot pyrolysis tests as well as for biochars after PHT. Different conditions of particle size, changes in volume occupied within the basket (half or full-filled), and moisture were tested.

3. Results and discussion

3.1 Characterization of CRD slow pyrolysis biochars from pilot-scale, and PHT trial run

The physicochemical characteristics of biochars from CRD wood, before and after the PHT trial run, inclusive of proximate and elemental analysis, surface area, micropore volume, and stability indices, along with metal content, TGA/DTG, TGA R50, FTIR, and SEM-EDX analysis will be discussed in the following sections. Characterizations of CRD biomass as is, will also be included wherever deemed necessary for comparison purposes.

3.1.1 Physicochemical properties

As tabulated in Table 17, the proximate and elemental analysis parameters of biochar varied with increasing pyrolysis temperature. For a larger mass of feedstock, both biochars exhibited a carbon content of >80%. Temperature profile patterns in Supplementary figure 20 revealed substantial heat loss, with thermocouples showing a 250–300 °C gap between the furnace temperature and the internal retort temperature. However, this discrepancy arises due to biomass shrinkage and volume reduction during thermal degradation, causing the thermocouple inside the biomass stack to lose contact and hang freely in the headspace rather than remaining embedded within the material. As a result, the thermocouple readings may not accurately reflect the true temperature experienced by the biomass, which could be a bit higher than 425 °C or 525 °C, respectively. During biochar formation, its gradual increase in thermal conductivity facilitates heat transfer between surrounding particles, resulting in an exothermic environment within the retort. This effect suggests that the internal temperature could have exceeded what was recorded, in spite of being lower in the headspace of the retort. Consequently, the thermal inertia projected may underestimate the actual heat exposure inside the biomass matrix.

Throughout this work, for convenience-sake, pilot-scale slow pyrolysis biochar produced at a furnace temperature of 650 °C with an average internal temperature recorded at 425 °C will now be called **B425,** and the batch produced at a furnace temperature of 850 °C with an average internal temperature recorded at 525 °C will be called **B525** for all characterization results and discussions. B525 that harbors superior properties, after the PHT trial run for 30 min, will now be called **HTB525**. 'B' and 'HTB' represent biochar and heat-treated biochar, respectively.

Table 17: Proximate, elemental, stability, calorific performance, and morphological characteristics of CRD biomass and biochars. In proximate analysis alone, the weights for CRD biomass and biochars are

expressed as wt%DB to only account for carbons that are volatile and not other volatiles like moisture and light extractives.

Metrics	CRD wood biomass	B425	B525	HTB525	Coal	Coke
Proximate analysis (wt%) for coal and coke, (wt%DB) for CRD wood, B425, B525, and HTB525						
Moisture	0	0	0	0	6	1.34
Volatiles/VC for CRD	82.35	27.74	23.31	16.19	41.50	**10.30**
FC	16.48	67.78	70.59	76.33	39.60	**88.00**
Ash	1.17	4.48	6.10	7.48	12.90	**0.40**
Elemental analysis (wt%)						
C	49.88	80.16	85.11	87.00	80.70	87.00
H	6.12	1.83	1.52	1.27	5.80	3.50
S	0.10	0.65	0.56	0.62	3.60	7.90
N	0.99	0.97	0.80	1.05	1.20	1.10
O	41.74	11.91	5.91	2.58	8.70	**0.50**
Stability indices: Van-Krevelen parameters, TSF (%), and R50						
H/C	1.47	0.27	0.21	0.18	0.86	0.48
O/C	0.63	0.11	0.05	0.02	0.08	**0.004**
TSF	16.68	70.96	75.18	82.50	48.83	89.52
R50	0.52	0.57	0.58	0.58	N.A*	N.A*
Calorific value (MJ/kg) and pH						
HHV	20.28	28.86	30.81	31.49	20.60	27.20
pH	N.A*	8.1	8.9	9.3	N.A*	N.A*
BET surface area (m^2/g) and micropore volume (cm^3/g)						
BET surface area	N.A*	71.35	188.33	202.09	4.13	4.40
Micropore volume	N.A*	0.08981	0.09570	0.09652	N.A*	N.A*
Reference	**Present study**	**Present study**	**Present study**	**Present study**	Safarian, 2023	Safarian, 2023

***N.A – Not analyzed**

CRD wood feedstock containing dyes and resins can introduce heteroatoms such as sulfur and nitrogen into the biochar matrix upon pyrolysis. Although, being forest wood-derived, this CRD wood is classified as a low-ash feedstock (1.17%) as confirmed from Table 17. However, inorganics and metals in treated wood may have contributed to increasing ash content in biochar, particularly during prolonged heating. B425 exhibited 4.48% ash, a 283-fold increase compared to the initial biomass. The gradual decomposition of VC may expose previously bound inorganics (*e.g.*: organometallics like Ca-O-C, Na-O-C), increasing biochar ash content. Additionally, heat-sensitive acidic functionalities decompose, raising the biochar pH to 8.1, indicating a shift to greater hydrophobicity - potentially due to a reduction in protonic groups (6.12% to 1.83%) and oxygenic groups (41.74% to 11.91%). At this pyrolysis temperature, FC content stabilizes at 67.78%, forming aromatic structures. The carbon content of B425 increased to 80.16%, marking a 60–61% rise relative to the original CRD wood. The TSF at 70.96%, suggested improved stability due to thermal conversion and propagating FC.

For B525, TSF increased to 75.18%, indicating enhanced thermal stability with severity in pyrolysis temperature. The Van-Krevelen parameters diminished further (plotted in Supplementary figure 21), confirming the dominant influence of temperature and prolonged BRT (Wijitkosum, 2023). The O/C ratio decreased from 0.63 in the biomass feedstock to 0.05, while H/C dropped from 1.47 to 0.21, highlighting carbon enrichment, developing stability through crystallinity, and heightened aromaticity as reported by Wystalska & Kwarciak-Kozłowska, 2021. These values align with the International Biochar Initiative (IBI) guidelines for carbon sequestration and soil applications, which require H/C < 0.7 and O/C < 0.4 (Maaoui et al., 2023). The HHV of B425 and B525 were 28.86 MJ/kg and 30.81 MJ/kg, respectively - higher than the initial CRD wood (20.28 MJ/kg), making them viable fuel sources due to their energetic C-C, C-H, and C-O bonds (Maaoui et al., 2023). Similar to the trend seen for B425, a pH of 8.9 for B525 resulted from increased ash content, reducing hydrophilicity. Relative to B425, the higher pyrolysis temperature led to 6.2% more carbon, 50.4% less oxygen, 16.9% lower sulfur, and a 16% reduction in VC for B525. Additionally, FC content increased by 4–5%, validating the notion that higher pyrolysis temperatures decrease flammable fractions while increasing stable carbon structures. The growth of aromatic structures and improved structural ordering likely resulted from the transition of amorphous carbon into localized carbon-rich layered sheets/rings (Guizani et al., 2019). Without activation, B525 achieved a surface area of 188.33 m^2/g and micropore volume of 0.0957 cm^3/g, representing a 164% increase in surface area and a 7% rise in microporosity compared to the B425, as shown in Table 17. Higher pyrolysis temperature and the same BRT of 4 h facilitated gradual melting of biomass's holocellulose, lignin, and volatiles, with a release of light gases, rather

than any sudden particle implosions benefiting micropore formation (Chatterjee et al., 2020). Slow pyrolysis also gave a satisfactory result in yield of biochar, with 30% for B425 and 25% for B525, relative to the original biomass weight. Ash content increased by 36–37%, however, high ash may inhibit FC growth. On the ash forefront, there were some interesting outcomes during the acclimatization tests performed with CRD biomass to analyze the feedstock's behavior under scaled-up conditions.

For HTB525, PHT had a significant impact, considering that the temperature was unchanged during activation, i.e, same as the average internal temperature recorded in the retort during pyrolysis. The char appeared uniform, non-glossy, and crisp, indicating that the deposition of condensates or tarry material on biochar was low. Relative to only B525, PHT enhanced its properties, increasing carbon content to 87%, reducing oxygen to 2.58%, improving Van-Krevelen parameters (H/C: 0.18, O/C: 0.02), lowering VC to 16.19%, and raising FC to 76.33%. Especially, FC in HTB525 is in agreement with that of woody biomass-derived biochars mentioned in Woolf et al., 2021. This can be linked to a strong interdependence between VC, FC, and H/C, as similarly observed by Aller et al., 2017. However, here the authors use the term $H/C_{organic}$ as a more organic carbon centric term, to predict biochar stability. Ash content also rose to 7.48%, while pH increased to 9.3, suggesting a reduction in acidic surface functionalities and potential applications in soil amendments (Song et al., 2023). A second phase of dehydration, dehydrogenation, and deoxygenation, similar to that observed during initial pyrolysis, likely occurred during PHT, further reducing hydrogen and oxygen content. Continuous removal of volatiles, prevented premature condensation, enhancing hydrophobicity and lowering chemical instability (del Campo et al., 2021). HHV increased to 31.49 MJ/kg, indicating concentration of energy-rich FC, making it suitable for metallurgical applications. TSF also rose by 9.7%, suggesting PHT promoted chemically and thermally stable aromatics with well-ordered carbon structures. Surface area and micropore volume increased by 7.3% (to 202.09 m^2/g) and 7.5% (to 0.09652 cm^3/g), respectively, reinforcing the positive role of PHT. Yield loss after PHT at 30 min was around 15% that reflects the decomposition of carbon constituents, and highlights the need to optimize activation temperature and duration to balance property improvements with yield retention. A higher initial pyrolysis temperature (with long BRT) may be yet another aspect that could be considered to scale its physicochemical performance, albeit, yield loss would be much higher even before PHT.

3.1.1.1 Comparison to metallurgical grade coal and coke

From Table 17, B425, with slightly higher oxygen content and O/C ratio, exhibits properties comparable to metallurgical coal. However, B525 surpasses all key characteristics of metallurgical coal, making it a stronger, sustainable substitute. Lower ash content of CRD wood biochars can also conserve the quality of metal product with less impurities. HTB525, on the other hand, closely matches specific metallurgical coke grades itself, sharing similar elemental analysis properties, including equivalent carbon, lower hydrogen (H/C), nitrogen, and sulfur - which helps reduce NO_x and SO_x emissions. However, HTB525 contains five times more oxygen and a higher O/C than coke. Coke is also superior in terms of lower volatile content and higher FC. Its thermal stability (via TSF) remains higher than all CRD wood biochars. An important characteristic, albeit, is high calorific potential of these biochars. Notably, B425, B525, and HTB525, all exhibit more HHV than coal and coke, indicating enhanced fuel efficiency due to high carbon content as stated by Safarian, 2023. Bulk density of B425, B525, and HTB525 experienced a proportional increase between 200-600 kg/m^3 due to the decomposition of moisture, combustible volatiles, and concentration of carbon-rich, dense compact structures (Rambhatla et al., 2025). An increase in heat treatment severity and the apparent devolatilization led to the formation of biochar with more micropores (meso and macropores formation was lowered), although with shrinkage and volume reduction (Dufourny et al., 2019). Higher bulk density could reduce biochar friability, making it denser and resistant to weathering, owing to high pyrolysis temperature, PHT, and ordered crystallites formation (Dufourny et al., 2019). Albeit, this should be confirmed by Raman, NMR, XRD or similar techniques. It can also facilitate the use of greater volumes of biochar to be processed in a given time, and could even reduce transportation costs. This validates PHT as a promising approach, as it successfully aligns with some major hypotheses in this article: reducing volatiles and oxygenates, increasing carbon content, FC, and HHV - all critical for improving biochar's performance as a metallurgical ingredient.

Further investigation into longer PHT durations is warranted to assess its impact on physicochemical properties before drawing definitive conclusions.

3.1.2 Metals

3.1.2.1 Inherent AAEM in CRD biomass

As part of the physicochemical characterization, metal content in CRD biomass, B425, B525, and HTB525 was analysed as in Supplementary table 11. CRD biomass ash contains a significant metal fraction, primarily AAEM (Na, K, Ca, Mg, Ba) and heavy metals (Pb, Ni, Cu, Cd, Cr). These metals interact with biomass carbon and, under prolonged BRT, could alter reaction pathways, increase gas production, and induce secondary char formation during pyrolysis (Changi et al., 2015). While secondary char formation can enhance biochar yield, it is rich in volatiles which originate from the cracking of tarry compounds or condensed volatiles, thereby, contributing to oxidative instability and self-heating risks. AAEM salts (carbonates, sulfates, nitrates) could concentrate in biochar, influencing its chemical properties, including an increase in pH from 8.1 (B425) to 8.9 (B525) due to the accumulation of these salts. This occurs when AAEM in ash substitutes biomass protons in phenolic, acidic, or carbonyl groups, leading to salt formation (Puri et al., 2024). Complementarily, the role of ash in biochar self-heating remains an important area for further study.

Metal analysis of CRD wood revealed that 87% of total metals were AAEM, with alkaline earth metals (Ca: 53.27%, Mg: 6.27%, Ba: 0.42%) comprising 59.96%, while alkali metals (K: 13.58%, Na: 13.45%) made up 27.03%. The AAEM concentration in biochar decreased significantly with increasing pyrolysis temperature, dropping from 87% in CRD feedstock to 11% in B425 and 7% in B525, representing a 76.72% and 84.10% reduction, respectively. This suggests that biomass's actual heat exposure during pyrolysis was higher than thermocouple readings, partly leading to AAEM volatilization. AAEM content amidst metals analyzed in HTB525 increased again to 18%, mostly composed of divalent species where Ca, Mg, and Ba constituted for 87-88%. This may still prove that PHT at moderately high temperatures could lead to accelerated volatilization of simple alkali metals. Fe and other metals in CRD wood were in the range of Fe>Al>Mn>Zn>Cu>Pb>Cr>Co. Heavy metals accounted for <1% of total metals in raw biomass, following the order Cu > Pb > Cr > Ni > Cd. With rising pyrolysis temperatures, Cd, Ni, and Cu concentrations increased, indicating their persistence in the solid biochar matrix. Hence, it is proved that pyrolysis can stabilize heavy metals into mineral complexes, reducing their mobility. This enhances biochar's environmental benefits, as it can immobilize and capture heavy metals, preventing leaching into soil or water and mitigating ecotoxicity risks, even when disposed after use.

3.1.2.2 Effect of inherent AAEM in CRD biomass on pyrolysis equipment

The presence of AAEM in CRD wood can lead to reactor slagging, fouling, and agglomeration as illustrated in Supplementary figure 23 (A)(B)(C). These issues stem from the melting behavior of inherent ash constituents. **Slagging** occurs when high pyrolysis temperatures cause these to melt, forming a glassy clinker-like residue that is difficult to remove once cooled (Smith et al., 2018). Monovalent K and Na lower the ash melting temperature, increasing clinker formation, whereas divalent Ca, Ba, and Mg elevate melting temperatures, reducing residue deposition (Koppejan & Van Loo, 2012). Since almost 60% of CRD wood's AAEM is composed of Ca, Mg, and Ba, the effect of slagging may thus, be slowed. Typically, Si in ash also stabilizes melting processes, delaying thermal degradation, but CRD biomass lacks substantial Si. Projecting from the findings in Saidur et al., 2011, woody biomass like CRD can be placed under "Ca, K-rich and Si-lean" feedstocks, unlike herbaceous or agricultural residues, which are "Si, Ca-rich and K-lean." **Fouling** is initiated when K and Na volatilize and react with Cl in biomass, forming alkali chlorides that condense on reactor walls, reducing equipment efficiency (Morris et al., 2018). Since Na^+ and K^+ salts volatilize more easily than Ca^{2+} and Mg^{2+}, they readily participate in gas-phase reactions during pyrolysis (Abioye et al., 2023). These gases contain H, C, O, and non-metal heteroatoms, along with sulfates, phosphates, chlorides, and nitrates that can produce acidic compounds (H_2SO_4, H_3PO_4, HCl, HNO_3), causing corrosion at temperatures above 700 °C (Uroic Stefanko & Leszczynska, 2020; Kern et al., 2012). However, CRD wood has lower sulfur, nitrogen, and phosphorus, reducing the risk of corrosion-related fouling. **Agglomeration** occurs when alkali metals melt over biomass or biochar particles, forming rigid residues that may trigger coating-induced agglomeration (Morris et al., 2018; Gao et al., 2022). This phenomenon is shown in Supplementary figure 23 (B) despite not utilizing any heat carrier medium in the pyrolyzer owing to its configuration. To mitigate agglomeration, an approach was proposed by Ren et al., 2024 that involves using additives which contain divalent or trivalent metal salts with the heat carrier medium. These additives could react with alkali metal derivatives, raising their overall melting temperature and delaying coating and aggregation of heat carrier medium. This works well especially in fluidized bed reactors where bed material's fluidization is of utmost importance. Albeit, in our case, future pyrolysis experiments in the retort can be carried out without any heat carrier medium that could reduce the chances of this occurrence and also to avoid the use of any chemical additives.

3.1.3 TGA/DTG/TGA R50

To analyze TGA results, weight loss curves of biomass and biochars were examined as a function of temperature during thermal degradation (Figure 28 (A)). Four samples - CRD biomass, B425, B525, and HTB525, were tested under an air atmosphere with a heating rate of 10 °C/min. The characterization aimed to evaluate the decomposition of residual organic matter, the stability of biochar carbon against thermal degradation, and the influence of ash content on biochar behavior.

CRD biomass exhibits three distinct stages of decomposition during TGA as shown in Table 18 and Figure 28 (B). In the first stage (below 150 °C), a 2.38% weight loss occurs due to the evaporation of intrinsic moisture, light volatiles, and some extractives (*e.g.:* gums, resins, pigments, terpenes), highlighting its hygroscopic nature. As pyrolysis severity increases, resulting biochars show lower weight loss (<1.6%) in this region due to their reduced moisture and labile volatile content. In the second phase (200–400 °C), biomass undergoes a sharp weight loss of 66.95% at 345.87 °C, attributed to the breakdown of hemicellulose, cellulose, and unstable volatile organic compounds. This rapid degradation suggests a high holocellulose content relative to lignin. For instance, amorphous cellulose may have likely decomposed into levoglucosan, oxygenates whereas hemicellulose breaks down to release CO, CO_2, and light pyrolysis gases (Paajanen et al., 2021). For biochars, the reduction in organic fractions and increased thermal stability shift combustion peaks beyond this phase towards the right, indicating advanced carbonization and reduced presence of amorphous carbon. Weight loss in this region was minimal for B525 (5.83%), followed by HTB525 (7.16%) due to their high FC and low VC. There is however, a slight difference seen via an increase in weight loss during the second phase for HTB525 which could be attributed to any remnants of removed volatiles from PHT, left loosely-attached to the pores or surface of biochar. In contrast, B425 exhibited higher weight loss (18.11%), obviously reflecting its lower pyrolysis production temperature and higher VC.

Table 18: Weight loss percentages encountered by CRD biomass, B425, B525, and HTB525 in each stage of TGA. Up to two decimal places were considered for accuracy

Sample analyzed	Weight loss in each phase of TGA (%)			
	First phase (<150 °C)	Second phase (200-400 °C)	Third phase (400-600 °C)	600-900 °C
CRD biomass	2.38	66.95	27.80	0.09
B425	1.58	18.11	74.33	1.01
B525	1.07	5.83	87.40	1.09
HTB525	1.56	7.16	81.71	8.02

For all biochars, peak degradation occurs in the third phase (400–600 °C) with a weight loss range of 74–88%. The melting temperatures, increasing with thermal stability, were 511.17 °C (B425), 549.93 °C (B525), and 551.76 °C (HTB525). This phase marks lignin breakdown, where higher biochar formation temperatures promote greater lignin conversion, aromatic condensation, and the transition from amorphous to crystalline carbon. As crystallinity increases, higher energy is required to cleave aromatic structures, raising biochar melting temperatures (Om Prakash et al., 2020). In contrast, CRD biomass showed only a 27.8% weight loss in this phase, with a melting temperature near 500 °C, as 70% of its polymer decomposition had already occurred earlier. Residual aromatic lignin linkages continued degrading between 400–600 °C, though depolymerization could have likely begun in the 200–400 °C range (Lu & Gu, 2022). Beyond 600 °C, weight loss was minimal in B425 (1.01%) and B525 biochar (1.09%), attributed to highly stable lignin aromatics, heat-resistant mineral salts, and resolute ash components. However, HTB525 exhibited an unexpected 8.02% weight loss, likely due to the decomposition of non-crystalline organics, weakly aromatized carbon, and less rigid lignin sub-units. The final ash content in all biochars was <10%, aligning with experimental calculations.

Increasing pyrolysis temperature from biomass to B425 and B525 enhanced biochar thermal stability, with the R50 recalcitrance parameter rising from 0.52 to 0.57 (Category B biochar). However, HTB525 showed only a slight increase to 0.58, indicating that PHT had minimal additional impact. This can also be shown by their overlapping curves in Figure 28 (C). Meanwhile, it was noted that TSF exhibited a significant jump from 16.68% in biomass to 82.5% in HTB525. Results suggest that stronger TGA R50 stability correlates positively with TSF and FC but negatively with Krevelen parameters (H/C, O/C) and VC. With minimal surface volatiles, HTB525's

good physical and chemical stability make it highly suitable for carbon sequestration and high-temperature metallurgical applications.

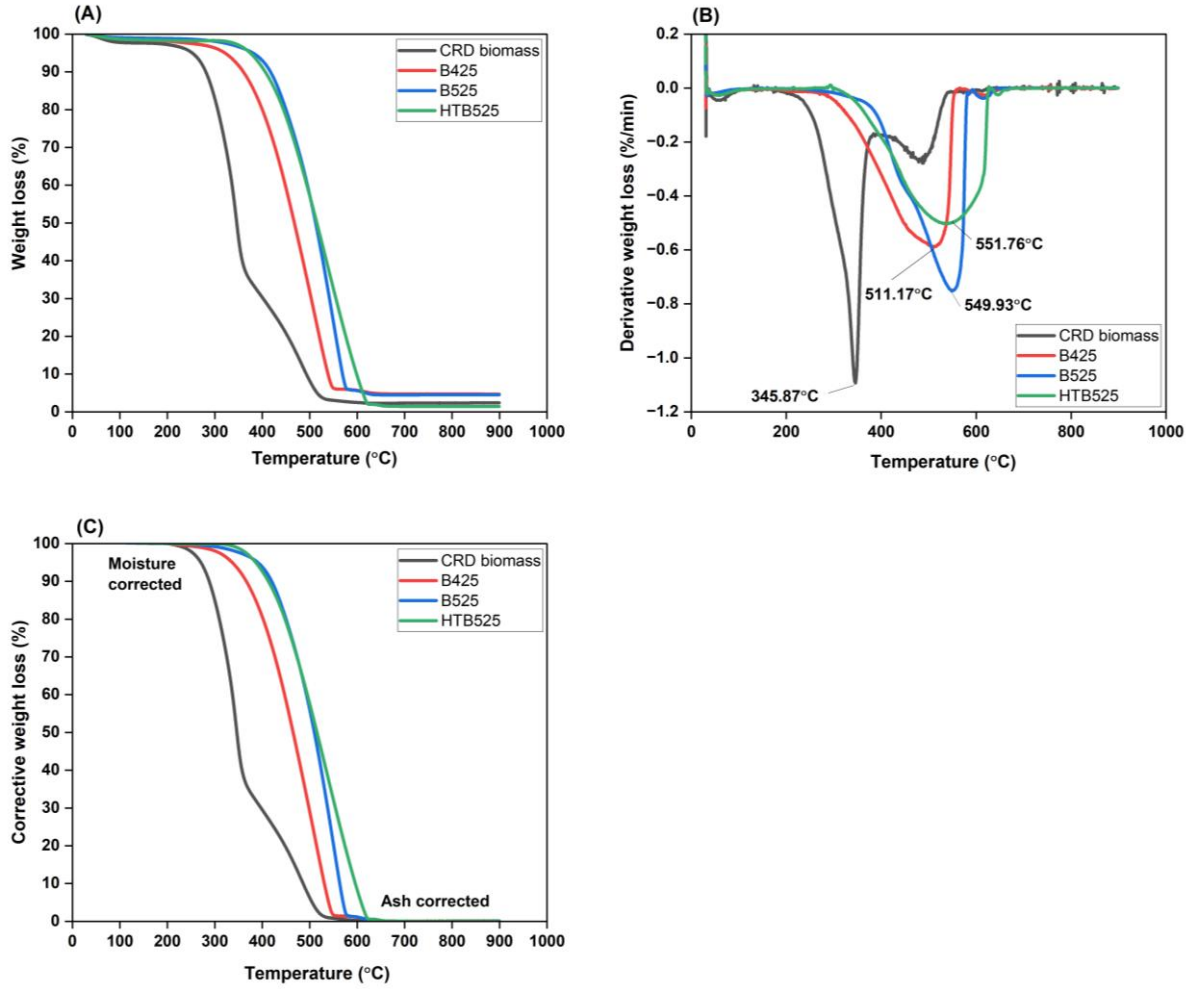

Figure 28: Thermal decomposition analysis of CRD biomass, B425, B525, and HTB525. (A): TGA curves; (B) DTG and associated melting temperatures; and (C) moisture and ash corrected TGA for calculating R50 index

3.1.4 FTIR

FTIR spectral analysis of B425, B525, and HTB525 used band assignments from Johnston, 2017 and Sajjadi et al., 2019 to identify functional groups and their variations with increasing pyrolysis temperature and secondary treatment. The analysis is rendered in Figure 29.

All biochars exhibited aromatic C-H bending vibrations between 700–840 cm^{-1}, alongside O-H bending vibrations likely from distorted acidic surface groups. The 800–940 cm^{-1} band showed peaks indicating O-H vibrations in metal/mineral-O-H linkages, as increasing pyrolysis temperature (especially in HTB525) concentrated metals in biochar due to decomposition of labile hydrocarbons. The 1020–1280 cm^{-1} zone saw a reduction in peak intensity, suggesting loss of C-O vibrations in the polysaccharide regions of hemicellulose and cellulose, with minimal signals in B525 and HTB525, indicating their pre-stabilized state due to faster decarboxylation, decarbonylation, and carbon cracking to light gases. Similarly, C-OH stretching vibrations linked to hydroxyl, carboxyl, ester, and amide groups diminished, suggesting enhanced pyrolytic conversion in high-temperature biochars. B425 exhibited higher strain here due to mild conversion relative to its counterparts. It may have retained surface oxygenates which may even promote CEC (Lago et al., 2021). O-H bending in phenols and C-H deformations in methyl groups (<1440 cm^{-1}) confirmed aromatic backbone formation through dehydrogenation, isomerization, cyclization, and aromatization reactions, with HTB525 showing the strongest peak intensity due to dominant thermal effects. Aromatic skeletal vibrations (till 1510 cm^{-1}) further reinforced the formation of condensed aromatics at higher pyrolysis temperatures, while intense C=C stretching (1510–1610 cm^{-1}) in B525 suggested

maturation and strong aromaticity, leading to increased hydrophobicity due to the removal of protons and oxygen species (Luo et al., 2024). However, HTB525 showed a relatively lower peak intensity here, indicating optimal conjugation.

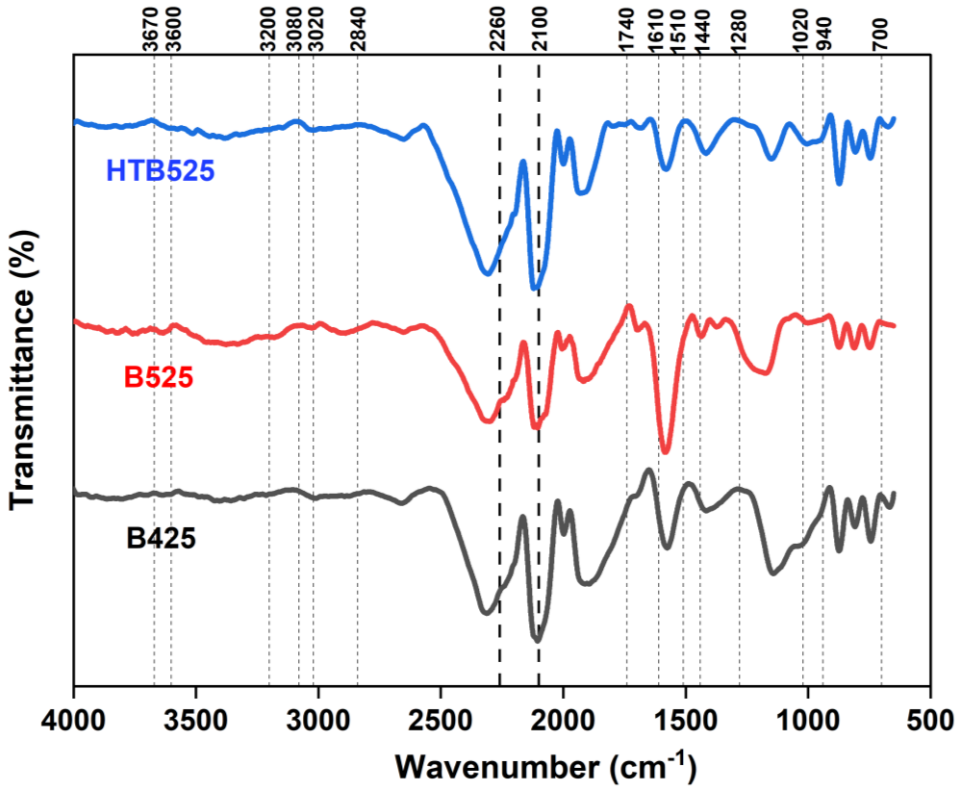

Figure 29: FTIR bands of B425, B525, and HTB525

Moisture presence (1610–1740 cm^{-1}) weakened with increasing pyrolysis and PHT. From 1740-2100 cm^{-1}, C=O vibrations from aldehydes, ketones, carboxylic acids, and esters due to lignin degradation are also observed. Since C=O groups are polar, B525 and HTB525 retained only fewer oxygen moieties, suggesting lower reactivity, making them suitable for carbon sequestration. An important band, 2100-2260 cm^{-1} depicts the C≡C stretching vibrations in multi-aromatics shown with the maximum intensity in HTB525, suggesting a positive relation with heat treatment. Aliphatic C-H vibrations (2840–3020 cm^{-1}), associated with methyl and methylene groups, were dull, indicating the presence of residual organic matter from incomplete polymer decomposition. This finding is consistent with Singh et al., 2016. The 3020–3080 cm^{-1} region displayed C-H aromatic vibrations, signifying a strong progress in carbonization from B425 to HTB525, confirming strengthened C-C and C=C linkages. Beyond 3020 cm^{-1}, no distinct peaks were detected, suggesting minimal hydrogen-bonded O-H groups, indicating low moisture adsorption in high-temperature biochars as projected from Luo et al., 2024.

3.1.5 SEM-EDX

To explain the positive impacts of PHT on slow pyrolysis biochar, a SEM analysis of only B525 [Figure 30 (A) (B) (C)] and HTB525 [Figure 30 (D) (E) (F)] were considered as it outlined some significant findings.

The micrographs revealed a rough, porous network at 250X and 500X magnifications for both biochars. Due to a long BRT and controlled heating rate, no sudden implosions or intra-particle explosions occurred, leading to non-widened pore sizes. However, at 1000X magnification for B525 [Figure 30 (C)], some hierarchical porosity was observed, though this sample exhibited a lower surface area, contrary to the findings in Malhotra et al., 2023, where hierarchical porosity enhanced specific surface area. In this figure, some pores appear clogged with settled residual tar or may be metallic constituents considering CRD wood had sizeable AAEM content. Kuryntseva et al., 2023 stated that condensed volatiles can also settle in these pores and transform during secondary pyrolysis or carbonization. In HTB525, PHT facilitated gas escape (*e.g.:* CO_2, CO, CH_4, H_2O), volatilization of weak organics, and densification of microporosity, forming interconnected porous structures [Figure 30 (F)] amid graphitized carbon, consistent with Ma et al., 2016. Glossy indentations all over HTB525 represent desorbed

inorganic elements initially intercalated within the matrix, later volatilized, leaving well-defined, unclogged spaces following a pore reaming-like effect. Thermal activation also smoothened surface textures possibly due to enhanced carbonization.

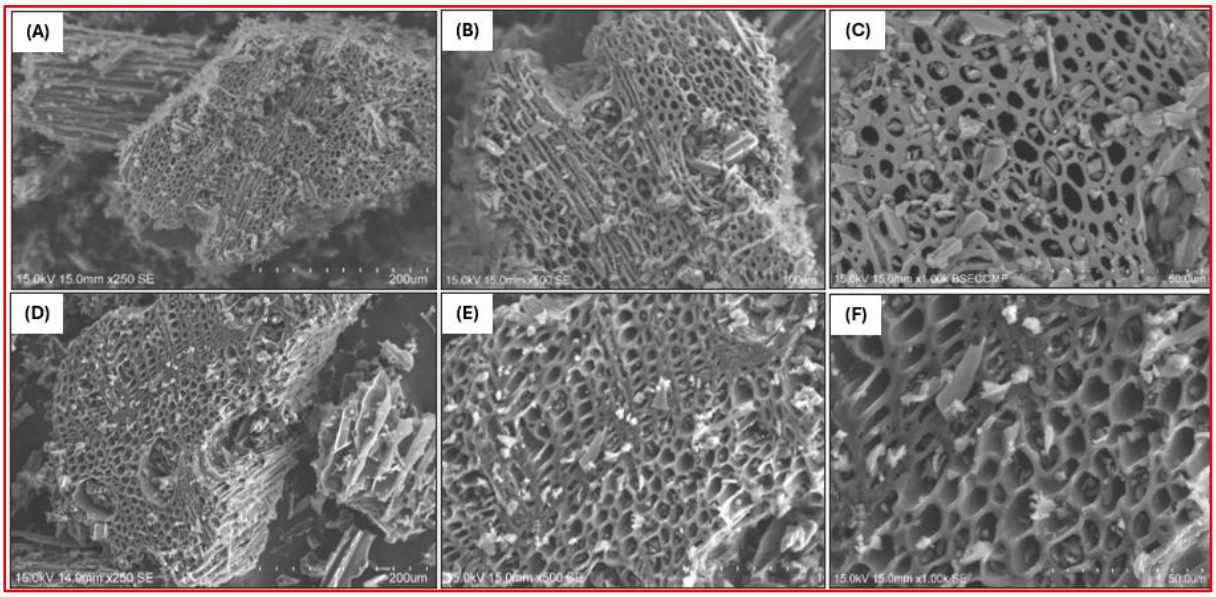

Figure 30: SEM micrographs of: (A) 250X, (B) 500X, (C)1000X - B525; and (D) 250X, (E) 500X, (F) 1000X - HTB525; to enunciate the effect of PHT

Nowadays, a recommended method for activated biochar production involves metal salt impregnation into biomass as is, followed by high-temperature pyrolysis (600–900 °C) (Adeniyi et al., 2023; Fuertes et al., 2018). However, CRD biomass naturally contains metallic elements (especially AAEM), enabling mild, in-borne/in-situ activation with no externally incurred chemicals, energy, and related process costs. While surface areas were not exceptional, they were notably improved even at a moderate pyrolysis and PHT temperatures. Therefore, couple of key advantages in this thermal-only activation approach is the minimal introduction of surface reactive groups or volatiles, and enhanced chemical and thermal stability, without the necessity for adverse operation conditions. EDX analysis presented in Figure 31 (bottom), further confirmed that HTB525 embraced a minor reduction in oxidative reactivity that could be a stepping stone for PHT in promoting biochar's stability and permeance.

EDX spectra confirmed high carbon presence in B525 (90.8%) and HTB525 (91.7%), demonstrating effective aromatics formation as heat-labile volatile compounds decomposed during the 30 min PHT. This is higher than the carbon content derived from elemental analysis (85.11% and 87%, respectively). Oxygen content decreased from 9.1% to 8% in the EDX spectra due to PHT, suggesting a reduction in surface functionalities like hydroxyls, carbonyls, carboxylic acids, and sulphonics, which are typically responsible for surface reactivity. Once again, there is a difference w.r.t elemental analysis that measured oxygen contents as 5.91% and 2.58%, before and after PHT, respectively. Nevertheless, the similar decreasing trends are positive notes. PHT also momentarily concentrated ash elements (mainly AAEM), as oxygen and VC were structurally freed, a trend that may continue in EDX spectra of HTBs for longer durations. This will be another hypothesis to verify.

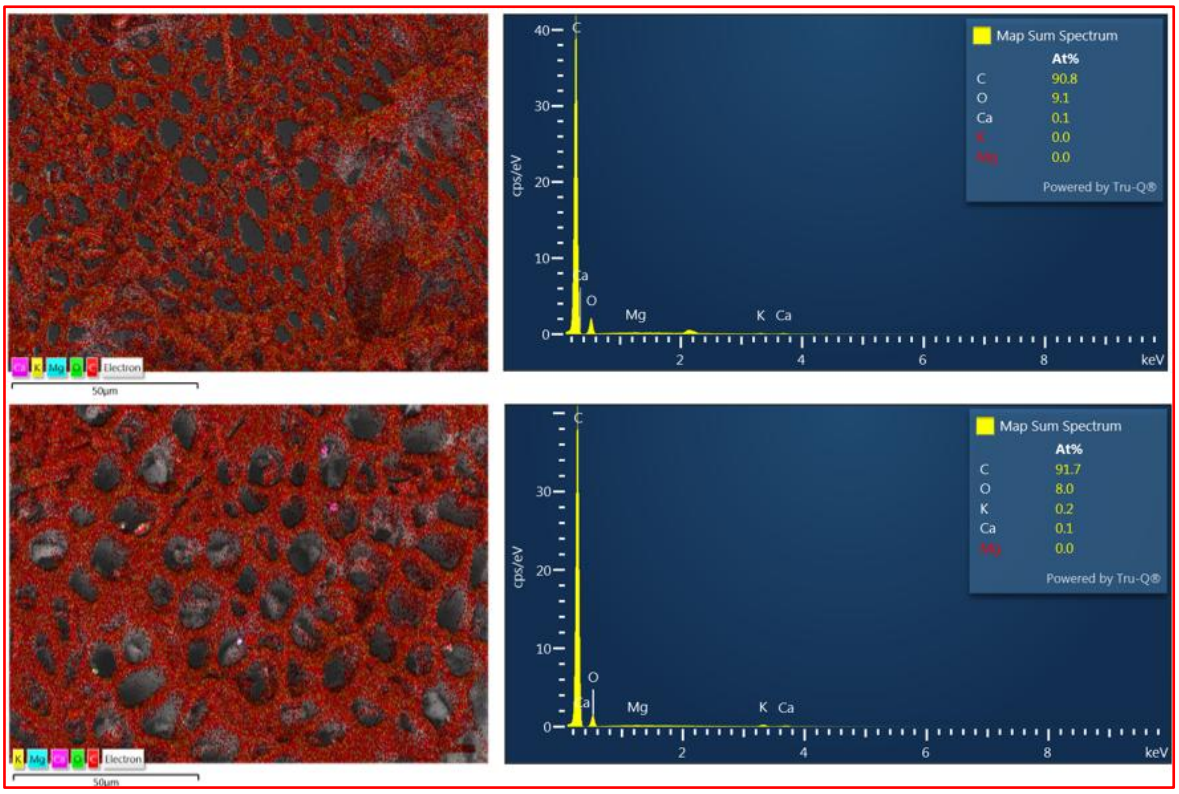

Figure 31: EDX spectra of B525 (top) and HTB525 (bottom)

3.2 Self-heating behavior

The self-heating performance of B425, B525, and HTB525 are discussed as separate cases to distinguish between their characteristics and link their influence with other under-explained metrics namely: biochar particle size, moisture content, and/or volume inside a container (square steel baskets here) of a given shape and size. The latter three cases generally, may act interdependently. In each case, self-heating experiments were conducted as triplicates and the mean values of biochar temperature is reported.

3.2.1 B425

In the first batch of basket heating experiments, B425 was tested under various conditions as mentioned above, at an ambient oven temperature of 140 °C with constant airflow, programmed for 5-7 h. As shown in Figure 32, when biochar lumps (<5 % intrinsic moisture) occupied half the steel basket volume, the self-heating test showed an exponential trend, and smoldering occurred. In spite of loose packing and sufficient air voids, flammability concerns arose probably due to high surface oxygen, labile functionalities, and high VC. When biochar lumps filled the entire basket, the self-heating failure was even more pronounced, as restricted inter-particle spacing led to faster heat transfer and eventual ignition. Figure 32 illustrates this, showing accelerated heat uptake due to spatial constraints, however, with ignition occurring just over 3 h in both cases, indicating only a delay in heat conductivity but similar terminal outcomes. The illustration also presents tests where 20-25% added moisture surprisingly did not prevent the same outcome as before, but merely delayed heat absorption. Once moisture saturated, B425 still approached the ignition threshold temperature at around 4.5 h since the start, confirming that moisture alone cannot mitigate self-heating risks. A clue in self-heating tests for biochar is that once the curves start going exponentially, they will mostly not show any plateauing behavior. The key takeaway is that biochar's self-heating tendencies are primarily governed by its physicochemical properties, which are dictated by pyrolysis conditions. Another concluding assumption here is that since large lumps themselves, failed the test, the fines of B425 will not have to go through the process since it is evident that generating more surface area could lead to faster air uptake and reactivity by the biochar.

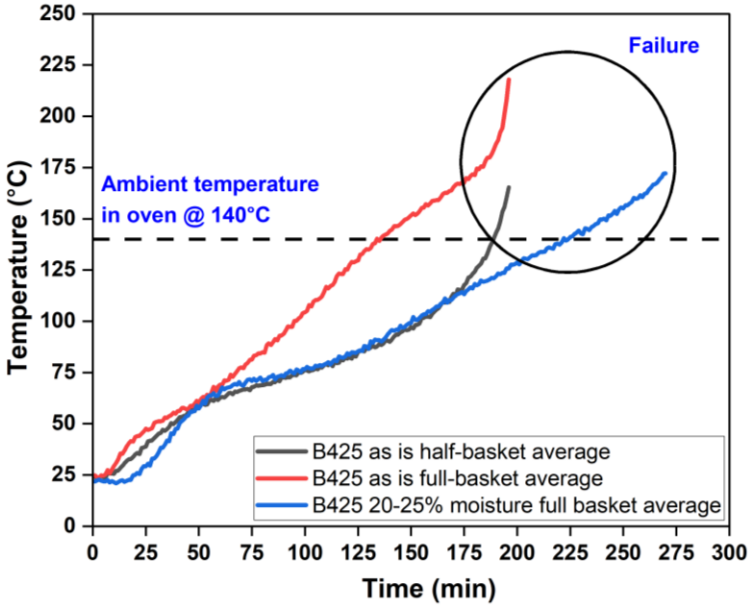

Figure 32: Self-heating curves for B425: with particle size as lumps - occupying half (black line) and full (red line) volumes of the basket with inherent moisture as is without any drying; or moisture addition and with 20-25% moisture addition (blue line)

3.2.2 B525

From Figure 33, in the **first test**, B525 lumps (also <5 % moisture) were subjected to self-heating test at 140 °C with half and full basket volumes. Both samples passed the self-heating test after nearly 7 h since the start, with the full basket reaching slightly over 140 °C before temperature stabilization. The half-filled basket showed delayed heat generation due to better heat dissipation. However, constrained inter-particle distances when the basket was full, led to faster heat transfer within the initial 3 h. This highlights the critical role of heat conductivity in determining self-heating behavior, with poor thermal conductors like CRD wood, trapping heat due to an internal temperature barrier, while its carbonized forms like B525 exhibit faster heat dissipation due to their crystallinity, stable and concentrated aromatic backbone, with a low surface area-to-volume ratio when taken as lumps, that reduces the chances for adsorbing reactive elements in ambient air. In the **second test**, dried (<1% moisture) and moisture-enhanced (20-25%) B525 lumps were both, tested at full basket volumes since the actual effect of dense packing in realistic conditions could be analyzed. Dried lumps heated up in the same manner and reached the ambient oven temperature in about 2.5 h as B525 lumps with moisture as is, in Test 1 did, after which the temperature stabilized. Voids within biochar lumps and in the basket, enabled constant heat transfer to the surroundings, reducing ignition risk. Moisture addition, however, could have played a dual role: a) delaying oxidation by absorbing internal heat; and b) evenly distributing heat.

Results confirmed that the presence of moisture had minimized thermal runaway, supporting Miura, 2016, where it was found that moisture blocks oxygen diffusion and subsequently slows its adsorption. However, excessive drying (<1% moisture) increased reactivity according to Xi et al., 2022, who noted that bituminous coal with 9.4–10.3% moisture, maintains a stable state w.r.t combustion reactions where the oxygen in ambient air, could have established an equilibrium with oxygen in the pores of coal. Although, a lower moisture content, increased the risk of self-heating was the conclusion derived from reviewing this study. Surprisingly, following drying, B525 still passed the self-heating test, hinting those physicochemical properties significantly influences self-heating behavior with particle size. However, moisture beyond a critical threshold, can also promote oxidation (Pan et al., 2020). Hydrophilic surface groups (*e.g.:* -OH, -COOH, C=O, -SO_3H) may cause wetting reactions generating exothermicity, that could increase the formation of localized temperature hotspots. Excessive wetting could also reduce the fraction of combustible hydrocarbons that could be valorized and decrease the final energy released per unit mass of fuel. The last externality is a crucial point if biochar is used in energy applications as in metallurgy. However, temporary energy content does not determine ignition potential solely. The overall carbon structure split between amorphous and graphitic phases, and FC levels play a crucial role. Graphitic biochars with strong C=C bonds require high activation energy to be broken down. As a result of this molecular rigidity, such carbons may resist ignition.

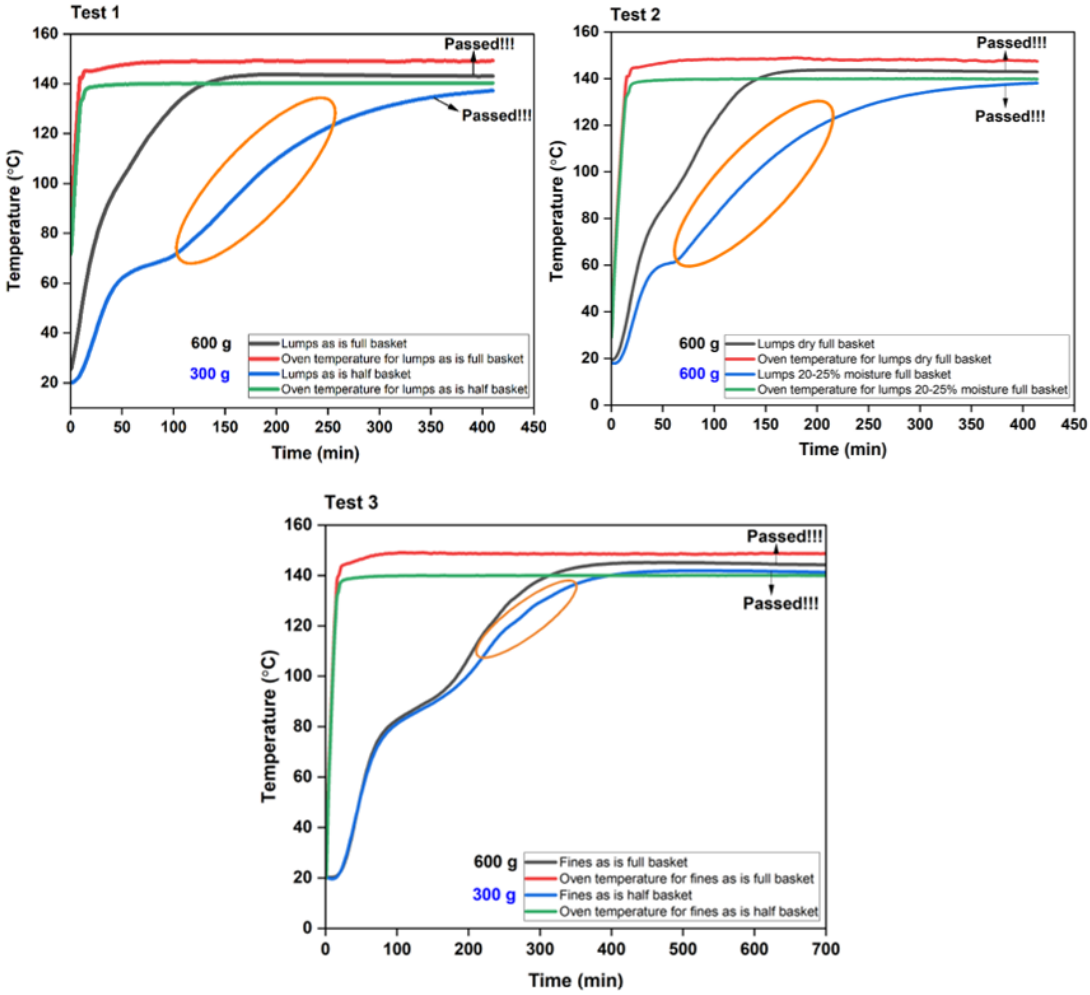

Figure 33: Three self-heating test batches for B525 at 140 °C

In the **third test**, B525 biochar was ground into fines and examined under half vs full basket conditions. Unlike lumps, fines heated up more rapidly due to their higher surface area to volume ratio upon diminution and compaction, exposing more reactive sites for oxygen to adsorb. Thus, an exception in this test was to raise the testing time up to 12 h to check the sensitivity of these fines under a longer duration. However, bulk temperature did not peak drastically, allowing the biochar to pass the ignition test. Also, owing to the presence of developed carbon structures towards the end of thermochemical transformation due to decomposition of holocellulose and lignin, the propensity to be structurally/chemically unstable may be subdued especially at higher pyrolysis temperatures, which could have balanced the high reactivity. From del Campo et al., 2021 as a conceptual foundation for low-temperature carbons, an inverse trend could be applied concurrent to our findings here, that higher-temperature biochars like B525 with low oxygen, low volatiles, and high ash, could manifest low reactivity. B525's low VC and reactive surface groups, may have decreased oxygen adsorption, depromoting self-heating and combustion. B525, exhibited great thermal performance in all tested conditions and passed the tests.

Another opening for deeper future investigations is biochar ash's role on reactivity and its influence on self-heating, *i.e*, whether or not they impart any specific inertness to the biochar based on their percentages.

3.2.3 HTB525

As concluded in the previous tests for B525, the tendency for self-heating is also governed by the pyrolysis parameters, presence of decomposable volatiles in biochar post-pyrolysis, surface area, porosity, and post-production passivation techniques (to minimize the effect of combustible contents). In this case, for HTB525, two self-heating tests were conducted where volume in the basket and moisture content were alone varied, but the particle size was kept in the range of fines. This was done to provide a more holistic view on sensitive cases for biochar to flame. To confirm if a superior performance in terms of sustaining high temperature conditions for a long duration without flammability could be possible to achieve, HTB525's slow ignition trends or heat

accumulation if any, was tested for about 24 h at 120 °C. A key inclusion here is the comparison with B525 as dry fines, and in full basket volume, at 120 °C for 24 h as well, to discern the effect of PHT if any w.r.t shape of the curves under such a sensitive atmosphere. All the experiments are depicted in Figure 34.

For **test 1**, HTB525 fines as is (<5% moisture), in half and full basket volumes, were considered. Due to a larger volume in the latter case, the fines showed a rise in bulk temperature slightly over 120 °C due to intricate packing and lower heat diffusion before the curve saturated. Mostly, micropores were observable for this biochar via SEM imaging that can validate the constricted size of porous channels limiting diffusion and hastening uptake of heat even before 100 min of incubation time. Elemental analysis also reassured that surface oxygen concentration for this biochar was around 2.58% that promulgated its reduced reactive nature after PHT. At the end, this biochar did not show any signs of self-heating which may point the discussion trajectory once again to HTB525's physicochemical properties and PHT effects. In **test 2**, even though, the peak temperature reached is around 120 °C only for both samples, the duration to reach this stage was considerably more for the wet fines relative to fines as is. From the curves, it can be seen that it takes at least around 9 h since the start of the oven heating experiment in case of added moisture. Whereas, for fines as is, the ramp in temperature to 120 °C, was witnessed around 3-3.5 h since initiation because there is less moisture to absorb the sustained heat for a long time till internal exothermicity reaches a state of equilibrium with ambient temperature. The findings infer that the role of moisture is key to curtail self-ignition, especially at high volumes and small particle sizes of biochar.

In **test 3**, B525 and HTB525 were tested as dry fines in full basket volumes to project the effect of particle size, surface area, and porosity altogether. Due to narrow pores, heat evolution is hindered. This is worsened by a non-strangulated surface availability for the adsorption of ambient reactive species for fine particles. A fast rise in temperature is obvious for B525, well below 100 min, indicating no delay due to poor heat dissipation within the basket. HTB525 reached close to the oven temperature after 3-3.5 h but plateaued just like B525 with no other marked difference. The saturation in temperature for both samples, could be attributed to the reduction in volatiles, and increase in thermal maturity with pyrolysis temperature or PHT or both. This statement could also be underpinned by high FC, TSF, TGA R50 index, and a decrease in Van-Krevelen indices respectively, for both biochars, implying deoxygenation (low surface reactivity), dehydrogenation, and aromatization as corroborated by the FTIR analysis between 1280-1610 cm^{-1}. A similar concept on aromaticity and surface reactivity linked to Van-Krevelen parameters was noted in Thauront et al., 2024. For HTB525, since ash increased to 7.48%, inert and non-volatilized mineral matter could have contributed to reduced oxidative reactivity as well. Metals, non-metals, and inorganics in ash can latch onto organic residues in biomass and biochar that could collectively inhibit their degradation, thermally (Puri et al., 2024). In general, all three tests passed the basket-heating runs emphasizing the beneficial role of high pyrolysis temperature or PHT to impede ignition.

It may be concluded from all self-heating tests that every metric tested, has been responsible in its own way to impart an influence on biochar's ignition behavior. Pyrolysis conditions still govern the overall reactivity followed by presence or absence of PHT. Even in most conducive cases of small particle size, large volume, and least moisture content, if the biochars have seen high temperatures in controlled heating rates and sufficient BRT during their production or secondary passivation, they may not ignite. Due to positive results, further PHT rounds for B525 at the same temperature but with different durations will thus, be tested, mainly to check its effect on proximate analysis and thermal stability parameters.

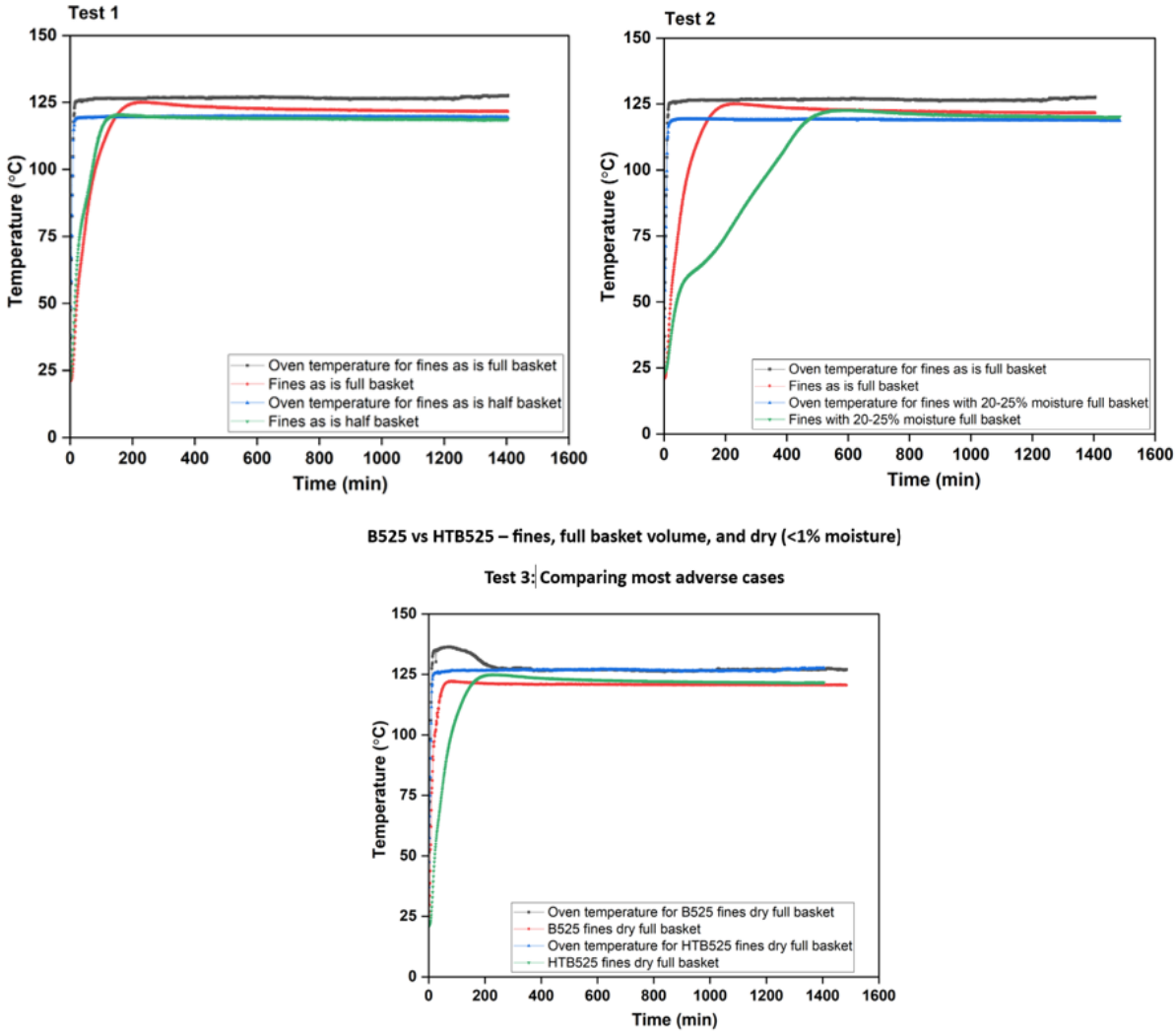

Figure 34: Three self-heating test batches for HTB525 at 120 °C

3.2.4 Comparison to similar biochar self-heating tests

Upon reviewing similar works, self-heating depends on five factors and this list is non-exhaustive. **Firstly**, biomass nature plays a crucial role. Studies like Zhao et al., 2013 emphasized that biomass chosen for pyrolysis, through its biochemical composition, can dictate the susceptibility of final biochar to ignite spontaneously. Font, 2020 shared that a heterogeneous feedstock can display variability in reactivity depending on the inherent content of hemicellulose, cellulose, and lignin. For CRD wood under this category of raw material, a high holocellulose and low lignin can increase carbon loss via tar and pyrolysis gas, and decrease FC in the biochar product leading to a disturbance in its chemical and structural stability. With this, high surface-borne volatiles also surge the probability of biochar to undergo exothermic oxidation reactions and ignite easily. The auto-ignition temperature for FC is higher than for volatiles. Ashman et al., 2018 believed that high ash percentages can suppress these reactions although, there is a risk of its AAEM content to catalyze oxidative processes. **Secondly**, pyrolysis parameters and biochar properties also govern self-heating. According to Dufourny et al., 2019, Dzonzi-Undi et al., 2014, and Phounglamcheik et al., 2020, high pyrolysis temperatures and long BRT subtled volatiles in biochars, reducing their reactivity. Including a PHT step to passivate higher temperature biochar also alleviated self-heating potential as proved in our case with HTB525. Any meagre oxygen availability during torrefaction or pyrolysis can exacerbate the activity of reactive oxy-functional groups on biochar and eventual self-ignition (Evangelista et al., 2018). This could lead to incomplete conversion of biomass carbon and retain a large portion of volatiles in the carbonized char leading to more chemical degradation in the presence of a harsh, reactive atmosphere during post-production stages (Schwarzer et al., 2021). Since volatiles is one of the main root causes, the discussion on its role in biochar self-heating could be readily compared our results in this study. Low temperature biochars like B425, can retain residual tars and condensed pyrolysis gas as trapped entities within the

pores and on the surface especially without proper suction from the pyrolysis zone. This can initiate a thermal runaway due to clogged pores blocking diffusion of heat to the environment leading to internal exothermicity. Sometimes, blocked pores can lead to localized oxidation of volatiles from within, that create sudden hotspots causing temperature shoot-ups (Riva et al., 2020).

Thirdly, biochar particle size is yet another caveat. Especially, for low temperature biochars like B425, small particles could have offered a large surface area for air adsorption that may have accelerated oxidation and heat build-up (Castells et al., 2020). Curtailed and dense micropores with a probable accumulation of volatiles can only worsen the situation. On the other hand, B525 and HTB525 as dry fines and at full basket volume, passed the heating test comfortably, that may be edged to a lower volatiles content despite high surface area and microporosity. As an extrapolated finding from Preimesberger et al., 2024, larger spaces in big particles like lumps, managed heat efficiently due to widened pores allowing faster heat dissipation even in maximum volume and after drying. **Fourthly**, our take on the role of moisture in dampening self-heating was confirmed from Itoh et al., 2020. It basically acts a buffering agent under thermal stress by absorbing any excess heat generated internally. However, too high moisture could cause microbial activity and lead to biological oxidation (Dzonzi-Undi et al., 2014). This statement is not asserted here and may require further work for verification. **Fifthly**, packed volumes increase the risk of temperature build up due to confined, insulated conditions and inadequate heat dissipation, especially large stockpiles (Wei et al., 2023, Krigstin et al., 2018). Once again, this is interdependent on biochar properties, particle size, and moisture content since there are cases in our self-heating tests where biochar as fines, at full basket volume, with very low moisture, low volatiles content, and high thermal stability, that have passed the test convincingly.

Since Restuccia, 2017 reported that irregular shape of piles may cause uneven oxygen permeation between the boundary layers and the core, thereby influencing faster self-heating, all our tests were carried out only in square baskets according to protocol, thereby maintaining an even shape of the container. Even though, long storage time was discussed in a related work (Zhao et al., 2013) to have increased the likelihood of oxidation of biomass-based materials, it has not been proved via our work and hence, no conclusive evidence is available for discussion on this metric. Another conclusion from the self-heating studies conducted is that if biochar particles of even finer size (*e.g.*: 1-100 µm) were considered, the self-heating test results may show large differences (could fail) as more surface area will be exposed. Since the least particle size, we could achieve for biochar using the current milling device is only about 500 µm as used in this study, lower ranges could not be tested.

3.3 Characterization of B525 PHT at longer durations (30-90 min)

Except the physicochemical characterization, TGA/DTG/TGA R50, FTIR, and SEM EDX were only carried out for B525 samples from the first set of PHT runs between 30-90 min, as an example.

3.3.1 Physicochemical properties

To discern the effect of thermal passivation on proximate analysis parameters, stability, and surface area of biochar, two rounds of PHT with B525 were carried out in the same temperature but at five different residence times (30-90 min) as shown in Table 19. This is mainly to ascertain the robustness of the activation process and forge a sense of reliability in the derived quantitative findings. More replicates were not carried out due to the mandatory downtime of the rotary retort-furnace assembly to fix the distorted temperature probe elements that occurred during experimentation.

Table 19: Characterizations of B525 after PHT at different durations. Metrics that experience a downward trend are marked in red. Up to two decimal places were considered for accuracy

Metric	B525				
	30 min	45 min	60 min	75 min	90 min
First set of PHT runs					
VC (wt%DB)	16.17	15.81	15.64	14.92	14.43
Ash (wt%DB)	6.96	7.22	7.31	7.98	8.02
FC (wt%DB)	76.87	76.97	77.05	77.10	77.55
TSF (%)	82.62	82.96	83.13	83.79	84.31
BET surface area (m^2/g)	218.88	247.22	271.80	376.41	292.87

Micropore volume (cm^3/g)	0.099793	0.111929	0.122945	0.158739	0.130419
Loss in yield (wt%)	15.21	16.95	17.65	18.70	20.80
Second set of PHT runs					
VC (wt%DB)	16.88	16.59	15.21	14.56	13.98
Ash (wt%DB)	7.08	7.21	7.23	7.61	8.13
FC (wt%DB)	76.04	76.20	77.56	77.83	77.89
TSF (%)	81.83	82.12	83.60	84.24	84.78
BET Surface area (m^2/g)	212.40	241.95	271.88	356.50	301.59
Micropore volume (cm^3/g)	0.088228	0.115629	0.122093	0.149322	0.131855
Loss in yield (wt%)	14.05	15.95	16.65	17.9	20.15

In both rounds, similar trends are observed for VC, ash, and FC of biochar. Increase in residence time subjected the biochar to undergo steady decomposition with reinforcement of the carbon skeleton, and also develop microporosity (Sajjadi et al., 2019). In the first round, VC decreased by about 11% for PHT at 90 min relative to only 30 min. Whereas, in the second set of runs, VC reduced by almost 17% between the extremities of residence time suggesting that residual surface functional groups rich in labile, hydrophilic carbon (*e.g.:* -COOH, C-OH) species may have degraded with sustained high temperature conditions, and more stable C-C, C=C links are formed due to dehydrogenation, deoxygenation, isomerization, and aromatization reactions, contributing to lower heterogeneous structures and developed chemical stability (Zhang et al., 2022). Pearson's coefficient, r, for VC from the first and second rounds of PHT was -0.98 which suggests PHT duration to have a strong negative correlation on heat-labile biochar contents. Complementarily, FC increased by a small margin (Pearson's coefficient, r, was 0.90 and 0.93 respectively, showing a positive correlation with PHT time) from 30-90 min for both rounds of PHT which bolsters the fact that condensed aromatics forming stacks of carbon sheets slowly begin to fill the activated biochar matrix. Concentrated FC also explains the increase in TSF from 81-85% with PHT duration, also showing a highly positive correlation (Pearson's coefficient, r, was 0.98 for both rounds). According to Lataf et al., 2022, FC content may influence yields of biochars too. Due to high resistance of ash, it continues to not react during activation and increases further during both rounds: by 15.2% in the first set, and by 14.8% in the second set, showing almost identical performances as VC drops. The yield loss ranged from 14-21 wt%. There was a clear increase mainly with growing heat treatment time with the maximum loss at 90 min. Further time or temperature increase could have led to volatilization and thermal breakdown of biochar carbon in the form of C_1-C_3 gases, tars, and VOCs. This is explained by a strongly positive correlation with PHT time (Pearson's coefficient, r, was 0.98 for both rounds of PHT).

As far as surface area is concerned, PHT increased microporosity between 30-75 min by 72%, from 218.88 m^2/g to 376.41 m^2/g in the first run, and by 68%, from 212.4 m^2/g to 356.5 m^2/g in the second run. Continuous lignin degradation with condensation of aromatics, could lead to this increase (Chatterjee et al., 2020). However, these pores expanded at 90 min and faced a decline in surface area within 15 min for both runs to 292.87 m^2/g and 301.59 m^2/g, respectively. The Pearson's coefficient, r, for both these runs were only moderate at 0.73 and 0.83 respectively, indicating a sudden change in the direction of correlation at the PHT time of 90 min. This may be due to loss of microporosity with increase in heat treatment time in the last 15 min and generation of mesopores by etching of micropores as shown by the SEM micrographs in Figure 37 and Figure 38. Surface area of these B525 samples that underwent PHT was consistent with the co-pyrolysis air activation process in Kearns et al., 2019 which resulted in biochars with a surface area ranging from 110-330 m^2/g, although for CRD wood biochars here, no air was used for PHT. Xiao, 2022 mentioned that post-pyrolysis air activation can also be followed between temperatures of 400-600 °C for achieving optimum surface area. Here, it was observed that any surface area increase, occurs within the first 15 min after which it may decline due to reorientation of biochar's structure. Eventhough this trend was according to B525's PHT from 30-90 min, the duration for surface area increase was pushed till 75 min in our case because no external air was used in the activation process that in turn could have delayed any deformation or burn-off, and resulted in a late structural collapse with formation of larger pores. A similar perturbation in correlation was observed in the case of micropore volume for both PHT runs that showed only a moderate Pearson's coefficient, r, at 0.77 and 0.85 respectively, due to loss in microporsity after 75 min.

From these experiments, we may conclude that porosity, surface area and surface functional groups can be controlled depending upon the applications under focus. In case of metallurgical applications, a moderately-high surface area could be beneficial for efficient oxidation-reduction reactions between the biochar-derived biocoke, air, CO, and the metal ore (*e.g.:* Fe_2O_3). Albeit, the surface area could also cause ignition issues during logistics. At the same time if the porosity is very high, its structural integrity will be compromised, which means it may not be able to withstand the heavy loads subjected over it.

3.3.2 TGA/DTG/TGA R50

For B525 after PHT, there is very little weight loss of <2% in the first degradation phase below 150 °C at all residence times of 30-90 min due to lower contents of moisture and light volatiles. This can be seen from Table 20. The second phase between 200-400 °C showed discontinuous weight loss patterns for all biochars which still revealed the presence of residual holocellulose, extractives, and unstable volatiles. Despite being variable, maximum weight loss in this region did not exceed 6%, highlighting growing FC content (76-78 %) and reducing VC (17-14%), concurring with the proximate analysis results back in Table 19. In the third phase of 400-600 °C as shown in Figure 35 (B), a small peak at 471.04 °C was exclusively seen despite a major peak at 569.31°C, for PHT at 30 min. For higher residence times, the melting temperatures recorded were 574.78 °C (45 min), 588.23 °C (60 min), 589.37 °C (75 min), and 592.11 °C (90 min), indicating a shift in lignin decomposition towards the right. Albeit, from Figure 35 (A), the TGA curves seem to overlap at 75 min and 90 min of PHT time, evident from the narrow difference of melting temperatures (<3 °C). A clear distinction with respect to biochar weight loss can be made here. The weight loss decreases from 87.63% at 30 min to 48.71% at 90 min. Intact lignin in biochar may slowly transform into aromatic crystalline carbon rings since prolonged heat treatment could confer a partly turbostratic arrangement. Unstable functional groups of lignin such as methoxy, methyl, hydroxyl, and carbonyl groups may also be cleaved resulting in the elimination of volatiles incurring thermal stability and resistance to degradation. However, Sajjadi et al., 2019 stated that biochars usually find it hard to reach an appreciable turbostratic or completely carbonized stature since immensely high temperature, long BRTs, and carefully optimized activation conditions are key. Hence, at the end of pyrolysis or activation, biochar will most likely contain only a heterogeneous composition of at least some amorphous and enriched graphitic carbon, but rarely, 100% of the latter.

Table 20: Weight loss percentages encountered by B525 at different PHT durations. Up to two decimal places were considered for accuracy

Biochar sample	Weight loss in each phase of TGA (%)			
	First phase (<150 °C)	Second phase (200-400 °C)	Third phase (400-600 °C)	600-900 °C
B525 PHT 30 min	1.60	2.79	87.63	6.94
B525 PHT 45 min	0.98	1.22	74.50	19.96
B525 PHT 60 min	1.18	2.39	62.28	28.21
B525 PHT 75 min	1.51	5.37	50.72	39.26
B525 PHT 90 min	1.24	2.64	48.71	41.34

As a second distinction, above 600 °C, residual amorphous carbon and weak aromatics in stable biochars may still oxidize at high temperatures as ascribed by rising weight loss from 6.94% to 41.34% for PHT at 30-90 min, respectively. Increase in duration of heat treatment could also lead to volatilization of simple mineral matter in biochar. For example, carbonate salts of AAEM in ash can degrade to AAEM-oxide and CO_2 leading to loss of biochar carbon and subsequent weight reduction. This could hold true for mineral salts like $CaCO_3$ that form Cao and CO_2 at temperatures near or above 600 °C (Clemente et al., 2018). Inorganics can sometime act as molecular shields to biochar carbon and other volatiles. Thus, once they may begin to melt at high oxidising temperatures, the otherwise concealed biochar constituents are then exposed, thermally degraded, and could face substantial weight loss. These conclusions are derived from the DTG plot in Figure 35 (B) between 600-900 °C, where a faint peaking can be observed at 641.13 °C, 666.44 °C, 687.87 °C, 763.79 °C, and 764.48 °C for B525 at 30-90 min PHT, respectively.

For estimating thermal stabilities, the R50 recalcitrance parameter was calculated from the corrected thermograms as in Figure 35 (C). PHT at 30 min had R50 at 0.596 followed by 0.618 at 45 min, 0.627 at 60 min, 0.644 at 75 min, and 0.659 at 90 min (10-11% increase from 30 min to 90 min). Maturity of carbon is therefore, directly

proportional to duration of heat treatment as well as the ideal temperature. There is a steady promotion in R50 values heading towards the category A biochar that signifies least degradation relative to other biochar classes.

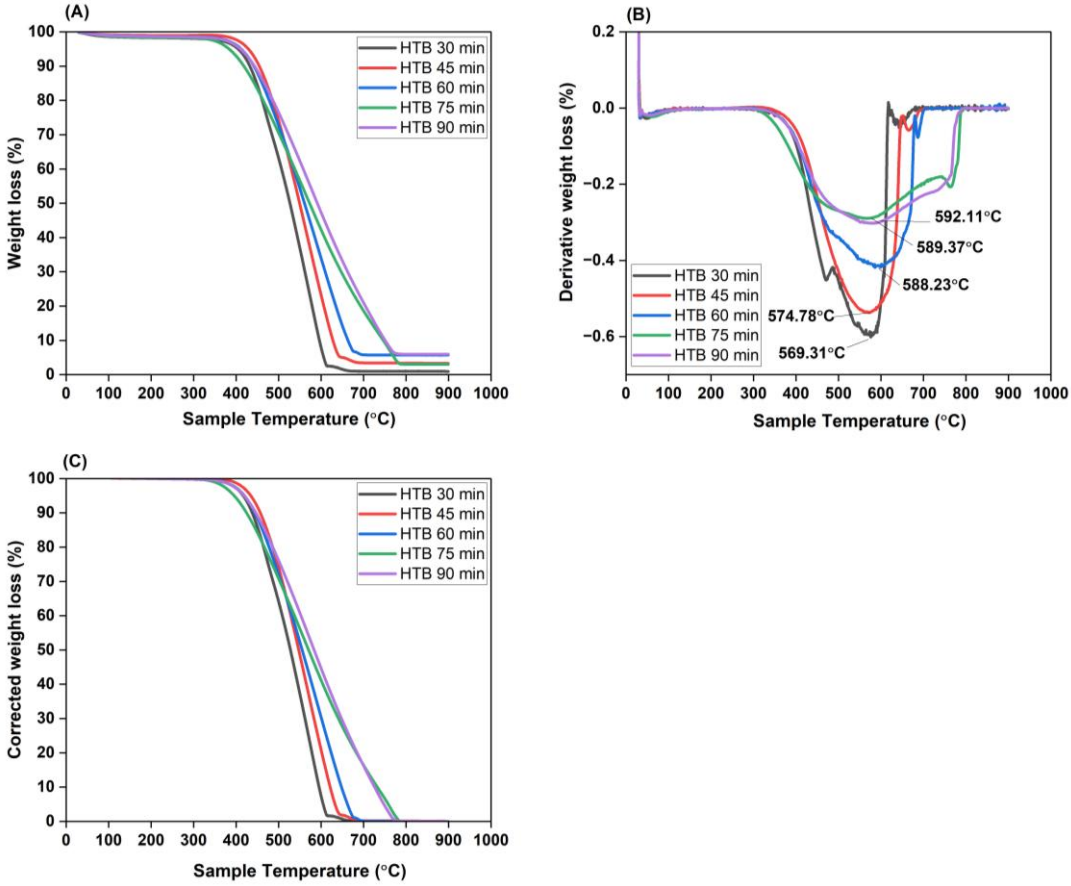

Figure 35: Thermal decomposition analysis of B525 after PHT for 30-90 min (also referred to as only HTB: heat-treated biochar). (A): TGA curves; (B) DTG and associated melting temperatures; and (C) moisture and ash corrected TGA for calculating R50 index

3.3.3 FTIR

For B525 at 30-90 min PHT in Figure 36, 700-840 cm^{-1} showed some aromatic C-H vibrations associated to the bending of protons in carbon rings that is a characteristic shown by high temperature, stable biochars. Loss of structural hydrogen can also mean lowering acidity and hydrophobicity that is highlighted by O-H bending vibrations in this region. Since residence time of biochar during heat treatment increases by 15 min in each round, heat becomes pervasive and gradually opens up metal linkages upon the volatilization of hydroxyl groups attached to biochar carbon. Increasing peak heights within 800-940 cm^{-1} from 30-75 min indicate melting of simple metal matter like monovalent alkalis. At 90 min, the peak height diminishes that could mean such metal matter have already been partly volatilized. Similar to pyrolysis biochars covered before, the HTBs here showed decreasing intensities for carbohydrate C-O vibrations between 1020-1280 cm^{-1} from 30-90 min. This is because the organic holocellulose residues reduced with stronger degrees of heat treatment upheld by superior decomposition rates of oxygen species via CO_2, CO, and light volatiles. Hence, the peak height is maximum for short residence times where biochar has a sizeable organics content left due to less duration available for reacting with ambient heat. This pattern holds true for C-OH vibrations related to left-over carbohydrate degradation products such as carboxylic acids, esters, amides, and levoglucosan that is high for HTB with incomplete initial carbonization. Whereas, C-H bending vibrations in methoxy, methyl, and methylene groups, coupled with O-H bending vibrations in phenols, suggest hydrogen transfer, dehydrogenation, isomerization, and aromatic conversions of biochar carbon. It is observable by more articulated peaks as heat treatment time increases reinforcing its positive effects on a stable backbone development.

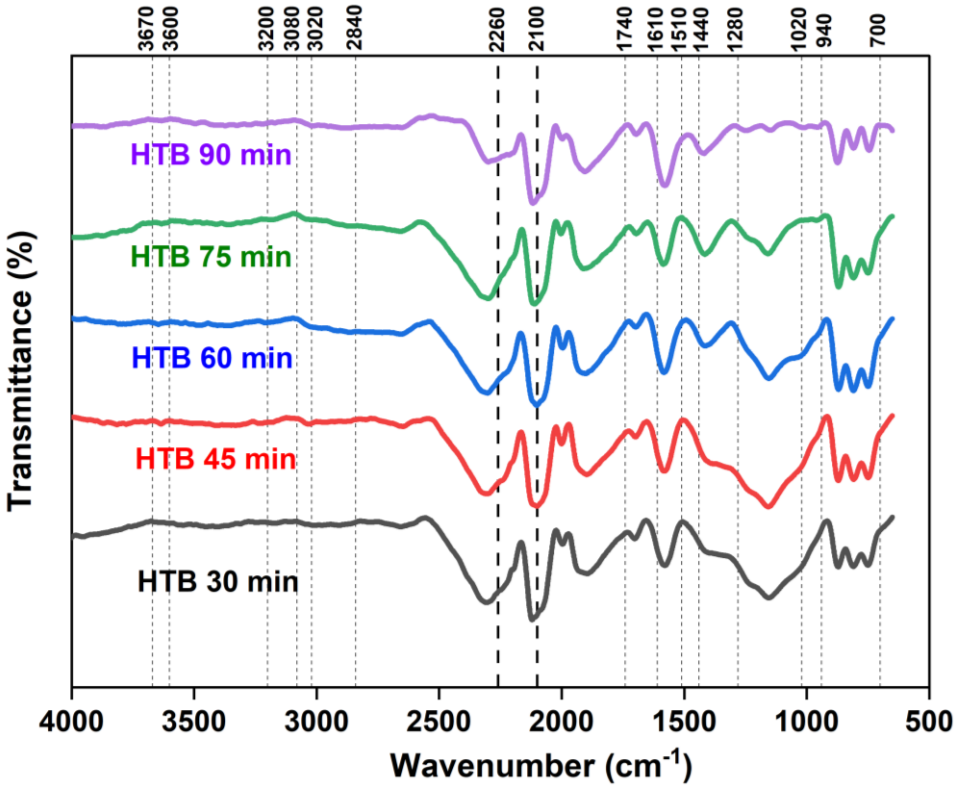

Figure 36: FTIR bands of B525 after PHT for 30-90 min

C=C stretching vibrations between 1510-1610 cm^{-1}, showed no clear distinction between different heat treatment times. The intensity was almost similar in each case proving that condensation of carbon and its thermal maturation progressed in all HTBs. Until 1740 cm^{-1}, all biochars displaced a meagre vibration amidst the C=O plane for lignin subunits like aldehydes, ketones, esters, and ethers showing their susceptibility for deformation. No difference in peak heights were seen here, however, there is an even reduced presence of oxygen once secondary heat treatment begins when compared to the FTIR spectra of B425 and B525 from Figure 29. Yet again, 2100-2260 cm^{-1} manifests C≡C stretching vibrations as in aromatic ring clusters where all heat treatment times almost showed the same intensity with no marked difference. Around 2250 cm^{-1}, C≡N stretching vibrations are mostly seen for higher treatment times probably suggesting the occurrence of denitrogenation and strengthening of C≡C. At lower treatment times, this nitrile group which is polar in nature contributes to structural stability. 3020-3080 cm^{-1} bands in Figure 36 manifested increasing disturbances in the aromatic C-H linkages that could mean more condensation of carbon rings with heat treatment. Over 3200 cm^{1}, no peaks related to hydrogen-bonded O-H functionalities were observed that highlights a resilient hydrophobicity and less reactive nature.

3.3.4 SEM-EDX

The SEM micrographs at 250, 500 and 1000X magnifications for B525 at 60 min and 90 min PHT, indicated that pore obstruction by volatiles and/or inorganics was greatly avoided in both specimens. In Figure 37 (A)(B)(C), the porous structure at 60 min, appears soft and ordered, with mostly homogeneous morphology, as heat treatment severity increases like Hadey et al., 2022 suggested. Although, unlike PHT at 60 min, pore sizes at 90 min seemed to manifest higher heterogeneity (

Figure *37* (D)(F)). To affirm this finding, generation of enlarged openings directly on the surface of biochar particles, can be seen in Figure 38 (A)(B)(C) upon reducing the magnification to 50X and 100X. These appear in the grounds of meso or macropores which may be generated by rampant cracking of biochar carbon or tarry material in the initial pores, trapped gas evolution/escape, removal of less-stable inorganics, or even bulk loss of volatiles, as construed from Mishra et al., 2024. Widening of pores may have also occured due to a structural reorganization of any unconverted biomass in biochars where thin and fragile walls between the adjacent micropores may collapse under increasing thermal stress that could cause pore coalition owing to internal overpressure (Shafiq & Capareda, 2021, Jerzak et al., 2022). As the degree of carbonization increases, stable aromatic sheets in biochar may become rigid and tend to stabilize these larger pores, but now, with reduced surface

area. This can be supported by the surface area of B525 at 90 min PHT which lowered to 292.87 m^2/g. Even in the second heat treatment run, the same sample showed a surface area of 301.59 m^2/g at 90 min PHT. High heat treatment times can hence, produce biochars with big, interconnected pores that could support diffusion phenomenon for water, nutrients, and other large molecules, increasing its suitability for use in soil amendment procedures (increases soil porosity) (An et al., 2022).

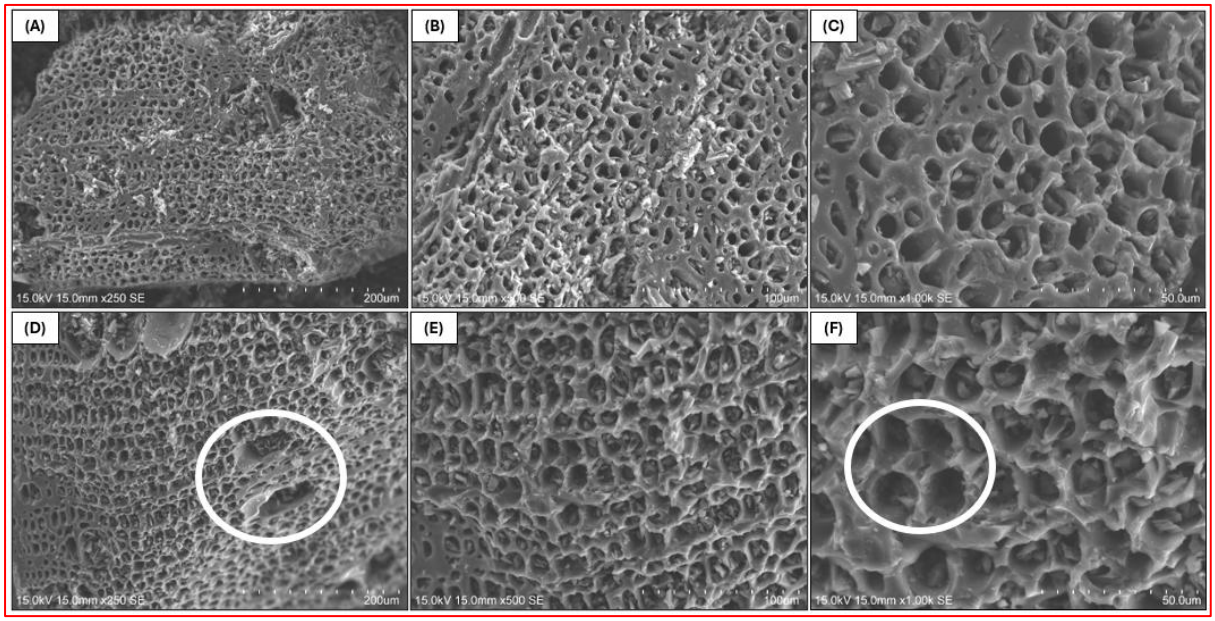

Figure 37: SEM micrographs of: (A) 250X, (B) 500X, (C)1000X - B525 PHT at 60 min; and (D) 250X, (E) 500X, (F) 1000X - B525 PHT at 90 min; to enunciate the effect of duration

Ideally, the dynamic nature of these biochars may not affect their applications in carbon sequestration and metallurgy because they still retain greater thermal stability. In larger pores, the bulk of the material is farther away from the boundary layer and only a small fraction of internal porosity is accessible, limiting the surface area-to-volume ratio and reactivity of biochar. A slight concern although, would be to strike a balance between the conservation of stable biochar carbon and elimination of volatiles, but without loss of yields during activation since the proportion of unimpaired FC holds key for the two applications under focus in this work.

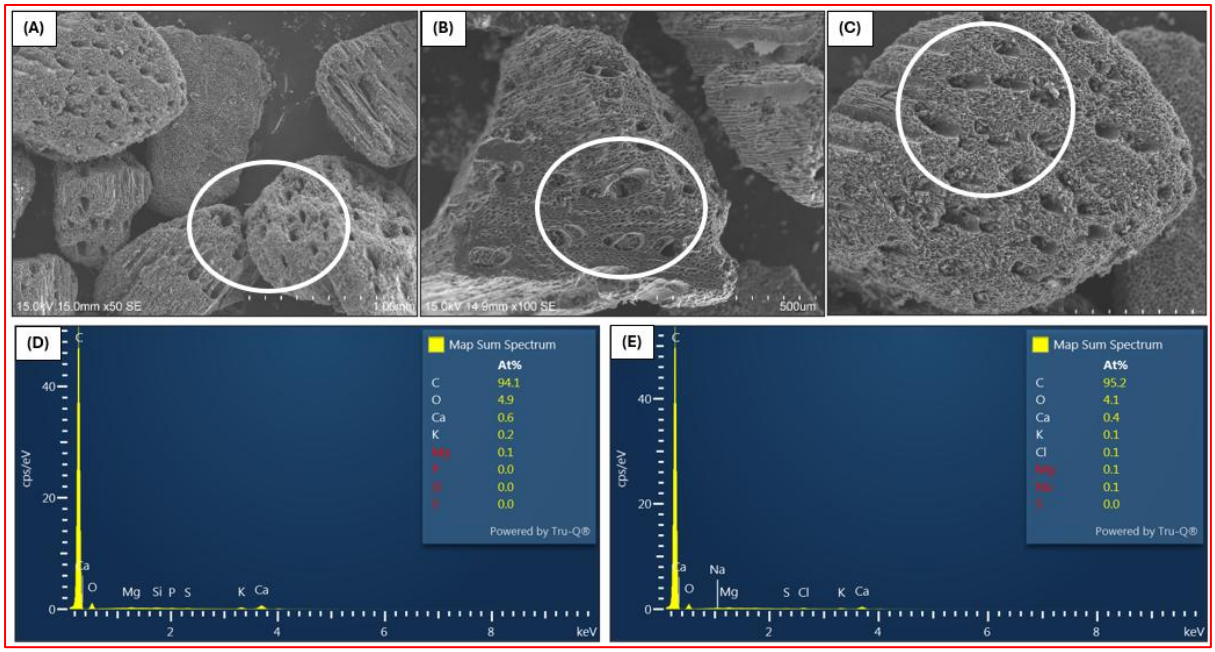

Figure 38: SEM micrographs of: (A) 50X, (B) 100X, (C)100X - B525 PHT at 90 min; (D) EDX spectra of B525 PHT at 60 min and; (E) 90 min

EDX analysis in Figure 38 (D)(E) confirmed that PHT of B525 at 60 min and 90 min is beneficial for interspersing greater carbon into the biochar matrix, at 94.1% and 95.2%, respectively. Relative to the EDX spectra of B525 (90.8% carbon) and HTB525 (91.7%), heat treatment duration has definitely played a critical part in responsibly improving carbon conversion. A limitation in the availability of surface oxygen is also seen at PHT of 60 min (4.9%), that is 46% lower than B525, and 38% lower than HTB525. Similarly, a low oxygen concentration was observed for B525 PHT at 90 min (4.1%), banking on the positive approach of secondary thermal activation, to tailor its chemical make-up. Unfaltering AAEM in ash seems to take a hit when high heat treatment time reduced the concentration of Ca (0.6% to 0.4%) and K (0.2% to 0.1%) at 90 min. The presence of Cl at PHT of 90 min may also mean that AAEM existed in other salt forms like chlorides. These may exist as trapped species within the biochar carbon structure before being volatilized as chlorinated hydrocarbons or organo-chloride compounds, at high temperatures and residence times.

4. Discussion and Conclusion

CRD activities produce significant amount of wastes around the world that is leading to growing concerns regarding their management. Chemically treated wood components in the CRD waste are non-recyclable due to their poor quality. Additionally, its heterogeneous composition and variations w.r.t geography and sourcing practices, place all the focus on landfilling them as an easy way out. Landfill disposal also causes environmental problems like release of GHGs due to the anaerobic processes, ground water contamination, soil degradation, and other societal issues. To taper such externalities, alternative treatment technologies like thermochemical pyrolysis can not only reduce this wood waste but can also contribute to bioenergy and bioproducts generation. Biochar is a promising product from pyrolysis that has immense industrial value. The properties of biochar can be adjusted by optimizing pyrolysis process conditions, feedstock pre-treatment, and even post-production activations. Depending upon these tailored properties, the most appropriate applications could be selected. However, the foundation of CRD wood pyrolysis is a relatively underexplore field in terms of scaling up laboratory trials to pilot or even demonstration stages for understanding their transformation process to biochar and the ideal conditions for conversion. The discussion here evaluates experimental investigations, and the findings derived.

The pilot-scale biochar production indicated that pyrolysis temperature has the dominant effect on biochar physicochemical characteristics. Higher temperature biochar (B525) showed enhanced carbon content and a reduction in oxygen and hydrogen that could signify carbonization and aromatic carbon condensation. This can be corroborated by low Van-Krevelen H/C and O/C highlighting chemical stability. Surface-bound volatiles decrease with temperature and may have reinforced B525's oxidative reactivity and passed self-heating tests. B525's thermal stability indices like TSF and TGA R50 are superior relative to B425 that could be due to developing crystalline carbon with increase in pyrolysis temperature. As far as chemical, steam, and CO_2 activation techniques have progressed, simple means of passivation have not yet been discussed at a broader forefront that neither require extra resources not cause secondary pollution. In general, the activation of biochar, whether through physical methods in reactive atmospheres or chemical processes, is conducted to mainly optimize the reactivity of functional groups, reduce unstable volatiles, and to alter the surface area based on specific applications. B525, having undergone a 30 min PHT trial run (HTB525), showed improved properties. An additional drop in H/C and O/C may mean sufficient progress towards this biochar's graphitization trajectory. A simultaneous increase in FC suggests a positive influence exerted by the secondary thermal activation step in the elimination of labile carbon. However, it is to be remembered that PHT is duration dependent where beyond a limit, benefits pertinent to biochar characteristics could diminish. One such situation was encountered in our case where there was a decrease in biochar surface area due to pore coalescence beyond 75 min of PHT duration. Increasing PHT to 90 min also decreased yield of the heat-treated biochar by 20-21%. Hence, a balance between PHT temperature and duration is key for future trials.

Self-heating tests confirmed that biochar's thermal and chemical reactivity depends on its physicochemical properties, particle size, moisture content, and volume within a container. Both B525 and HTB525 successfully passed self-heating evaluations, even under extreme conditions, owing to optimized pyrolysis and PHT parameters. This suggests that biochar produced under these conditions is safe for storage and handling, reducing the risks of spontaneous combustion. As discussed in various sections that focused on self-heating behavior, the interaction of biochar with ambient oxygen species may increase when surface area and/or reactive volatiles are

more readily available, which could undermine its effectiveness in applications such as carbon sequestration, where its recalcitrance and stability are critically necessitated. Metallurgy, however, could bypass a high surface area that can aid in efficient solid-gas phase reactions. Thermal and chemical stability are also crucial factors for these two applications. To achieve these benefits, biochar must be produced and/or activated, at least under moderately high temperatures to rearrange structural carbon into aromatics-rich carbon sheets. At this point, surface area might also be increased, presenting a significant trade-off concerning the reactivity of biochar and most importantly, yield.

Consequently, this situation opens up a promising avenue for future research aimed at investigating thermal activation methods that could balance carbon stability, surface area, yield, and oxidative reactivity, all at once. This could be done by testing different activation temperatures (even >600 °C), and different PHT durations (even < 30 min), via a robust design of experiments (DOE) to provide a detailed understanding of their synergistic effects. Following this PHT, a self-heating test could be conducted to correlate activated biochar properties and their vulnerability to combust. Other ways of reducing volatiles content like post-pyrolytic water quenching, with or without a complementary PHT, could also be explored. There are two advantages to this method: a) rapid water quenching of hot biochar could resemble a mild steam activation process that may cause additional volatiles release and porosity generation; and b) salts of AAEM like Na and K could form their respective hydroxides (NaOH, KOH) when in contact with water that may penetrate into biochar and also lead to surface negative functionalities supporting CEC. For the latter advantage, an auxiliary PHT could aid in an alkali activation process leading to superior morphology and high surface area of biochar that could be suitable for adsorption applications. However, this could lead to contaminated water with leached biochar volatiles comprising of many hydrocarbons.

Ultimately, any application where biochar substitutes fossil fuels, questions the economic viability of the idea. Especially, CRD wood with large variability in feedstock w.r.t location, geography, sourcing practices, availability, and supply chain, may pose uncertainties for scaling up biochar production. Nevertheless, supporting policies and financial subsidies always offer a positive outlook to anchor biochar utilization for emissions reduction.

Author Contributions: Conceptualization, methodology, validation, formal analysis, investigation, data curation, writing—original draft preparation, editing, visualization - **Aravind Ganesan**. Supervision, review, mentorship – **Simon Langlois**. Supervision, review, editing, mentorship - **Olivier Rezazgui**. Supervision, review, editing, mentorship - **Younès Bareha**. Project administration – **Cyrine Boussabbeh**. Supervision, mentorship – **Simon Barnabé**. Supervision, review, mentorship – **Patrice Mangin**. All authors have read and agreed to the published version of the manuscript.

Funding: This research was funded by MITACS, through Escouade Energie, Citeq, and supported by Innofibre, and I^2E^3 – UQTR, Québec, Canada. The work was conducted at Innofibre – Centre d'Innovation des Produits Cellulosiques, Trois-Rivières and at the Institute for Innovation in Ecomaterials, Ecoproducts, and Ecoenergies (I^2E^3), University of Québec Trois-Rivières (UQTR), Québec, Canada.

Conflicts of Interest: The authors declare no conflict of interest. The funders had no role in the design of the study; in the collection, analyses, or interpretation of data; in the writing of the manuscript; or in the decision to publish the results.

5. References

Abioye, K. J., Harun, N. Y., Sufian, S., Yusuf, M., Jagaba, A. H., Ekeoma, B. C., ... & Ibrahim, H. (2023). A review of biomass ash related problems: mechanism, solution, and outlook. Journal of the Energy Institute, 101490.

Adeniyi, A. G., Iwuozor, K. O., Emenike, E. C., Ogunniyi, S., Amoloye, M. A., & Sagboye, P. A. (2023). One-step chemical activation for the production of engineered orange peel biochar. Emergent Materials, 6(1), 211-221.

Akhtar, A., Krepl, V., & Ivanova, T. (2018). A combined overview of combustion, pyrolysis, and gasification of biomass. Energy & Fuels, 32(7), 7294-7318.

Ali, L., Palamanit, A., Techato, K., Ullah, A., Chowdhury, M. S., & Phoungthong, K. (2022). Characteristics of biochars derived from the pyrolysis and Co-pyrolysis of rubberwood sawdust and sewage sludge for further applications. Sustainability, 14(7), 3829.

Aller, D., Bakshi, S., & Laird, D. A. (2017). Modified method for proximate analysis of biochars. Journal of analytical and applied pyrolysis, 124, 335-342.

Al-Swadi, H. A., Al-Farraj, A. S., Al-Wabel, M. I., Ahmad, M., Usman, A. R., Ahmad, J., ... & Rafique, M. I. (2024). Impacts of kaolinite enrichment on biochar and hydrochar characterization, stability, toxicity, and maize germination and growth. Scientific Reports, 14(1), 1259.

An, N., Zhang, L., Liu, Y., Shen, S., Li, N., Wu, Z., ... & Han, X. (2022). Biochar application with reduced chemical fertilizers improves soil pore structure and rice productivity. Chemosphere, 298, 134304.

Ashman, J. M., Jones, J. M., & Williams, A. (2018). Some characteristics of the self-heating of the large scale storage of biomass. Fuel Processing Technology, 174, 1-8.

Ba, Y., Cen, K., Wang, L., Jia, D., Kan, T., & Chen, D. (2023). Study on synergistic effect of co-pyrolysis of wood chips and its gasification tar on the biochar and subsequent activated carbon upgrading using response surface method. Industrial Crops and Products, 205, 117558.

Bakshi, S., Banik, C., & Laird, D. A. (2020). Estimating the organic oxygen content of biochar. Sci Rep 10: 13082.

Basu, P. (2018). Biomass gasification, pyrolysis and torrefaction: practical design and theory. Academic press.

Bluvshtein, N., Villacorta, E., Li, C., Hagen, B. C., Frette, V., & Rudich, Y. (2020). Early detection of smoldering in silos: Organic material emissions as precursors. Fire safety journal, 114, 103009.

Bowring, S. P., Jones, M. W., Ciais, P., Guenet, B., & Abiven, S. (2022). Pyrogenic carbon decomposition critical to resolving fire's role in the Earth system. Nature Geoscience, 15(2), 135-142.

Castells, B., Amez, I., Medic, L., & García Torrent, J. (2020). Particle size influence on the transport classification labels and other flammability characteristics of powders. Applied Sciences, 10(23), 8601.

Cely, P., Gascó, G., Paz-Ferreiro, J., & Méndez, A. (2015). Agronomic properties of biochars from different manure wastes. Journal of analytical and applied pyrolysis, 111, 173-182.

Changi, S. M., Faeth, J. L., Mo, N., and Savage, P. E. (2015). Hydrothermal reactions of biomolecules relevant for microalgae liquefaction. Industrial Eng. Chem. Res. 54 (47), 11733–11758. doi:10.1021/acs.iecr.5b02771

Channiwala, S. A., & Parikh, P. P. (2002). A unified correlation for estimating HHV of solid, liquid and gaseous fuels. Fuel, 81(8), 1051-1063.

Chaparala, S. V., & Raj, A. (2016). Reaction mechanism for the oxidation of zigzag site on polycyclic aromatic hydrocarbons in soot by O2. Combustion and Flame, 165, 21-33.

Chatterjee, R., Sajjadi, B., Chen, W. Y., Mattern, D. L., Hammer, N., Raman, V., & Dorris, A. (2020). Effect of pyrolysis temperature on physicochemical properties and acoustic-based amination of biochar for efficient CO2 adsorption. Frontiers in Energy Research, 8, 85.

Chen, X., Yan, H., Ma, L., Fang, Q., Deng, S., Wang, X., & Yin, C. (2023). Moisture content effects on self-heating in stored biomass: An experimental study. Energy, 285, 129391.

Chen, Z., Feng, Q., Yue, R., Chen, Z., Moselhi, O., Soliman, A., ... & An, C. (2022). Construction, renovation, and demolition waste in landfill: a review of waste characteristics, environmental impacts, and mitigation measures. Environmental Science and Pollution Research, 29(31), 46509-46526.

Clemente, J. S., Beauchemin, S., Thibault, Y., MacKinnon, T., & Smith, D. (2018). Differentiating inorganics in biochars produced at commercial scale using principal component analysis. ACS omega, 3(6), 6931-6944.

Colomba, A., Berruti, F., & Briens, C. (2022). Model for the physical activation of biochar to activated carbon. Journal of Analytical and Applied Pyrolysis, 168, 105769.

Czajczyńska, D., Anguilano, L., Ghazal, H., Krzyżyńska, R., Reynolds, A. J., Spencer, N., & Jouhara, H. (2017). Potential of pyrolysis processes in the waste management sector. Thermal science and engineering progress, 3, 171-197.

del Campo, B., Brumm, T., & Keren, N. (2021). Fast pyrolysis biochar flammability behavior for handling and storage. ACI Avances en Ciencias e Ingenierías, 13(2), 23-23.

Dufourny, A., Van De Steene, L., Humbert, G., Guibal, D., Martin, L., & Blin, J. (2019). Influence of pyrolysis conditions and the nature of the wood on the quality of charcoal as a reducing agent. Journal of Analytical and Applied Pyrolysis, 137, 1-13.

Dzonzi-Undi, J., Masek, O., & Abass, O. (2014). Determination of spontaneous ignition behavior of biochar accumulations. Int. J. Sci. Res, 3(8), 656-661.

Edeh, I. G., & Mašek, O. (2022). The role of biochar particle size and hydrophobicity in improving soil hydraulic properties. European Journal of Soil Science, 73(1), e13138.

Evangelista, B., Arlabosse, P., Govin, A., Salvador, S., Bonnefoy, O., & Dirion, J. L. (2018). Reactor scale study of self-heating and self-ignition of torrefied wood in contact with oxygen. Fuel, 214, 590-596.

Fernandez-Anez, N., Meyer, A. K., Elio, J., Kleppe, G., Hagen, B. C., & Frette, V. (2021). Behaviour of smoldering fires during periodic refilling of wood pellets into silos. Journal of Loss Prevention in the Process Industries, 72, 104565.

Font, R. (2020). Analysis of the spontaneous combustion and self-heating of almond shells. Fuel, 279, 118504.

Fuertes, A. B., Ferrero, G. A., Diez, N., & Sevilla, M. (2018). A green route to high-surface area carbons by chemical activation of biomass-based products with sodium thiosulfate. ACS Sustainable Chemistry & Engineering, 6(12), 16323-16331.

Gale, M., Nguyen, T., Moreno, M., & Gilliard-AbdulAziz, K. L. (2021). Physicochemical properties of biochar and activated carbon from biomass residue: influence of process conditions to adsorbent properties. ACS omega, 6(15), 10224-10233.

Ganesan, A., Rezazgui, O., Burgos, J. B., Mangin, P. J., & Barnabé, S. (2025). Valorization of lignocellulosic biomass forest residues in quebec via the integrated hydropyrolysis and hydroconversion (IH2) technology: A review. Biomass and Bioenergy, 193, 107516.

Ganesan, A., Rezazgui, O., Langlois, S., Boussabbeh, C., & Barnabé, S. (2025). Pyrolytic conversion of construction, renovation, and demolition (CRD) wood wastes in Québec to biochar: Production, characterization, and identifying relevant stability indices for carbon sequestration. Science of the Total Environment, 965, 178650.

Gao, W., Zhang, M., & Wu, H. (2022). Bed agglomeration during fast pyrolysis of bio-oil derived fuels in a fluidized-bed reactor. Fuel, 328, 125359.

Guizani, C., Jeguirim, M., Valin, S., Peyrot, M., & Salvador, S. (2019). The Heat Treatment Severity Index: A new metric correlated to the properties of biochars obtained from entrained flow pyrolysis of biomass. Fuel, 244, 61-68.

Hadey, C., Allouch, M., Alami, M., Boukhlifi, F., & Loulidi, I. (2022). Preparation and characterization of biochars obtained from biomasses for combustible briquette applications. The Scientific World Journal, 2022(1), 2554475.

Hansen, S., & Sadeghian, P. (2020). Recycled gypsum powder from waste drywalls combined with fly ash for partial cement replacement in concrete. Journal of Cleaner Production, 274, 122785.

Harvey, O. R., Kuo, L. J., Zimmerman, A. R., Louchouarn, P., Amonette, J. E., & Herbert, B. E. (2012). An index-based approach to assessing recalcitrance and soil carbon sequestration potential of engineered black carbons (biochars). Environmental science & technology, 46(3), 1415-1421.

Howell, A., Helmkamp, S., & Belmont, E. (2022). Stable polycyclic aromatic carbon (SPAC) formation in wildfire chars and engineered biochars. Science of The Total Environment, 849, 157610.

Itoh, T., Iwabuchi, K., Maemoku, N., Chen, S., & Taniguro, K. (2020). Role of ambient pressure in self-heating torrefaction of dairy cattle manure. Plos one, 15(5), e0233027.

Janes, A., Vignes, A., & Dufaud, O. (2019). Ignition temperatures of dust layers and bulk storages in hot environments. Journal of loss prevention in the process industries, 59, 106-117.

Jerzak, W., Reinmöller, M., & Magdziarz, A. (2022). Estimation of the heat required for intermediate pyrolysis of biomass. Clean Technologies and Environmental Policy, 24(10), 3061-3075.

John, V., Braga, A. R. D. O., Danielli, C. K. A. D. O., Sousa, H. M., Danielli, F. E., de Araujo, R. O., ... & Guerra, J. F. C. (2024). Characterization of Biochar Produced in a Mobile Handmade Kiln from Small-Sized Waste Biomass for Agronomic and Climate Change Benefits. Agronomy, 14(8), 1861.

Johnston, C. T. (2017). 18 Biochar analysis by Fourier-transform infra-red spectroscopy. Biochar: a guide to analytical methods, 199.

Kearns, J. P., Shimabuku, K. K., Knappe, D. R., & Summers, R. S. (2019). High temperature co-pyrolysis thermal air activation enhances biochar adsorption of herbicides from surface water. Environmental Engineering Science, 36(6), 710-723.

Kern, S., Halwachs, M., Kampichler, G., Pfeifer, C., Pröll, T., & Hofbauer, H. (2012). Rotary kiln pyrolysis of straw and fermentation residues in a 3 MW pilot plant–Influence of pyrolysis temperature on pyrolysis product performance. Journal of Analytical and Applied Pyrolysis, 97, 1-10.

Khatibi, M., Nahil, M. A., & Williams, P. T. (2023). Improving the Quality of Bio-oil Using the Interaction of Plastics and Biomass through Copyrolysis Coupled with Nonthermal Plasma Processing. Energy & Fuels, 38(2), 1240-1257.

Koppejan, J., & Van Loo, S. (2012). The handbook of biomass combustion and co-firing. Routledge.

Krigstin, S., Wetzel, S., Jayabala, N., Helmeste, C., Madrali, S., Agnew, J., & Volpe, S. (2018). Recent health and safety incident trends related to the storage of woody biomass: A need for improved monitoring strategies. Forests, 9(9), 538.

Kuryntseva, P., Karamova, K., Galitskaya, P., Selivanovskaya, S., & Evtugyn, G. (2023). Biochar functions in soil depending on feedstock and pyrolyzation properties with particular emphasis on biological properties. Agriculture, 13(10), 2003.

Laadila, M. A., LeBihan, Y., Caron, R. F., & Vaneeckhaute, C. (2021). Construction, renovation and demolition (CRD) wastes contaminated by gypsum residues: Characterization, treatment and valorization. Waste Management, 120, 125-135.

Lago, B. C., Silva, C. A., Melo, L. C. A., & de Morais, E. G. (2021). Predicting biochar cation exchange capacity using Fourier transform infrared spectroscopy combined with partial least square regression. Science of The Total Environment, 794, 148762.

Lataf, A., Jozefczak, M., Vandecasteele, B., Viaene, J., Schreurs, S., Carleer, R., ... & Vandamme, D. (2022). The effect of pyrolysis temperature and feedstock on biochar agronomic properties. Journal of Analytical and Applied Pyrolysis, 168, 105728.

Lebelo, R. S. (2016). Thermal stability investigation in a reactive sphere of combustible material. Advances in Mathematical Physics, 2016(1), 9384541.

Leng, L., Huang, H., Li, H., Li, J., Zhou, W., 2019. Biochar stability assessment methods: a review. Sci. Total Environ. 647, 210–222. https://doi.org/10.1016/j. scitotenv.2018.07.402.

Leng, L., Xu, X., Wei, L., Fan, L., Huang, H., Li, J., ... & Zhou, W. (2019). Biochar stability assessment by incubation and modelling: Methods, drawbacks and recommendations. Science of the Total Environment, 664, 11-23.

Liu, J., Zhou, Z., Jin, L., Wang, T., Ou, S., Wang, S., ... & Jueraiti, M. (2022). Effect of coal dust content on the low-temperature oxidation of silo coal. ACS omega, 7(42), 37442-37451.

Locaspi, A., Debiagi, P., Pelucchi, M., Hasse, C., & Faravelli, T. (2021). A predictive physico-chemical model of biochar oxidation. Energy & Fuels, 35(18), 14894-14912.

Lu, X., & Gu, X. (2022). A review on lignin pyrolysis: pyrolytic behavior, mechanism, and relevant upgrading for improving process efficiency. Biotechnology for Biofuels and Bioproducts, 15(1), 106.

Luo, Q., Deng, Y., Li, Y., He, Q., Wu, H., & Fang, X. (2024). Effects of pyrolysis temperatures on the structural properties of straw biochar and its adsorption of tris-(1-chloro-2-propyl) phosphate. Scientific Reports, 14(1), 25711.

Ma, X., Zhou, B., Budai, A., Jeng, A., Hao, X., Wei, D., ... & Rasse, D. (2016). Study of biochar properties by scanning electron microscope–energy dispersive X-ray spectroscopy (SEM-EDX). Communications in Soil Science and Plant Analysis, 47(5), 593-601.

Maaoui, A., Trabelsi, A. B. H., Abdallah, A. B., Chagtmi, R., Lopez, G., Cortazar, M., & Olazar, M. (2023). Assessment of pine wood biomass wastes valorization by pyrolysis with focus on fast pyrolysis biochar production. Journal of the Energy Institute, 108, 101242.

Maier, D. (2021). Building materials made of wood waste a solution to achieve the sustainable development goals. Materials, 14(24), 7638.

Malhotra, J. S., Valiollahi, R., & Wiinikka, H. (2023). From wood to supercapacitor electrode material via fast pyrolysis. Journal of Energy Storage, 57, 106179.

Mazerolle, D., Rezaei, H., Bronson, B., Nguyen, L., & Preto, F. (2019). Sieving and acid washing as a pretreatment to fast pyrolysis of a high ash hog fuel. Energy & Fuels, 33(6), 5352-5359.

Mishra, R. K., Singh, B., & Acharya, B. (2024). A comprehensive review on activated carbon from pyrolysis of lignocellulosic biomass: An application for energy and the environment. Carbon Resources Conversion, 100228.

Miura, K. (2016). Adsorption of water vapor from ambient atmosphere onto coal fines leading to spontaneous heating of coal stockpile. Energy & Fuels, 30(1), 219-229.

Morris, J. D., Daood, S. S., Chilton, S., & Nimmo, W. (2018). Mechanisms and mitigation of agglomeration during fluidized bed combustion of biomass: A review. Fuel, 230, 452-473.

Mukome, F. N., Zhang, X., Silva, L. C., Six, J., & Parikh, S. J. (2013). Use of chemical and physical characteristics to investigate trends in biochar feedstocks. Journal of agricultural and food chemistry, 61(9), 2196-2204.

Niu, Z., Liu, G., Yin, H., Zhou, C., Wu, D., & Tan, F. (2021). A comparative study on thermal behavior of functional groups in coals with different ranks during low temperature pyrolysis. Journal of Analytical and Applied Pyrolysis, 158, 105258.

Oliveira, F. R., Patel, A. K., Jaisi, D. P., Adhikari, S., Lu, H., & Khanal, S. K. (2017). Environmental application of biochar: Current status and perspectives. Bioresource technology, 246, 110-122.

Om Prakash, M., Raghavendra, G., Panchal, M., & Ojha, S. (2020). Thermogravimetric analysis of biochar from Arhar fiber powder prepared at different pyrolysis temperatures. In Innovative Product Design and Intelligent Manufacturing Systems: Select Proceedings of ICIPDIMS 2019 (pp. 429-437). Springer Singapore.

Özbay, G., Özçifçi, A., Toker, E. S. K. H., & Baysal, E. (2015). Bio-char Production from Pyrolysis of Furniture Products Waste.

Paajanen, A., Rinta-Paavola, A., & Vaari, J. (2021). High-temperature decomposition of amorphous and crystalline cellulose: reactive molecular simulations. Cellulose, 28, 8987-9005.

Pan, R., Hu, D., Chao, J., Wang, L., Ma, J., & Jia, H. (2020). The heat of wetting and its effect on coal spontaneous combustion. Thermochimica acta, 691, 178711.

Panahi, H. K. S., Dehhaghi, M., Ok, Y. S., Nizami, A. S., Khoshnevisan, B., Mussatto, S. I., ... & Lam, S. S. (2020). A comprehensive review of engineered biochar: production, characteristics, and environmental applications. Journal of Cleaner Production, 270, 122462.

Pandit, J. K., Watson, M., & Qader, A. (2020). Reduction of greenhouse gas emissions in steel production. NSW Department of Primary Industries) Available at https://www. resourcesregulator.nsw.gov. au/sites/default/files/2022-11/report-reduction-of-ghg-emissions-in-steel-industries. pdf.

Pariyar, P., Kumari, K., Jain, M. K., & Jadhao, P. S. (2020). Evaluation of change in biochar properties derived from different feedstock and pyrolysis temperature for environmental and agricultural application. Science of the Total Environment, 713, 136433.

Pereira, R. C., Kaal, J., Arbestain, M. C., Lorenzo, R. P., Aitkenhead, W., Hedley, M., ... & Maciá-Agulló, J. A. (2011). Contribution to characterisation of biochar to estimate the labile fraction of carbon. Organic Geochemistry, 42(11), 1331-1342.

Phounglamcheik, A., Wang, L., Romar, H., Kienzl, N., Broström, M., Ramser, K., ... & Umeki, K. (2020). Effects of pyrolysis conditions and feedstocks on the properties and gasification reactivity of charcoal from woodchips. Energy & Fuels, 34(7), 8353-8365.

Phounglamcheik, A.; Johnson, N.; Kienzl, N.; Strasser, C.; Umeki, K. Self-Heating of Biochar during Postproduction Storage by O2 Chemisorption at Low Temperatures. Energies 2022, 15, 380. https:// doi.org/10.3390/en15010380

Preimesberger, C., Wondrak, M., Solt-Rindler, A., Pfeifer, C., & Hansmann, C. (2024). Size-and temperature-dependent oxidative pyrolysis and auto-ignition of spherical beech and spruce wood. Biomass Conversion and Biorefinery, 14(14), 15535-15548.

Puri, L., Hu, Y., & Naterer, G. (2024). Critical review of the role of ash content and composition in biomass pyrolysis. Frontiers in Fuels, 2, 1378361.

Puri, L., Hu, Y., & Naterer, G. (2024). Critical review of the role of ash content and composition in biomass pyrolysis. Frontiers in Fuels, 2, 1378361.

Ram, M., Mondal, M. K., (2022). Chapter 12 – Biomass Gasification: a step toward cleaner fuel and chemicals. Biofuels and Bioenergy – Opportunities and Challenges. 253-276.

Rambhatla, N., Panicker, T. F., Mishra, R. K., Manjeshwar, S. K., & Sharma, A. (2025). Biomass pyrolysis for biochar production: Study of kinetics parameters and effect of temperature on biochar yield and its physicochemical properties. Results in Engineering, 25, 103679.

Ren, Congjing, Peng Zhang, Qi Song, Zhengliang Huang, Yao Yang, and Yongrong Yang. "Particle agglomeration and inhibition method in the fluidized pyrolysis reaction of waste resin." Chinese Journal of Chemical Engineering 67 (2024): 135-147.

Ren, Z., Wang, D., Qin, Z., & Liu, Z. (2023). Effects of pore size, water content, and oxygen-containing functional groups on oxygen adsorption in bituminous coal. Scientific Reports, 13(1), 10373.

Restuccia, F. (2017). Self-heating ignition of natural reactive porous media (Doctoral dissertation, Imperial College London).

Restuccia, F., Mašek, O., Hadden, R. M., & Rein, G. (2019). Quantifying self-heating ignition of biochar as a function of feedstock and the pyrolysis reactor temperature. Fuel, 236, 201-213.

Riva, L., Cardarelli, A., Andersen, G. J., Buø, T. V., Barbanera, M., Bartocci, P., ... & Nielsen, H. K. (2020). On the self-heating behavior of upgraded biochar pellets blended with pyrolysis oil: Effects of process parameters. Fuel, 278, 118395.

Rombolà, A. G., Greggio, N., Fabbri, D., Facchin, A., Torri, C., Pulcher, R., ... & Buscaroli, A. (2023). Changes of labile, stable and water-soluble fractions of biochar after two years in a vineyard soil. Environmental Science: Advances, 2(11), 1587-1599.

Rudra, A., Petersen, H. I., & Sanei, H. (2024). Molecular characterization of biochar and the relation to carbon permanence. International Journal of Coal Geology, 291, 104565.

Safarian, S. (2023). To what extent could biochar replace coal and coke in steel industries?. Fuel, 339, 127401.

Saidur, R., Abdelaziz, E. A., Demirbas, A., Hossain, M. S., & Mekhilef, S. (2011). A review on biomass as a fuel for boilers. Renewable and sustainable energy reviews, 15(5), 2262-2289.

Sajjadi, B., Chen, W. Y., & Egiebor, N. O. (2019). A comprehensive review on physical activation of biochar for energy and environmental applications. Reviews in Chemical Engineering, 35(6), 735-776.

Sakhiya, A. K., Baghel, P., Pathak, S., Vijay, V. K., & Kaushal, P. (2020, October). Effect of process parameters on slow pyrolysis of rice straw: product yield and energy analysis. In 2020 International Conference and Utility Exhibition on Energy, Environment and Climate Change (ICUE) (pp. 1-9). IEEE.

Schmidt, H. P., Abiven, S., Hagemann, N., & Meyer zu Drewer, J. (2022). Permanence of soil applied biochar. Biochar J, 69-74.

Schwarzer, L., Jensen, P. A., Wedel, S., Glarborg, P., Karlström, O., Holm, J. K., & Dam-Johansen, K. (2021). Self-heating and thermal runaway of biomass–Lab-scale experiments and modeling for conditions resembling power plant mills. Fuel, 294, 120281.

Šelešovský, J. (2010). Thermal loading of explosives—Finite difference method with time step reduction. Journal of hazardous materials, 174(1-3), 289-294.

Shafiq, M., & Capareda, S. C. (2021). Effect of different temperatures on the properties of pyrolysis products of Parthenium hysterophorus. Journal of Saudi Chemical Society, 25(3), 101197.

Singh, B., Fang, Y., & Johnston, C. T. (2016). A fourier-transform infrared study of biochar aging in soils. Soil Science Society of America Journal, 80(3), 613-622.

Smith, A. M., Whittaker, C., Shield, I., & Ross, A. B. (2018). The potential for production of high quality bio-coal from early harvested Miscanthus by hydrothermal carbonisation. Fuel, 220, 546-557.

Söderqvist, H. (2019). Carbon Stability of Biochar: Methods for assessment and indication.

Song, S., Cong, P., Wang, C., Li, P., Liu, S., He, Z., ... & Yang, Z. (2023). Properties of biochar obtained from tropical crop wastes under different pyrolysis temperatures and its application on acidic soil. Agronomy, 13(3), 921.

Sørmo, E., Silvani, L., Thune, G., Gerber, H., Schmidt, H. P., Smebye, A. B., & Cornelissen, G. (2020). Waste timber pyrolysis in a medium-scale unit: Emission budgets and biochar quality. Science of the Total Environment, 718, 137335.

Sudhakar, A., Remya, N., & Varghese, G. K. (2017). Estimation of effect of sugarcane bagasse biochar amendment in landfill soil cover on geotechnical properties and landfill gas emission. Environmental Quality Management, 27(2), 33-39.

Sun, C., Chen, T., Huang, Q., Zhan, M., Li, X., & Yan, J. (2020). Activation of persulfate by CO2-activated biochar for improved phenolic pollutant degradation: performance and mechanism. Chemical Engineering Journal, 380, 122519.

Suriapparao, D. V., & Vinu, R. (2018). Effects of biomass particle size on slow pyrolysis kinetics and fast pyrolysis product distribution. Waste and biomass valorization, 9, 465-477.

Tang, J., Zhu, W., Kookana, R., & Katayama, A. (2013). Characteristics of biochar and its application in remediation of contaminated soil. Journal of bioscience and bioengineering, 116(6), 653-659.

Thauront, J. L., Soja, G., Schmidt, H. P., & Abiven, S. (2024). A critical re-analysis of biochar properties prediction from production parameters and elemental analysis. Global Change Biology. Bioenergy, 16(11).

Uroić Štefanko, A., & Leszczynska, D. (2020). Impact of biomass source and pyrolysis parameters on physicochemical properties of biochar manufactured for innovative applications. Frontiers in Energy Research, 8, 138.

Wang, W., Bai, J., & Lu, Q. (2021). Pyrolysis temperature and feedstock alter the functional groups and carbon sequestration potential of Phragmites australis-and Spartina alterniflora derived biochars. GCB Bioenergy 13: 493–506.

Wani, I., Sharma, A., Kushvaha, V., Madhushri, P., & Peng, L. (2020). Effect of pH, volatile content, and pyrolysis conditions on surface area and O/C and H/C ratios of biochar: towards understanding performance of biochar using simplified approach. Journal of Hazardous, Toxic, and Radioactive Waste, 24(4), 04020048.

Weber, K., Heuer, S., Quicker, P., Li, T., Løvås, T., & Scherer, V. (2018). An alternative approach for the estimation of biochar yields. Energy & Fuels, 32(9), 9506-9512.

Wei, J., Yao, C., & Sheng, C. (2023). Modelling Self-Heating and Self-Ignition Processes during Biomass Storage. Energies, 16(10), 4048.

Wijitkosum, S. (2023). Influence of pyrolysis temperature and time on biochar properties and its potential for climate change mitigation. Journal of Human, Earth, and Future, 4(4), 472-485.

Woolf, D., Lehmann, J., Ogle, S., Kishimoto-Mo, A. W., McConkey, B., & Baldock, J. (2021). Greenhouse gas inventory model for biochar additions to soil. Environmental science & technology, 55(21), 14795-14805.

Wystalska, K., & Kwarciak-Kozłowska, A. (2021). The effect of biodegradable waste pyrolysis temperatures on selected biochar properties. Materials, 14(7), 1644.

Xi, Z., Xi, K., Lu, L., & Li, X. (2022). Investigation of the influence of moisture during coal self-heating. Fuel, 324, 124581.

Xiao, F. (2022). A review of biochar functionalized by thermal air oxidation. Environmental Functional Materials, 1(2), 187-195.

Yuan, H., Restuccia, F., Richter, F., & Rein, G. (2019). A computational model to simulate self-heating ignition across scales, configurations, and coal origins. Fuel, 236, 1100-1109.

Zhang, H., Liao, W., Zhou, X., Shao, J., Chen, Y., Zhang, S., & Chen, H. (2022). Coeffect of pyrolysis temperature and potassium phosphate impregnation on characteristics, stability, and adsorption mechanism of phosphorus-enriched biochar. Bioresource Technology, 344, 126273.

Zhao, L., Cao, X., Mašek, O., & Zimmerman, A. (2013). Heterogeneity of biochar properties as a function of feedstock sources and production temperatures. Journal of hazardous materials, 256, 1-9.

Zhu, X., Li, C., Li, J., Xie, B., Lü, J., & Li, Y. (2018). Thermal treatment of biochar in the air/nitrogen atmosphere for developed mesoporosity and enhanced adsorption to tetracycline. Bioresource technology, 263, 475-482.

6. Supplementary figures, tables, and information

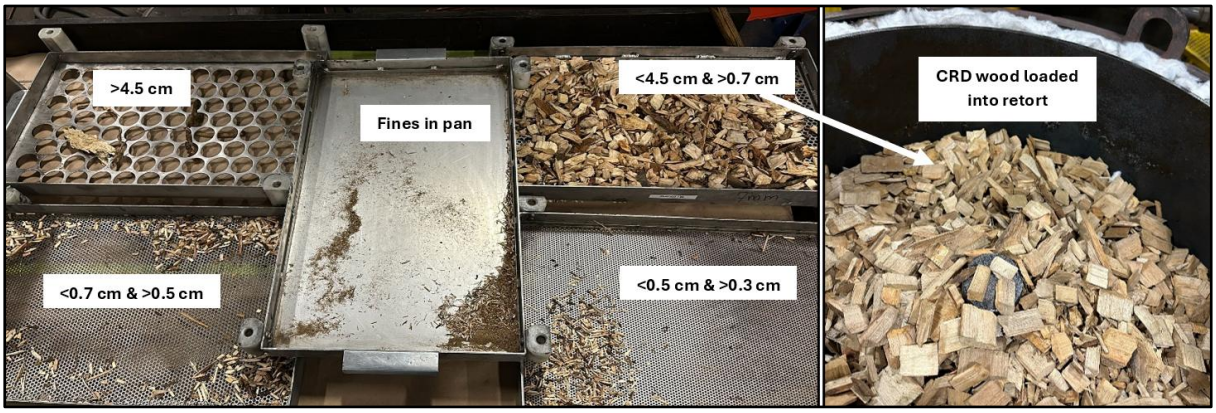

Supplementary figure 17: CRD wood size separation using a mechanical vibrating sieve

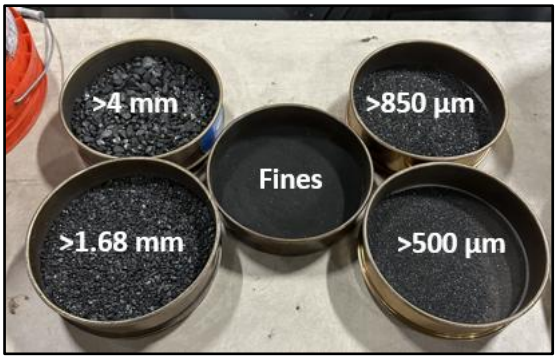

Supplementary figure 18: Vibrational sieving of biochar to collect fines for self-heating tests

Supplementary figure 19: Biochar basket self-heating set-up with adiabatic ovens

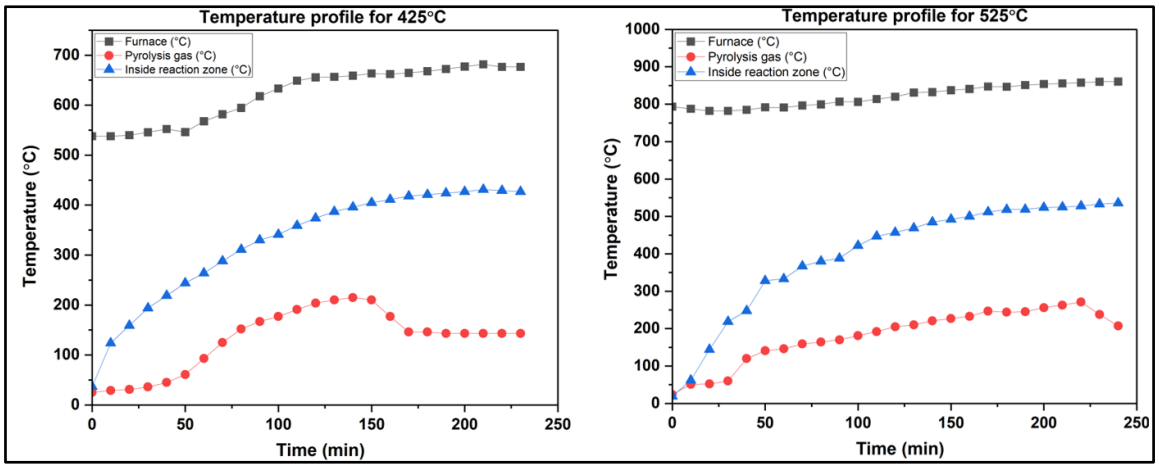

Supplementary figure 20: Temperature profiles during slow pyrolysis cycles of CRD biomass in the pilot retort

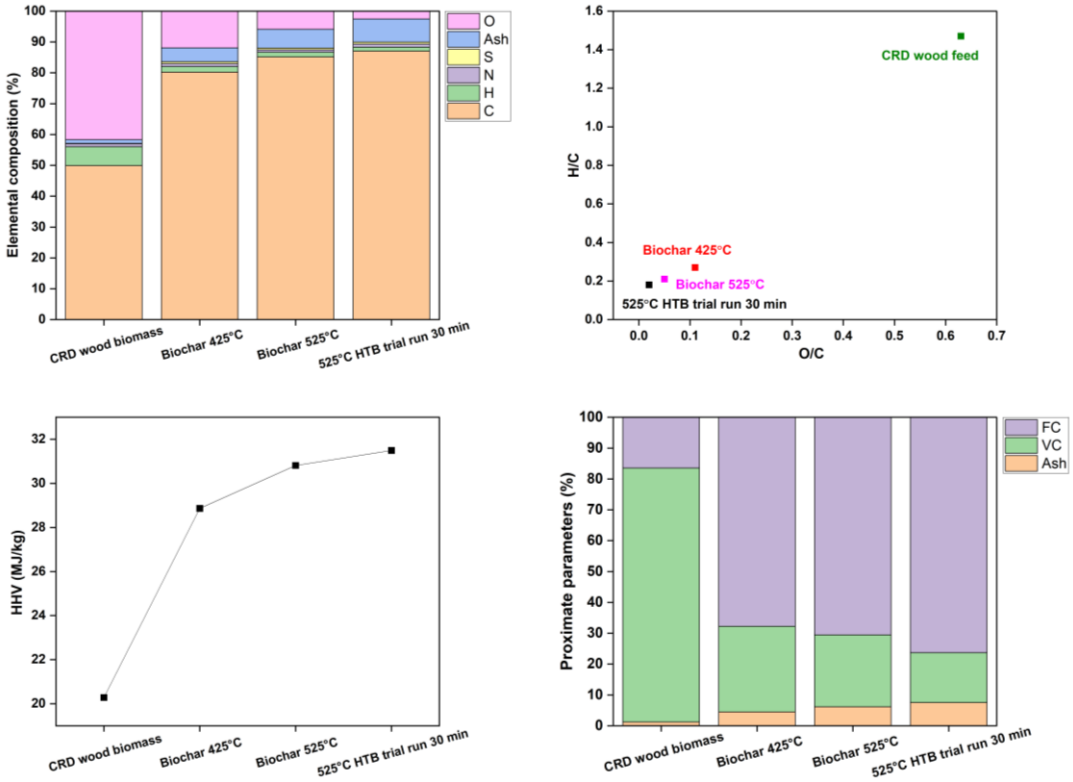

Supplementary figure 21: Elemental composition, Van-Krevelen performance, variation in HHV, and proximate analysis with pyrolysis temperature for B425 and B525

Supplementary figure 22: Nuances analyzed during troubleshooting activities performed on CRD wood biochar from acclimatization runs

During slow pyrolysis acclimatization tests (before the production of B425 and B525), there were notable observations in the physical appearance of the char product which needed some troubleshooting prior to the actual experimental tests. On these grounds, upon a thorough investigation, if pyrolysis gas from the retort is not withdrawn from the reaction zone in a timely manner (via opening valve V4 in Figure 26), oxygenated volatiles in the vapor phase might cause a few issues to biochar w.r.t settling. Sometimes, even with rapid pyrolysis gas evacuation, once the furnace's power is switched off towards the end of the cycle, oxygenates that typically exit to the combustion chamber, may backtrack into the pyrolysis unit. When these re-entering gases come into contact with hot biochar, smoldering reactions could occur unnoticed. This phenomenon may have led to the formation of a layer of biochar at the base of the retort particularly near the exhaust pipe venting pyrolytic volatiles, that turned to ash likely due to post-production combustion. In contrast, biochar from the rest of the retort, remained relatively clean with significantly lower ash presence. Hence, a main practice that was imbibed from the acclimatization runs was to remove the retort from the kiln immediately after pyrolysis and not letting it stay inside. To pictorially explain this issue, vibrational sieving of biochar was carried out as in Supplementary figure 22 to dust-off any visible ash (seen in the pan) and separate it from the rest of the char. Another observation was the repercussion of inefficient retort sealing, which allowed infiltration of either hot furnace air during pyrolysis or the ambient air. Thus, a second practice was to always ensure efficient, air-tight sealing of the retort. These findings underscore the critical importance of process efficiency in both equipment design and operational procedures to prevent unintended air exposure and ensure optimal biochar quality.

Supplementary table 11: Metal content in CRD biomass, B425, B525, and HTB525

Sample	Units	CRD biomass	B425	B525	HTB525
Al	mg/kg	12043	240641	240642	240643
Ba	mg/kg	1165	17482	7946	2967
Ca	mg/kg	149284	951	1024	2174
Cd	mg/kg	2	191630	222289	158328
Co	mg/kg	69	22	18	33
Cr	mg/kg	86	19	28	83
Cu	mg/kg	613	1243	1068	113
Fe	mg/kg	16086	1297	598	116
K	mg/kg	38043	9505	9830	11738
Mg	mg/kg	17566	28797	19934	77748
Mn	mg/kg	5587	13474	12574	20877
Mo	mg/kg	24	2792	2345	8129
Na	mg/kg	37685	6	11	17
Ni	mg/kg	5	18736	14233	2748
Pb	mg/kg	561	37	45	68
V	mg/kg	21	1422	7647	71
Zn	mg/kg	1389	29	27	12
Total metals	**mg/kg**	**280229**	**528083**	**540259**	**525865**
AAEM only	mg/kg	243743	56741	38745	94644
AAEM only	%	87	11	7	18

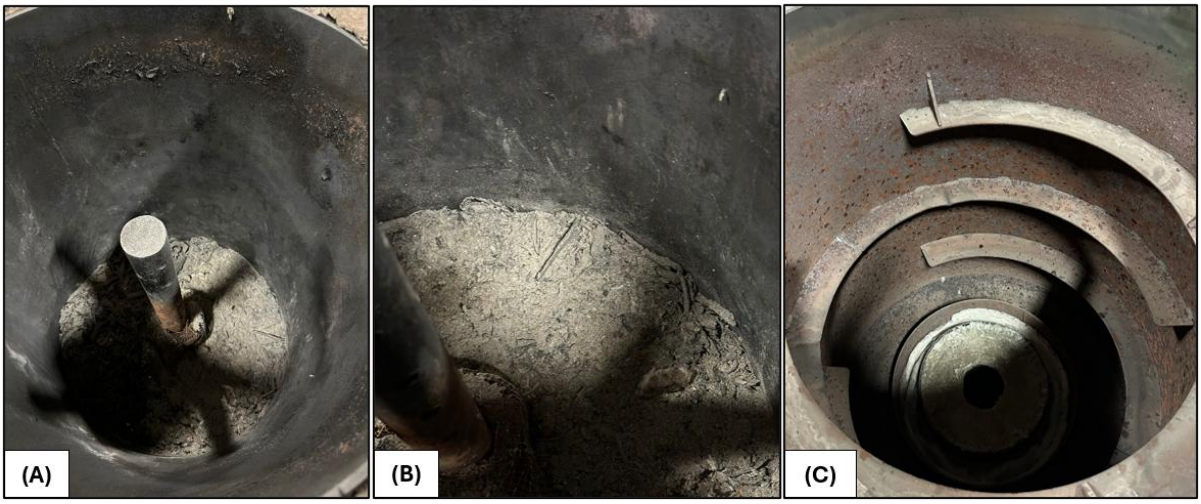

Supplementary figure 23: Probable long-term effects of AAEM-rich CRD biomass on the pilot retort: A) slagging/fouling; B) Residue agglomeration; C) Corrosion

CHAPTER 5 – SCIENTIFIC ARTICLE (4)

Kinetic analysis of construction, renovation, and demolition (CRD) wood pyrolysis using model-fitting and model-free methods by thermogravimetric analysis (TGA)

Aravind Ganesan[1,2,*], Simon Barnabé[1], Younès Bareha[1], Simon Langlois[2], Olivier Rezazgui[2], Cyrine Boussabbeh[2]

[1] Institut d'Innovations en Écomatériaux, Écoproduits et Écoénergies, Pavillon CIPP, Université du Québec à Trois-Rivières, boul. des Forges, Trois-Rivières G8Z 4M3, Québec, Canada

[2] Cégep de Trois-Rivières, Pavillon des Sciences, 3500 Rue de Courval, Trois-Rivières, G8Z 1T2, Québec, Canada
Innofibre – Centre d'Innovation des Produits Cellulosiques, 3351, boul. des Forges C.P.97. Trois-Rivières G9A 5E6, Québec, Canada

* Correspondence: Aravind.Ganesan@uqtr.ca

Published article DOI: https://doi.org/10.3390/en18102496

Abstract

Pyrolysis of construction, renovation, and demolition (CRD) wood is a complex thermochemical route that encompasses various processes including devolatilization, diffusion, phase transitions, condensation, aromatization, and char production. Its physicochemical characteristics are similar to those of woody biomass, categorizing it as a low-ash feedstock. Analysis of its biopolymeric composition indicates that lignin content ranges from 24-32%, demonstrating the presence of both hardwood and softwood species. As a result, there is a significant potential for generating biochar and biooil, rich in aromatics from this feedstock. The metal analysis revealed notably high concentrations of alkali and alkaline earth metals (AAEM) (86-87%), as well as heavy metals such as Cu, Cr, Pb, and Zn, indicating a diverse chemical composition and varying levels of conditioning or treatment. Thermogravimetric analysis (TGA) was conducted on CRD wood at varying heating rates of 10, 20, 30, and 40 °C/min under inert conditions mimicking pyrolysis, reaching a maximum analysis temperature of 900 °C, to determine the kinetic and thermodynamic parameters using both model-fitting methods like Coats-Redfern (CR) and model-free methods such as Ozawa-Flynn-Wall (OFW), Kissinger-Akahira-Sunose (KAS), and Friedman (FM). The thermal degradation profile of CRD wood biomass displayed three distinct stages, which were fitted to theoretical models to derive activation energy (E_a), pre-exponential factor (A), and overall model fit (R^2), in addition to the changes in Gibbs free energy (ΔG), heat of enthalpy (ΔH), and entropy (ΔS) throughout the pyrolysis process. The biomass demonstrated its highest weight loss during the second phase of TGA according to the differential thermograms (DTG), with melting temperatures (T_m) ranging from 350-400 °C as heating rates increased. The CR method indicated that diffusion (D1, D2, D3, D4) and phase interfacial (R1, R2, R3) models presented the strongest correlation ($R^2 > 0.99$) with peak E_a requirements observed at 30 °C/min. The average E_a for diffusion models at 30 °C/min was 114.96 kJ/mol. Model-free methods, particularly OFW and KAS, yielded activation energy values between 172-185 kJ/mol, whereas the FM method calculated these values to be slightly higher, ranging from 185-196 kJ/mol for conversion rates (α) of 0.2-0.8, respectively. The ΔH values from these methods ranged from 179-192 kJ/mol, ΔG values were between 215-275 kJ/mol, and ΔS ranged from -60 J/mol·K to -130 J/mol·K. Thermodynamic parameters suggested that CRD wood pyrolysis is an endothermic and non-spontaneous process, thriving on external energy. Negative ΔS dictated very low randomness in pyrolysis which could be due to the stable, carbon-enriched biochar product formation. Consequently, the pyrolysis of CRD biomass demonstrated a complex conversion pathway involving numerous parallel, sequential, and isolated reactions occurring in a seemingly disorganized manner. Nevertheless, the findings from the TGA data and the kinetic/thermodynamic calculations are consistent and align with similar research conducted on the pyrolysis of woody biomass.

Key words: Biomass, thermochemical, pyrolysis, thermogravimetric, kinetics, thermodynamics

1. Introduction

Construction, renovation, and demolition (CRD) activities generate huge volumes of waste. Particularly, countries where the construction of residential, commercial, and industrial spaces utilizes substantial quantities of wood, fall under this case. According to Laadila et al., 2021, over 500 million tons (Mt) of CRD waste were generated annually across Canada, USA, and Europe. Management and disposal of CRD wood residues create numerous environmental and economic challenges. This also includes furniture parts that are organically contaminated wood fibers without a promising scope for reuse (Kumar et al., 2024). Such wood contains treated, tinted, or composite materials infused with chemicals like polyaromatic hydrocarbons (PAHs), heavy metals, paints, lubricants, and resins, making them non-recyclable and deteriorating in quality (Ganesan et al., 2025). Especially, chromated copper arsenate (CCA) remnants in CRD wood waste disposal could face major hurdles in terms of disposal due to rising restrictions (Gmar et al., 2022). A common, non-advisable practice followed for their disposal is usually landfilling which causes problems when these toxic substances from CRD wood waste leach into surrounding soil and groundwater posing serious risks to human and ecosystem health. Anaerobic decomposition of organic fractions in wood waste within landfills can produce harmful greenhouse gases (GHGs) like methane and carbon dioxide contributing to the climate crisis (O'Dwyer et al., 2018). Inadequate monitoring, lack of public awareness, absence of strict regulations for landfilling, and economic/technological burden inflicted on recycling technologies for CRD wood, allow handlers to look for easy disposal methods. Even simple sorting is complicated due to large variability in wood composition with geography and provincial sourcing practices. These externalities exacerbate an already growing strain on limited landfill spaces. Hence, alternative waste management technologies are needed to pave the way for valorizing CRD wood residues to bioenergy, biochemicals, and bioproducts.

Waste forest wood, whether sequestered directly from the forests or sourced from CRD sites, are typically low-value feedstock harboring scarce probability to be reused or recycled. The economic value of such wastes could be improved by efficient thermochemical conversion technologies such as torrefaction, gasification, or pyrolysis (Kizha & Han, 2016). Pyrolysis has immense potential in serving as a recovery pathway for refused wood residues mainly due to its distinct product stream, moderate operation conditions, and relatively simplistic operation/instrumentation than gasification (Ganesan et al., 2025). Upon depolymerization of biomass in low or no oxygen, the transformation yields three major products with high energy and oxygen content: solid biochar, liquid pyrolysis oil or biooil, and pyrolysis gas (Rao et al., 2022). Depending upon the application under focus, pyrolysis can either be carried out at low or high temperatures. For instance, low-temperature pyrolysis (<500°C) produces cyclic, stable aromatics as in biochar whereas temperatures >600°C produce pyrolysis gas that are partly condensible into biooil (Zhang et al., 2023). Biooil can serve as a foundation for producing platform chemicals or can be upgraded to fuel intermediates (Guedes et al., 2018). Pyrolysis gas, commonly referred to as energy-rich syngas, made of CO, CO_2, H_2, and other light C_1-C_3, can also serve as a base for liquid synfuels or can be combusted in boilers/furnaces for energy generation, surrounding it from a resource-recovery perspective (Mouneir & El-Shamy, 2024). Biochar may serve as a partial substitute for fossil coal and carbon black in hard-to-abate industrial sectors such as metallurgy, automobiles, construction, agriculture, soil remediation, biogas production, air and water purification (Peters et al., 2015, Ibitoye et al., 2024, Hasan et al., 2024, Legan et al., 2022). For a complex feedstock like CRD wood, pyrolysis may even trap all inherent hazardous components and immobilize them within the biochar product. But these biochars can eventually cause toxicity concerns because it may contain original PAHs from the wood feed as well as volatile organic compounds (VOCs), dioxins, and free radicals that are persistent (Han et al., 2022).

For safe pyrolysis, other non-wood contaminants like nails, plastics, concrete, glass, and rubber have to be removed without fail during the pre-treatment stages to avoid complications with reactor operation and efficient biomass conversion. On that note, for a smooth conversion, CRD wood biomass has to be uniformly size-treated via shredding, grinding or milling, to reduce particle size so that heat transfer, bulk density, and energy density limitations are subdued (Mlonka-Mędrala et al., 2019). Whenever biochar is leveraged to address environmental or industrial challenges, its stability determines the resistance towards chemical, thermal, or microbial degradation while enabling it to act as a carbon sink (Adhikari et al., 2024). The nature of feedstock and pyrolysis parameters like temperature, heating rate, and biomass residence time (BRT) govern this stability factor through the physicochemical properties of biochar as understood from Altıkat et al., 2024. The final quality and intended applications depend on how the biomass feedstock is pre-treated, what the process optimization steps are, and the scale of production.

Biopolymers in biomass such as cellulose, hemicellulose (together called holocellulose), and lignin contents have specific decomposition pathways that take place at different temperatures and different stages. Solid-gas phase reactions involving multiple reactive species makes the prediction of pyrolysis reaction modelling cumbersome (Ranzi et al., 2017). To understand what pyrolysis does to CRD wood biomass, getting to know the kinetics and thermodynamics is beneficial. Kinetics describes the nature and type of chemical reactions occurring during pyrolysis and the energy required to form intermediate complexes and products whereas thermodynamics describes how energy enters and leaves a system during these chemical reactions. Usually, pyrolysis may contain single-step reactions proceeding individually or multiple competitive biomass breakdown reactions that proceed simultaneously or sequentially underscoring the intricacies of this process (Silva et al., 2023). Yield, ion exchange capacities, influence of ash, pore size, volatile content, and carbon arrangement in biochar are invariably dictated by the thermal degradation profiles too. Therefore, careful consideration of the various temperatures, heating rates, conversion rates, and selecting appropriate kinetic models are very important to forecast pyrolysis behavior. Thermogravimetric analysis (TGA) is a systematic and structured method to under chemical kinetics of biomass pyrolysis. According to Branca & Galgano, 2024, for fitting experimental data, assumptions based on different theoretical models are used via model-fitting methods. Whereas, the biomass conversion rate with the associated temperature required for that conversion at different heating rates is applied to the experimental TGA data via model-free or isoconversional methods (used interchangeably). Kinetic parameters such as activation energy and thermodynamic parameters like enthalpy (ΔH), entropy (ΔS), and Gibbs free energy (ΔG), can be calculated at each heating rate employed to study the influence of pyrolysis process parameters on biomass decomposition (Thejaswini et al., 2023).

To the best of our knowledge, there has not been a detailed study on the reaction kinetics and thermodynamics of CRD wood waste pyrolysis. Hence, two unique aspects are undercovered here. The first novelty element in this work surrounds the utilization of an underexplored, heterogeneous, and real-world biomass feedstock in the form of CRD wood rejects, laden with organic and inorganic contaminants, to disseminate practical findings on its thermal degradation behaviour. The second novelty element focuses on extracting kinetic and thermodynamic parameters from the CRD wood TGA weight loss data under multiple heating rates, and comparing the results yielded from different models. So, this dual emphasis on feedstock physicochemical/biochemical composition and robust pyrolysis modelling framework could result in meaningful contributions to the field of sustainable waste materials management.

To assist in answering these questions, the objectives of our study will be to: a) succinctly explain the theory behind model-fitting and model-free techniques with necessary equations along with the benefits and drawbacks of adapting to these methods; b) investigate the physicochemical characteristics of biomass, and understand its surface chemical make-up; and c) analyze the thermochemical degradation reactions via TGA at different heating rates and calculate kinetic and thermodynamic parameters. Approaching these measures would facilitate understanding a robust pyrolysis processes using CRD wood as a substrate for biochar production.

To engage with the aforesaid objectives, the idea behind each model is explored initially, followed by carrying out a compositional, proximate, ultimate, and metal analysis of the CRD wood waste to understand the physicochemical properties of the feedstock. Next, the surface chemistry of CRD wood was also studied using Fourier Transform Infrared (FTIR) spectroscopy to project its composition and structural framework. Subsequently, TGA experiments using CRD wood biomass at four different heating rates: 10, 20, 30, and 40°C/min are carried out and the data is cleaned and curated to be analyzed according to the methods under consideration. Firstly, for the model-fitting methods, the Coats-Redfern (CR) approximation is utilized. For isoconversional methods, the Ozawa-Flynn-Wall (OFW), Kissinger-Akahira-Sunose (KAS), and Friedman (FM) models are used. Based on the computed activation energy, pre-exponential factor, and other constants, the thermodynamic parameters are calculated. Finally, a prognosis of matching suitable reaction models to specific biomass conversion rates is also attempted.

2. Theory, materials and methods

All analysis were performed using the same CRD wood waste, instrumentation, methods, and by the same technician, like what has been elucidated in Ganesan et al., 2025. The characterization techniques have been explained here again, for clarity.

2.1 Foundational derivation

Different biomass sources exhibit different reactions due to variability in composition (Zhong et al., 2023). Therefore, an exact determination of reaction kinetics during biomass thermal decomposition is almost impossible (Rambhatla et al., 2024). To understand the pyrolytic conversion of CRD wood into biochar, TGA of this biomass is carried out at same or different heating rates in the presence of nitrogen as an inert carrier gas. An effective TGA test can mimick crucial process conditions such as the temperature, BRT, heating rate, and feed particle size that are usually interdepending, operational factors in a pyrolysis process which help in critically determining the composition of resulting products (Fanezouné et al., 2024). Through a kinetic study, the activation energy of a feedstock can be computed to evaluate its reactivity, for estimating its conversion efficiency, and also for scale-up considerations to larger pyrolyzers during the design phase (Patidar et al., 2022).

Rate of reaction for biomass in an isothermal condition is given as:

$$\frac{d\alpha}{dt} = k * f(\alpha)$$

Equation 1

Here, k is the reaction rate constant, which is temperature dependent, dα/dt is the change in mass of biomass taken for the analysis with respect to time (also referred to as biomass conversion rate), and f(α) is a differential function representing reaction models, and governed by different reaction schemes presented in Table 21.

$$k = \left(\frac{\frac{d\alpha}{dt}}{f(\alpha)}\right)$$

Equation 2

In the above equation, α that represents a fractional change in mass of biomass reactant, can be represented as:

$$\alpha = \frac{(x_o - x_t)}{(x_o - x_{f)}}$$

Equation 3

Here, x_o is the initial mass of biomass sample taken for the kinetic study by TGA, x_f is the final mass of sample at the end of TGA, and x_t is the mass of sample in the TGA cycle at a given time t. Decomposition rate of biomass as a function of temperature can be construed by the Arrhenius equation as follows:

$$k = A * \exp\left(\frac{-E_a}{RT}\right)$$

Equation 4

In the above expression, A is the pre-exponential or frequency factor (s^{-1} or min^{-1}) which represents the extent of molecular collisions in the wake of thermal decomposition at a given time and temperature, E_a is the activation energy required to cleave the bonds between feedstock biopolymers, namely cellulose, hemicellulose, and lignin (J/mol), R is the universal gas constant (8.3145 J/mol.K), and T is the temperature at which a particular stage of conversion proceeds (K). Upon substituting the reaction rate constant k from Equation 2 within the global one-step Arrhenius expression in Equation 4, we arrive at:

$$\frac{d\alpha}{dt} = A * \exp\left(\frac{-E_a}{RT}\right) * f(\alpha)$$

Equation 5

For a specific heating rate (K/min or K/s adopted during TGA, the temperature of the system is ramped up with respect to time and is hence, a non-isothermal process (Note: K/min is also the same as °C/min due to the same magnitude with respect to a common time frame. An increase in K by one unit is identical to an increase in °C by one unit).

$$\beta = \frac{dT}{dt} \textbf{ (or) } dt = \frac{dT}{\beta}$$

Equation 6

By inserting the above heat rate expression and substituting for dt in Equation 5, we arrive at:

$$\beta\left(\frac{d\alpha}{dT}\right) = A * \exp\left(\frac{-E_a}{RT}\right) * f(\alpha)$$

Equation 7

Equation 7 can be re-written as:

$$\left(\frac{d\alpha}{dT}\right) = \left(\frac{A}{\beta}\right) * \exp\left(\frac{-E_a}{RT}\right) * f(\alpha)$$

Equation 8

This serves as the basic expression that could be leveraged for model-fitting and model-free methods to be built further.

2.2 Model-fitting and model-free TGA methods rooting from foundational equations

Generally, to perform a kinetic analysis and calculate corresponding parameters, TGA can incorporate two approaches: model-fitting and model-free methods, that can detail a thermal decomposition process (Zsinka et al., 2024).

2.2.1 Model-fitting methods

As the name suggests, model-fitting method assumes that the experimental data obtained from any thermal decomposition reaction should fit into a pre-theorized model (Arenas et al., 2019). This is where the predicted term f(α) as in the aforementioned equations comes into play, to describe the relationship between the degree of biomass conversion or α and the overall rate of reaction, where only a single heating rate is sufficient. As outlined in Table 21, various forms of f(α) can take shape according to the type of reaction mechanism chosen for analysis that provide the output values of E_a and A (Postawa et al., 2022, Rambhatla et al., 2024, Patidar et al., 2022, Fanezouné et al., 2024).

Chemical reactions can be classified into first, second, and third order based on how the reaction rate relates to the concentrations of reactants. First-order reactions are reliant on the concentration of a single reactant, second-order reactions involve two reactants, and third-order reactions may include combinations of three reactants or elevated powers of one reactant. In biomass pyrolysis, biopolymers such as cellulose and lignin act as reactants, enabling numerous simultaneous reactions within the biomass. This study emphasizes these three orders, as higher-order reactions are uncommon and necessitate substantial energy to surpass activation energy barriers for multiple reactants to effectively collide. Furthermore, the diffusion mechanism pertains to the rate-limiting step regarding the movement of reactants, intermediates, and products through a medium (White et al., 2011), which can be characterized as one-dimensional, two-dimensional, or three-dimensional diffusion. One-dimensional diffusion occurs in a singular direction, like within linear, constrained porous channels. Two-dimensional diffusion takes place at surfaces or boundaries, while three-dimensional diffusion involves movement in all spatial directions, typical of bulk solid regions. In systems related to biomass pyrolysis, mass and heat transfer are affected by these types of diffusion, which are influenced by reaction time, residence time, and temperature. Phase interfacial reactions occur at the junctions between solids and liquids or gases, influenced by aspects such as adsorption, diffusion, and desorption processes (Pecha et al., 2019). The rate of these reactions depends on factors such as surface area, composition, particle size, residence time, temperature, and the presence of reactive atmospheres. In the process of converting biomass to biochar, heat transfer mechanisms namely, convection from the carrier gas and conduction from the surrounding biomass, are crucial. This conversion can result in the creation of secondary char and pyrolytic volatiles through random nucleation and growth mechanisms, where surface superstructures evolve into new phases that may display isotropic or anisotropic qualities (Zhang et al., 2022). This transformation might depend on how long surface clusters remain on the biochar and the temperature conditions that facilitate repolymerization and polycondensation reactions, akin to the processes seen in hydrothermal carbonization (HTC)-derived biochar (Pfersich et al., 2023). Given its carbonaceous nature, biochar

remains inherently reactive and continues to undergo various phase interfacial reactions even after its production, which is evident by its tendency to self-ignite when exposed to heat or air adsorption.

Table 21: Probable reaction mechanisms exhibited (non-exhaustive) during biomass pyrolysis. [Adapted from equations in (Mishra et al., 2018, Rambhatla et al., 2024, Patidar et al., 2022, Fanezouné et al., 2024)]. Here, g(α) is the integral function of f(α).

Reaction model	Type/mechanism	Denotation	f(α)	g(α)
Chemical	First-order	F_1	$1-\alpha$	$-\ln(1-\alpha)$
	Second-order	F_2	$(1-\alpha)^2$	$(1-\alpha)^{-1}-1$
	Third-order	F_3	$(1-\alpha)^3$	$[(1-\alpha)^{-2}-1]/2$
Diffusion	One-dimensional	D_1	0.5α	α^2
	Two-dimensional	D_2	$[-\ln(1-\alpha)]^{-1}$	$(1-\alpha)\ln(1-\alpha)+\alpha$
	Three-dimensional Jander (J)	D_3	$1.5(1-\alpha)^{2/3}[1-(1-\alpha)^{1/3}]^{-1}$	$[1-(1-\alpha)^{1/3}]^2$
	Three-dimensional Ginstling-Brounshtein (GB)	D_4	$1.5[(1-\alpha)^{-1/3}-1]^{-1}$	$(1-2\alpha/3)-(1-\alpha)^{2/3}$
Phase interfacial	One-dimensional	R_1	1	α
	Two-dimensional	R_2	$2(1-\alpha)^{1/2}$	$1-(1-\alpha)^{1/2}$
	Three-dimensional	R_3	$3(1-\alpha)^{2/3}$	$1-(1-\alpha)^{1/3}$
Nucleation and growth	Two-dimensional	A_2	$2(1-\alpha)[-\ln(1-\alpha)]^{1/2}$	$[-\ln(1-\alpha)]^{1/2}$
	Three-dimensional	A_3	$3(1-\alpha)[-\ln(1-\alpha)]^{2/3}$	$[-\ln(1-\alpha)]^{1/3}$

2.2.1.1 Arrhenius model

From Equation 8, it is important to note that heating rate is brought in here and matters mostly when the temperature profile as a function of time is combined with the Arrhenius expression during non-isothermal reactions. This can be seen in complex reaction models to theoretically simulate real-world thermal depolymerization processes like pyrolysis, gasification, or combustion where how much time a sample is subjected to a particular temperature can alter the conversion rate. Such models also introduce the element of non-equilibrium dynamics such as complex heat transfer mechanisms. On the other hand, the standalone Arrhenius equation assumes a steady-state reaction where the temperature during a conversion process is held constant (isothermal) with negligible changes. Eventhough this model assumes a system under equilibrium, it is not used here to imply that pyrolysis by itself, is a reversible process. However, it is highlighted here just as a relative empirical approximation that could be used to discern the critical role of heating rate as in a non-isothermal and non-equilibrium system, and also to arrive at a comparison between kinetic parameters derived from the two cases. Equation 8 is simplified as:

$$\frac{\left(\frac{d\alpha}{dt}\right)}{f(\alpha)} = A * \exp\left(\frac{-E_a}{RT}\right)$$

Equation 9

Here, by applying the natural logarithms on both sides, we conclude with the expression of the basic Arrhenius model:

$$\ln\left(\frac{\left(\frac{d\alpha}{dt}\right)}{f(\alpha)}\right) = \ln(A) + \frac{1}{T}\left(\frac{-E_a}{R}\right) \textbf{ (or) } \ln(k) = \ln(A) + \frac{1}{T}\left(\frac{-E_a}{R}\right)$$

Equation 10

Plotting $\ln\left(\frac{\left(\frac{d\alpha}{dt}\right)}{f(\alpha)}\right)$ or ln(k) versus (1/T) results in a straight line with a negative slope of ($-E_a/R$) while the y-axis intercept can be used to directly calculate A (Mahmood et al., 2021). With respect to $\ln\left(\frac{\left(\frac{d\alpha}{dt}\right)}{f(\alpha)}\right)$, different reaction models and the equations for calculating their corresponding f(α) is described in Table 21.

2.2.1.2 Coats-Redfern (CR) model

The CR method is a model-fitting technique used in chemical kinetics to study thermal decomposition of solid biomass matter, irrespective of woody or non-woody nature (Mian et al., 2019). It is being widely used by researchers for analysing the pyrolysis of lignocellulosic materials. The CR model functions as an integral of Equation 1. To understand how we land at the CR expression and for calculation clarity, Fanezouné et al., 2024 states that a primary model function for biomass pyrolysis kinetics can be interpreted as:

$$f(\alpha) = (1-\alpha)^n$$

Equation 11

where n is the order of reaction (1, 2, 3,….n). Also, unlike the Arrhenius model, the CR model does not assume a steady-state or isothermal model and can function effectively by following different heating rates (β). So, by substituting Equation 11 in Equation 8,

$$\left(\frac{d\alpha}{dT}\right) = \left(\frac{A}{\beta}\right) * \exp\left(\frac{-E_a}{RT}\right) * (1-\alpha)^n$$

Equation 12

Upon rearranging this equation, it can be formulated as:

$$\left(\frac{d\alpha}{(1-\alpha)^n}\right) = \left(\frac{A}{\beta}\right) * \exp\left(\frac{-E_a}{RT}\right) * dT$$

Equation 13

Now, introduction of the term g(α), i.e, the integral conversion of f(α) linking the extent of reaction to temperature and time, takes precedence which is based on a specific reaction mechanism encountered by biomass during pyrolysis. Integrating within the limits of α=0 and α=α at T=0 and T=T respectively (Wang et al., 2018, Mishra et al., 2018):

$$g(\alpha) = \int_0^{\alpha}\left(\frac{d\alpha}{(1-\alpha)^n}\right) = \int_0^{T}\left(\frac{A}{\beta}\right) * \exp\left(\frac{-E_a}{RT}\right) * dT$$

Equation 14

After integrating Equation 14 on the LHS first,

$$\frac{1-(1-\alpha)^{1-n}}{1-n} = \left(\frac{A}{\beta}\right)\int_{T_0}^{T} \exp\left(\frac{-E_a}{RT}\right) * dT$$

Equation 15

Following the recommendations in Mishra et al., 2018, after integration on RHS, Equation 15 becomes:

$$\frac{1-(1-\alpha)^{1-n}}{1-n} = \left(\frac{ART^2}{\beta E_a}\right) * \left(1-\frac{2RT}{E_a}\right) * \exp\left(\frac{-E_a}{RT}\right)$$

Equation 16

Rearranging Equation 16**,**

$$\frac{1-(1-\alpha)^{1-n}}{T^2(1-n)} = \left(\frac{AR}{\beta E_a}\right) * \left(1-\frac{2RT}{E_a}\right) * \exp\left(\frac{-E_a}{RT}\right)$$

Equation 17

From Wang et al., 2018, assuming that $\left(1-\frac{2RT}{E_a}\right) \ll 1$ and can be neglected, Equation 17 can be reframed as:

$$\frac{1}{T^2} * \frac{1-(1-\alpha)^{1-n}}{(1-n)} = \left(\frac{AR}{\beta E_a}\right) * \exp\left(\frac{-E_a}{RT}\right)$$

Equation 18

Applying natural logarithms on both sides of Equation 18, we get:

$$\ln\left(\frac{1}{T^2} * \frac{1-(1-\alpha)^{1-n}}{(1-n)}\right) = \ln\left(\frac{AR}{\beta E_a}\right) + \frac{1}{T}\left(\frac{-E_a}{R}\right)$$

Equation 19

Albeit the above equation is valid for n≠1. According to Chen et al., 2022, pyrolysis of lignin-based solids is a first-order reaction where n=1. Moreover, according to Altynbaeva et al., 2018, CR method adopts the basis of a single-stage first-order reaction during thermochemical breakdown of a solid fuel. Thus, Equation 19 becomes:

$$\ln\left(\frac{-\ln(1-\alpha)}{T^2}\right) = \ln\left(\frac{AR}{\beta E_a}\right) + \frac{1}{T}\left(\frac{-E_a}{R}\right)$$

Equation 20

By inserting the integral function once again in Equation 20, we can simplify the expression as:

$$\ln\left(\frac{g(\alpha)}{T^2}\right) = \ln\left(\frac{AR}{\beta E_a}\right) + \frac{1}{T}\left(\frac{-E_a}{R}\right)$$

Equation 21

For different reaction models (chemical reaction, diffusion, phase interfacial, nucleation and growth) and associated mechanisms, the corresponding value of g(α) can be used from Table 21 to calculate kinetic parameters. Plotting $\ln\left(\frac{g(\alpha)}{T^2}\right)$ versus $\left(\frac{1}{T}\right)$ gives a straight line with a negative slope equivalent to $\left(\frac{-E_a}{R}\right)$. With the known value of E_a, it is possible to calculate A using the y-axis intercept $\ln\left(\frac{AR}{\beta E_a}\right)$.

Four key shortcomings of model-fitting methods are: a) The value of E_a is subjected to heavily depend on the reaction model assumed when in reality, there is significant possibility of a process to manifest itself by several other models; b) Secondly, if the wrong model is chosen, the reliability of the measured kinetic parameter value can be questionable; c) Thirdly, a model-fitting method like CR may function harmoniously only at one specific heating rate at a given time where different reaction mechanisms can be tested under one roof for satisfactoriness rather than several heating rates simultaneously as in iso-conversional models; d) Fourthly, despite providing an overview of E_a under many assumed models, it is a highly time-consuming method. Henceforth, while using model-fitting methods, it is advisable to assume as many reaction models as possible to help in quantitative analysis of E_a from more than a single perspective. In fact, it may be safe to say that convoluted processes such as pyrolysis can exhibit a myriad of simultaneous (parallel), sequential or both types of reactions at once. When using this approach, it could be possible to also narrow down on the ideal model using correlation coefficient (R^2) and simple cross-comparison.

2.2.2 Model-free or iso-conversional methods

Model-free kinetic methods do not assume that a chemical reaction progresses as per a pre-selected model under only a single heating rate. It considers the possibility of addressing complex chemical reactions at multiple heating and conversion rates (Emiola-Sadiq et al., 2021). Here, different values of α (ranging from 0-1) are used to calculate E_a without the necessity for g(α) intervention, thereby, offering greater flexibility to the method (Najafi et al., 2024). It is here that common slow pyrolysis heating rates are employed (10-40°C/min in our case) in the presence of nitrogen to detect variations in E_a at each stage of α. Different values of α are obtained at different phases of pyrolysis due to which kinetic parameters under variable heating rates need to be compared and fitted separately one after the other (Chen et al., 2022). In other words, we will be plotting for one α value (eg: α=0.1) at all four heating rates (10, 20, 30, and 40°C/min), proceed to the next conversion value (eg: α=0.2) at the four

heating rates, and so on till α=1. Variations in extracted E_a for instance, may indicate that biomass decomposition in a pyrolysis-like setting encompasses an interplay of many different reaction mechanisms and not just one that improves overall dependability and robustness of the derived values of E_a. Although it is not necessary to use g(α) to calculate E_a, model-free methods do need this function to calculate A and still depend upon a specific reaction model and mechanism. This is without a doubt, a notable drawback of model-free methods that accentuates a limitation towards fully characterizing both kinetic parameters without the role of assumptions. Also, model-free methods are criticised since they are too simplistic and general in describing a complex process like pyrolysis (Fanezouné et al., 2024).

There are different model-free methods used in practice of approximating E_a of pyrolysis reactions like FM, KAS, OFW, Vyazovkin (VZ), and distributed activation energy model (DAEM) that forge high simplicity during calculations. Among these, FM, KAS, and OFW will be used in this study as representative methods. They are appreciable to analyse complex reactions as a function of biomass conversion value, α. From the expressions studied in Mishra et al., 2020 and Li et al., 2022, the following Table 22 illustrates the expression for these methods, values of constants/variables, and the procedure for plotting to evaluate kinetic parameters.

Table 22: Model-free or isoconversional methods

Model-free method	Equation	Procedure for plotting
OFW	$\ln(\beta) = \ln\left(\frac{AE_a}{Rg(\alpha)}\right) - 2.315 - 0.457\frac{E_a}{RT}$ **Equation 22**	Plot $\ln(\beta)$ versus $\frac{1}{T}$ to obtain a straight line with a negative slope of $-0.457\frac{E_a}{R}$ to calculate E_a. Using this and an assumed reaction model/mechanism for g(α), A can be calculated from the y-axis intercept, $\ln\left(\frac{AE_a}{Rg(\alpha)}\right)$.
KAS	$\ln\left(\frac{\beta}{T^2}\right) = \ln\left(\frac{AE_a}{Rg(\alpha)}\right) - \frac{E_a}{RT}$ **Equation 23**	Plot $\ln\left(\frac{\beta}{T^2}\right)$ versus $\frac{1}{T}$ to obtain a straight line with a negative slope of $-\frac{E_a}{R}$ to calculate E_a. Using this and an assumed reaction model/mechanism for g(α), A can be calculated from the y-axis intercept, $\ln\left(\frac{AE_a}{Rg(\alpha)}\right)$.
FM	$\ln\beta\left(\frac{d\alpha}{dT}\right) = \ln[(Af(\alpha))^n] - \frac{E_a}{RT}$ (or) $\ln\left(\frac{d\alpha}{dt}\right) = \ln[(Af(\alpha))^n] - \frac{E_a}{RT}$ **Equation 24**	Plot $\ln\beta\left(\frac{d\alpha}{dT}\right)$ or $\ln\left(\frac{d\alpha}{dt}\right)$ versus $\frac{1}{T}$ to obtain a straight line with a negative slope of $-\frac{E_a}{R}$ to calculate E_a. Using this and an assumed reaction model/mechanism for f(α), A can be calculated from the y-axis intercept, $\ln[(Af(\alpha))^n]$.

2.3 Thermodynamic study

During pyrolysis, thermodynamic parameters such as ΔH, ΔS, and ΔG are calculated using the following equations adapted from Singh et al., 2021.

$$\Delta H = E_a - RT_m$$

Equation 25

$$\Delta G = E_a - RT_m \ln\left(\frac{K_B \times T_m}{hA}\right)$$

Equation 26

$$\Delta S = \left(\frac{\Delta H - \Delta G}{T_m}\right)$$

Equation 27

In the above equations, T_m is the maximum thermal decomposition temperature of CRD wood biomass that was obtained from DTG curves at each heating rate (10-40°C/min). E_a is the activation energy derived using isoconversional models of OFW, KAS, and FM at each heating rate and conversion stage. Pre-exponential factor, A, was also calculated from the respective plot using the intercept. K_B is the Boltzmann constant of 1.381×10^{-23} J/K and h is the Plank's constant, 6.626×10^{-34} J/s.

Equation 25 is however, a general and simplified expression that could be used to calculate the thermodynamic parameters and may not cover all intricacies posed by multi-step biomass pyrolysis reactions. Rather, it conservatively represents a general overview of the wood matrix decomposition. If over-simplification of pyrolysis especially by neglecting critical energy barriers occurs, activation energy calculations could be erroneous, inevitably influencing entropies since they are very small.

2.4 CRD wood biomass sample preparation for characterization and kinetic analysis

Non-recyclable CRD wood sourced from "BRQ Fibre et Broyure" in Trois-Rivières, Québec, was delivered in pails to the Innofibre facility Figure 39 (A). After being collected, the CRD wood underwent mechanical sieving using a Labtech vibrational sieving unit to separate it into different particle sizes (>4.5 cm till >0.3 cm) after screening and removal of contaminants Figure 39 (B). In fact, no washing was performed due to the risk of creating contaminated wastewater from the leaching of impurities present in the CRD wood. Once the size separation was completed, the selected biomass fraction in Figure 39 (C) was dried for an entire night at 105 °C. Given that sieving only led to particle sizes of up to 0.3 cm, it was necessary to mill the CRD wood further. A Retsch SM300 mill (3 kW motor and rpm: 100-3000), featuring a high-speed tungsten carbide rotor and screens with openings as small as 500 µm, or a Thomas Wiley mill with a similar mesh size, was utilized to produce fine particles as in Figure 39 (D) from the biomass for subsequent analysis.

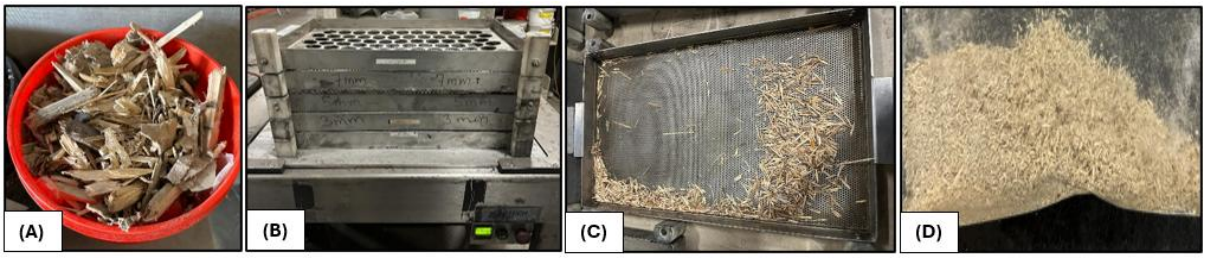

Figure 39: CRD wood sample conditioning and preparation: (A) CRD wood waste sourced in pails from the local provider; (B) vibrational sieving of CRD wood; (C) contaminant separated CRD wood of relevant particle size (<5mm and >3mm); (D) Milled CRD wood fines for characterization and TGA experimentation

2.5 Physicochemical characterization

Proximate analysis was employed to evaluate ash content, volatile carbon (VC), and fixed carbon (FC) in biomass. For the ash measurement, 1 g of dry biomass fines was placed into a crucible and heated in a muffle furnace with a similar procedure as in ISO 1171 and ASTM D1762-84. Beginning at room temperature, the sample was heated to 106 °C at a rate of 5 °C/min and maintained at this temperature for 1 hour to ensure that most residual moisture is removed. Then the temperature was increased at the same rate from 106 °C to 550 °C to decompose labile extractives and organics under controlled heat transfer. At 550°C, the wood sample was held for a duration of 4-6 hours for further degradation of any combustible biomass components. The sample was then allowed to cool to room temperature in a desiccator to prevent any hygroscopic effects, after which the ash was weighed to ascertain the proportion of biomass remaining. For volatile carbon, 1 g of dry biomass fines was subjected to heating at 900 °C for 7 minutes in a sealed crucible, after which it was cooled and weighed to quantify the carbon lost. VC is utilized in certain contexts in this study to specifically refer to labile carbon, distinguishing it from other volatile components. FC was calculated using the relation: FC = 100 − (VC + ash), as weight percent dry basis (wt%DB), where VC and ash will also be represented as wt%DB (Armynah et al., 2019).

For the ultimate analysis, an Elementar Vario Macro Cube examined 1-200 mg of dry biomass fines for elements such as carbon, hydrogen, nitrogen, and sulfur, utilizing helium (purity >99.996%) as the carrier gas and oxygen (purity >99.996%) for combustion up to 1200 °C. The oxygen content was determined by calculating the difference from 100%, using the percentages of all individual elements and ash, as given in: [$\text{oxygen} = 100 - (\text{carbon} + \text{hydrogen} + \text{nitrogen} + \text{sulfur} + \text{ash})$]. It is derived from Nzediegwu et al., 2021.

The higher heating value (HHV) of CRD wood biomass was determined using a similar approach outlined by Channiwala & Parikh, 2022. This approach correlated the calorific value with elemental composition obtained from ultimate analysis of the biomass sample. For metal detection in biomass, an Agilent Technologies 4210 Microwave Plasma Atomic Emission Spectrometer (MP-AES) was utilized, which featured a nitrogen fuel source and an SPS 4 autosampler. This apparatus allowed for the simultaneous analysis of multiple elements by aerosolizing the biomass sample into a nitrogen plasma to produce monoatomic ions. The device guaranteed accurate measurements of the inorganic content by completely digesting the organic materials found in the biomass.

2.6 Composition analysis

The presence of extractives, structural carbohydrates, and lignin in CRD wood biomass were analyzed according to National Renewable Energy Laboratory (NREL, United States of America Department of Energy) procedures as described in NREL/TP-510-42619 and NREL/TP-510-42618, respectively.

2.7 FTIR

The distribution of surface functional groups in biomass was examined using an Agilent Technologies Cary 630 spectroscope, with Microlab PC software for operation. About 1 g of dry biomass fines was placed on a diamond crystal surface that was regularly cleaned with ethanol. The analysis was performed in transmittance mode over a spectral range of 500–4000 cm^{-1} to determine the chemical bonds present in the material. Baseline and peak corrections were applied to the obtained spectra, followed by signal smoothing.

2.8 TGA

In order to examine the weight loss pattern of biomass in relation to temperature, a PerkinElmer TGA 8000 analyzer was utilized. This device was also able to assess proximate analysis parameters such as moisture, VC, FC, and ash. Only 8 mg of biomass fines in their original, non-dried state were needed per vial for the analyzer. Since TGA was leveraged to analyze the pyrolysis kinetics of CRD wood, the process gas used during heating was compressed nitrogen with a purity level exceeding 99.996%. The system was capable of accurately reaching temperatures up to 1200 °C with adjustable heating rates. For this research, 10, 20, 30, and 40 °C/min were employed, reaching a maximum temperature of 900 °C to investigate the transformation of biomass to biochar. Differential thermogravimetric (DTG) curves were generated by differentiating the weight loss features from the original thermogram in relation to time and plotting them against temperature. This led to the identification of different peaks indicating the points of maximum weight loss or melting of the sample during TGA, along with the corresponding temperatures, providing insights into biomass chemical composition and hydrocarbon structure.

3. Results and discussion

3.1 Physicochemical properties of CRD wood – Comparative analysis with other biomass feedstock

The proximate and ultimate analysis parameters of CRD wood biomass were analyzed as shown in Table 23. Elemental composition, particularly carbon content in CRD wood, resembled hard woods like beech and poplar at 49-50% despite containing softwood residues in the bale. In terms of carbon content, MSW outperformed all the feedstock with carbon content at 76.26% due to a heterogeneous composition involving plastics and other hydrocarbon-rich residues. Oxygen (41.74%) and hydrogen (6.12%) were also equivalent to the ranges in hard wood species. These bolster the role of CRD wood biomass to be used in bioenergy applications for the production of biofuels, biochemicals, and bioproducts. Low sulfur (if any, from gypsum dust) and nitrogen content in CRD wood also mean that the release of NOx and SOx could be starved during pyrolysis. For proximate parameters, CRD wood is a low-ash biomass at 1.17% relative to high-ash agricultural residues like rice husk at 14.20% or medium-ash sources like MSW (8.26%).

Table 23: Physicochemical properties of CRD wood in comparison with different biomass sources. References are mentioned below the characterization results in the table

Biomass	Pinewood	Rice husk	Beech	Wheat straw	Miscanthus*	Madhuca Longifolia	Poplar sawdust*	Palm kernel*	MSW	CRD wood*
Proximate analysis										
Moisture (wt%)	4.01	10.10	15.20	11.63	---	5.98	---	---	2.75	---
Volatiles (wt%)	64.37	52.30	84.87	65.32	83.30	71.26	83.60	79.68	51.13	**82.35**
FC (wt%)	24.89	23.40	14.53	15.17	14.40	18.24	15.40	16.78	37.86	**16.48**
Ash (wt%)	6.73	14.20	0.60	7.88	2.30	4.50	1.00	3.54	8.26	**1.17**
Ultimate analysis										
C (wt%)	54.53	34.99	49.38	44.12	47.50	47.20	49.47	43.84	76.26	**49.88**
H (wt%)	6.56	4.58	6.17	6.34	6.10	5.90	5.89	6.13	6.88	**6.12**
S (wt%)	0.09	---	0.01	---	0.10	1.20	0.05	0.06	0.28	**0.10**
N (wt%)	0.94	1.95	0.28	0.63	1.00	3.60	1.40	3.11	3.32	**0.99**
O (wt%)	31.14	34.18	43.55	39.99	45.30	42.10	43.12	46.86	13.25	**41.74**
Van-Krevelen parameters										
H/C	1.44	1.57	1.50	1.72	1.54	1.50	1.43	1.68	1.07	**1.47**
O/C	0.43	0.73	0.66	0.68	0.72	0.67	0.65	0.80	0.13	**0.63**
Calorific value										
HHV (MJ/kg)	22.33	14.09	19.3	15.29	15.82	---	19.50	16.83	29.70	**20.28**
Reference	Maaoui et al., 2023	Chakravarty et al., 2024	Giglio et al., 2021	Radojevic et al., 2018	Fischer et al., 2024; Szufa et al., 2021	Thiru et al., 2024	Paredes et al., 2024	Punsuwan et al., 2014; Gani et al., 2024	Uwaoma et al., 2022	**Present study**

*** Expressed in wt% DB**

However, as delineated in Figure 40, the metal content in CRD wood, mainly alkaline and alkaline earth metals (AAEM) (86-87%), was very high which may result in secondary reactions by acting as indirect catalysts leading to excess loss of carbon or could cause technical snags in reactor equipment through slagging, fouling or bed agglomeration (Wang et al., 2022, Cao et al., 2023). But, among AAEM, alkaline earth metals like Ca, Ba, and Mg constituted for 59.96% whereas alkaline metals made up just 27.03%. So, there could be a possibility where the melting of ash may be pushed towards relatively higher temperatures since presence of divalent species dominated this AAEM fraction. On the contrary, the other possibility with high AAEM could be secondary char formation (Liu et al., 2025). Grafmüller et al., 2022 stated that AAEM, when present with woody biomass, under pyrolysis temperatures of 350-750°C, may increase the yield of biochar through secondary reactions. This holds true for an AAEM-rich feedstock like CRD wood. Additionally, CRD wood contains some heavy metallic contaminants like Cu, Cr, and mild levels of As. Other heavy metals detected were mainly Zn and Pb. All these metals are part of preservatives, paints, varnishes, roofings, and surface coatings in conditioned CRD wood that are usually part of residential buildings, electricity poles, and hand rails dating back to 1960s-1990s. The VC in CRD wood (82.35%) matches VC in poplar (83.60%) and beech (84.87%) confirming highly decomposable fractions. Also, due to high volatiles and low ash, woody biomass could produce biochar product with high FC (Elhenawy et al., 2024). Also, due to the lower ash content that minimizes presence of non-combustible materials, HHV of CRD wood biomass is relatively high at 20.28 MJ/kg rendering it suitable for bioenergy applications (Nhuchhen & Afza, 2017). On the contrary, a high ash rice husk had a low HHV at 14.09 MJ/kg. Wheat straw with moderate ash also had a low HHV of 15.29 MJ/kg. Another pattern observed is that as volatiles increase, HHV decreases due to the non-availability of stable carbon. This was true for MSW (51.13%) and pinewood (64.37%) relative to CRD wood (82.35%), where the increase in volatiles decreased HHV from 29.70 MJ/kg, 22.33 MJ/kg, and 20.28%, respectively.

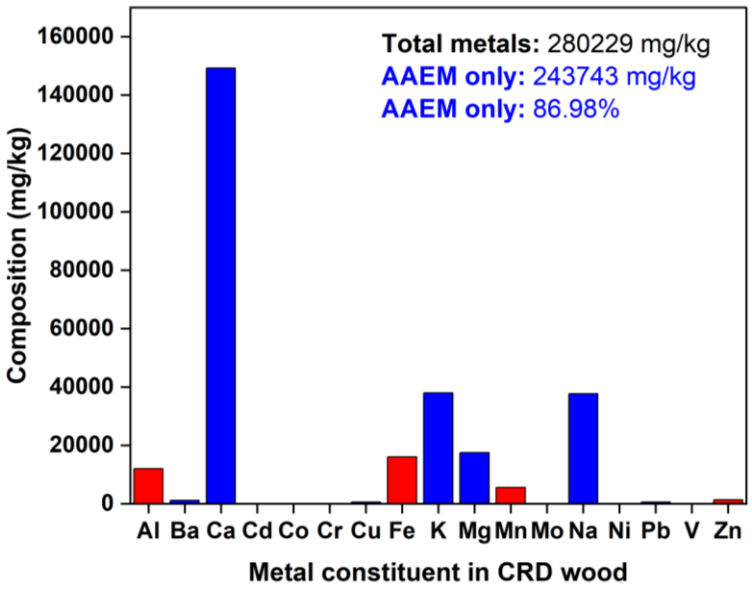

Figure 40: Metal constituents in CRD wood. Blue bars represent AAEM in CRD wood and red bars denote other metals

3.2 CRD wood compositional analysis

To achieve a representative and robust analysis of CRD wood biomass received, samples from four different sections of the pail, post-sample preparation steps, were subjected to compositional analysis. Percentages of extractives, holocellulose and lignin were listed in Table 24, which may explain the nature of biomass transformation to biochar. Extractives soluble in hot water and ethanol ranged from 2-3.5% and 2.5-4% respectively, that are usually eliminated as volatiles. Since total lignin varied from 24-31%, it is conclusive that CRD wood is composed of both hard and softwood and may be called together as 'wood waste' that has a comparable lignin content, recorded at 28.9% as in Li et al., 2024. From Yildiz et al., 2025, biochar produced from agriculture wastes like buckwheat husk (holocellulose: 73.72%, lignin: 24.73%), spent coffee grounds (holocellulose: 31.58%, lignin: 23.65%), hazelnut shell (holocellulose: 62.31%, lignin: 28.30%), and waste grass biomass like hemp (holocellulose: 25.81%, lignin: 20.69%), miscanthus (holocellulose: 63.11%. lignin: 25.48%) were also compared. Greater the lignin, more the structural complexity due to the presence of aromatics, and greater may be the biochar yields (Dhyani & Bhaskar, 2018). However, lignin content in biochar is not a solely conclusive indicator of mechanical strength/integrity and yield of biochar (Gurtner et al., 2023, Dufourny et al., 2019). Although, lignin, if softened and melted to form condensed aromatic structures, the overall bulk density and resistance towards breakage may increase (Wang et al., 2022). Carbon content and stability of biochar could be largely conserved as well. Total holocellulose content in CRD wood varied from 68-77%. With six-carbon sugars like glucose (44-54%), galactose (0.5-2.5%), mannose (2-10%) and five-carbon sugars like xylose (8-24%), arabinose (0-1.5%), hemicellulose decomposition in CRD wood to pyrolysis gases at lower temperatures is plausible. The overall contribution to char formation is low for hemicellulose. Cellulose decomposition could favor both condensed volatiles and intermediates (high temperatures) and some char (lower temperature) formation. It is determined by the temperature, BRT, and heating rate employed during the process (Xia et al., 2021).

Table 24: Biochemical composition of CRD wood lots from the same bale

Biomass constituents	Lot 1	Lot 2	Lot 3	Lot 4
Hot Water Extractives (wt%)	3.2	2.0	3.1	2.7
Ethanol Extractives (wt%)	3.7	3.0	2.8	4.0
Total extractives (wt%)	**6.9**	**5.0**	**5.9**	**6.7**

Insoluble Lignin (wt%)	19.7	20.5	26.1	25.3
Total Lignin (wt%)	**24.9**	**26.2**	**30.2**	**29.7**
Glucan (wt%)	50.9	44.2	46.9	53.1
Xylan (wt%)	19.2	23.2	8.0	10.1
Arabinan (wt%)	0.0	0.1	0.9	1.3
Galactan (wt%)	0.6	0.8	2.5	2.4
Mannan (wt%)	2.0	2.3	9.7	10.0
Total holocellulose (wt%)	**72.7**	**70.6**	**68.0**	**76.9**

3.3 FTIR spectroscopy analysis

FTIR spectral distribution of the CRD wood biomass is shown in Figure 41. A high concentration of specific functional groups in the CRD wood biomass feed is denoted by strong transmittance peaks of infrared light through the sample which demonstrate specific vibrational patterns: stretching or bending. Spectral band assignments from Johnston, 2017 and Nanda et al., 2013 were used to match the transmittance peaks in CRD wood biomass to relevant functionalities. Firstly, the distinct peak at 3320 cm^{-1} indicates O-H stretching vibrations as in moisture, carboxylic acids, alcohols, and phenols. Secondly, the distinct peak at 2892 cm^{-1} could signify C-H stretching in aliphatic hydrocarbons as in alkanes that are subunits of most biomass polymers. Thirdly, the spectral band at 2003 cm^{-1} highlights stretching vibrations in alkynes (C≡C) that may be ascribed to polyaromatics with maximal carbon condensation. Next, carbonyl stretch (C=O) in aldehydes, ketones, esters, and carboxylic acids appears around 1730 cm^{-1} that stem from hemicellulose in CRD wood. Actually, this contributes to the loss of biomass carbon as CO and CO_2 during the onset of pyrolysis. A subdued peak at 1503 cm^{-1} and 1265 cm^{-1} means there are faint aromatic C-C and aromatic C-O ring stretching actions respectively, amidst the biomass carbon skeleton. Methyl, methylene or methoxy groups of biomass lignin also exhibit these vibrations owing to the presence of dense organic residues in biomass. A sharp band at 1022 cm^{-1} may be due to C-O stretching in aliphatic ethers (C-O-R) and alcohols (C-O-H) that are key building blocks of carbohydrates/polysaccharides. The 799 cm^{-1} band could be an extractive in biomass showcasing the C-H bend in alkynes, phenyl rings, or aromatics followed by the band at 664 cm^{-1} stemming from C-H vibrations in alkenes.

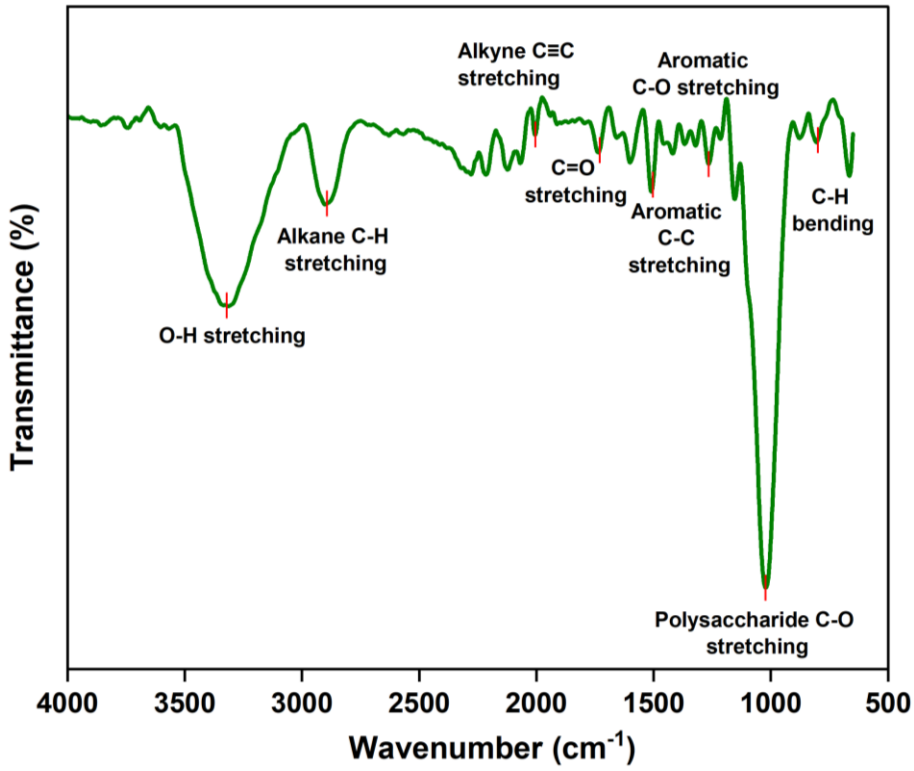

Figure 41: FTIR spectral distribution of CRD wood with functional group attributes

3.4 TGA analysis and effect of heating rate

The thermal stability of CRD wood biomass was verified by TGA and DTG curves. The weight loss exhibited by biomass under four different heating rates: 10, 20, 30, and 40°C/min along with their stages of thermal degradation under an inert nitrogen atmosphere mimicking pyrolysis, are studied as in Figure 42. From the TGA plot in Figure 42 (A), it is evident that an increase in heating rate pushes the degradation temperature slightly higher (to the right) as reported in Mukherjee et al., 2021. This is because, an increase in heating rate means that there is less time for heat to permeate from the surface to the core of the biomass particle and that too, only non-linearly. So, the weight loss encountered is restricted as a surface effect rather than occurring throughout the particle and is hence low. At a lower heating rate, an inverse phenomenon where there is gradual heat transfer that devolatilizes biomass constituents to fruition under an ample time frame, is clear. Biomass's outer layer and the core inside reach almost similar temperatures, allowing a linear thermal behaviour. This is validated by maximum weight loss (72.73%) between 200-400°C for the heating rate of 10°C/min followed by 69.45%, 64.95%, and 60.85% for the heating rates 20, 30, and 40°C/min respectively. However, despite an increase in heating rate by every 10°C/min, the profile for degradation curves is unchanged, as concurred from Raza et al., 2023.

If we look more closely at the DTG peaks for these heating rates, weight loss happens in three stages. The first stage occurs <150°C where evaporation of moisture and other surface bound volatiles occur (Almusafir & Smith, 2024). Around 5-7% weight loss happened here. As seen in Figure 42 (B) (C), within the second stage from 200-400°C, melting temperatures of biomass (T_m) for each heating rate is observed to increase with increase in heating rate (367.41°C for 10°C/min to 389.62°C for 40°C/min) validating our earlier finding that greater BRT at that specific temperature means that there is adequate time for biomass to experience loss of structural integrity by efficiently exposing its biopolymers for cleavage, signifying an ongoing pyrolysis process (Apaydın Varol & Mutlu, 2023). This region encompasses extractives, VOCs, hemicellulose, and cellulose breakdown respectively with peak decomposition mainly between 350-400°C. Since cellulose is a straight chain, crystalline polymer, it needs greater energy to collapse and hence, disintegrates after relatively less-stable hemicellulose degrades to a large extent. Biomass carbon (eg: carbon loss via CO_2 and CO) and heteroatom (eg: H_2S, SO_2, NH_3) rejection reactions from holocellulose followed by the simultaneous heat uptake to initiate destabilization of lignin aromatics (eg: phenols) are key reactions that increase gas and condensible volatiles yield. From the conversion (α) plot in Figure 42 (D), we can see that 80% (α=0.8) is completed around 400°C. In this second stage, profound mass loss of 60-73% took place. Beyond this point, the third stage of decomposition is rather slow and proceeds

well-spaced out due to complex lignin fractions and other heavy molecular weight compounds. Moreover, since CRD wood contains noticeable AAEM and other metals/inorganics in its ash fraction, that could be stable up to a certain level and delays breakdown. This is when char generation peaks due to both primary and secondary pyrolysis reactions. It is safe to say that no additional peaks were observed which means that significant degradation of inorganic material may not be accounted for. At the end of the process, about 20% of initial mass of CRD wood remains. All in all, there was another interesting observation. At higher heating rates of 30 and 40°C/min, decomposition peaks appear to overlap which indicates that degradation of biomass polymers may not be completely separated processes and could occur sharply within a narrow temperature range, and as synchronous steps. As concluded by Gonzalez-Aguilar et al., 2022 and Mukherjee et al., 2021, the thermal decomposition patterns remained fairly consistent across all the heating rates tested.

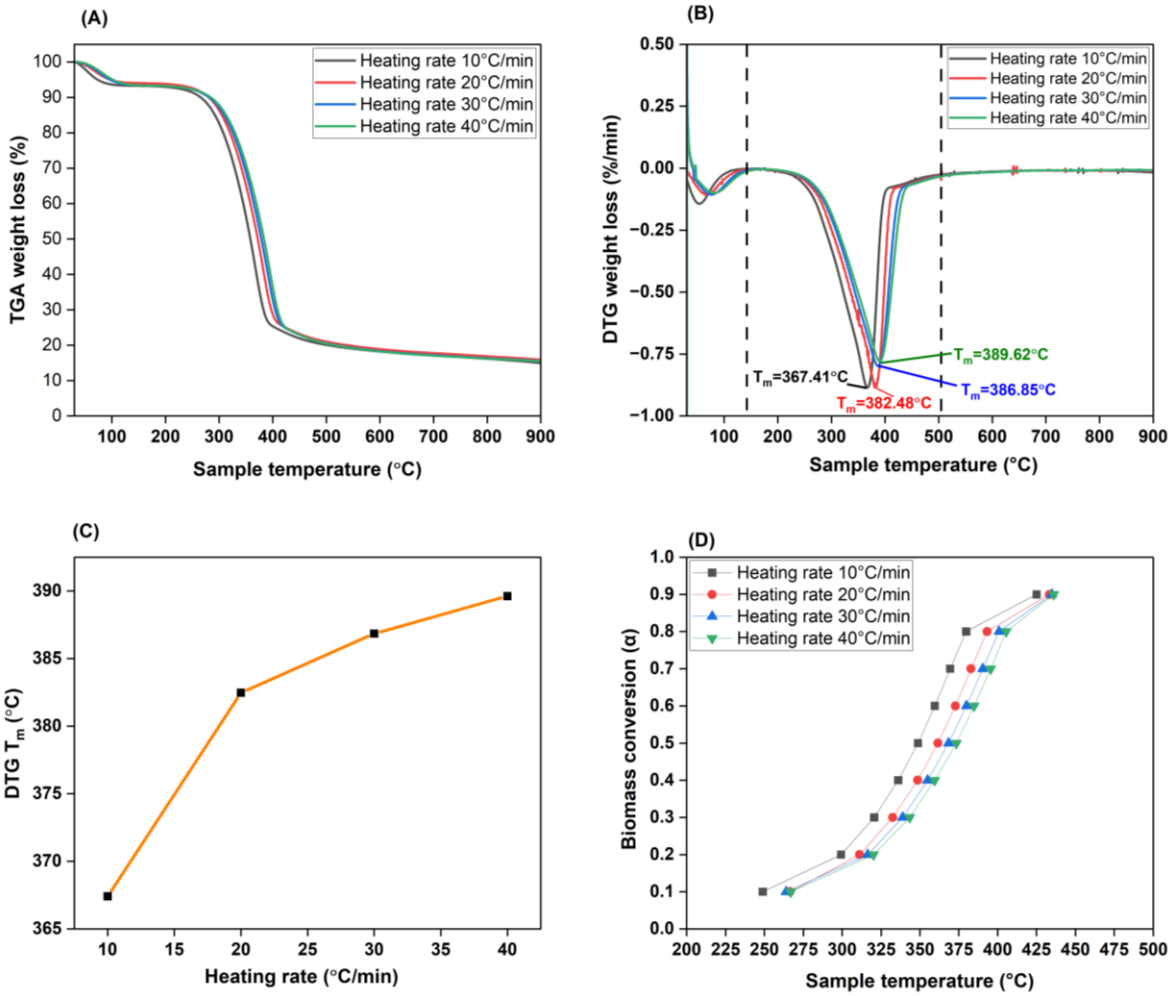

Figure 42: TGA and biomass conversion analysis. A difference between ash measured by proximate analysis and ash in the TGA curve, may be due to slower conversion due to the heating rates chosen. The ash levels in (A) may match the proximate analysis results if a test with heating rates < 10°C/min was chosen to allow sufficient depolymerization time considering the complexity of the feedstock

3.5 Kinetic analysis of CRD wood pyrolysis

3.5.1 Model-fitting method

Being a model-fitting technique, the CR method fits TGA data of biomass pyrolysis to various kinetic models for calculating the activation energies and pre-exponential factors. The calculations in Table 25 surrounded all models for the four different heating rates, i.e, 10-40°C/min. The correlation factor (R^2) was used to judge the probability of each reaction model being interplayed. No marked increase in activation energy existed between different heating rates, although it was maximum for 30°C/min as shown in Figure 43 (A-D).

For chemical reaction models (F_1, F_2, and F_3), an increase in reactants necessitated either higher temperature or reaction time because of a high activation energy demand. This is to overcome any heat or mass transfer limitations during pyrolysis attributed mainly to the rampant molecular collisions within CRD wood biomass contributing to complex, overlapping reactions. It ranged from 65-68 kJ/mol for F_1 to 129-133 kJ/mol for F_3 as heating rate increased, indicating energy-intensive heterogeneous structures competing in the reaction. This is supported by a concomittant increase of the pre-exponential factor as well. However, average R^2 is between 0.92-0.98 suggesting a relatively lower correlation of these reaction models w.r.t. their counterparts. Due to the highest activation energies recorded for F_3 (more than any other reaction model tested), it may be possible to assign its role for higher conversion stages ($\alpha > 0.6$) too where a thorough rearrangement of biochar's chemical structure is probable as concluded by Calin et al., 2024.

For the diffusion model, activation energies collectively ranged from 98-129 kJ/mol with a dominant effect from linear (D_1), planar (D_2), and spherical (D_3) diffusion mechanisms. These models dominate the thermochemical data of CRD wood as extrapolated from the findings in Dhaundiyal et al., 2018. Average R^2 is > 0.99 highlighting their pivotal part in thermal decomposition where migration of volatiles and pyrolysis products could happen through porous channels and at the boundary layers. Diffusion was deemed suitable for coconut shell feedstock with a comparable activation energy of 68.9 kJ/mol granting appreciable bioenergy potential (Monir et al., 2024). A high correlation factor for diffusion model was also shown for feedstock like wood sawdust and wheat straw (Saleem et al., 2024). In case of any energy applications for CRD wood, D_1, D_2, and D_3 models may govern the diffusion of ambient air/oxygen and volatile matter that initiate ignition and proceed till final combustion. This concept was also proposed by Hadey et al., 2020. As in Hassan et al., 2024, D_3 model showed the highest activation energy for pyrolysis of MSW which could contain easily decomposable constituents. Whereas, in CRD wood D_3 model (125-129 kJ/mol with $R^2 > 0.99$) corresponded to a high activation energy for carrying forward diffusion within constricted spaces, especially upon clogging of porous channels with residual tar. It may also mean that surface-based diffusion has lower resistance and takes place more freely until an intermediate or product layer forms that impedes any progress. Due to high activation energies overall, F_3, D_1, D_2, and D_3 models can be attributed to the second (200-400°C) and third (400-600°C) stages of the TGA cycle where majority of disintegration reactions happen for CRD wood pyrolysis. An average activation energy of up to 84 kJ/mol was obtained by Tariq et al., 2023 for almond shell pyrolysis using CR method where the decomposition reactions occur in the range of 150-550°C as well. All these results were commensurate with CRD wood.

The occurrence of phase interfacial reactions (R_1, R_2, R_3) are also explainable due to a high correlation of > 0.99. The results here are comparable to Sobek & Werle, 2020 where D_3 and R_3 majorly drove the biomass decomposition along with F_1, F_2, …F_n. This means that decomposition of biomass could begin from the surface towards the less-reacted, unconverted core. As a result of constant interaction between reactants and products at an interphase, product layers are formed and sequentially shift from the outside to the inside of the biomass particle. This is why biochar production is favored at lower heating rates since it allows sufficient time for this gradual conversion. Activation energy here was lower than chemical reaction and diffusion models, at 43-60 kJ/mol. Finally, only less energy (15-30 kJ/mol) was needed for secondary pyrolytic intermediates and product formation through A_2 and A_3 nucleation mechanisms ($R^2 = 0.97$-0.99). For this mechanism, inherent AAEM and other inorganics may have coincidentally aided in secondary charring and volatiles formation by behaving as catalysts.

1

Table 25: Activation energy (E_a), pre-exponential factor (A), and model correlation (R^2) of different pyrolysis reaction models (albeit, non-exhaustive list) evaluated using the CR method

Reaction model	Type/mechanism	Heating rate = 10°C/min			Heating rate = 20°C/min			Heating rate = 30°C/min			Heating rate = 40°C/min		
		Activation energy, E_a (kJ/mol)	Pre-exponential factor, A (min^{-1})	R^2 from plot	Activation energy, E_a (kJ/mol)	Pre-exponential factor, A (min^{-1})	R^2 from plot	Activation energy, E_a (kJ/mol)	Pre-exponential factor, A (min^{-1})	R^2 from plot	Activation energy, E_a (kJ/mol)	Pre-exponential factor, A (min^{-1})	R^2 from plot
Chemical	First-order (F_1)	65.82	5.0873×10^{4}	0.9882	67.34	1.0329×10^{5}	0.9888	66.40	1.0953×10^{5}	0.9881	66.40	1.3118×10^{5}	0.9864
	Second-order (F_2)	94.62	3.0881×10^{7}	0.9559	94.62	6.1763×10^{7}	0.9563	96.89	9.7105×10^{7}	0.9563	95.55	6.9599×10^{7}	0.9524
	Third-order (F_3)	129.70	6.4717×10^{10}	0.9217	129.70	1.29434×10^{11}	0.9219	132.90	2.1212×10^{11}	0.9219	131.05	1.2162×10^{11}	0.9172
Diffusion	One-dimensional (D_1)	98.06	1.2944×10^{7}	0.9992	98.06	2.5889×10^{7}	0.9993	100.22	3.9199×10^{7}	0.9993	99.07	2.8758×10^{7}	0.9997
	Two-dimensional (D_2)	110.51	1.0282×10^{8}	0.9993	110.51	2.0565×10^{8}	0 .9996	112.97	3.1433×10^{8}	0.9996	111.67	2.1457×10^{8}	0.9992
	Three-dimensional J (D_3)	125.69	6.4219×10^{8}	0.9958	125.69	1.2844×10^{9}	0.9963	128.54	1.9907×10^{9}	0.9963	127.04	1.2459×10^{9}	0.9949
	Three-dimensional GB (D_4)	115.52	6.8969×10^{7}	0.9986	115.52	1.3794×10^{8}	0.9989	118.12	2.1179×10^{8}	0.9989	116.75	1.4021×10^{8}	0.9981
Phase interfacial	One-dimensional (R_1)	43.95	3.3309×10^{2}	0.9990	43.95	6.6618×10^{2}	0.9990	44.93	9.9444×10^{2}	0.9990	44.26	9.6170×10^{2}	0.9995
	Two-dimensional (R_2)	54.03	1.7353×10^{3}	0.9977	54.03	3.4705×10^{3}	0.9977	55.25	5.2249×10^{3}	0.9982	54.56	4.7584×10^{3}	0.9970
	Three-dimensional (R_3)	57.76	2.7237×10^{3}	0.9953	57.76	5.4473×10^{3}	0.9953	59.08	8.2295×10^{3}	0.9958	58.24	7.3348×10^{3}	0.9943
Nucleation and growth	Two-dimensional (A_2)	27.83	16.139	0.9845	27.83	3.2278×10^{1}	0.9845	28.48	48.360	0.9853	27.92	49.806	0.9819
	Three-dimensional (A_3)	15.17	0.799	0.9784	15.17	1.5984	0.9784	15.53	2.3829	0.9795	15.14	2.6205	0.9739

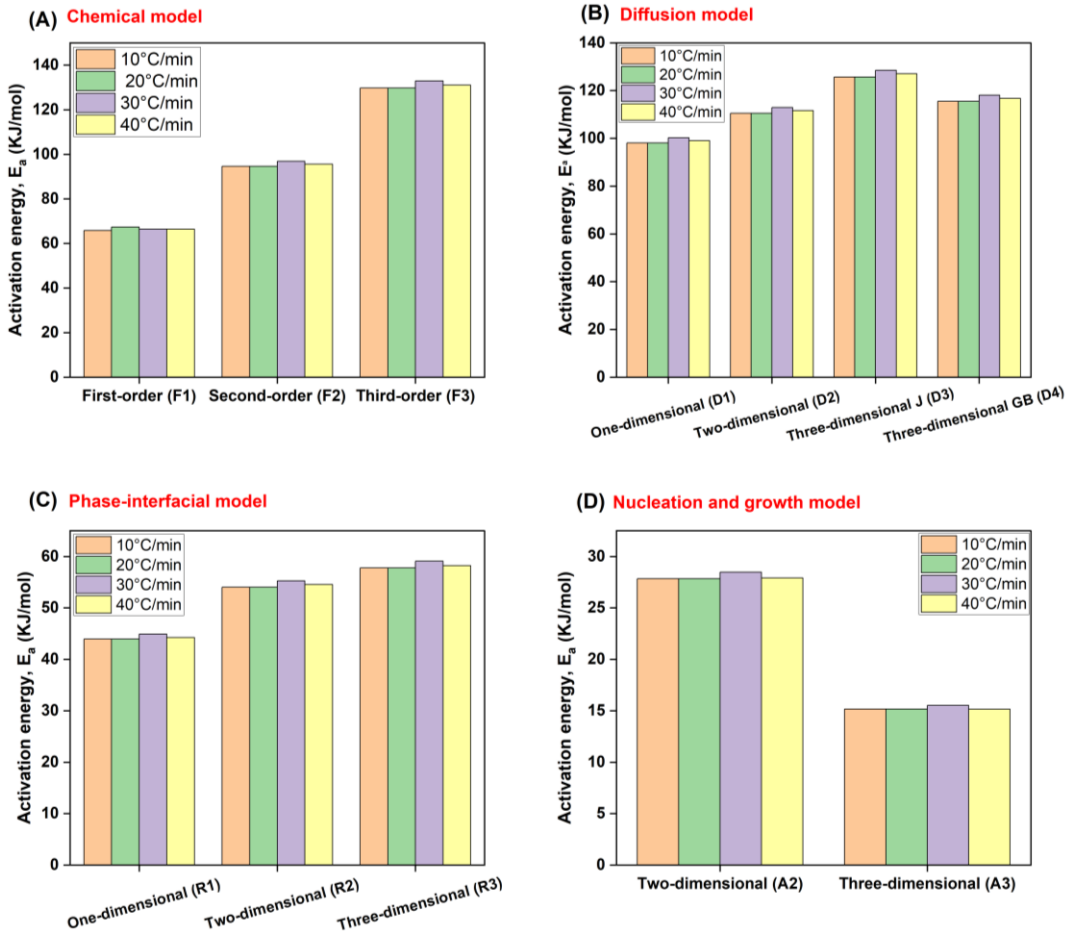

Figure 43: Dominant effect of heating rate only expressed at 30°C/min for all reaction models assumed in the CR method: (A) chemical model; (B) diffusion model; (C) phase-interfacial model; (D) nucleation and growth model

As depicted in Figure 43 (A-D), a notable difference in activation energies existed only at a heating rate of 30°C/min that may signify maximum conversion at this point unlike the ideal TGA curves where thermal decomposition temperatures increased closely (367-390°C) with step-wise increase of heating rate owing to reduced depolymerization time especially near the less conductive core. Same trends were observed for all other models too. Raza et al., 2023 reported a similar finding where activation energies increased till a specific heating rate after is stabilized or dropped. Although, this could be the case only till the maximum conversion is attained after which activation energies may decrease. This was also concurred from Mishra & Mohanty, 2018. On the whole, since each reaction model has a different but reasonably high correlation factor ($R^2 \geq 0.92$) and variable activation energies, it is difficult to assign the most suitable pathway mainly because pyrolytic decomposition of biomass could be viewed as a simultaneous process rather than being assumed as an individualistic system. This was exactly proved by Mian et al., 2019.

3.5.2 Model-free methods

Model-free or isoconversional methods like OFW, KAS, and FM did not rely on any pre-determined reaction models for computing variable activation energies of biomass pyrolysis reactions (Fischer et al., 2024). Instead, biomass conversion rate or α was relied upon for thermal degradation studies. However, as outlined in Shrivastava et al., 2023, isoconversional models have limitations wherein they assume only a single-step reaction and could neglect the role of competing reactions. On the other hand, kinetic analysis of CRD wood by CR method proved that competing reaction models are plausible for a thermochemical process like pyrolysis. A kinetic analysis, whether performed using model-fitting or model-free methods, considers biomass particles that weigh between 6-8 mg, i.e, very small. Henceforth, the temperature on the surface can reach the centre of the same particle within a short time frame that disregards any heat transfer limitations. However, in actual pyrolysis reactors, the particle

sizes of biomass can increase from a few cm to several inches and to even logs. This is where the importance of heat conductivity is compromised, but in reality, the temperature requirements rise drastically to satiate high activation energies for biomass conversion. Thus, a TGA-based study may mostly function depending upon kinetics only and could often overlook particle size, heating rate, composition of biomass (percentages of holocellulose and lignin), and the externalities caused by them. From Figure 44 (A-B), KAS and OFW plots together, seemed to slightly differ from FM plot.

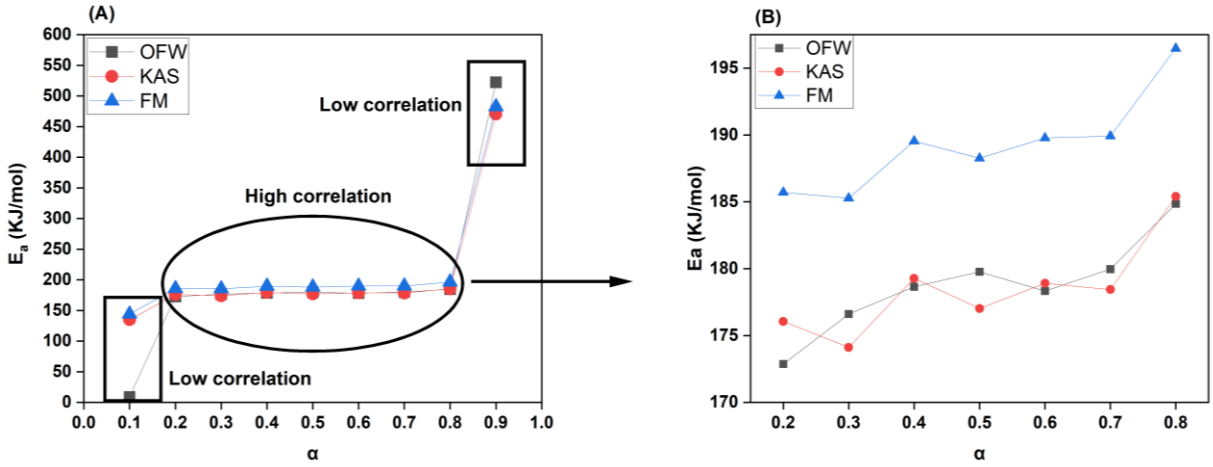

Figure 44: Variation in activation energies between OFW, KAS, and FM methods: (A) for α = 0.1-1.0; (B) for α = 0.2-0.8 only

For reference, the calculated kinetic parameters with the model correlation for each conversion stage is listed in Table 26. For this tabulation, α > 0.8 and α < 0.2 were not considered due to relatively low R^2 (0.41-0.64 for α = 0.1; 0.90-0.93 for α = 0.9) and non-linearity. For other conversion rates, R^2 is > 0.99 except for α = 0.2, under KAS and FM methods (R^2 = 0.98). A high correlation means that activation energies derived at these conversion rates using the three methods are accurate and dependable. The activation energies under OFW, KAS, and FM methods for α = 0.2-0.8 ranged from 172-185 kJ/mol, 176-186 kJ/mol, and 185-197 kJ/mol, respectively. This work discovered very minimal differences between overall activation energy requirements, along with increase in heating and conversion rates which may suggest fairly quick chemical reactions for activated intermediates formation, as stated in Bisen et al., 2024. An α = 0.8 showed the highest activation energy since the decomposition in this phase may have occurred against highly stable aromatics in lignin and resolute inorganics/AAEM in ash.

Table 26: Kinetic parameters of CRD wood pyrolysis computed by OFW, KAS, and FM isoconversional methods

Conversion rate , α	OFW method			KAS method			FM method		
	Activation energy, E_a (kJ/mol)	Pre-exponential factor, A (min^{-1})	R^2 from plot	Activation energy, E_a (kJ/mol)	Pre-exponential factor, A (min^{-1})	R^2 from plot	Activation energy, E_a (kJ/mol)	Pre-exponential factor, A (min^{-1})	R^2 from plot
0.1	8.85	49.51005146	0.414	135.06	2.08822E+12	0.599	144.09	2.9616E+14	0.637
0.2	172.87	8.40043E+14	0.990	176.05	1.6275E+15	0.987	185.71	2.15137E+17	0.988
0.3	176.61	7.47933E+14	0.997	174.12	4.35321E+14	0.998	185.27	8.42214E+16	0.998
0.4	178.65	6.27054E+14	0.996	179.28	6.85439E+14	0.996	189.54	1.17277E+17	0.997
0.5	179.77	4.95313E+14	0.997	177.02	2.79223E+14	0.999	188.26	6.43149E+16	0.999
0.6	178.33	2.6664E+14	0.999	178.91	2.85704E+14	0.997	189.77	6.86145E+16	0.998
0.7	179.97	2.79517E+14	0.999	178.44	1.98226E+14	0.998	189.92	6.3583E+16	0.998
0.8	184.86	5.32708E+14	0.999	185.41	5.66593E+14	0.997	196.47	2.06678E+17	0.997
0.9	522.38	7.94663E+39	0.927	470.58	4.06828E+35	0.901	482.38	1.04521E+38	0.905

FC in CRD wood biomass at 16-17% could also be targeted for decomposition during this stage. A significant difference in activation energy between each conversion rate was not observed since they varied very narrowly just like the TGA curves. Moreover, there was no defined increase in activation energy, and it was more or less

adopting a partly sinusoidal pattern. These fluctuations could be due to complex multi-step reactions as discussed in Patidar et al., 2022. We may, hence, infer that 82-83% of VC in CRD wood biomass's holocellulose component could be targeted from α = 0.2-0.7. A momentary jump in E_a could indicate that VC in biomass was either from heavier lignin bridges or was part of an organo-metallic linkage (eg: Fe-O-C; AAEM-O-C) which demand high energy for cleavage (metal content co-existing with biomass carbon and manifesting different degradation behaviours). Since the activation energy crosses 170 kJ/mol even at an initial conversion rate of 0.2, we may conclude that the overall rate of the reaction was slow. A summary plot of all isoconversional methods for the conversion rates between 0.2-0.8 is shown in Figure 45 (A-C).

CRD wood may thus, be an ineffective direct fuel source because it needs a high energy to start reacting. Converting it into biochar will help ease conductivity and heat transfer issues resulting in faster reaction times.

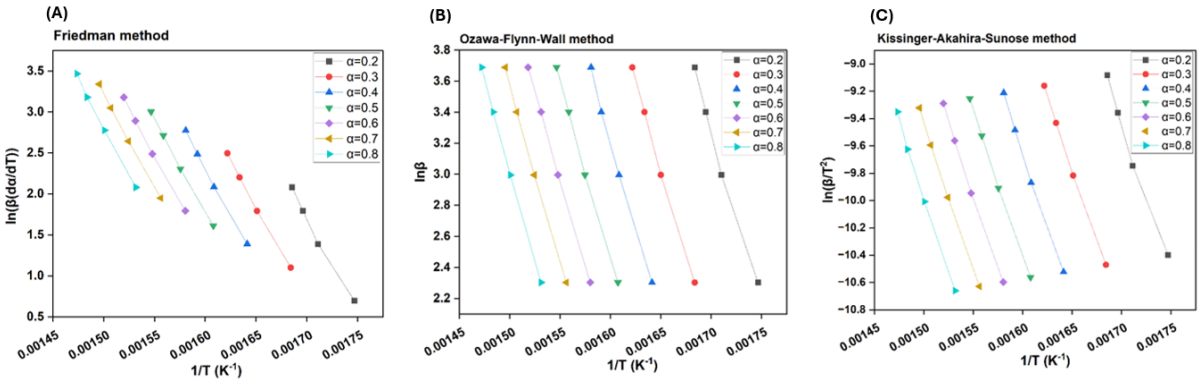

Figure 45: (A) Friedman (FM) method; (B) Ozawa-Flynn-Wall (OFW) method; and (C) Kissinger-Akahira-Sunose (KAS) method - plots for α=0.2-0.8

3.6 Thermodynamic parameters

For thermodynamic parameters, α < 0.2 and α > 0.8 are not considered because of low correlation factors encountered during the calculation of activation energies. As tabulated in Table 27, for OFW, KAS, and FM methods, ΔH did not vary largely with heating rates. Likewise, a lower influence of increasing conversion rates on ΔH also meant that the difference in energy requirement between reactants and the intermediates is less, that can aid in faster formation of activated complexes. Concomittantly, positive values of ΔH indicated endothermic (exothermic if ΔH < 0) reaction steps with heat absorption for biomass conversion and is in agreement with the findings from Shagali et al., 2023. ΔH was 179-180 kJ/mol, 179-181 kJ/mol, and 190-192 kJ/mol for OFW, KAS, and FM methods. This is in line with the findings for another woody biomass (*Ficus Nitida*) as discussed in Tabal et al., 2021. ΔG which describes the spontaneity of a reaction or a system indicated a minorly increasing trend with positive values for all heating rates, conversion rates, and methods. This means that the process was not spontaneous (only if ΔG < 0) and needed an external energy source to drive all parallel, sequential, and competing reactions. A ΔG of 215-230 kJ/mol was observed for both OFW and KAS methods between 0.2-0.8 conversion rates that represented consistent results. However, for FM method, ΔG ranged a bit higher from 250-275 kJ/mol. This is in agreement to the studies mentioned in Patil et al., 2023.

A chemical reaction like pyrolysis usually supports greater disorderliness and randomness represented by the system's entropy (ΔS > 0) where a solid biomass material breaks down into volatiles, gases, and oil which are relatively fluidic and harbor greater molecular freedom. On the contrary, as in Table 27, the ΔS values for OFW (-60 to -80 J/mol.K), KAS (-60 to -85 J/mol.K), and FM (-110 to -130 J/mol.K) non-isothermal methods are largely negative (ΔS < 0) which may mean that biomass sample under consideration could have lower molecular freedom and needs more energy to embrace further structural transformations during pyrolysis, as reflected from Kumar et al., 2024. Low ΔS could also be hinting that biomass may have undergone very gradual physical/chemical transformations, consistent with Singh et al., 2021. On a thermodynamical forefront, negative ΔS could arise from the formation of a more ordered or stable activated complex when some decomposition reactions unfolded as agreed in Lei et al., 2023, who used a heterogeneous and moderate-ash biomass feedstock (wheat straw). In other words, structural rearrangements of biomass in its intermediate state could have introduced a certain degree of resistance towards degradation. Given the highly heterogeneous nature of CRD wood feedstock composed of variable lignin percentages, painted or treated surfaces laden with diverse organic and inorganic constituents, localized chemical re-ordering could be plausible. This could lead to a limited molecular motion and

thus, negative ΔS. Interestingly, negativity in ΔS decreases with increase in α till a certain point signifying growing randomness in the system, before it increases yet again at higher α – possibly due to the influence of ash matter or the formation of stable metal-organic carbon complexes under high temperature decomposition.

3.7 Summary

To summarize, the kinetic analysis of CRD wood pyrolysis utilizing model-fitting and model-free methods has provided notable insights in the topic of thermochemical decomposition of complex heterogeneous biomass. This work has revealed that reasonable lignin content and low ash makes waste CRD wood a promising feedstock for pyrolytic biochar production. The decomposition process exhibited three distinctive breakdown phases: till 150°C, 200-400°C, and 400-600°C, amidst where peak weight loss occurred between 350-400°C. Under the four different heating rates (10-40°C/min) tested, the model-fitting CR method derived activation energies ranging from 65-133 kJ/mol for the chemical reaction models (F_1, F_2, F_3), 98-129 kJ/mol for the diffusion reaction models (D_1, D_2, D_3, D_4), 43-60 kJ/mol for phase interfacial reaction models (R_1, R_2, R_3), and 15-29 kJ/mol for random nucleation and growth reaction models (A_2, A_3). A peak in activation energies was seen especially at 30°C/min for all schemes. Model-free or isoconversional OFW, KAS, and FM methods yielded activation energies between 172-196 kJ/mol for the conversion rates of 0.2-0.8. Thermodynamical evaluations indicated positive values of ΔH and ΔG signifying an endothermic and non-spontaneous pyrolysis process.

Subsequent work in the domain of CRD wood pyrolysis kinetics and thermodynamics proffer under-stated research gaps. Firstly, CRD wood from different regions could be tested to understand the effect of feedstock variability with geography, demolition practices, and pre-processing/pre-treatment steps, on thermal decomposition behaviour. Secondly, different heating rates under 10°C/min can be experimented to discriminate TGA over significant slower pyrolysis conditions and their role on intrinsic heat transfer for a given biomass particle size. Another interesting area of work could be to estimate kinetic and thermodynamic behaviour of CRD wood co-pyrolysis with other organic substrates. On the whole, the present manuscript is important for the readers since it addresses the pressing issue of CRD wood waste management and also offers a viable valorization pathway via pyrolysis. Through the kinetic and thermodynamic analysis, the work contributes to some nascent knowledge on the interplay of pyrolysis independent variables like heating rate and temperature, the biochemical composition of CRD wood, and their synergistic influence on its strucutral breakdown.

Table 27: ΔH, ΔG, and ΔS calculated for each heating rate according to every isoconversional method

	Ea and A estimated from OFW method											
Conversion rate, α	Heating rate = 10°C/min Tm = 367.41			Heating rate = 20°C/min Tm = 382.48			Heating rate = 30°C/min Tm = 386.85			Heating rate = 40°C/min Tm = 389.62		
	ΔH (kJ/mol)	ΔG (kJ/mol)	ΔS (J/molK)	ΔH (kJ/mol)	ΔG (kJ/mol)	ΔS (J/molK)	ΔH (kJ/mol)	ΔG (kJ/mol)	ΔS (J/molK)	ΔH (kJ/mol)	ΔG (kJ/mol)	ΔS (J/molK)
0.1	3.52	-109.52	176.48	3.40	-112.44	176.68	3.36	-113.28	176.73	3.34	-113.82	175.99
0.2	167.54	216.73	-76.79	167.42	217.64	-76.60	167.38	217.90	-76.55	167.36	218.07	-76.23
0.3	171.28	219.86	-75.83	171.16	220.75	-75.64	171.12	221.00	-75.58	171.10	221.17	-75.26
0.4	173.32	220.96	-74.36	173.20	221.82	-74.17	173.16	222.08	-74.11	173.14	222.23	-73.80
0.5	174.44	220.82	-72.40	174.32	221.66	-72.21	174.28	221.90	-72.15	174.26	222.05	-71.85
0.6	173.00	216.08	-67.25	172.88	216.85	-67.06	172.84	217.07	-67.00	172.82	217.20	-66.72
0.7	174.64	217.97	-67.65	174.52	218.74	-67.45	174.48	218.96	-67.40	174.46	219.10	-67.12
0.8	179.53	226.30	-73.01	179.40	227.14	-72.81	179.37	227.39	-72.76	179.35	227.54	-72.45
0.9	517.05	872.53	-554.95	516.93	880.64	-554.76	516.89	883.00	-554.71	516.87	884.49	-552.39
	Ea and A estimated from KAS method											
Conversion rate, α	Heating rate = 10°C/min Tm = 367.41			Heating rate = 20°C/min Tm = 382.48			Heating rate = 30°C/min Tm = 386.85			Heating rate = 40°C/min Tm = 389.62		
	ΔH (kJ/mol)	ΔG (kJ/mol)	ΔS (J/molK)	ΔH (kJ/mol)	ΔG (kJ/mol)	ΔS (J/molK)	ΔH (kJ/mol)	ΔG (kJ/mol)	ΔS (J/molK)	ΔH (kJ/mol)	ΔG (kJ/mol)	ΔS (J/molK)
0.1	129.73	146.98	-26.93	129.61	147.14	-26.31	129.57	147.18	-26.14	129.55	147.21	-26.03
0.2	170.72	223.44	-82.29	170.60	224.43	-80.40	170.56	224.71	-79.87	170.54	224.89	-79.54
0.3	168.79	214.48	-71.33	168.66	215.30	-69.69	168.63	215.54	-69.23	168.61	215.69	-68.94

0.4	173.95	222.06	-75.10	173.83	222.94	-73.38	173.79	223.19	-72.89	173.77	223.36	-72.59
0.5	171.70	215.02	-67.64	171.57	215.79	-66.08	171.54	216.01	-65.64	171.51	216.15	-65.37
0.6	173.58	217.03	-67.83	173.46	217.80	-66.27	173.42	218.02	-65.83	173.40	218.17	-65.55
0.7	173.11	214.61	-64.79	172.98	215.33	-63.30	172.95	215.54	-62.88	172.93	215.68	-62.62
0.8	180.08	227.18	-73.52	179.96	228.03	-71.83	179.92	228.28	-71.35	179.90	228.44	-71.06
0.9	465.26	768.12	-472.81	465.13	774.99	-461.94	465.10	776.98	-458.88	465.07	778.25	-456.96
	Ea and A estimated from FM method											
Conversion rate, α	**Heating rate = 10°C/min Tm = 367.41**			**Heating rate = 20°C/min Tm = 382.48**			**Heating rate = 30°C/min Tm = 386.85**			**Heating rate = 40°C/min Tm = 389.62**		
	ΔH (kJ/mol)	**ΔG (kJ/mol)**	**ΔS (J/molK)**	**ΔH (kJ/mol)**	**ΔG (kJ/mol)**	**ΔS (J/molK)**	**ΔH (kJ/mol)**	**ΔG (kJ/mol)**	**ΔS (J/molK)**	**ΔH (kJ/mol)**	**ΔG (kJ/mol)**	**ΔS (J/molK)**
0.1	138.76	182.40	-68.13	138.64	183.18	-67.93	138.60	183.40	-67.88	138.58	183.54	-67.59
0.2	180.38	259.11	-122.90	180.26	260.71	-122.71	180.22	261.17	-122.65	180.20	261.47	-122.14
0.3	179.94	253.67	-115.11	179.81	255.15	-114.91	179.78	255.58	-114.86	179.75	255.86	-114.38
0.4	184.22	259.71	-117.86	184.09	261.24	-117.67	184.06	261.68	-117.61	184.03	261.96	-117.12
0.5	182.94	255.23	-112.86	182.81	256.68	-112.67	182.77	257.10	-112.62	182.75	257.37	-112.14
0.6	184.44	257.08	-113.40	184.32	258.54	-113.21	184.28	258.96	-113.15	184.26	259.23	-112.68
0.7	184.60	256.83	-112.77	184.47	258.28	-112.58	184.44	258.70	-112.52	184.41	258.97	-112.05
0.8	191.14	269.65	-122.57	191.01	271.25	-122.38	190.98	271.71	-122.32	190.95	272.00	-121.81
0.9	477.05	809.47	-518.94	476.93	817.04	-518.75	476.89	819.23	-518.69	476.87	820.62	-516.53

4. Conclusion

TGA was employed for assessing thermal stability and kinetic behaviour of CRD wood biomass under pyrolysis conditions. Different heating rates were utilized to analyze its thermochemical decomposition, revealing that the degradation is very complex, harbors multiple reaction steps, and could be jointly influenced by the feedstock's biochemical and surface chemical composition. For calculating kinetic parameters of pyrolysis, the weight loss data from TGA was ascribed to model-fitting and model-free/isoconversional methods which enabled the calculation of activation energies: the former method dependent on specific assumptions pertaining to different reaction models, while the latter method without any assumptions of such reaction schemes and only functioning on the basis of biomass conversion levels (α). The CR method's perspective ranked pyrolytic transformation based on the degree of fit or correlation obtained by ascribing TGA data to each model equation. The highest R^2 (consistently >0.99) was however, achieved only for the diffusion and phase interfacial models, thereby, bolstering their criticality in biomass pyrolysis. Higher heating rates during TGA also shifted peak melting temperatures of biomass constituents to higher temperatures necessitating optimization towards the direction of slow pyrolysis with low heating rates and long BRT. This could make sure there is gradual, yet steady heat transfer from the surface to the core of every biomass particle aiding complete conversion. On the other hand, the model-free OFW, KAS, and FM methods offered simple and time-effective calculations of pyrolysis kinetic parameters. Simple and straightforward estimations could be drawn for most biomass conversion stages (α=0.2-0.8) where the highest R^2 (mostly >0.99) was obtained. Extrapolating activation energies to specific energy demands across the pyrolytic transformation of CRD wood was possible and also corroborated with findings from similar works. Overall, despite a detailed outlook, experimental TGA data was well-aligned with kinetic models. Even thermodynamically speaking, these TGA tests that mimicked pyrolysis-like conditions, proved that CRD wood thermal degradation is an energy intensive process. The TGA results could be crucial for scaling up pyrolysis of CRD wood since they offer inputs on the decomposition kinetics of a biomass material within thermochemical settings. Moreover, insights on stability, reactivity, and disintegration of biomass polymers at specific conditions of temperature, heating rate and BRT could be obtained, which are essentialities for designing pyrolysis systems.

As much as the benefits of TGA-based kinetic parameter approximations have been discussed, acknowledging its limitations also remains vital. Firstly, these tests are conducted with meagre amounts of feedstock (8-10 mg) under controlled laboratory settings that may not represent pilot, demonstration, or industrial scale settings that are largely dynamic environments. Secondly, the particle size of biomass and the role of heat transfer within the particle differ largely between such settings. Thirdly, nuances in larger pyrolysis systems such as residence and eventual settling of volatiles on biomass, cracking of volatiles and their role in carbon polymerization to PAHs, and the interplay of any vacuum/suction effects across the reactor may not be achieved within TGA set-ups. Lastly, based on the different methods used to calculate kinetic parameters, especially model-fitting methods like CR, there could be inaccuracies posted due to the selection of wrong reaction models, assumptions, and corresponding findings derived that may fail to capture some intricacies of pyrolysis at higher scales.

Author Contributions: Conceptualization, methodology, validation, formal analysis, investigation, data curation, writing—original draft preparation, editing, visualization - **Aravind Ganesan**. Supervision, mentorship – **Simon Barnabé**. Supervision, review, mentorship – **Simon Langlois**. Supervision, review, editing, mentorship - **Olivier Rezazgui**. Supervision, review, editing, mentorship - **Younès Bareha**. Project administration – **Cyrine Boussabbeh**. Supervision, review, mentorship – **Patrice Mangin**. All authors have read and agreed to the published version of the manuscript.

Funding: This research was funded by MITACS, through Escouade Energie, Citeq, and supported by Innofibre, and I^2E^3 – UQTR, Québec, Canada. The work was conducted at Innofibre – Centre d'Innovation des Produits Cellulosiques, Trois-Rivières and at the Institute for Innovation in Ecomaterials, Ecoproducts, and Ecoenergies (I^2E^3), University of Québec Trois-Rivières (UQTR), Québec, Canada.

Data Availability Statement: Data will be shared upon request.

Acknowledgments: Due credits to the technicians, researchers, and colleagues who were a critical part of this work.

Conflicts of Interest: The authors declare no conflict of interest. The funders had no role in the design of the study; in the collection, analyses, or interpretation of data; in the writing of the manuscript; or in the decision to publish the results.

5. References

Adhikari, S., Moon, E., Paz-Ferreiro, J., & Timms, W. (2024). Comparative analysis of biochar carbon stability methods and implications for carbon credits. *Science of the Total Environment*, *914*, 169607.

Almusafir, R., & Smith, J. D. (2024). Thermal Decomposition and Kinetic Parameters of Three Biomass Feedstocks for the Performance of the Gasification Process Using a Thermogravimetric Analyzer. *Energies*, *17*(2), 396.

Altıkat, A., Alma, M. H., Altıkat, A., Bilgili, M. E., & Altıkat, S. (2024). A Comprehensive Study of Biochar Yield and Quality Concerning Pyrolysis Conditions: A Multifaceted Approach. *Sustainability*, *16*(2), 937.

Altynbaeva, D., Astafev, A., & Tabakaev, R. (2018). Kinetics of biomass low-temperature pyrolysis by coats–redfern method. In *MATEC Web of Conferences* (Vol. 194, p. 01058). EDP Sciences.

Apaydın Varol, E., & Mutlu, Ü. (2023). TGA-FTIR analysis of biomass samples based on the thermal decomposition behavior of hemicellulose, cellulose, and lignin. *Energies*, *16*(9), 3674.

Arenas, C. N., Navarro, M. V., & Martínez, J. D. (2019). Pyrolysis kinetics of biomass wastes using isoconversional methods and the distributed activation energy model. *Bioresource technology*, *288*, 121485.

Armynah, B., Tahir, D., Tandilayuk, M., Djafar, Z., & Piarah, W. H. (2019). Potentials of biochars derived from bamboo leaf biomass as energy sources: effect of temperature and time of heating. *International Journal of Biomaterials*, *2019*(1), 3526145.

Branca, C., & Galgano, A. (2024). Kinetic Modelling of Biomass Pyrolysis Processes. *Processes*, *12*(4), 706.

Bisen, D., Chouhan, A. P. S., Sarma, A. K., Rajamohan, S., Elumalai, P. V., Balasubramanian, D., & Cherie, A. (2024). Thermogravimetric analysis of rice husk and low-density polyethylene co-pyrolysis: kinetic and thermodynamic parameters. *Scientific Reports*, *14*(1), 31798.

Călin, C., Sîrbu, E. E., Tănase, M., Győrgy, R., Popovici, D. R., & Banu, I. (2024). A Thermogravimetric Analysis of Biomass Conversion to Biochar: Experimental and Kinetic Modeling. *Applied Sciences*, *14*(21), 9856.

Cao, J., Yu, Y., & Wu, H. (2023). Primary release and transformation of inorganic and organic sodium during fast pyrolysis of sodium-loaded lignin. *Proceedings of the Combustion Institute*, *39*(3), 3439-3446.

Chakravarty, K. H., Sadi, M., Chakravarty, H., Andersen, J., Choudhury, B., Howard, T. J., & Arabkoohsar, A. (2024). Pyrolysis kinetics and potential utilization analysis of cereal biomass by-products; an experimental analysis for cleaner energy productions in India. *Chemosphere*, *353*, 141420.

Channiwala, S. A., & Parikh, P. P. (2002). A unified correlation for estimating HHV of solid, liquid and gaseous fuels. *Fuel*, *81*(8), 1051-1063.

Chen, L., Hu, J., Han, Q., Xie, A., Zhou, Z., Yang, J., ... & Wu, F. (2022). Application of distributed activation energy model and Coats-Redfern integration method in the study of industrial lignin pyrolysis kinetics. *Biomass Conversion and Biorefinery*, 1-11.

Dhaundiyal, A., Singh, S. B., Hanon, M. M., & Rawat, R. (2018). Determination of kinetic parameters for the thermal decomposition of parthenium hysterophorus. *Environmental and Climate Technologies*, *22*(1), 5-21.

Dhyani, V., & Bhaskar, T. (2018). A comprehensive review on the pyrolysis of lignocellulosic biomass. *Renewable energy*, *129*, 695-716.

Dufourny, A., Van De Steene, L., Humbert, G., Guibal, D., Martin, L., & Blin, J. (2019). Influence of pyrolysis conditions and the nature of the wood on the quality of charcoal as a reducing agent. *Journal of Analytical and Applied Pyrolysis*, *137*, 1-13.

Elhenawy, Y., Fouad, K., Mansi, A., Bassyouni, M., Gadalla, M., Ashour, F., & Majozi, T. (2024). Experimental analysis and numerical simulation of biomass pyrolysis. *Journal of Thermal Analysis and Calorimetry*, 1-15.

Emiola-Sadiq, T., Zhang, L., & Dalai, A. K. (2021). Thermal and kinetic studies on biomass degradation via thermogravimetric analysis: a combination of model-fitting and model-free approach. *ACS omega*, *6*(34), 22233-22247.

Fanezouné, C. K., Dhahak, A., Peixinho, J., & El Bari, H. (2024). Thermogravimetric analysis and kinetic modeling for empty fruit bunch date palm pyrolysis. *Bioresource Technology Reports*, *27*, 101916.

Fischer, O., Lemaire, R., & Bensakhria, A. (2024). Thermogravimetric analysis and kinetic modeling of the pyrolysis of different biomass types by means of model-fitting, model-free and network modeling approaches. *Journal of Thermal Analysis and Calorimetry*, 1-23.

Ganesan, A., Rezazgui, O., Burgos, J. B., Mangin, P. J., & Barnabé, S. (2025). Valorization of lignocellulosic biomass forest residues in quebec via the integrated hydropyrolysis and hydroconversion (IH2) technology: A review. *Biomass and Bioenergy*, *193*, 107516.

Ganesan, A., Rezazgui, O., Langlois, S., Boussabbeh, C., & Barnabé, S. (2025). Pyrolytic conversion of construction, renovation, and demolition (CRD) wood wastes in Québec to biochar: Production, characterization, and identifying relevant stability indices for carbon sequestration. *Science of The Total Environment*, *965*, 178650.

Gani, A., Desvita, H., Munawar, E., Mamat, R., Nizar, M., Darnas, Y., & Sarjono, R. E. (2024). Comparative analysis of HHV and LHV values of biocoke fuel from palm oil mill solid waste. *Case Studies in Chemical and Environmental Engineering*, *9*, 100581

Giglio, E., Vitaali, G., Lanzini, A., & Santarelli, M. (2021). Integration between biomass gasification and high-temperature electrolysis for synthetic methane production. *Biomass and Bioenergy*, *148*, 106017.

Gmar, M., Bouafif, H., Bouslimi, B., Braghiroli, F. L., & Koubaa, A. (2022). Pyrolysis of chromated copper arsenate-treated wood: investigation of temperature, granulometry, biochar yield, and metal pathways. *Energies*, *15*(14), 5071.

Gonzalez-Aguilar, A. M., Cabrera-Madera, V. P., Vera-Rozo, J. R., & Riesco-Ávila, J. M. (2022). Effects of heating rate and temperature on the thermal pyrolysis of expanded polystyrene post-industrial waste. *Polymers*, *14*(22), 4957.

Grafmüller, J., Böhm, A., Zhuang, Y., Spahr, S., Müller, P., Otto, T. N., ... & Hagemann, N. (2022). Wood ash as an additive in biomass pyrolysis: effects on biochar yield, properties, and agricultural performance. *ACS Sustainable Chemistry & Engineering*, *10*(8), 2720-2729.

Guedes, R. E., Luna, A. S., & Torres, A. R. (2018). Operating parameters for bio-oil production in biomass pyrolysis: A review. *Journal of analytical and applied pyrolysis*, *129*, 134-149.

Gurtner, D., Kresta, M., Hupfauf, B., Götz, P., Nussbaumer, R., Hofmann, A., & Pfeifer, C. (2023). Mechanical strength characterisation of pyrolysis biochar from woody biomass. *Energy*, *285*, 129366.

Hadey, C., Malika, A., Mohammed, A., & Fatima, B. (2020). A study on the biomass wastes' combustion process and their biochar.

Han, H., Buss, W., Zheng, Y., Song, P., Rafiq, M. K., Liu, P., ... & Li, X. (2022). Contaminants in biochar and suggested mitigation measures–a review. *Chemical Engineering Journal*, *429*, 132287.

Hasan, M., Chakma, S., Liang, X., Sutradhar, S., Kozinski, J., & Kang, K. (2024). Engineered Biochar for Metal Recycling and Repurposed Applications. *Energies*, *17*(18), 4674.

Hassan, A. M. M., Asif, M., Hussain, T., Sajjad, R., Yasmin, F., & Khandaker, M. U. (2024). Pyrolysis of municipal solid waste: Kinetics and thermodynamic parameters via Coats-Redfern method. *Applied Chemical Engineering*, 1872-1872.

Ibitoye, S. E., Loha, C., Mahamood, R. M., Jen, T. C., Alam, M., Sarkar, I., ... & Akinlabi, E. T. (2024). An overview of biochar production techniques and application in iron and steel industries. *Bioresources and bioprocessing*, *11*(1), 65.

Johnston, C. T. (2017). 18 Biochar analysis by Fourier-transform infra-red spectroscopy. *Biochar: a guide to analytical methods*, 199.

Kizha, A. R., & Han, H. S. (2016). Processing and sorting forest residues: Cost, productivity and managerial impacts. *Biomass and Bioenergy*, *93*, 97-106.

Kumar, I., Tirlangi, S., Kathiresan, K., Sharma, V., Madhu, P., Sathish, T., ... & Murugan, P. (2024). Co-pyrolysis of furniture wood with mixed plastics and waste tyres: assessment of synergistic effect on biofuel yield and product characterization under different blend ratio. *Scientific reports*, *14*(1), 24584.

Kumar, V. K., Hallad, S. C., & Panwar, N. L. (2024). Thermogravimetric pyrolysis investigation of pistachio shell for its potential of thermal properties, kinetics and thermodynamics. *Discover Energy*, *4*(1), 7.

Laadila, M. A., LeBihan, Y., Caron, R. F., & Vaneeckhaute, C. (2021). Construction, renovation and demolition (CRD) wastes contaminated by gypsum residues: Characterization, treatment and valorization. *Waste Management*, *120*, 125-135.

Legan, M., Gotvajn, A. Ž., & Zupan, K. (2022). Potential of biochar use in building materials. *Journal of Environmental Management*, *309*, 114704.

Lei, J., Ye, X., Wang, H., & Zhao, D. (2023). Insights into pyrolysis kinetics, thermodynamics, and the reaction mechanism of wheat straw for its resource utilization. *Sustainability*, *15*(16), 12536.

Li, J., Shang, Y., Wei, W., Liu, Z., Qiao, Y., Qin, S., & Tian, Y. (2022). Comparative study on pyrolysis kinetics behavior and high-temperature fast pyrolysis product analysis of coastal zone and land biomasses. *ACS omega*, *7*(12), 10144-10155.

Li, J., Sun, W., Lichtfouse, E., Maurer, C., & Liu, H. (2024). Life cycle assessment of biochar for sustainable agricultural application: A review. *Science of The Total Environment*, 175448.

Liu, N., Huang, H., Feng, J., Li, R., Huang, X., & Wu, Y. (2025). Effects of alkali and alkaline earth metals in biomass on co-pyrolysis characteristics and product distribution of coal and biomass. *Fuel*, *389*, 134551.

Maaoui, A., Trabelsi, A. B. H., Abdallah, A. B., Chagtmi, R., Lopez, G., Cortazar, M., & Olazar, M. (2023). Assessment of pine wood biomass wastes valorization by pyrolysis with focus on fast pyrolysis biochar production. *Journal of the Energy Institute*, *108*, 101242.

Mahmood, H., Shakeel, A., Abdullah, A., Khan, M. I., & Moniruzzaman, M. (2021). A comparative study on suitability of model-free and model-fitting kinetic methods to non-isothermal degradation of lignocellulosic materials. *Polymers*, *13*(15), 2504.

Mian, I., Li, X., Jian, Y., Dacres, O. D., Zhong, M., Liu, J., ... & Rahman, N. (2019). Kinetic study of biomass pellet pyrolysis by using distributed activation energy model and Coats Redfern methods and their comparison. *Bioresource technology*, *294*, 122099.

Mishra, R. K., & Mohanty, K. (2018). Pyrolysis kinetics and thermal behavior of waste sawdust biomass using thermogravimetric analysis. *Bioresource technology*, *251*, 63-74.

Mishra, R. K., Mohanty, K., & Wang, X. (2020). Pyrolysis kinetic behavior and Py-GC–MS analysis of waste dahlia flowers into renewable fuel and value-added chemicals. *Fuel*, *260*, 116338.

Mlonka-Mędrala, A., Magdziarz, A., Dziok, T., Sieradzka, M., & Nowak, W. (2019). Laboratory studies on the influence of biomass particle size on pyrolysis and combustion using TG GC/MS. *Fuel*, *252*, 635-645.

Monir, M. U., Shovon, S. M., Akash, F. A., Habib, M. A., Techato, K., Abd Aziz, A., ... & Prasetya, T. A. E. (2024). Comprehensive characterization and kinetic analysis of coconut shell thermal degradation: Energy potential evaluated via the Coats-Redfern method. *Case Studies in Thermal Engineering*, *55*, 104186.

Mouneir, S. M., & El-Shamy, A. M. (2024). A review on harnessing the energy potential of pyrolysis gas from scrap tires: Challenges and opportunities for sustainable energy recovery. *Journal of Analytical and Applied Pyrolysis*, *177*, 106302.

Mukherjee, A., Okolie, J. A., Tyagi, R., Dalai, A. K., & Niu, C. (2021). Pyrolysis kinetics and activation thermodynamic parameters of exhausted coffee residue and coffee husk using thermogravimetric analysis. *The Canadian Journal of Chemical Engineering*, *99*(8), 1683-1695.

Najafi, H., Golrokh Sani, A., & Sobati, M. A. (2024). Thermogravimetric and thermo-kinetic analysis of sugarcane bagasse pith: a comparative evaluation with other sugarcane residues. *Scientific Reports*, *14*(1), 2076.

Nanda, S., Mohanty, P., Pant, K. K., Naik, S., Kozinski, J. A., & Dalai, A. K. (2013). Characterization of North American lignocellulosic biomass and biochars in terms of their candidacy for alternate renewable fuels. *Bioenergy Research*, *6*, 663-677.

Nhuchhen, D. R., & Afzal, M. T. (2017). HHV predicting correlations for torrefied biomass using proximate and ultimate analyses. *Bioengineering*, *4*(1), 7.

Nzediegwu, C., Naeth, M. A., & Chang, S. X. (2021). Elemental composition of biochars is affected by methods used for its determination. *Journal of Analytical and Applied Pyrolysis*, *156*, 105174.

O'Dwyer, J., Walshe, D., & Byrne, K. A. (2018). Wood waste decomposition in landfills: An assessment of current knowledge and implications for emissions reporting. *Waste Management*, *73*, 181-188.

Paredes, R., Castells, B., & Tascón, A. (2024). Thermogravimetric Assessment of Biomass: Unravelling Kinetic, Chemical Composition and Combustion Profiles. *Fire*, *7*(11), 396.

Patidar, K., Singathia, A., Vashishtha, M., Sangal, V. K., & Upadhyaya, S. (2022). Investigation of kinetic and thermodynamic parameters approaches to non-isothermal pyrolysis of mustard stalk using model-free and master plots methods. *Materials Science for Energy Technologies*, *5*, 6-14.

Patil, Y., Ku, X., & Vasudev, V. (2023). Pyrolysis characteristics and determination of kinetic and thermodynamic parameters of raw and torrefied Chinese fir. *ACS omega*, *8*(38), 34938-34947.

Pecha, M. B., Arbelaez, J. I. M., Garcia-Perez, M., Chejne, F., & Ciesielski, P. N. (2019). Progress in understanding the four dominant intra-particle phenomena of lignocellulose pyrolysis: chemical reactions, heat transfer, mass transfer, and phase change. *Green chemistry*, *21*(11), 2868-2898.

Peters, J. F., Iribarren, D., & Dufour, J. (2015). Biomass pyrolysis for biochar or energy applications? A life cycle assessment. *Environmental science & technology*, *49*(8), 5195-5202.

Pfersich, J., Arauzo, P. J., Modugno, P., Titirici, M. M., & Kruse, A. (2023). Evaluation of the Char Formation During the Hydrothermal Treatment of Wooden Balls. *Global Challenges*, *7*(12), 2300169.

Postawa, K., Fałtynowicz, H., Szczygieł, J., Beran, E., & Kułażyński, M. (2022). Analyzing the kinetics of waste plant biomass pyrolysis via thermogravimetry modeling and semi-statistical methods. *Bioresource Technology*, *344*, 126181.

Punsuwan, N., & Tangsathitkulchai, C. (2014). Product Characterization and Kinetics of Biomass Pyrolysis in a Three-Zone Free-Fall Reactor. *International Journal of Chemical Engineering*, *2014*(1), 986719.

Radojević, M., Janković, B., Jovanović, V., Stojiljković, D., & Manić, N. (2018). Comparative pyrolysis kinetics of various biomasses based on model-free and DAEM approaches improved with numerical optimization procedure. *PLoS One*, *13*(10), e0206657.

Rambhatla, N., Panicker, T. F., Mishra, R. K., Manjeshwar, S. K., & Sharma, A. (2024). Biomass pyrolysis for biochar production: Study of kinetics parameters and effect of temperature on biochar yield and its physicochemical properties. *Results in Engineering*, 103679.

Ranzi, E., Debiagi, P. E. A., & Frassoldati, A. (2017). Mathematical modeling of fast biomass pyrolysis and bio-oil formation. Note I: kinetic mechanism of biomass pyrolysis. *ACS Sustainable Chemistry & Engineering*, *5*(4), 2867-2881.

Rao, Y. K., Dhanalakshmi, C. S., Vairavel, D. K., Surakasi, R., Kaliappan, S., Patil, P. P., ... & Lalvani, J. I. J. (2022). Investigation on forestry wood wastes: pyrolysis and thermal characteristics of Ficus religiosa for energy recovery system. *Advances in Materials Science and Engineering*, *2022*(1), 3314606.

Raza, M., Abu-Jdayil, B., & Inayat, A. (2023). Pyrolytic kinetics and thermodynamic analyses of date seeds at different heating rates using the Coats–Redfern method. *Fuel*, *342*, 127799.

Saleem, M., & Bahadar, A. (2024). In-Depth Study on Synergic Interactions and Thermo-Kinetic Analysis of (Wheat Straw and Woody Sawdust) Biomass Co-Pyrolysis over Mussel Shell-Derived CaO Catalyst Using Coats–Redfern Method. *Catalysts*, *14*(9), 655.

Shagali, A. A., Hu, S., Li, H., Chi, H., Qing, H., Xu, J., ... & Xiang, J. (2023). Thermal behavior, synergistic effect and thermodynamic parameter evaluations of biomass/plastics co–pyrolysis in a concentrating photothermal TGA. *Fuel*, *331*, 125724.

Shrivastava, D. K., Singh, A. K., & Chakraborty, J. P. (2023). Model-free isoconversional methods to determine the intrinsic kinetics and thermodynamic parameters during pyrolysis of boiled banana peel: influence of inorganic species. *Bioresource Technology Reports*, *24*, 101676.

Silva, J., Teixeira, S., & Teixeira, J. (2023). A review of biomass thermal analysis, kinetics and product distribution for combustion modeling: From the micro to macro perspective. *Energies*, *16*(18), 6705.

Singh, R. K., Patil, T., Pandey, D., & Sawarkar, A. N. (2021). Pyrolysis of mustard oil residue: a kinetic and thermodynamic study. *Bioresource Technology*, *339*, 125631.

Sobek, S., & Werle, S. (2020). Kinetic modelling of waste wood devolatilization during pyrolysis based on thermogravimetric data and solar pyrolysis reactor performance. *Fuel*, *261*, 116459.

Szufa, S., Piersa, P., Adrian, Ł., Czerwińska, J., Lewandowski, A., Lewandowska, W., ... & Knapczyk, A. (2021). Sustainable drying and torrefaction processes of miscanthus for use as a pelletized solid biofuel and biocarbon-carrier for fertilizers. *Molecules*, *26*(4), 1014.

Tabal, A., Barakat, A., & Aboulkas, A. (2021). Pyrolysis of ficus nitida wood: determination of kinetic and thermodynamic parameters. *Fuel*, *283*, 119253.

Tariq, R., Saeed, S., Riaz, M., & Saeed, S. (2023). Kinetic and thermodynamic evaluation of almond shells pyrolytic behavior using Coats–Redfern and pyrolysis product distribution model. *Energy Sources, Part A: Recovery, Utilization, and Environmental Effects*, *45*(2), 4446-4462.

Thejaswini, N., Annapureddy, P. K. R., Rammohan, D., & Kishore, N. (2023). Kinetics and thermodynamics of non-isothermal pyrolysis of Terminalia chebula branches at different heating rates. *International Journal of Chemical Kinetics*, *55*(11), 673-687.

Thiru, S., Kola, R., Thimmaraju, M. K., Dhanalakshmi, C. S., Sharma, V., Sakthi, P., ... & Lalvani, J. I. J. (2024). An analytical characterization study on biofuel obtained from pyrolysis of Madhuca longifolia residues. *Scientific Reports*, *14*(1), 14745.

Uwaoma, R. C., Schröer, B. J., Strydom, C. A., Bunt, J. R., Matjie, R. H., Mphahlele, K., & Meyer, J. A. (2022). Kinetics, thermodynamics, and thermal decomposition characteristics of co-pyrolysis of municipality solid waste residue hydrochar and< 1.5 g/cm3 fraction of South African discarded fine coal. *Bioresource Technology Reports*, *18*, 100998.

Wang, L., Lei, H., Liu, J., & Bu, Q. (2018). Thermal decomposition behavior and kinetics for pyrolysis and catalytic pyrolysis of Douglas fir. *RSC advances*, *8*(4), 2196-2202.

Wang, W., Lemaire, R., Bensakhria, A., & Luart, D. (2022). Analysis of the catalytic effects induced by alkali and alkaline earth metals (AAEMs) on the pyrolysis of beech wood and corncob. *Catalysts*, *12*(12), 1505.

Wang, T., Tang, L., Xu, J., Ding, L., & Chen, X. (2022). Influence of organic binders on the pyrolysis performance of rice straw pellets. *Journal of Analytical and Applied Pyrolysis*, *161*, 105366.

White, J. E., Catallo, W. J., & Legendre, B. L. (2011). Biomass pyrolysis kinetics: a comparative critical review with relevant agricultural residue case studies. *Journal of analytical and applied pyrolysis*, *91*(1), 1-33.

Xia, C., Cai, L., Zhang, H., Zuo, L., Shi, S. Q., & Lam, S. S. (2021). A review on the modeling and validation of biomass pyrolysis with a focus on product yield and composition.

Yildiz, M. J., Wurzer, C., Robinson, T., Wietecha, J., & Mašek, O. (2025). Biochar from pellets: Influence of binders and pyrolysis temperature on physical properties of pyrolyzed pellets. *Sustainable Materials and Technologies*, e01327.

Zhang, X., Chen, C., Tang, C., & Wang, Y. (2022). Morphological control of biochar with emerging functionalities by thermodynamic and kinetic approaches. *Accounts of Materials Research*, *3*(5), 525-539.

Zhang, Y., Liang, Y., Li, S., Yuan, Y., Zhang, D., Wu, Y., ... & Xia, C. (2023). A review of biomass pyrolysis gas: Forming mechanisms, influencing parameters, and product application upgrades. *Fuel*, *347*, 128461.

Zhong, Y., Ding, Y., Lu, K., Mao, S., & Li, C. (2023). Kinetic parameters and reaction mechanism study of biomass pyrolysis by combined kinetics coupled with a heuristic optimization algorithm. *Fuel*, *334*, 126622.

Zsinka, V., Tarcsay, B. L., & Miskolczi, N. (2024). Determination of Kinetic and Thermodynamic Parameters of Biomass Gasification with TG-FTIR and Regression Model Fitting. *Energies*, *17*(8), 1875.

CHAPTER 6 - THESIS CONCLUSION

The global pursuit of sustainable waste management practices and carbon-neutral energy systems has underscored the urgent need to valorize organic residues such as construction, renovation, and demolition (CRD) wood waste. This dissertation provides a comprehensive exploration of the potential of CRD wood as a feedstock for biochar production via slow pyrolysis, demonstrating its applicability across environmental, industrial, and energy sectors. By systematically examining the effects of process parameters, material characterization, stability indices, scalability, and practical use cases, the study reinforces the critical role of pyrolysis in circular economy pathways. Each chapter's insights converge toward a central conclusion: CRD wood biochar, when produced under optimized conditions, offers a technically viable, environmentally beneficial, and economically promising solution to the growing burden of construction waste.

At its core, this work validates the hypothesis that pyrolysis is an efficient thermochemical method for converting heterogeneous, non-recyclable CRD wood residues into stable, carbon-rich biochar. The findings reveal that slow pyrolysis under controlled conditions - specifically at moderate (400–600 °C) to high (>600 °C) temperatures and adequate biomass residence time (BRT) - results in a desirable transformation of feedstock. Higher pyrolysis temperatures consistently enhance key parameters: carbon content, fixed carbon (FC), thermostable fraction (TSF), Van-Krevelen indices (H/C, O/C), and surface area. Such properties not only reinforce the stability of the resulting biochar but also determine its usability in downstream industrial applications. Across multiple reactor configurations, including laboratory-scale horizontal tube furnace, semi-pilot rotary retort-kiln furnace, and pilot-scale retort-kiln furnace assemblies, pyrolysis parameters were optimized to balance thermal efficiency and product quality. The reproducibility of physicochemical properties across scales suggests that CRD wood biochar production can be viably scaled for commercial operations, an essential prerequisite for industry adoption.

A significant contribution of this study lies in the multi-index approach adopted for assessing biochar quality and stability. While proximate and ultimate analyses offered initial insights into elemental composition, more advanced techniques - Fourier Transform Infrared Spectroscopy (FTIR), Raman spectroscopy, thermogravimetric analysis (TGA), TGA-R50, and scanning electron microscopy (SEM) coupled with energy dispersive X-ray spectroscopy (SEM-EDX) - were employed to derive deeper structural and morphological insights. The results confirm that no single index is sufficient to assess biochar stability comprehensively. For instance, the H/C and O/C ratio were found to decrease significantly with increasing temperature, signalling progressive aromatization and carbon condensation. However, these parameters alone could not elucidate the structural integrity or ash composition. Raman spectroscopy complemented these findings by providing the I_D/I_G ratios that quantified the extent of graphitic condensation. TGA-R50 values and thermostable fractions further correlated well with chemical stability, reinforcing the importance of integrating thermal and molecular indicators. These analytical approaches collectively support the interpretation that CRD wood biochar, especially those produced above 600°C, exhibits high recalcitrance, low volatile matter, and favorable carbon architecture, making it suitable for carbon sequestration, pollutant adsorption, and metallurgy.

Temperature emerged as the most influential factor amidst all experimental findings, shaping not just the yield but also the stability, reactivity, and porosity of the biochar. At elevated temperatures (800–850 °C), carbon content reached up to 90%, while FC increased to 70-78%, and surface area ranged from 220-380 m²/g depending on post-treatment. These characteristics are ideal for applications demanding high thermal stability, such as metallurgical reductants or advanced adsorbents. However, optimization also entailed trade-offs. The highest surface area was observed at moderate temperatures (600 °C), after which it began to decline due to micropore collapse and mesopore formation. Furthermore, post-heat treatments (PHTs) enhanced aromaticity and reduced volatile content, but extended durations (*e.g.*: 90 min) also resulted in notable yield losses (~20%). The findings reiterate the necessity for application-specific tailoring. For instance, moderately pyrolyzed biochars (500–600 °C) offer a balance between porosity and surface functionality, rendering them ideal for water treatment or soil remediation. In contrast, high-temperature biochars (>700 °C), with their condensed aromatic networks and minimal volatiles, are more suitable for metallurgical applications and long-term carbon storage.

The study recognizes the inherent challenges posed by the heterogeneous composition of CRD wood waste. Varying levels of lignin, cellulose, hemicellulose, and inorganic contaminants such as alkali and alkaline earth metals (AAEM) and heavy metals (Cu, Cr, Pb, Zn) were identified. These compositional disparities influence pyrolysis behavior, product yield, and the environmental suitability of the resulting biochar. For instance, AAEMs, while catalyzing certain pyrolysis reactions, also risk increasing ash content and degrading biochar stability. Pre-treatment methods such as acid washing were shown to effectively leach out such metals, thereby improving

thermal degradation patterns and final product quality. The presence of lignin in higher concentrations, particularly in hardwood-derived CRD wood, was beneficial for producing biochar with greater aromaticity and thermal resilience. Thermogravimetric studies identified three distinct degradation stages in CRD biomass, with the main devolatilization occurring between 200–400 °C, highlighting the significance of this temperature window in process control. The kinetic and thermodynamic modeling further confirmed that CRD wood pyrolysis is endothermic and non-spontaneous, necessitating external energy input and precise thermal management.

A notable achievement of this dissertation was the successful demonstration of pilot-scale slow pyrolysis using rotary retort furnaces. By processing 3–4 kg of feedstock under optimized conditions, comparable or superior biochar properties were achieved relative to bench-scale trials. Such scalability is vital for the commercialization of pyrolysis systems that aim to process regional CRD waste volumes sustainably. Additionally, the emergence of mobile pyrolysis units presents a compelling opportunity to reduce logistical costs and facilitate on-site biochar production at waste generation sites. This decentralized model aligns with circular economy goals by minimizing transport emissions and maximizing local resource valorization. The economic analysis, though preliminary, supports the viability of pyrolysis ventures in regions like Québec, Canada. Despite recovery costs ranging from $31.6/t to $181/t, depending on CRD wood quality, the strategic integration of pyrolysis into waste management systems could offset these expenses through carbon credits, renewable energy incentives, and biochar co-product valorization.

Biochar derived from CRD wood demonstrated a wide array of potential applications, including soil amendments and pH regulation, water and wastewater treatment, carbon sequestration and GHG mitigation, and metallurgical reductants. Moderate-temperature biochars with alkaline pH and high CEC support soil remediation and fertility enhancement, while B600-type biochars facilitate over 90% removal efficiency of methyl orange dye in water treatment. High-temperature biochars with low H/C and O/C ratios are excellent candidates for long-term carbon storage, and B800 and post-heat-treated biochars meet key benchmarks for blast furnace applications due to their fixed carbon, thermal resilience, and low volatile content. However, safe storage and handling are crucial due to the potential for biochar self-heating. Optimized biochars like HTB525 have passed self-heating assessments under elevated temperature and moisture conditions, but storage protocols need to be established based on particle size, moisture, and volume-to-surface ratio to prevent auto-ignition hazards.

Yet, several areas to improve, surround CRD wood biochar production in terms of operation, characterization, engineering, and even logistics. However, the first and foremost problem to counter is the inconsistent quality and contamination levels in CRD wood waste that varies with geography, chemical treatment type, CRD practices, sourcing and storing the waste, as well as the recycling centers' techniques to process these residues. These differ largely, region-wise. The thermal degradation patterns of CRD wood during pyrolysis was validated via kinetic and thermodynamic analysis that also agreed with the complexity of this feedstock. Other challenges w.r.t economical feasibility of scaling up pyrolysis reactors, and the need for sustainable co-product utilization/credits to make such ventures profitable, loom greatly over this valorization technique. Nevertheless, since pyrolysis is a globally well-established process for at least a couple of decades now and with even more efficiency, technical know-how to handle a complex feedstock like CRD wood may not pose a substantial threat to project owners. Nowadays, portable mobile pyrolysis units are gaining worldwide attention where different feedstock streams can be treated together under optimized conditions at the waste generation sites itself, thereby, reducing the burden on logistical costs. The next challenge circumvents CRD wood biochar's self-heating risk that might be detrimental during downstream supply chain steps such as storage and transportation. In this case, our findings may have opened an opportunity for further research in this area either via advanced thermal imaging, heat transfer, or experimental modelling studies that can extrapolate ideal biochar handling practices at suitable storage scales and volumes. It also lays the path for post-pyrolysis biochar passivation steps like thermal activation that could be accomplished without the use of chemicals or reactive atmospheres. Physical or chemical activation are greatly beneficial but also have a disadvantage - unnecessarily add to process costs if apt reusability or activation agent looping designs are not adopted, and downstream water pollution.

Lastly, a myriad of diverse potential research prospects in this area, await! The first suggestion will necessitate researchers to be circumspective when using the Van-Krevelen index, H/C, since this could represent both organic and inorganic carbon in biomass/biochar. Since the transformative pathway taken by biomass's organic carbon throughout the course of pyrolysis to aromatized/graphitized carbon, forms a better foundation to describe its stability, reactivity, or permeance, the index $H/C_{organic}$ could rather be used for referring only to the organic carbon maceralization. Secondly, another technique called Inertinite reflectance/benchmark (R_o) for biochar stability

evaluation with regard to carbon-dioxide reduction and removal projects, can be adopted. Thirdly, while examining biochar self-ignition behaviour, particle sizes <100 μm would have to be tested since an increase in surface area to volume ratio could offer additional interesting insights about this metric like a drastic increase in active site availability for ambient air adsorption (both on the surface and in pores). Fourthly, secondary thermal activation for shorter durations (0-30 min) and higher temperatures (>600 °C) could be tested to reduce biochar volatiles content, and to increase carbon content and FC, that are critical pre-requisites for an application like blast-furnace reductants where any marked changes distant to properties of conventional metallurgical coke, may prove to be an irreversible externality w.r.t final metal quality. Quenching biochar immediately after production may leach volatiles and some weak ash elements too – but once again with the problem of water contamination. Finally, a lifecycle analysis (LCA) and a technoeconomic analysis (TEA) have to be performed to analyze the overall carbon footprint and costs/profitability sustained right from feedstock sourcing to end product generation/usage. Albeit, the suggestions provided here are non-exhaustive.

Ultimately, this work bolsters the role of pyrolysis in the conversion of a problematic, non-recyclable, and end-of-life lignocellulosic biomass residue like CRD wood into valuable bio-based materials, thus contributing to sustainable waste management, decarbonization, and fostering a circular economy.